FLYWHEEL STABILIZED, MAGNETICALLY TORQUED ATTITUDE CONTROL SYSTEM FOR METEOROLOGICAL SATELLITES STUDY PROGRAM

FINAL REPORT
25 MAY 1964 THROUGH 20 SEPTEMBER 1964
CONTRACT NO. NAS5-3886

FACILITY FORM 602
X65 16862 (ACCESSION NUMBER)
108 (PAGES)
CR-63453 (NASA CR OR TMX OR AD NUMBER)
2C (THRU)
(CODE)
03 (CATEGORY)

Prepared for

NATIONAL AERONAUTICS AND SPACE ADMINISTRATION
GODDARD SPACE FLIGHT CENTER
GREENBELT, MARYLAND

Prepared by

ASTRO-ELECTRONICS DIVISION
DEFENSE ELECTRONIC PRODUCTS
RADIO CORPORATION OF AMERICA
PRINCETON, NEW JERSEY

AVAILABLE TO U.S. GOVERNMENT AGENCIES ONLY

(NASA-CR-139049) FLYWHEEL STABILIZED, MAGNETICALLY TORQUED ATTITUDE CONTROL SYSTEM FOR METEOROLOGICAL SATELLITE STUDY PROGRAM Final Report, 25 May - 20 Sep. 1964 (Radio Corp. of America) 108 p
N74-75438
Unclas
00/99 44769

AED R-2493

Issued: 4 December 1964

FLYWHEEL STABILIZED, MAGNETICALLY TORQUED ATTITUDE CONTROL SYSTEM FOR METEOROLOGICAL SATELLITES STUDY PROGRAM

FINAL REPORT
25 MAY 1964 THROUGH 20 SEPTEMBER 1964
CONTRACT NO. NAS5-3886

Prepared for

NATIONAL AERONAUTICS AND SPACE ADMINISTRATION
GODDARD SPACE FLIGHT CENTER
GREENBELT, MARYLAND

Prepared by

ASTRO-ELECTRONICS DIVISION
DEFENSE ELECTRONIC PRODUCTS
RADIO CORPORATION OF AMERICA
PRINCETON, NEW JERSEY

AVAILABLE TO U.S. GOVERNMENT AGENCIES ONLY

AED R-2493

Issued: 4 December 1964

Page intentionally left blank

Page intentionally left blank

PREFACE

This report presents the results of the detailed design studies performed to determine a firm approach toward a final specification for a three-axes attitude control system for meteorological satellites. The study described was performed by the Astro-Electronics Division of RCA, under Contract No. NAS5-3886, for the National Aeronautics and Space Administration, Goddard Space Flight Center. The period covered by the report extends from 25 May 1964 through 13 October 1964.

TABLE OF CONTENTS

Section		Page
1.0	SUMMARY	1.1- 1
	1.1 Introduction	1.1- 1
	1.2 System Constraints	1.2- 1
	1.3 Summary of Results	1.3- 1
2.0	SYSTEMS ANALYSIS	2.1- 1
	2.1 Coordinate Systems	2.1- 1
	2.2 General Magnetic-Field Equations	2.2- 1
	2.3 General Dynamical Equations	2.3- 1
	2.3.1 Dynamic Equations	2.3- 1
	2.3.2 Momentum Considerations	2.3- 3
	2.3.3 Control Considerations	2.3- 5
	2.3.4 Disturbance Analysis	2.3- 8
3.0	PRELIMINARY DESIGN ANALYSIS	3.1- 1
	3.1 Pitch-Axis-Stabilization Control Subsystem	3.1- 1
	3.1.1 General	3.1- 1
	3.1.2 Discussion and Parametric Results	3.1- 4
	3.1.3 Preliminary Design of Subsystem	3.1-11
	3.1.4 Summary of Significant Parameters and Performance	3.1-40
	3.2 Magnetic Control Subsystems	3.2- 1
	3.2.1 General	3.2- 1
	3.2.2 Quarter Orbit Magnetic Attitude Control (QOMAC)	3.2- 3
	3.2.3 Magnetic-Bias Torquing	3.2-12
	3.2.4 Momentum Control	3.2-15
	3.2.5 Coil Designs	3.2-22
	3.2.6 Summary of Parameters	3.2-29
	3.3 Nutation-Control Subsystem	3.3- 1
	3.3.1 General	3.3- 1
	3.3.2 Description of Spacecraft Motion	3.3- 1
	3.3.3 Nutation-Damper Operation	3.3- 4
	3.4 Sensor Subsystem	3.4- 1
	3.4.1 General	3.4- 1
	3.4.2 Mathematical Description of Sensor Subsystem	3.4- 4

TABLE OF CONTENTS (Continued)

Section			Page
		3.4.3 Discussion and Parametric Results	3.4-10
	3.5	Command and Control Subsystem	3.5- 1
		3.5.1 General	3.5- 1
		3.5.2 Clock Compatibility	3.5- 3
		3.5.3 Clock Interface	3.5- 3
		3.5.4 Attitude-Control Programmer Analysis	3.5- 3
		3.5.5 Momentum-Control Programmer Analysis	3.5- 4
		3.5.6 Programmer Design	3.5- 4
		3.5.7 Auxiliary Functions	3.5- 7
	3.6	Telemetry Subsystem	3.6- 1
		3.6.1 General	3.6- 1
		3.6.2 Attitude-Data Transmission Techniques	3.6- 1
		3.6.3 Housekeeping-Data Transmission Techniques	3.6- 3
	3.7	Launch-Mode and Initial-Alignment	3.7- 1
		3.7.1 General	3.7- 1
		3.7.2 Discussion and Parametric Results	3.7- 1
		3.7.3 Preliminary Design of Subsystem	3.7- 3
		3.7.4 Summary of Significant Parameters and Performance	3.7- 5
	3.8	Data-Processing Subsystem and Ground Commands	3.8- 1
		3.8.1 Specifications and General Operation	3.8- 1
		3.8.2 Equipment Requirements	3.8- 3
		3.8.3 Attitude and Momentum Determinations and Command Computation	3.8- 4
4.0		SYSTEM ACCURACY ANALYSIS	4.1- 1
	4.1	Pointing Accuracy	4.1- 1
		4.1.1 Pitch-Axis	4.1- 1
		4.1.2 Roll and Yaw Axes	4.1- 1
	4.2	Jitter Accuracy	4.2- 1
		4.2.1 Pitch-Axis	4.2- 1
		4.2.2 Roll and Yaw Axes	4.2- 1
	4.3	Summary	4.3- 1
5.0		SYSTEM RELIABILITY AND FAILURE-MODE ANALYSIS	5.1- 1
	5.1	General	5.1- 1
	5.2	Failure-Mode and Effects Analysis	5.2- 1
	5.3	Reliability Analysis	5.3- 1
		5.3.1 System Description	5.3- 1
		5.3.2 Operating Time	5.3- 1

TABLE OF CONTENTS (Continued)

Section		Page
	5.3.3 Reliability Block Diagram	5.3- 2
	5.3.4 Part Failure-Rates	5.3- 2
	5.3.5 Survival Probability	5.3- 5
	5.3.6 Additional Analyses	5.3- 6
6.0	SYSTEM-PERFORMANCE TEST REQUIREMENTS	6.1- 1
	6.1 Pitch-Axis Simulation	6.1- 1
	6.1.1 Component Testing	6.1- 1
	6.1.2 Subsystem Evaluation	6.1- 1
	6.1.3 "Torque-Free" Testing of the Pitch-Axis-Stabilization Control Subsystem	6.1- 2
	6.1.4 Tentative Specifications for Air-Bearing Test	6.1- 3
	6.2 Nutation-Damper Operation	6.2- 1
	6.3 Magnetic Testing	6.3- 1
	6.4 Horizon Sensor	6.4- 1
7.0	SYSTEM ENGINEERING	7.1- 1
	7.1 General	7.1- 1
	7.2 Mechanical Design	7.2- 1
	7.2.1 Control-Equipment Packaging	7.2- 1
	7.2.2 Control-Equipment Geometry	7.2- 1
	7.2.3 Electro-Mechanical Design	7.2- 8
	7.3 System Power Requirements	7.3- 1
	7.3.1 Initial Alignment or Transient Upset	7.3- 1
	7.3.2 Operational Mode	7.3- 3
	7.4 System Interfaces	7.4- 1
	7.4.1 Power	7.4- 1
	7.4.2 Telemetry	7.4- 1
	7.4.3 Command and Control	7.4- 1
8.0	APPROACH TO SYSTEM SPECIFICATIONS	8.1- 1
	8.1 General	8.1- 1
	8.2 System-Input Specifications	8.2- 1
	8.3 Subsystem Specifications	8.3- 1
	8.4 Component Specifications	8.4- 1
9.0	CONCLUSIONS AND RECOMMENDATIONS	9.1- 1
	9.1 Conclusions	9.1- 1
	9.1.1 Summary of Results	9.1- 1

TABLE OF CONTENTS (Continued)

Section		Page
	9.1.2 Performance Verification	9.1- 2
	9.1.3 Ground Stations	9.1- 2
	9.2 Recommendations	9.2- 1
	9.2.1 Review Need for Rockets	9.2- 1
	9.2.2 Development of the Pitch-Axis Drive	9.2- 1
	9.2.3 Pitch-Axis Attitude Sensing	9.2- 1
	9.2.4 Alternate Sources for Pitch-Axis-Stabilization Control Motor	9.2- 2
	9.2.5 Computer Analysis	9.2- 4
	9.2.6 Data Transmission	9.2- 6
10.0	BIBLIOGRAPHY	10.0- 1

LIST OF ILLUSTRATIONS

Figure		Page
1.3- 1	Elevation View of FSMTMS General Arrangement	1.3- 2
1.3- 2	Functional Block Diagram of the Flywheel Stabilized, Magnetically Torqued Attitude Control System	1.3- 5
2.1- 1	Drawing Depicting the Orbital Coordinates Used for Systems Analysis	2.1- 2
2.1- 2	Drawing Depicting the Geomagnetic Coordinates Used for Systems Analysis	2.1- 2
2.1- 3	Drawing Depicting the Vehicle Coordinates Used for Systems Analysis	2.1- 3
2.3- 1	Euler Angles Used to Describe Spacecraft Body Motion	2.3- 2
2.3- 2	Dynamic Weight Versus System Momentum	2.3- 3
2.3- 3	Minimum Dynamic Weight Versus Damping-Time-Constant	2.3- 4
3.1- 1	Block Diagram of the Pitch-Axis-Stabilization Control Subsystem	3.1- 2
3.1- 2	Block Diagram of the Pulse-Width-Modulator (PWM) Error Detector	3.1- 4
3.1- 3	Error-Measurement Characteristics	3.1- 5
3.1- 4	Bode Plot for the Recommended Pitch-Axis-Stabilization Control Subsystem Using Lag-Lead Compensation	3.1- 8
3.1- 5	Block Diagram of the Analog Computer Setup	3.1-13
3.1- 6	Typical Results Obtained from the Analog Computer Study	3.1-15
3.1- 7	Typical Results Obtained from the Analog Computer Study	3.1-16
3.1- 8	Typical Results Obtained from the Analog Computer Study	3.1-17
3.1- 9	Typical Results Obtained from the Analog Computer Study	3.1-19
3.1-10	Typical Results Obtained from the Analog Computer Study	3.1-21
3.1-11	Typical Results Obtained from the Analog Computer Study	3.1-23
3.1-12	Photograph of Subsystem Simulator for Demonstrating Pitch-Axis-Stabilization Control	3.1-25
3.1-13	Schematic Diagrams and Transfer Functions of Various Compensation-Amplifier Techniques	3.1-27
3.1-14	Noise Model for an Operational Amplifier	3.1-27
3.1-15	Earth-Detecting Circuit	3.1-29
3.1-16	Schematic Representation of Experimental Vapor-Lubrication System	3.1-34
3.1-17	Summary of Procedure Data Used to Determine Prediction of Lubricant Loss-Rate	3.1-35

LIST OF ILLUSTRATIONS (Continued)

Figure		Page
3.2-1	Principles of Magnetic Attitude Control	3.2- 2
3.2-2	Phasing and Cycling of Coil Current in QOMAC Torquing	3.2- 6
3.2-3	Geometry of ϕ_{max} and λ Shown in $\hat{t}$, $\hat{b}$, $\hat{n}$, Coordinates	3.2- 8
3.2-4	Effect of Dipole Model on QOMAC Start Angle	3.2-10
3.2-5	Momentum-Control Coil Requirements	3.2-19
3.2-6	Effect of Attitude Error on Average Spin-Torque	3.2-19
3.2-7	New Switching-Angles As a Function of Pitch-Axis Error	3.2-20
3.2-8	Momentum-Control Deviation of Ideal Switchdng Angle (From $+\pi/2$ and $-\pi/2$ Orbit Angle)	3.2-21
3.2-9	Effect of Momentum-Control Orbit Start-Angle on Average Spin Torque	3.2-21
3.2-10	Precession Inherent to Momentum Control	3.2-23
3.2-11	QOMAC and Magnetic-Bias Coil, Weight Versus Current Characteristics	3.2-28
3.2-12	Momentum-Coil Weight Versus Current Characteristic	3.2-28
3.3-1	Spacecraft Orientation With Respect to the Coordinate Systems Defined in Section 2.1 of This Report	3.3- 2
3.4-1	Sketch Depicting the Definition of Sensor Geometry in a Spatial Orientation	3.4- 2
3.4-2	Sensitivity of the Half-Earth and Grazing Angles as a Function of the α-Angle with a Zero Roll-Angle	3.4-10
3.4-3	Sensitivity of the Half-Earth and Grazing Angles to the Roll Angle	3.4-11
3.4-4	Nominal Sensor Outputs Obtained Using Equations (3.4-5) and (3.4-6)	3.4-13
3.4-5	Error-Computation Curves Used to Determine Total Time-Spread for Worst-Case Radiance and Noise Variations	3.4-14
3.4-6	Worst-Case Output-Pulse Analysis for Dual (Vee) Sensor Configuration	3.4-15
3.4-7	Worst-Case Sensor Output-Pulses for Vertical Sensor Configuration	3.4-17
3.4-8	Variation of the Peak Value and Time-to-Peak as a Function of the Time Constant	3.4-18
3.4-9	Variation of the Peak Value and Time-to-Peak as a Function of the α-Angle	3.4-19
3.4-10	Effect of Clouds on Sensor Error for the Sky-to-Earth Interface	3.4-22
3.4-11	Effects of Clouds on Sensor Error for the Earth-to-Sky Interface	3.4-22

LIST OF ILLUSTRATIONS (Continued)

Figure		Page
3.5-1	Block Diagram of the Command and Control Subsystem, Including the Telemetry Subsystem	3.5- 2
3.5-2	Diagrammatic Representation of the Sequence of an Attitude/ Momentum Program	3.5- 5
3.5-3	Block Diagram of the Programmer	3.5- 6
3.5-4	Schematic Diagram of the Magnetic-Bias Stepping-Switch Control Circuit	3.5- 8
3.7-1	Despin History of TIROS' II to VIII Inclusive	3.7- 2
3.7-2	Total Initial Alignment Sequence for the Nominal Conditions	3.7- 8
3.8-1	Block Diagram of the Attitude-Data Acquisition Subsystem	3.8- 1
3.8-2	Block Diagram of a Serial Data-Controller	3.8- 2
3.8-3	Examples of Pre-Computed, Normalized Curves Available for Computing ϕ_{max} and λ	3.8- 7
5.3-1	Reliability Block Diagram and Mathematical Model With No Redundancy	5.3- 3
5.3-2	Reliability Block Diagram and Mathematical Model With Redundant Sensors	5.3- 3
5.3-3	Reliability Block Diagram and Mathematical Model With Redundant Sensors and Pitch-Axis Control Electronics	5.3- 4
6.2-1	Nutation-Damper Test Device	6.2- 2
6.3-1	Magnetometer Test Setup	6.3- 2
7.2-1	General Arrangement of the Gyromagnetic-Stabilization System	7.2- 3
7.2-2	Flywheel-Drive Assembly of the Gyromagnetic-Stabilization System	7.2- 5
7.2-3	Mirror Arrangement for the Gyromagnetic-Stabilization System	7.2-11
7.3-1	System Power Profile (Worst-Case Conditions)	7.3- 2
8.2-1	Gyromagnetic-Stabilization System Input Specifications	8.2- 3
8.3-1	Gyromagnetic-Stabilization, Subsystem- and Component-Level Specifications	8.3- 3

LIST OF TABLES

Table		Page
1.2-1	Summary of Constraints Imposed by the Launch Vehicle and the Orbital Parameters	1.2- 1
1.2-2	Summary of the Design Goals Established for Study Program	1.2- 2
1.3-1	Weight Summary	1.3- 3
1.3-2	Power Summary	1.3- 4
2.3-1	Summary of Disturbance Torques and Dynamic Effects	2.3- 9
3.1-1	Summary of D-C Motor Performance Requirements	3.1-30
3.1-2	Summary of Data Accumulated for Comparison of Four Types of D-C Motors	3.1-32
3.1-3	Summary Comparison of Inland Motor Type T-2170 with Performance Requirements	3.1-33
3.1-4	Summary of Water-Vapor Substitutes and Characteristics	3.1-35
3.1-5	Summary of Test Data Obtained on Oil-Loss Rates by Experimentation	3.1-36
3.1-6	List of Commonly Used Brush/Commutator Materials	3.1-37
3.1-7	Summary of Data Pertinent to Wear-Rate of Brushes and Obtained at RCA	3.1-39
3.1-8	Summary of Anticipated Power Consumptions for Pitch-Axis-Stabilization Control Subsystems	3.1-41
3.2-1	QOMAC Coil Parameters	3.2-26
3.2-2	Magnetic-Bias Coil Parameters	3.2-27
3.2-3	Momentum-Coil Parameters	3.2-27
3.2-4	Summary of Magnetic-Torque-Control Characteristics	3.2-29
3.4-1	Comparison of Type of Sensor and Sensor Errors for Roll/Yaw and Pitch	3.4-20
3.6-1	Summary of Telemetry Points and Parameters	3.6- 3
3.7-1	Summary of Times Required to Turn from θ Approximately Equal to 90^{o} to θ Approximately Equal to 10^{o}	3.7- 6
4.3-1	Summary of Pointing Accuracy and Jitter	4.3- 1
5.3-1	Reliability Analysis Summary	5.3- 7
5.3-2	Failure-Rates of High-Reliability Parts	5.3- 8
6.3-1	Comparison of Observed and Measured Results	6.3- 4
7.2-1	Summary of Weight and Moment-of-Inertia Data for FSMTMS System	7.2- 7
7.3-1	Initial Alignment Mode Power Requirements	7.3- 1
7.3-2	Normal Operational Power Requirements	7.3- 3
9.2-1	Comparison of Brushless D-C Motors	9.2- 5
9.2-2	Signal and Power Transfer Specifications	9.2- 6
9.2-3	Materials Combinations	9.2- 7

Section 1.0

SUMMARY

1.1 INTRODUCTION

The work performed during this study program was directed toward developing an attitude-control system which would be particularly well suited to spacecrafts which must perform a meteorological mission; however, the Statement of Work[5] defined the mission requirements in terms sufficiently broad that the design study is applicable to a wide range of spacecraft missions. Wherever possible, the fundamental design procedures are included in each of the subsystems which make up the complete attitude-control system. The application of these design procedures has been used to define the method for the attitude control of what the Statement of Work called the "500-lb. spacecraft." The 500-pound spacecraft can be considered as an example on which the design procedures developed in this study have been exercised.

The control system studied comprises three major and nearly independent subsystems. The first subsystem will provide control about the roll and yaw axes of the spacecraft by a technique of magnetic torquing which is nearly identical to that planned for the TIROS Wheel spacecraft. The principles of this technique are referred to as Quarter-Orbit Magnetic Attitude Control (QOMAC). The second major subsystem to be studied will provide control about the pitch axis of the spacecraft. This control will be effected through a closed-loop system, comprising a simple IR bolometer, compensation networks, and a torque motor which exchanges momentum between a flywheel mounted on an axis parallel with the spacecraft's pitch axis and the main spacecraft structure. The third subsystem provides control of the spacecraft pitch-axis momentum by an additional magnetic torquing technique.

Throughout this report, the attitude-control system will be called either the FSMTMS (Flywheel Stabilized, Magnetically Torqued Meteorological Satellite) Control System, or the Gyromagnetic Control System. Both names refer to the same design.

1.2 SYSTEM CONSTRAINTS

The study contract contained an evaluation of the system to determine the constraints imposed by the launch vehicle and the orbital parameters. The summary of these constraints is presented in Table 1.2-1.

Based on the launch vehicle and orbital parameters and the constraints imposed by these, the system was then analyzed to determine the satellite stabilization and control system parameters. This analysis yielded the parameters presented in Table 1.2-2; however, these parameters represent the design goals of the study program and are not the results of the study.

TABLE 1.2-1. SUMMARY OF CONSTRAINTS IMPOSED BY THE LAUNCH VEHICLE AND THE ORBITAL PARAMETERS

Applicable Parameter	Launch Vehicle	
	Thor Agena	Thor Delta (258 last stage)
Payload Weight	800 lb.	500 lb.
Altitude	500 N. M.	500 N. M.
Altitude Tolerance	± 50 N. M. *	± 50 N. M. **
Ellipticity	0.01*	0.013**
Inclination	80.976° retrograde	80.976° retrograde
Inclination Tolerance	± 0.81°*	± 0.84°**
Sun Angle	High-noon orbit	High-noon orbit
Sun-Angle Tolerance	Approx. 0.14°/day or 51°/year	Approx. 0.145°/day or 53°/year
Spin Rate	Not Applicable	125 rpm
Spin-Rate Tolerance	Not Applicable	± 10 rpm**
Tip-off Rate	0.5°/sec., roll and pitch* 0.3°/sec., yaw*	Not Applicable
Tip-off Angle	Not Applicable	± 8.0° Nutation Angle**
Environment	As per GSFC/NASA document "An Environmental Specification for A Meteorological Spacecraft Subsystem", dated April, 1964, and a stated "Q" Factor of 6.0	
Ground Stations	Gilmore Creek, Alaska	

NOTES:

*These values were obtained from NASA and all are 3σ values.

**These values were obtained from the Advanced TIROS program (TOS), and all are 3σ values.

TABLE 1.2-2. SUMMARY OF THE DESIGN GOALS ESTABLISHED FOR STUDY PROGRAM

Applicable Parameter	Launch Vehicle	
	Thor Agena	Thor Delta (258 last stage)
Configuration	See Figure 1.3-1	See Figure 1.3-1
Moments of Inertia (lb. in.^{2})	I_{yaw} = 430,000 I_{roll} = 950,000 I_{pitch} = 950,000	I_{yaw} = 90,720 I_{roll} = 130,317 I_{pitch} = 123,487
Voltage Available	-24.5 volts	-24.5 volts
Vehicle-Induced Disturbances	See Section 2.3.4 of this report for details	
Stabilization-System Weight	88 lb.	50 lb.
Power Used	10.3 watts	8.0 watts
Pointing Accuracy	± 1.0° maximum half-cone angle about the local vertical ± 1.0° in yaw	
Jitter Rate	Less than 0.05° sec., all axes	
Lifetime	Greater than 1 year	
Telemetry System, Command System, Communications System, Ground Stations	Maximum utilization of existing Nimbus equipment is required.	

1.3 DESCRIPTION OF THE GYROMAGNETIC-STABILIZATION ATTITUDE-CONTROL SYSTEM

Figure 1.3-1 is the elevation view of the gyromagnetic-stabilization attitude-control system studied as applied to the 500-pound spacecraft. Components are mounted on top of the struts attached to the sensory ring and to the sensory ring itself. If the axis of symmetry of the sensory ring is considered the yaw axis, then the axis of the flywheel assembly (which is normal to the yaw axis) is parallel to the spacecraft pitch axis. The operation of the stabilization system is such that the flywheel axis will be maintained normal to the orbit plane at the same time the sensory ring is forced to face toward the earth throughout the orbit. The flywheel will spin at approximately 150-rpm about an axis parallel to the spacecraft pitch axis, while the spacecraft itself will make one revolution per orbit about the spacecraft pitch axis. The attitude-control equipment mounted on the strut consists of the following.

- The flywheel-drive assembly including attitude sensors
- The roll-yaw control coil
- The pitch-axis control electronics
- The roll-yaw and momentum-control electronics
- The rockets (if required)
- Programmer interface electronics

The stabilization-system equipment mounted on the sensory ring includes the following.

- Yo-yo despin mechanism
- Momentum-control coil
- Nutation damper with expansion chambers

The last three items were placed on the sensory ring primarily to maintain minimum weight; these items could be mounted on the struts but only with severe penalties in performance or weight (increases). It would be particularly difficult to locate the yo-yo despin mechanism on the upper section; the other two items could be moved more easily, but with approximately a 5:1 increase in their weight if present performance is to be maintained.

Table 1.3-1 presents a weight breakdown of the complete gyromagnetic-stabilization attitude-control system. The initial design goal was 50 pounds; if the rockets are removed (which is one of the recommendations of the study), then the final attitude-control system weight for the 500-pound spacecraft is 41.5 pounds.

Figure 1.3-2 is a block diagram of the complete attitude-control system. The three major spacecraft elements are shown as the pitch-axis control subsystem, the momentum control subsystem, and the roll/yaw control subsystem; the fourth major part is the ground station which is actually an integral part of the momentum and roll/yaw control subsystems. In the design studied, the only direct command to the pitch-axis control subsystem is the turn-on command.

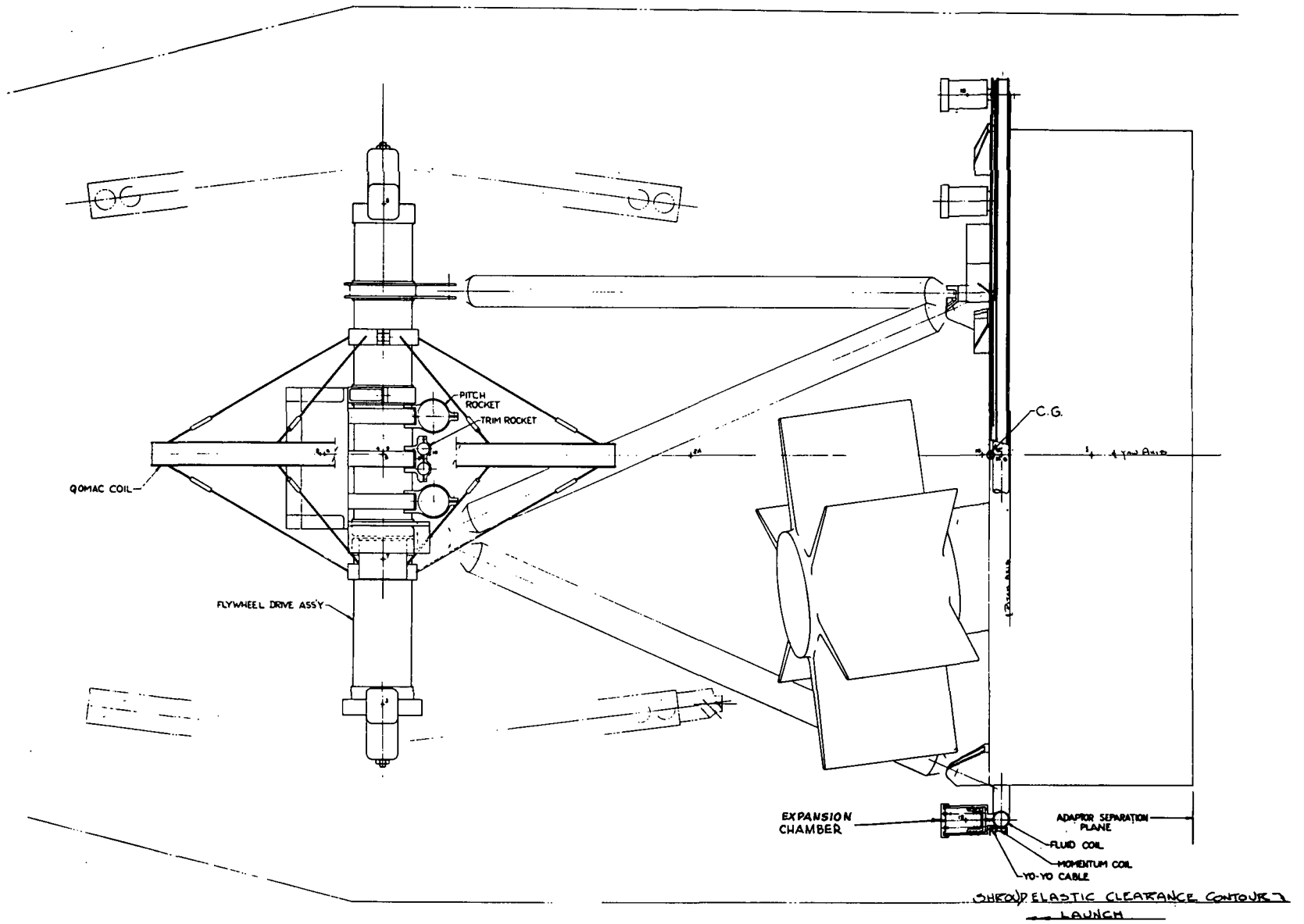

Figure 1.3-1. Elevation View of the Gyromagnetic-Stabilization Attitude-Control System General Arrangement

The sensors mounted on the rotating flywheel provide attitude information directly to the pitch-axis error-detecting elements which develop drive signals to the motor; these signals are proportional to the angular deviation between the local-vertical and the yaw axis. The sensors also transmit data to the ground where roll/yaw errors are computed and correction commands are generated for the roll/yaw control subsystem. The spin-rate of the flywheel with respect to the spacecraft is transmitted to ground as a measure of momentum error. The correction for momentum is initiated from ground command.

TABLE 1.3-1. WEIGHT SUMMARY

Unit	Weight (lbs.)
Flywheel units - 2 pieces	11.34
Housing assembly	7.64
Structure on Housing	1.22
Amplifier and signal conditioner	2.50
Coil bias stepping switch	.90
Computer command control	3.80
QOMAC coil and support	2.00
Rockets installed	3.40
Fluid damper	6.03
Momentum coil	1.60
Yo-yo despin device	4.50
Total	44.93 lbs..

The nutation damper is a completely passive device; it serves as the fine-control for the roll/yaw axes in that it reduces undesired motion about these axes. The pitch-axis oscillatory motion is damped by the action of its feedback control.

The subsystem elements shown in Figure 1.3-2 are described in the remainder of this report and their interaction with the spacecraft is also discussed. Wherever possible, existing command and control and data-processing equipments have been used in both the spacecraft and the ground station.

The power profile of the system studied is presented in Section 7.3; the continuous power required is shown in Table 1.3-2. The continuous drain after initial alignment occurs is 5.33 watts. The peak-demand occurs during initial alignment and is 14.1 watts.

A reliability and failure-mode analysis was performed for the attitude-control system studied. On the basis of the assumptions made in Section 5.0, the probability of successful operation for one year was computed as 0.923.

TABLE 1.3-2. POWER SUMMARY

Item	Operation Time	Equivalent Continuous Drain (watts)
Pitch-Axis-Control Stabilization Subsystem (Including "Vee" Sensors)	Continuous	4.8
Magnetic-Bias Coil	Continuous	0.204
QOMAC/Momentum Programmer and Decoder	Continuous	0.25
	1/2 orbit or 52 minutes every 4 days maximum	0.018
	1 orbit every 20 days maximum	0.007
	2.5 orbits every 20 days maximum	0.018
QOMAC Coil	1/2 orbit every 4 days maximum	0.005
	1 orbit every 20 days maximum	0.002
Momentum Coil	2.5 orbit every 20 days maximum	0.004
Telemetry Control Unit	15 minutes maximum twice a day	0.021
		Total 5.33 watts

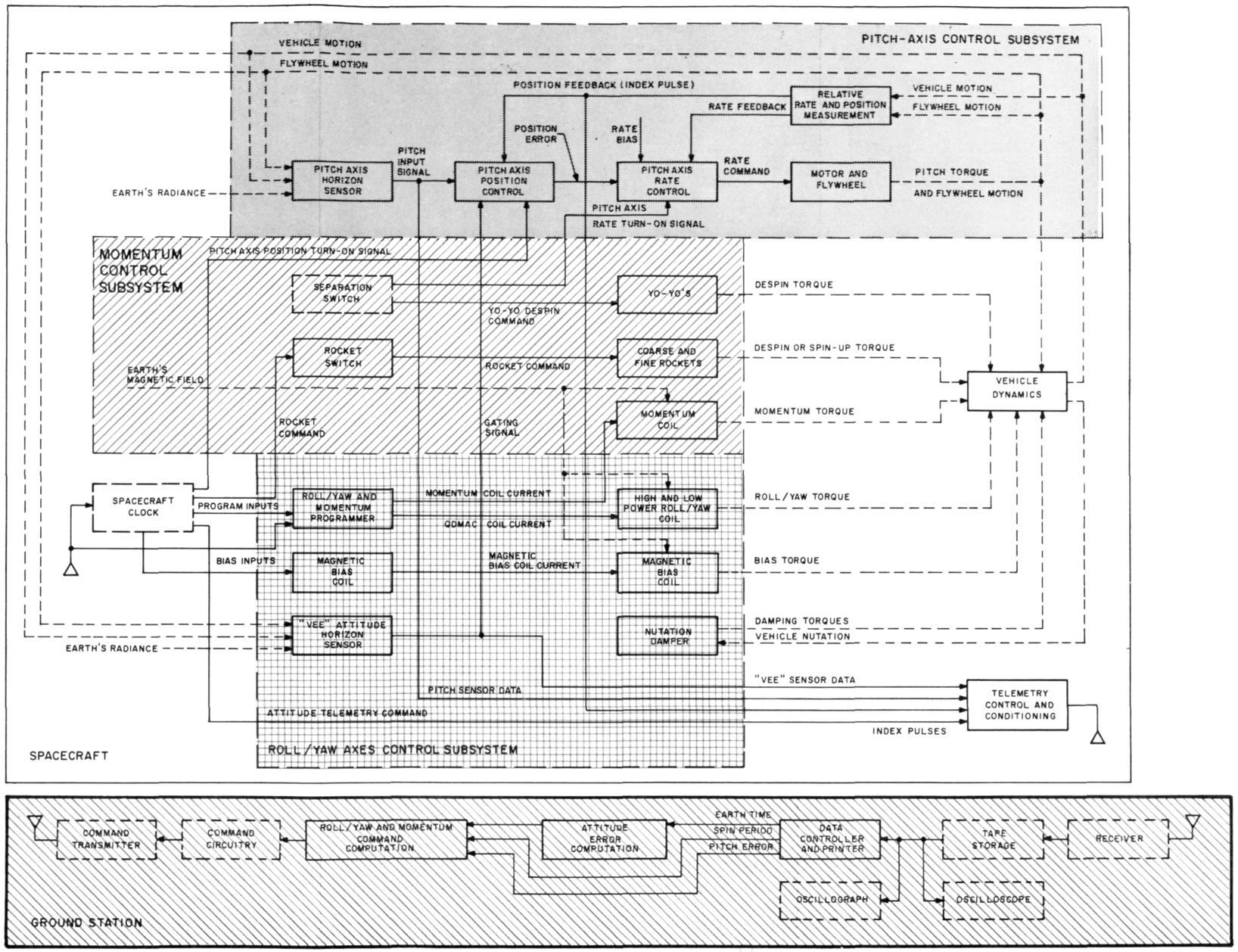

Figure 1.3-2. Functional Block Diagram of the Flywheel Stabilized, Magnetically Torqued Attitude Control System

Section 2.0

SYSTEMS ANALYSIS

2.1 COORDINATE SYSTEMS

Several orbital coordinate systems have been used during the Study Program. The primary systems used in this report are shown in Figure 2.1-1. The $\hat{X}, \hat{Y}, \hat{Z},$ coordinate system is inertially fixed; the $\hat{X}$ vector is along the lines of Aries, and the $\hat{Z}$ vector is along the spin axis of the earth. The $\hat{\ell}, \hat{b}, \hat{n},$ coordinate system is fixed with respect to the orbital plane; the unit vector $\hat{\ell}$ is along the orbit line of ascending nodes, and the unit vector $\hat{n}$ is along the orbit normal. The $\hat{\ell}, \hat{b}, \hat{n},$ system is related to the $\hat{X}, \hat{Y}, \hat{Z},$ system by the following two rotations:

- the first rotation is around $\hat{Z}$ and through the angle Ω ;
- the second rotation is around $\hat{n}$ and through the angle i .

The $\hat{r}, \hat{t}, \hat{n}$ coordinate system rotates with the spacecraft; the $\hat{r}$ vector is along the radius vector from the center of the earth to the spacecraft. The $\hat{r}, \hat{t}, \hat{n},$ system is related to the $\hat{\ell}, \hat{b}, \hat{n},$ system by only the following rotation:

- the rotation is around $\hat{n}$ and through the anomaly angle θ .

The geomagnetic coordinate systems developed for this report are shown in Figure 2.1-2. The $\hat{X}_m, \hat{Y}_m, \hat{Z}_m,$ system is a geomagnetic set with vectors $\hat{X}_m$ and $\hat{Y}_m$ in the geomagnetic equatorial plane, and vector $\hat{X}_m$ directed along the line of intersection of the geomagnetic and geographic equatorial planes.

The $\hat{r}, \hat{\nu}, \hat{\zeta},$ set is a geomagnetic-spherical coordinate system; vector $\hat{r}$ is along a line from the center of the earth to a point in space, and vector $\hat{\nu}$ is normal to vector $\hat{r}$ in the direction of geomagnetic latitude. The $\hat{X}_m, \hat{Y}_m, \hat{Z}_m,$ coordinate system is related to the $\hat{r}, \hat{\nu}, \hat{\zeta},$ by the following two rotations:

- the first rotation is around the vector $\hat{\zeta}$ and through the angle ν ;
- the second rotation is around the vector $\hat{Z}_m$ and through the angle ζ.

The $\hat{X}, \hat{Y}, \hat{Z},$ system is related to the $\hat{X}_m, \hat{Y}_m, \hat{Z}_m$ system by the following two rotations:

- the first rotation is around the vector $\hat{X}_m$ and through the angle i_m ;
- the second rotation is around the vector Z and through the angle $-\Omega_m$.

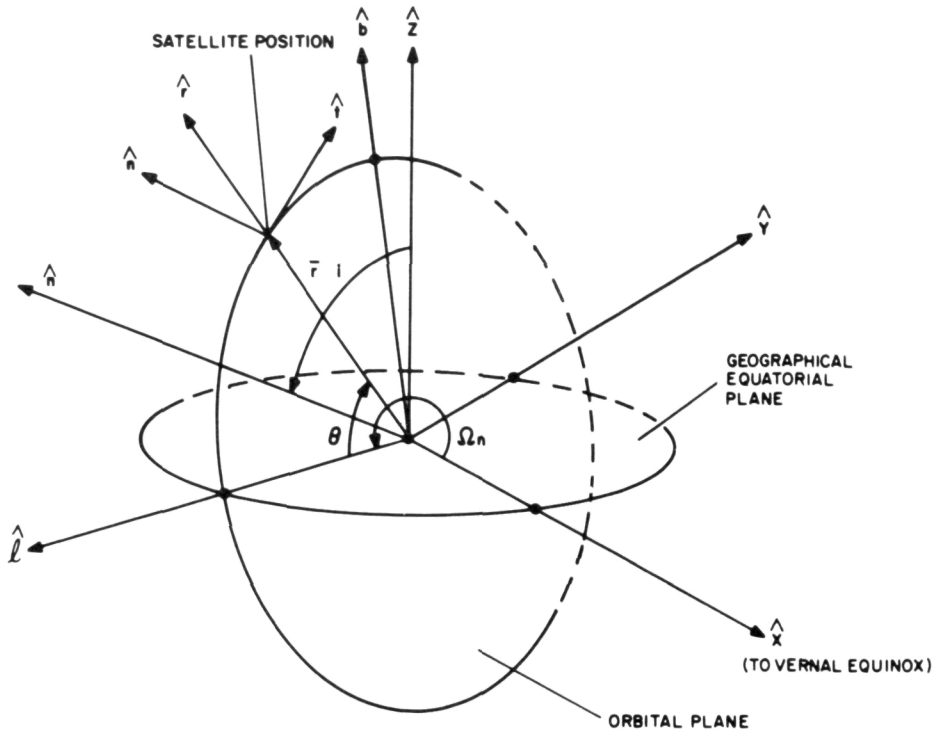

Figure 2.1-1. Drawing Depicting the Orbital Coordinates Used for Systems Analysis

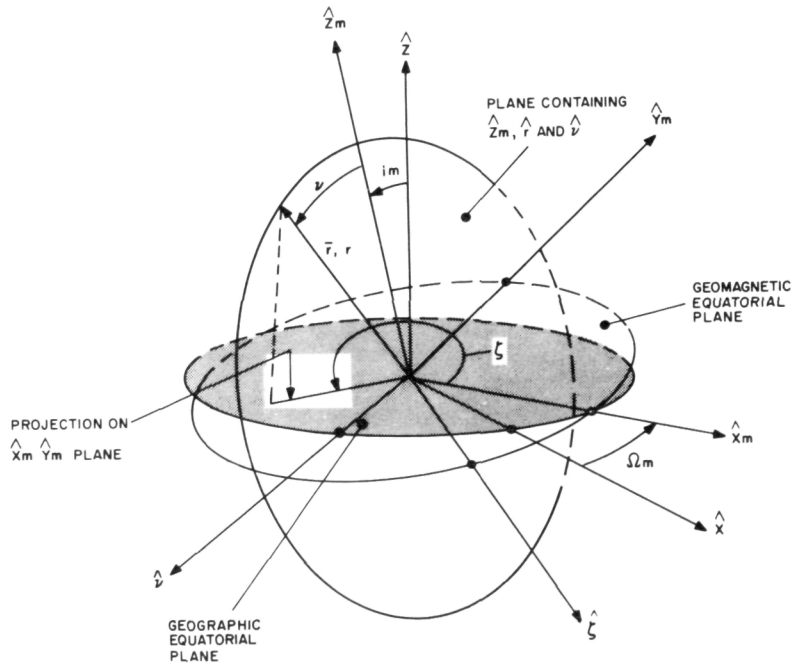

Figure 2.1-2. Drawing Depicting the Geomagnetic Coordinates Used for Systems Analysis

The vehicle coordinate system developed for use in this report is shown in Figure 2.1-3. The nominal orientation of the vehicle is along the $\hat{r}$, $\hat{t}$, $\hat{n}$ coordinate system; the pitch axis is along the vector $\hat{n}$ the yaw axis is along the vector $\hat{r}$, and the roll axis is along the vector $\hat{t}$. To consider deviations from the nominal condition, the following three rotations of the coordinate system are necessary:

- the first rotation is around the $\hat{r}$ axis and through the angle γ;
- the second rotation is around the $\hat{2}$ axis and through the angle ϕ;
- the third rotation is around the $\hat{1}$ axis and through the angle θ_p.

The angle ϕ is actually the roll angle of the vehicle; it is measured by a horizon sensor mounted on a flywheel with the spin axis of the flywheel along the $\hat{1}$ axis. The angle between axis $\hat{1}$ and the $\hat{r}$, $\hat{n}$, plane is defined as ψ; this angle is used in several sections of this report in place of the angle γ through the use of the identity

$$\tan \psi = \cos \phi \tan \gamma \qquad (2.1\text{-}1)$$

Note that the $\hat{1}$, $\hat{2}$, $\hat{3}$, coordinate system, as defined in Figure 2.1-3 is a left-hand coordinate system. This was done to be consistent with the derivation of magnetic-torquing equations previously presented(3).

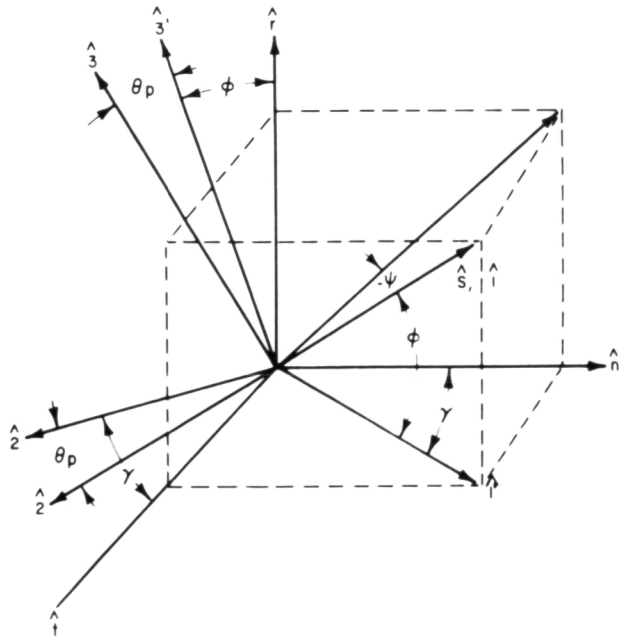

Figure 2.1-3. Drawing Depicting the Vehicle Coordinates Used for Systems Analysis

2.2 GENERAL MAGNETIC FIELD EQUATIONS

A simple canted-magnetic-dipole moment of 8.1×10^{25} emu-cgs units provides an excellent approximation of the geomagnetic field in the terrestial-spatial environment up to a maximum of 6 earth radii. This dipole model has the axis inclined from the polar axis of the earth by a value of 11.4^{o} (the value of angle i_m); it intersects the earth at a latitude of 78.6^{o}N, longitude 70.1^{o}W, and at a latitude of 78.6^{o}S, longitude 250.1^{o}W. This model has been used to predict the performance of magnetic torquing systems on other RCA programs (e.g., TIROS, Relay) with excellent results.

The earth's field components, due to a dipole source expressed in a spherical coordinate set as shown in Figure 2.1-2, is given by the following equation:

$$\begin{bmatrix} B_r \\ B_\nu \\ B_\zeta \end{bmatrix} = [C] = \begin{bmatrix} -\frac{2M_e}{r^3} \cos\nu \\ -\frac{M_e}{r^3} \sin\nu \\ 0 \end{bmatrix} \qquad (2.2\text{-}1)$$

where r is the instantaneous orbit radius and M_e is the geomagnetic dipole moment (8.1×10^{25} gauss-cm^3).

To perform the analyses presented in this report, it was necessary to obtain the value of the magnetic field (B) in both the $\hat{r}$, $\hat{t}$, $\hat{n}$, and $\hat{\ell}$, $\hat{b}$, $\hat{n}$, coordinate systems. It was, therefore, necessary to establish relationships between the angles ν and ζ, and the angles θ, i, i_m, and Ω ($\Omega = \Omega_n - \Omega_m$). These relationships were obtained by successive transformations about the $\hat{\zeta}$, $\hat{Z}_m$, $\hat{X}_m$, $\hat{Z}$, $\hat{\ell}$, and $\hat{n}$ axes and through the angles ν, ζ, i_m, Ω, i, and θ, respectively.

The final expression obtained from the transformations is of the following form

$$\begin{bmatrix} \hat{r} \\ \hat{t} \\ \hat{n} \end{bmatrix} = [M] \begin{bmatrix} \hat{r} \\ \hat{\nu} \\ \hat{\zeta} \end{bmatrix}; \quad M = \begin{bmatrix} m_{11} & m_{12} & m_{13} \\ m_{21} & m_{22} & m_{23} \\ m_{31} & m_{32} & m_{33} \end{bmatrix} \qquad (2.2\text{-}2)$$

where the "m" factors are trigonometric functions of the six rotational angles. The term $\hat{r}$ is transformed into itself; therefore, equation (2.2-2) yields the following:

$$m_{11} = 1; \qquad m_{12} = 0; \qquad m_{13} = 0 \qquad (2.2\text{-}3)$$

Equation (2.2-3) can be solved to obtain the necessary relationships between the angles ν and ζ, and the angles θ, i, i_m, and Ω. These relationships are as given in the following equation:

$$\nu = \cos^{-1}\left[-\cos\theta \sin\Omega \sin i_m - \sin\theta \cos i \cos\Omega \sin i_m + \sin\theta \sin i \cos i_m\right] \quad (2.2\text{-}4a)$$

$$\zeta = \cos^{-1}\left[\frac{\cos\theta \cos\Omega - \sin\theta \cos i \sin\Omega}{\sin\nu}\right] \quad (2.2\text{-}4b)$$

The total magnetic field, B, in the $\hat{r}$, $\hat{t}$, $\hat{n}$, coordinate set is then given by:

$$\begin{bmatrix} \overline{B}_r \\ \overline{B}_t \\ \overline{B}_n \end{bmatrix} = [M]\,[C] \begin{bmatrix} \hat{r} \\ \hat{t} \\ \hat{n} \end{bmatrix} \quad (2.2\text{-}5)$$

The use of the matrix operation and trigonometric algebra then yields the following[2]

$$B_r = \frac{2M_e}{r^3}\left[\cos\theta \sin\Omega \sin i_m + \sin\theta \cos i \cos\Omega \sin i_m - \sin\theta \sin i \cos i_m\right] \quad (2.2\text{-}6a)$$

$$B_t = \frac{M_e}{r^3}\left[\sin\theta \sin\Omega \sin i_m - \cos\theta \cos i \cos\Omega \sin i_m + \cos\theta \sin i \cos i_m\right] \quad (2.2\text{-}6b)$$

$$B_n = \frac{M_e}{r^3}\left[\sin i \cos\Omega \sin i_m + \cos i \cos i_m\right] \quad (2.2\text{-}6c)$$

The values for the $\hat{\ell}$, $\hat{b}$, $\hat{n}$, coordinate set is obtained by a simple rotation around vector $\hat{n}$ and through the angle $-\theta$ and yields:

$$B_\ell = \frac{M_e}{r^3}\left\{-\frac{3}{2}\sin i \cos i_m \sin 2\theta + \sin i_m \times \left[\frac{3}{4}(\cos i + 1)\sin(2\theta + \Omega) + \frac{3}{4}(\cos - 1)\sin(2\theta - \Omega) + \frac{1}{2}\right]\sin\Omega\right\} \quad (2.2\text{-}7a)$$

$$B_b = \frac{M_e}{r^3}\left\{\frac{3}{2}\sin i \cos i_m \cos 2\theta - \frac{3}{4}\sin i_m (\cos i - 1)\times\right.$$

$$\cos(2\theta - \Omega) - \frac{3}{4}\sin i_m (\cos i + 1)\cos(2\theta + \Omega) + \qquad (2.2\text{-}7b)$$

$$\left.\frac{1}{2}\cos i \sin i_m \cos\Omega - \frac{1}{2}\sin i \cos i_m\right\}$$

$$B_n = \frac{M_e}{r^3}\left\{\cos i \cos i_m + \sin i_m \sin i \cos\Omega\right\} \qquad (2.2\text{-}7c)$$

For accuracy, it is now necessary to include orbit ellipticity, ϵ, $[r = r(\theta)]$, and orbit longitude motion due to the oblateness precession of the orbital plane and rotation of the earth $[\Omega = \Omega(\theta)]$.

For an elliptical orbit,

$$r = \frac{(1+\epsilon) r_1}{1 + \epsilon\cos(\theta - \theta')} = \frac{(1+\epsilon)(h_1 + r_E)}{1 + \epsilon\cos(\theta - \theta')} \qquad (2.2\text{-}8)$$

where θ' is the orbit anomaly angle at perigee, h_1 is the orbit radius at perigee, and r_E is the radius of the earth. Thus,

$$\frac{1}{r^3} = \frac{1}{(1+\epsilon)^3}\frac{1}{(r_E + h_1)^3}[1 + \epsilon\cos(\theta - \theta')]^3 \qquad (2.2\text{-}9)$$

For small eccentricities, the equation (2.2-9) may be expanded, yielding the following approximate relation

$$\frac{1}{r^3} \simeq \frac{1}{(1+\epsilon)^3}\frac{1}{(r_E + h_1)^3}[1 + 3\epsilon\cos(\theta - \theta')] \qquad (2.2\text{-}10)$$

The precessional rate of the orbital plane due to the oblateness of the earth, $\dot{\Omega}_n$, is given by

$$\dot{\Omega}_n = 2.02 \times 10^{-6}\left(\frac{r_E}{r_1}\right)^{7/2}\left(\frac{1-\epsilon}{1+\epsilon}\right)^{7/4}\cos i \ \frac{rad.}{sec.} \qquad (2.2\text{-}11)$$

The precessional rate of the orbital plane contributes much less to the longitude motion than does the rotation of the earth, $\dot{\Omega}_m$, because:

$$\dot{\Omega}_m = \frac{360\ deg.}{24\ hr.} = \frac{15\ deg.}{hr.} = \frac{1}{240}\ \frac{deg.}{sec.} = 0.727 \times 10^{-4}\ \frac{rad.}{sec.} \qquad (2.2\text{-}12)$$

Therefore,

$$\dot{\Omega} = \dot{\Omega}_n - \dot{\Omega}_m \simeq \dot{\Omega}_m \qquad (2.2\text{-}13)$$

The angle between the line of nodes of the geographic and magnetic equatorial planes and the orbit ascending node can be expressed as:

$$\Omega = \Omega_0 + \dot{\Omega} t \qquad (2.2\text{-}14)$$

For small eccentricities,

$$\theta \simeq 2\pi \frac{t}{T} \qquad (2.2\text{-}15)$$

Then,

$$\Omega = \Omega_0 + \frac{\omega_0}{2\pi}\ T\theta \qquad (2.2\text{-}16)$$

where ω_0 is the earth's spin rate ($\omega_0 = \dot{\Omega}_m$) and T is the orbital period.

Combining these results yields the final field equations in the $\hat{r}$, $\hat{t}$, $\hat{n}$ orbital coordinate set for small eccentricities. These are given in the equation (2.2-17):

$$B_r = \frac{2M_e}{(1+\epsilon)^3 (r_E + h_1)^3} \left[1 + 3\epsilon \cos(\theta - \theta')\right] \left[\cos\theta \times \sin i_m \sin\left(\Omega_0 + \frac{\omega_0}{2\pi}\ T\theta\right) + \sin\theta \cos i \sin i_m \times \cos\left(\Omega_0 + \frac{\omega_0}{2\pi}\ T\theta\right) - \sin\theta \sin i \cos i_m\right] \qquad (2.2\text{-}17a)$$

$$B_t = \frac{M_e}{(1+\epsilon)^3 (r_E + h_1)^3} \left[1 + 3\epsilon \cos(\theta - \theta')\right] \left[\sin\theta \times \sin i_m \sin\left(\Omega_0 + \frac{\omega_0}{2\pi} T\theta\right) - \cos\theta \cos i \sin i_m \cos\left(\Omega_0 + \frac{\omega_0}{2\pi} T\theta\right) + \cos\theta \sin i \cos i_m\right] \quad (2.2\text{-}17b)$$

$$B_n = \frac{M_e}{(1+\epsilon)^3 (r_E + h_1)^3} \left[1 + 3\epsilon \cos(\theta - \theta')\right] \left[\sin i \times \sin i_m \cos\left(\Omega_0 + \frac{\omega_0}{2\pi} T\theta\right) + \cos i \cos i_m\right] \quad (2.2\text{-}17c)$$

Similarly, the final field equations in the $\hat{\ell}, \hat{b}, \hat{n}$ coordinate set, for small eccentricities, are:

$$B_\ell = \frac{M_e}{(1+\epsilon)^3 (r_E + h_1)^3} \left[1 + 3\epsilon \cos(\theta - \theta')\right] \left\{ -\frac{3}{2} \times \sin i \cos i_m \sin 2\theta + \sin i_m \left[\frac{3}{4}(\cos i + 1) \times \sin\left(2\theta + \Omega_0 + \frac{\omega_0}{2\pi} T\theta\right) + \frac{3}{4}(\cos i - 1) \times \sin\left(2\theta - \Omega_0 - \frac{\omega_0}{2\pi} T\theta\right) + \frac{1}{2} \sin\left(\Omega_0 + \frac{\omega_0}{2\pi} T\theta\right)\right]\right\} \quad (2.2\text{-}18a)$$

$$B_b = \frac{M_e}{(1+\epsilon)^3 (r_E + h_1)^3} \left[1 + 3\epsilon \cos(\theta - \theta')\right] \left\{ \frac{3}{2} \right.$$

$$\times \sin i \cos i_m \cos 2\theta - \frac{3}{4} \sin i_m (\cos i - 1)$$

$$\times \cos\left(2\theta - \Omega_0 - \frac{\omega_0}{2\pi} T\theta\right) - \frac{3}{4} \sin i_m (\cos i + 1) \qquad \text{(2.2-18b)}$$

$$\times \cos\left(2\theta + \Omega_0 + \frac{\omega_0}{2\pi} T\theta\right) + \frac{1}{2} \sin i_m \cos i$$

$$\left. \times \cos\left(\Omega_0 + \frac{\omega_0}{2\pi} T\theta\right) - \frac{1}{2} \sin i \cos i_m \right\}$$

$$B_n = \frac{M_e}{(1+\epsilon)^3 (r_E + h_1)^3} \left[1 + 3\epsilon \cos(\theta - \theta')\right] \left[\cos i \right.$$

$$\left. \times \cos i_m + \sin i_m \sin i \cos\left(\Omega_0 \frac{\omega_0}{2\pi} T\theta\right)\right] \qquad \text{(2.2-18c)}$$

2.3 GENERAL DYNAMICAL EQUATIONS

2.3.1 Dynamic Equations

The spacecraft described in this report has many of the properties of a simple spin-stabilized spacecraft. In developing the equations of motion, the following tentative assumptions have been made to determine the performance parameters described in Section 3.3 and 3.7 of this report.

- The roll, pitch, and yaw, axes of the spacecraft are the principle moments of inertia.
- The flywheel spin-axis is aligned with the pitch-axis.

These two assumptions permit the writing of the total momentum of the spacecraft with reference to the body coordinates $\hat{1}$, $\hat{2}$, and $\hat{3}$ described in Figure 2.3-1. The resulting momentum equation is

$$\bar{H} = (I_1\omega_1 + I_f\omega_f)\ \hat{1} + I_2\omega_2\ \hat{2} + I_3\omega_3\ \hat{3} \qquad (2.3\text{-}1)$$

Implicit in this equation are the following simplifying assumptions.

- The transverse moment-of-inertia of the flywheel is small compared to I_2 and I_3. This is demonstrated in Section 7.2 where the values of the flywheel and spacecraft are tabulated.
- The polar moment-of-inertia of the damper-fluid mounted on the $\hat{3}$ axis is negligible compared to I_3. This leads to the assumption that any momentum-contained fluid has negligible effect on the $\hat{3}$ axis of the spacecraft and is not included in equation (2.3-1).

Euler angles are used to describe the motion of the spacecraft-body fixed axes. These Euler angles are defined in Figure 2.3-1. The components of the spacecraft total angular-velocity vectors are as follows

$$\omega_1 = \dot{\psi}\cos\theta + \dot{\phi} \qquad (2.3\text{-}2a)$$

$$\omega_2 = \dot{\psi}\sin\theta\sin\dot{\phi}t + \dot{\theta}\cos\dot{\phi}t \qquad (2.3\text{-}2b)$$

$$\omega_3 = \dot{\psi}\sin\theta\cos\dot{\phi}t - \dot{\theta}\sin\dot{\phi}t \qquad (2.3\text{-}2c)$$

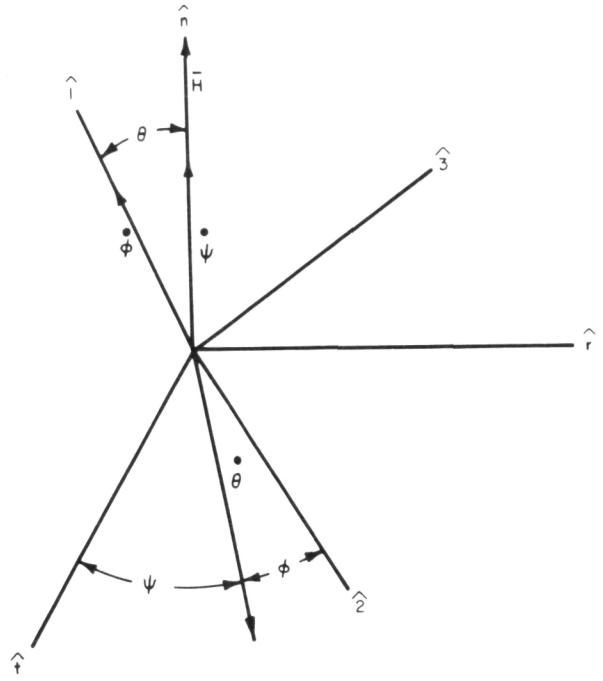

Figure 2.3-1. Euler Angles Used to Describe Spacecraft Body Motion

Motion of the $\hat{1}$ axis about the total $\bar{H}$ vector is given by the following equation.

$$\dot{\psi} = \frac{H}{\sqrt{I_2 I_3}} \; rad./sec. \tag{2.3-3}$$

As the $\hat{1}$ axis rotates about $\bar{H}$, the body rotates about the $\hat{1}$ axis at the rate $\dot{\phi}$. The equation for $\dot{\phi}$ is as follows

$$\dot{\phi} = \frac{\omega_1 (\sqrt{I_3 I_2} - I_{\hat{1}})}{\sqrt{I_3 I_2}} - \frac{I_f \omega_f}{\sqrt{I_3 I_2}} \tag{2.3-4}$$

Both $\dot{\psi}$ and $\dot{\phi}$ are important in describing the operation of the nutation damper discussed in Section 3.3. It should be pointed out that equation (2.3-4) is an approximation of the value for $\dot{\phi}$; the value is not a constant (as is implied) but actually is a function of the angle ψ. The details of the exact motion of a body with three

separate and distinct moments of inertia are too complex for discussion here. The departures from the exact motion have been studied and it can be positively assumed that, for the values of I_1, I_2, and I_3 used in the present study, good estimates for the initial design will result. A complete computer analysis will be initiated when the final design is more fully specified.

2.3.2 Momentum Considerations

To date, no determination has been made for a number which can be defined as the best, least, or safest, value for angular momentum to be used in this design study. RCA has had applicable experience with two types of spacecraft which have been orbited; there was an order of magnitude difference between their angular momentum. Both spacecraft performed their missions, but the spacecraft with the higher angular momentum was less sensitive to external and internal disturbances. This performance was the basis for the value of momentum which was selected. The value used throughout the study is 141 inch-lbs.-seconds.

After a number for angular momentum is established, it is possible to arrive at an optimum design. The criteria was established originally[2] and is summarized in Figures 2.3-2 and 2.3-3. The Figures show that, to meet a damping time-constant of 3 minutes, a damper-fluid weight of 11 pounds and a flywheel of 11 pounds are required. The values are the ones used at the start of the study program. However, as progress was made the weight totals began to mount until the design goal of 50 pounds total was almost exceeded. A decision was then made to reduce

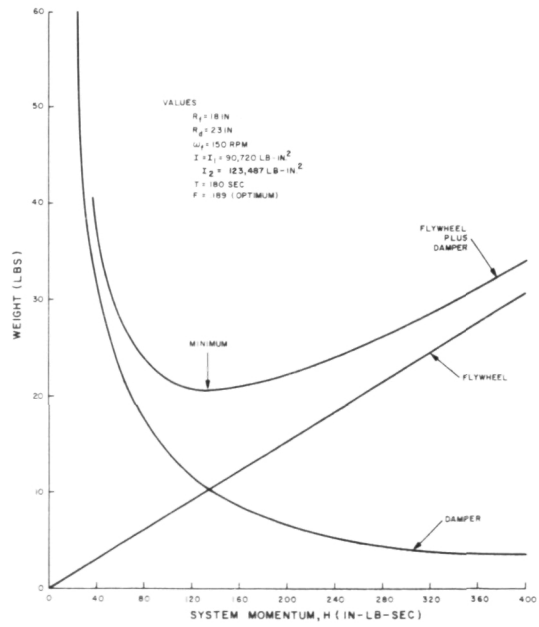

Figure 2.3-2. Dynamic Weight Versus System Momentum

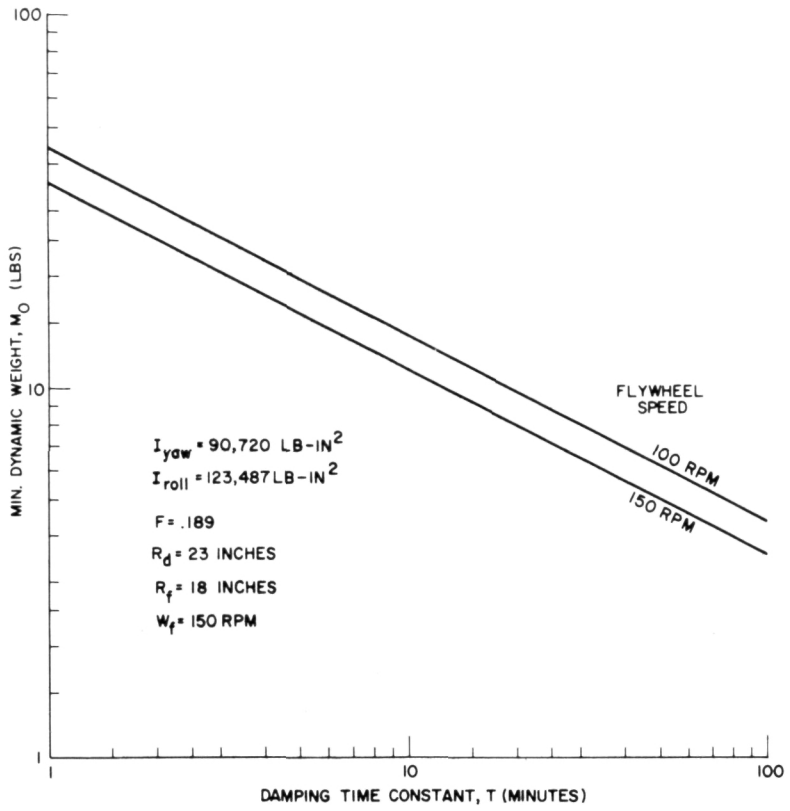

Figure 2.3-3. Minimum Dyanmic Weight Versus Damping Time-Constant

the damper-fluid weight to 3.48 pounds without affecting the flywheel; the results of this change caused the damping time to increase to 9.7 minutes. Figure 2.3-3 shows that the optimum total weight for the flywheel and damper for a 9.7-minute time constant would require only a total of 11.2 lbs. equally divided. Thus, the present time-constant could be obtained by reducing the flywheel weight from 11 pounds to 5.6 pounds and increasing the damper-fluid weight from 3.5 to 5.6 for a net weight reduction of 3.2 pounds. However, this change is not recommended because it would cause a decrease in the value of angular momentum in the system. Until further experience is obtained, it appears that a time-constant increase is a better compromise than an angular-momentum reduction. The design curves of Figure 2.3-2 and 2.3-3 should be considered only as a guide and not as a specification.

The speed of the flywheel has tentatively been set at 150-rpm nominal. This value includes a consideration of the life associated with rotating components, and is consistent with current experience at RCA. Higher speeds may be possible as the development progresses, however, doubling the speed would not have the effect of reducing the total control-system weight by 5.5 pounds (i.e., one-half the flywheel weight). The flywheels are made up of parts which are approaching their minimum

size; the mass which contributes substantially to the momentum is the scanner which has an irreducible minimum. With a minimum momentum of 141 in.-lb.-sec. specified, 150-rpm is not far from the optimum speed when all factors are considered.

2.3.3 Control Considerations

The control dynamics developed for the attitude control system are presented. The equations obtained are utilized in Section 3 of this report where the specific control modes and subsystems are discussed.

The fundamental equation defining the attitude motion of the spacecraft when acted upon by an external torque, T, is

$$\bar{T} = \left.\frac{d\bar{H}}{dt}\right|_I \qquad (2.3\text{-}5).$$

where I signifies the inertial axes. The time rate of change of $\bar{H}$ with respect to the inertial axes can be defined in terms of a rotating-axis system by the equation

$$\left.\frac{d\bar{H}}{dt}\right|_I = \left.\frac{d\bar{H}}{dt}\right|_R + \bar{\omega} \times \bar{H} \qquad (2.3\text{-}6)$$

where R signifies rotating axes and ω is the angular velocity of the rotating-axis system with respect to the inertial system. In general, $\bar{H}$ has components along all three axes of the spacecraft. However, for the present system the momentum about the axes perpendicular to the flywheel (or pitch axis) is extremely small when compared to the flywheel momentum. It can be neglected when considering the primary control modes of the system, but it is extremely important in considering nutation damping. The momentum about the pitch axis is defined as

$$\bar{H} = \left[(I_f \dot{\theta}_f) + (I_1 \dot{\theta}_1)\right] \hat{I} = |\bar{H}|\, \hat{I} \qquad (2.3\text{-}7)$$

where I_f and I_1 are flywheel and vehicle (without flywheel) moments of inertia about the pitch axis, $\dot{\theta}_f$ is the flywheel rate, and $\dot{\theta}_1$ is the vehicle pitch rate.

Substitution and solution for $\bar{T}$ yields

$$\bar{T} = \frac{d|\bar{H}|}{dt}\hat{I} + |\bar{H}|\frac{d\hat{I}}{dt} + |H|\,(\omega \times \hat{I}) \qquad (2.3\text{-}8)$$

The total torque on the vehicle is made up of components about axes $\hat{1}, \hat{2}, \hat{3}$, ($\bar{T}_1, \bar{T}_2, \bar{T}_3$) due to external disturbances and components and due to the three types of magnetic control employed (QOMAC torques $\bar{T}_Q$, magnetic-bias torques $\bar{T}_{MB}$, and magnetic momentum control torques $\bar{T}_{MM}$). Therefore, equation (2.3-8) can be written as

$$\bar{T}_{1f} + \bar{T}_1 + \bar{T}_2 + \bar{T}_3 + \bar{T}_Q + \bar{T}_{MB} + \bar{T}_{MM} = \frac{d|\bar{H}|}{dt}\hat{1} + |\bar{H}|\frac{d\hat{1}}{dt} + |\bar{H}|(\omega \times \hat{1}) \qquad (2.3\text{-}9)$$

where the subscript f (in $\bar{T}_{1f}$) denotes the flywheel.

For this discussion, only secular torques will be considered. The basic functions of the magnetic control subsystems and the torquing mode that is utilized for each of these functions are given in the following sections.

2.3.3.1 Initial Alignment

The initial alignment of the $\hat{1}$ (pitch) axis along the $\hat{n}$ axis is accomplished utilizing QOMAC. It is shown in Section 3.2 that

$$\tilde{\bar{T}}_Q = \tilde{\bar{T}}_{Q2}\hat{2} + |\tilde{\bar{T}}_{Q3}|\hat{3} \qquad (2.3\text{-}10)$$

where the symbol "$\simeq$" indicates an average torque.

2.3.3.2 Control of Momentum About the Pitch Axis

The control of momentum about the pitch axis utilizes magnetic momentum control. It is shown, in Section 3.2, that

$$\tilde{\bar{T}}_{MM} = |\tilde{\bar{T}}_{MM1}|\hat{1} + |\tilde{\bar{T}}_{MM2}|\hat{2} \qquad (2.3\text{-}11)$$

It is further shown that the $\hat{2}$ component is an undesired secular cross-coupling term that may be kept small through proper subsystem operation.

2.3.3.3 Cancellation of Secular Torques

The cancellation of secular torques caused by a vehicle residual-dipole along the $\hat{1}$ axis is accomplished utilizing magnetic-bias control. It is shown, in Section 3.2, that this cancellation can be made to a high degree of accuracy and is limited only by the coil-current control resolution.

2.3.3.4 Tracking of the Orbit Normal

The tracking of the orbit normal by the $\hat{1}$ axis utilizes magnetic bias control. This process can be mathematically expressed from equation (2.3-9) as

$$\tilde{\bar{T}}_{MB} - |\bar{H}|(-\omega_2\hat{3} + \omega_3\hat{2}) = |\bar{H}|\frac{d\hat{1}}{dt} \qquad (2.3\text{-}12)$$

where $\bar{\omega} = \omega_1\hat{1} + \omega_2\hat{2} + \omega_3\hat{3}$ and $\bar{T}_2$ and $\bar{T}_3$ have been neglected. It is shown in Section 3.2 that

$$\tilde{\bar{T}}_{MB} = |\tilde{\bar{T}}_{MB2}|\hat{2} + |\tilde{\bar{T}}_{MB3}|\hat{3} \qquad (2.3\text{-}13)$$

and that the magnitude and phase of $\bar{T}_{MB}$ and $|\bar{H}|(\omega \times \hat{1})$ can usually be made equal so that $|\bar{H}|d\hat{1}/dt$ equals zero and perfect average tracking is obtained (within coil-current resolution).

It should be noted that QOMAC can also perform this function but only by substantially increasing control complexity.

2.3.3.5 Correction for External Disturbance Torques

Correction for external disturbance torques $\bar{T}_2$ and $\bar{T}_3$, and for momentum-control cross-coupling torque $\bar{T}_{MM2}$ can be accomplished utilizing either magnetic bias or QOMAC control.

2.3.3.6 Pitch-Axis Pointing Control

Pitch-axis pointing control is obtained through the transfer of momentum between the flywheel and the verticle by a motor which is excited by the pitch-axis stabilization control subsystem. The dynamic equations defining the motion of the flywheel and the vehicle about the pitch axis can be obtained by summing torques about each of these bodies as follows.

$$M_f = I_f \ddot{\theta}_f + D(\dot{\theta}_f - \dot{\theta}_1) \tag{2.3-14}$$

$$M_1 = -I_1 \ddot{\theta}_1 + D(\dot{\theta}_f - \dot{\theta}_1) \tag{2.3-15}$$

where M_f is the Motor Torque minus Friction Torque plus T_{1f}, M_1 is the Motor Torque minus Friction Torque plus T_1, and D is the Motor Viscous Damping.

Combining equations (2.3-7) and (2.3-15) yields

$$-\frac{M_1}{I_1} = \ddot{\theta}_1 + \frac{D}{I_e}\dot{\theta}_1 - \frac{DH}{I_1 I_f} \tag{2.3-16}$$

where

$$I_e = \frac{I_1 I_f}{I_1 + I_f}$$

Using the Laplace Transform of equation (2.3-16) and solving for $\theta_p(s)$ yields

$$\theta_1(s) = \frac{-\frac{M_1 I_f}{D(I_1 + I_f)} + (\theta_1)_0\left(\frac{I_e}{D}S + 1\right) - \frac{I_e}{D}(\dot{\theta}_1)_0 + \frac{H(S)}{(I_f + I_1)}}{S\left(\frac{I_e}{D}S + 1\right)} \tag{2.3-17}$$

where the subscript $(\ )_0$ denotes the initial value and S is the Laplacian operator. Equation (2.3-17) is used in Section 3.1 of this report for the analysis of the pitch-axis-stabilization control subsystem.

2.3.4 Disturbance Analysis

2.3.4.1 Summary of Disturbance Torques and Effects

Table 2.3-1 presents a complete summary of all disturbance torques and a brief description of their dynamic effects. The development of this table is discussed in the following paragraphs.

TABLE 2.3-1. SUMMARY OF DISTURBANCE TORQUES AND DYNAMIC EFFECTS

Source of Disturbances	Disturbance Torque	Axis of Action	Effect of Disturbance on Spacecraft
1. Residual Magnetic Dipoles a. 1 ATM^2 (max.) along yaw axis	① Sinusoidal Torque, 200 dyne-cm amplitude, one cycle per orbit, zero average	① Pitch	① Sinusoidal modulation of momentum, $\pm 0.3\%$ peak change in momentum, zero average
	② Slowly changing torque, varies between -8 dyne-cm and +70 dyne-cm, one cycle per day, practically constant over one orbit	② Roll	② Slow precession of pitch axis around a cone, one complete cycle around cone per orbit, maximum half-cone angle of 0.027^o
b. 1 ATM^2 (max.) along roll axis	① Sinusoidal torque, 400 dyne-cm amplitude one cycle per orbit, zero average	① Pitch	① Sinusoidal modulation of momentum, $\pm 0.6\%$ peak change in momentum, zero average
	② Slowly changing torque, varies between -70 dyne-cm and +8 dyne-cm, one cycle per day, practically constant over one orbit	② Yaw	② Slow precession of pitch axis around a cone, one complete cycle around cone per orbit, maximum half-cone angle of 0.027^o
c. 0.035 ATM^2 (max.) along pitch axis (i.e. resolution capability of magnetic bias coil steps)	Sinusoidal torque components, two cycles per orbit:		Slow precession of pitch axis; sinusoidally varying rotations, two cycles per orbit:
	① 10 dyne-cm amplitude, zero average	① $\hat{h}$	① 0.004^o amplitude about $\hat{\ }$, zero average
	② -7 dyne-cm to +14 dyne-cm, +3.5 dyne-cm average	② $\hat{\ }$	② $+0.006^o$ to -0.002^o about $\hat{h}$, $+0.008^o$ net about $\hat{h}$ per orbit
2. Magnetic Hysteresis Losses for 15 lbs. of magnetic material	Secular drag torque, 6 dyne-cm average	Pitch	Slow decay of momentum, 0.4% per day
3. Solar Pressure	Cyclic torque pattern, symmetric about Sun Line, ± 13 dyne-cm peaks, zero average	Pitch	Cyclic modulation of momentum, $\pm 0.01\%$ peak change in momentum, one cycle per orbit, zero average
4. Impulsive Disturbances a. Micrometeorite impact	Maximum single impulse having 0.5 probability for 1 year is 6×10^{-4} in-lb-sec	Any Axis	Maximum attitude shift of 0.002^o, maximum change of momentum of 0.004%, max. rate about yaw axis of 2.5×10^{-5} rad/sec, max. rate about roll axis of 2×10^{-5} rad/sec
b. Uncompensated momentum of rotating equipment	Maximum momentum of tape recorder is 1.6×10^{-2} in.-lb.-sec. along yaw axis, torques are completely internal to satellite	No External Torque	Nutation of pitch axis, sinusoidal rotations about roll and yaw axes, one cycle in 5 minutes, zero average: — Roll axis amplitudes are 0.006^o angular rotation and 5×10^{-5} rad/sec ang. rate — Yaw axis amplitudes are 0.008^o ang. rotation and 7×10^{-5} rad/sec ang. rate
5. Gravity Gradient Effects a. 1 Degree angular displacement of pitch axis out of orbit plane	Orbit averaged torque of 2.7 dyne-cm axis normal to plane of pitch axis and orbit normal	Instantaneous torque about Roll Axis	Slow precession of pitch axis parallel to orbit plane in direction of average torque vector, 0.009^o per orbit
b. Steady-state pitch angle offset held by Type I pitch servo to compensate for difference between existing momentum and nominal design value	Torque proportional to offset angle, 4.6 dyne-cm per degree offset, acting to reduce offset and reduce difference between existing momentum and nominal design value.	Pitch	Slow reduction of difference between existing momentum and nominal design value, time constant of reduction is 60 days.
c. Angular deviation of geometric axes from axes of principal inertia by 0.1 degree	① Torque decreasing from 0.5 dyne-cm to zero exponentially	① Pitch	① Slow change of momentum until a difference between the existing momentum and the nominal design value is developed such that the Type I pitch servo holds a steady-state pitch angle off-set equal to the angle between the geometric roll axis and the principal inertia roll axis. Time constant of this convergence is 60 days. The equilibrium speed of the flywheel is 150 ± 3.2 rpm for 0.1^o angle.
	② Constant torque of 0.7 dyne-cm	② Roll	② Slow precession of pitch axis around cone, one complete cycle around cone per orbit, half-cone angle of 2.6×10^{-1} degrees.
6. Negligible Effects	Magnetic eddy-current losses; Incident radiation; High energy particles; Multibody effects; Earth oblateness; Aerodynamic drag; Dynamic Unbalances	All Axes	These effects produce perturbations of negligible magnitude

2.3.4.2 Residual Dipoles

The effect of residual dipoles along the roll- and yaw-axes has been computed utilizing the magnetic-momentum-control analysis presented in Section 3.2.4 of this report; it is shown there that commutating at 1/2-orbit intervals for a yaw-axis coil of 7.7 ATM^2 produces a 2% change in momentum per 1/2-orbit. Therefore, a 1 ATM^2 residual dipole would produce 1/7.7 of that value. The residual dipole direction is constant; therefore, cancellation occurs over the full orbit, and the torque is cyclic. The same analysis applies for the roll-axis dipole except that the average magnitude of the earth's magnetic field is greater by a factor of two. The motion about the roll-axis is computed in the same manner as is the momentum-control precession torque motion and has a net effect of zero over an orbit (again because of the dipole-direction constancy).

The effect of a residual dipole along the pitch-axis is computed in exactly the same manner as is used for the magnetic-bias calculations presented in Section 3.2.3 of this report. The cyclic motion about the vector $\hat{\ell}$ is equivalent to the instantaneous out-of-plane motion of vector $\hat{l}$ with respect to vector $\hat{n}$ discussed in that section.

2.3.4.3 Magnetic Hysteresis Losses

The momentum losses due to hysteresis have been estimated on the basis of an assumed 15 pounds of magnetic material in the spacecraft. It should be noted that the analysis used to obtain the loss rate of 0.4% per day is, by necessity, only an approximation because of limited information available about the distribution of the magnetic materials. Compared to present spacecraft decay rates, this value appears very conservative. For example, based on TIROS data extrapolated to a polar orbit, the best estimate on momentum decay (the FSMTMS and TIROS have similar total momentum values) is 0.3% per day. However, previous evaluations of TIROS data indicate that a maximum of 15% of this decay is due to hysteresis losses; the remaining 85% is due to eddy current losses which will be negligible for the FSMTMS (the spacecraft is not spinning and the flywheel has almost no induced eddy currents because of its construction). Consequently, the estimate used here is ten times the decay rate due to hysteresis that is predicted for the TIROS wheel satellite in a polar orbit.

2.3.4.4 Solar Pressure and Impulsive Disturbance

An analysis of these disturbances was previously submitted[2].

2.3.4.5 Gravity Gradient

A complete analysis of the effects of gravity torques was presented previously[3].

Section 3.0

PRELIMINARY DESIGN ANALYSIS

3.1 PITCH-AXIS-STABILIZATION CONTROL SUBSYSTEM

3.1.1 General

The function of the pitch-axis-stabilization control subsystem is to maintain the yaw axis in alignment with the local vertical after the initial alignment phase following payload separation. The subsystem must position the yaw axis within the required accuracy and within a reasonable time. This operation imposes the most severe dynamic requirement on the control subsystem and was, therefore, of prime consideration during the study program.

The vehicle is positioned about the pitch axis by means of momentum transfer between the flywheel and the vehicle. This momentum transfer is accomplished using d-c torque motor to couple the flywheel to the vehicle. A horizon scanner, mounted on the flywheel, generates a horizon pulse each time a change from cold space to warm earth is sensed. A variable-reluctance pickoff coil generates an index pulse each time a flywheel reference point passes a reference point on the vehicle. For a particular orbit altitude, this reference point is geometrically positioned so that the horizon pulse and the index pulse are time coincident when the vehicle yaw axis is aligned with the local vertical.

A block diagram of the pitch-axis-stabilization control subsystem is shown in Figure 3.1-1; the general operation of this subsystem is described in the following paragraphs.

The position error, or deviation of the body axis from the local vertical, is established by using a Pulse-Width-Modulation (PWM) Error Detector to measure the time difference between the horizon pulse and the index pulse. The error signal is a constant-amplitude, variable-pulse-width voltage; the width of the error signal is proportional to the angular error. The signal is shaped to an amplitude modulated voltage by the use of appropriate filtering; this voltage is properly compensated, by frequency-sensitive networks, and applied to a speed-control loop (tachometer loop). The voltages from the fixed-speed bias command and the compensated-position error voltage are compared (using a differential amplifier) with a signal proportional to the speed in the speed-control-loop error detector. The signal proportional to the speed is generated by a serial pulse encoder mounted integrally with the drive motor; the pulses are converted to a d-c

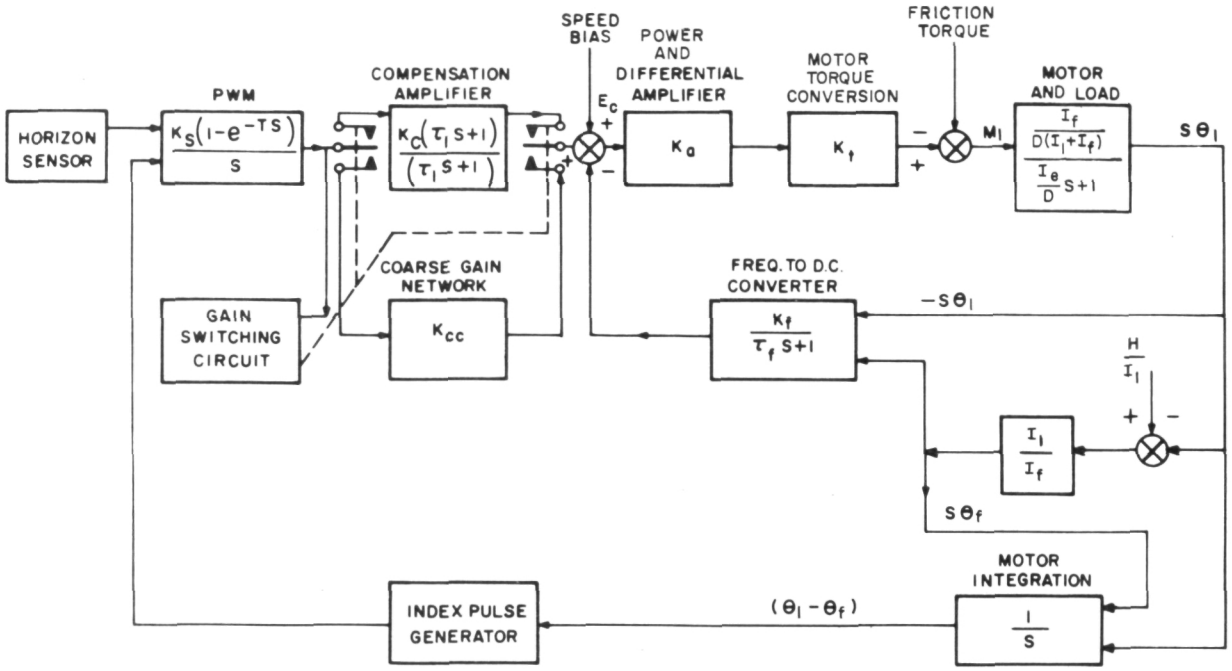

Figure 3.1-1. Block Diagram of the Pitch-Axis-Stabilization Control Subsystem

voltage by means of a frequence-to-d-c converter and are smoothed using a simple lag circuit. The output of the differential amplifier is fed to a power amplifier which supplies current to the drive motor; the drive motor then applies a torque between the flywheel and the vehicle to properly transfer momentum and reduce the position error toward a value of zero.

During initial acquisition, and prior to closed-loop position control the flywheel speed relative to the vehicle is increased to the speed commanded by the speed bias-voltage. The initiation of subsystem closed-loop position control is ground commanded after the 90^{o} Quarter-Orbit Magnetic Attitude Control (QOMAC) turn; and vehicle momentum less than or in excess of that required to rotate at the orbital rate is transferred to or from the vehicle by means of the control subsystem. While the control subsystem is performing this function, a low-gain loop is utilized, instead of the normal compensation, to compensate for potential saturation limit cycles. The switching is performed as a function of pointing error.

The control subsystem is constrained to maintain the pointing accuracy to within $\pm 1.0^{o}$ and the jitter rate to a value of 0.05^{o}/sec. or less. The subsystem inaccuracy is the root-mean-square value of all errors after stabilization (including control subsystem errors, sensor errors, and resolution errors). Furthermore, during initial acquisition, the subsystem must acquire control in the presence of an initial momentum deviation of $\pm 33\%$ of the nominal design momentum (or an

equivalent spacecraft spin-rate of about 8°/sec.) about the pitch axis. The initial momentum deviation will be the predominate disturbing influence; thus, a recovery from this disturbance ensures the capability of the subsystem to recover from any other expected disturbance.

Deviation in orbit height from the planned orbit will tend to cause a fixed error in pointing accuracy due to the geometric arrangement used to determine the local vertical. (For a 50-nautical mile deviation from the expected orbit, this error will be approximately 1.3 degrees.) It is possible that this fixed error may exist; therefore, the effect of the error on the type of control subsystem should be considered. Two types of control subsystems are possible: a Type I subsystem requires a fixed position error to maintain a fixed deviation from nominal wheel speed; a Type II subsystem requires a zero position error to maintain a fixed deviation from nominal wheel speed. Various configurations of Type I and Type II subsystems were evaluated and a Type I was selected which uses lag-lead compensation.[4] One of the major reasons for this selection was the compatibility of the Type I subsystem with the gravity-gradient torque over an extended period of time.[3] Furthermore, although the effect of the gravity-gradient torque is small, it will add or subtract momentum in the direction which will reduce the local-vertical offset to a value equal to the misalignment between the three principal axes of the spacecraft and the specified yaw axis. However, using a Type I subsystem, this misalignment can be kept to less than 0.1 degree.

Assuming the orbit height is the planned height, altitude deviations will still be present due to the ellipticity of the orbit. In the worst case, an eccentricity of 0.013 will cause an altitude deviation of approximately ±50 nautical miles, or a pointing inaccuracy of approximately ±1.3°. This error, if present, will be cyclic at a repetition rate of 1 cycle per orbit. The error pattern will be predictable and as such can be used in data interpretation or can be controlled by programming a correction into the system.

The previous errors are time-predictable errors which can be eliminated by ground command, if required. An additional alternative having considerable merit from several standpoints is to use a horizon splitter to generate the horizon pulse. This device utilizes horizon scanners sensing both the change from cold space to warm earth and of warm earth to cold space to determine the time the vehicle points to the earth. By splitting this time by use of computer circuitry the local vertical can be determined regardless of the altitude deviations.

The prime disadvantages of this unit are the inaccuracy of determining the earth to sky transition and the additional circuit complexity. A further discussion of the pros and cons of splitting versus non-splitting may be found in Section 3.4.

3.1.2 Discussion and Parametric Results

3.1.2.1 Error Measurement

To obtain the correct pitch-axis stabilization, the orientation of the vehicle yaw axis with respect to the local vertical must be known. It is necessary, therefore, to measure the angle in a plane normal to the spin axis between the local vertical and some reference position on the spacecraft. Assuming the spin axis has been nominally aligned normal to the orbital plane by magnetic means, the plane normal to the spin axis contains both the local vertical and the reference points on the vehicle. The orientation of the vehicle with respect to the local vertical is measured indirectly by the use of the horizon pulse and the index pulse. When the orbit height is known, proper offsetting of the index pulse will cause both the index and the pulses to occur in time coincidence when the spacecraft reference is in proper orientation with respect to the local vertical. The time difference of occurrence of the two pulses will be proportional to the angular deviation of the vehicle from the local vertical. The direction, or arithmetic sign, of the error is determined by the time relationship of the two pulses.

The block diagram of the Pulse-Width-Modulator Error Detector error measurement device is shown in Figure 3.1-2. The operation is given in the following paragraphs.

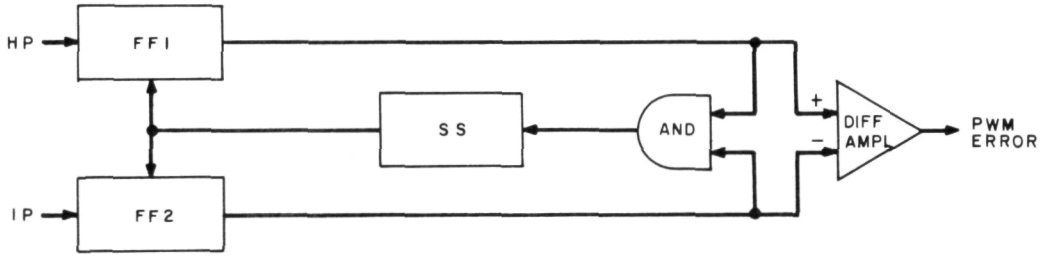

Figure 3.1-2. Block Diagram of the Pulse-Width-Modulator (PWM) Error Detector

The horizon pulse (H. P.) and the index pulse (I. P.) set flip-flop circuits 1 and 2 respectively. The outputs of the flip-flops are fed to a difference amplifier and a resetting circuit consisting of an "AND" gate and a monostable multivibrator (S. S.) The outputs of the flip-flops are of the same polarity; therefore, the output of the difference amplifier is the difference of the two inputs with the sign dependent upon which signal occurred first in time. When both flip-flops are set by their respective input pulses, a signal appears at the output of the "AND" circuit which triggers the single shot (monostable) multivibrator and resets both flip-flops.

The output of the difference amplifier is then a pulse with the width proportional to the angular error and the arithmetic sign indicative of the direction of the error. This pulse occurs once for each rotation of the flywheel, thus, the output of the error detector is of the sampled-data form. The error-measurement characteristics are shown in Figure 3.1-3.

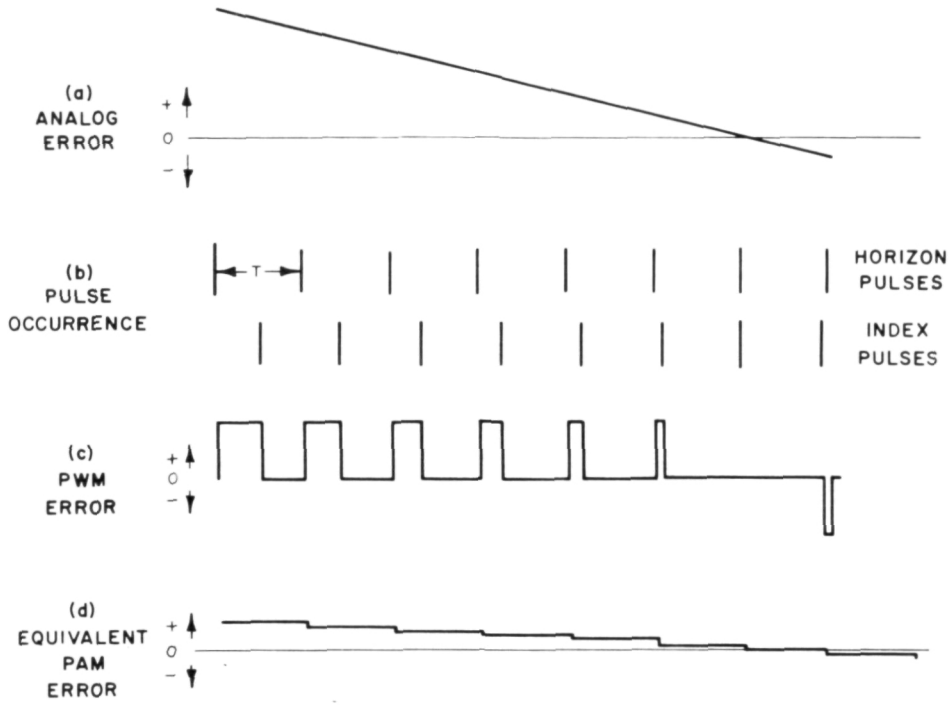

Figure 3.1-3. Error-Measurement Characteristics

Part c of this Figure illustrates the output of the error detector and the error signal reducing in time and overshooting. Part d of Figure 3.1-3 shows the equivalent pulse amplitude modulated signal. This equivalence is satisfactory for a linearized analysis if the areas of the corresponding PWM and PAM energy over each sample period are equal, and if the sampler is followed by a filter whose largest time constant is at least twice as great as the sampling period. When the substitution of the pulse amplitude modulated signal for the pulse width modulated signal is made the error detector can be conservatively represented as an amplitude sampler in cascade with a zero-order hold. The transfer function of this device has the characteristics, in Laplace form, of

$$H_s(S) = \frac{1 - e^{-TS}}{S};$$

where T is the sampling period
S is the Laplace operator

For a low-frequency response system, such as the one under study, this transfer function can be simplified and described for Bode plot analysis as:

$$H_s(j\omega) = \frac{T \sin \omega T/2}{T/2} \; e^{\frac{-jT\omega}{2}}$$

or, since the amplitude variation will in this case, be extremely small over the bandpass, as

$$H_s(S) = e^{\frac{-TS}{2}}$$

For the system under study, the flywheel speed and, hence, the sampling time (T) will vary; this will have the effect of changing the system phase shift because sampler phase-shift is a function of the sampling period.

This type of error measurement device was tested in a simulation of the Nimbus system on the analog computer and also on a System Demonstrator at RCA. The device performed satisfactorily.

3.1.2.2 Parametric Results

The pitch-axis-stabilization control subsystem design is based on the use of components of the lowest weight, smallest size, and lowest power consumption consistent with the performance requirements of the system. The design has been implemented using both analytical and computer techniques to achieve a subsystem compatible with the requirements of rapid capture-time, acceptable pointing accuracy, and jitter. The subsystem errors due to altitude deviations can be corrected, if required, by techniques which will impose no restraints on the stability of the subsystem. Therefore, the stability analysis has not included any requirements for altitude deviations.

The block diagram of the subsystem was shown in Figure 3.1-1; the interconnection and the transfer functions of the individual components are illustrated. The transfer function for the proposed subsystem was previously developed;[4] it is shown again in equation (3.1-1) for the low error, fine (high) gain condition.

$$\bar{G}_t = \frac{(1 - e^{-TS})}{S} \frac{K_s K_c \bar{G}_c}{S} \left(\frac{I_f}{I_f + I_1} \right) \left(\frac{\frac{K_t K_a}{D}}{1 + K_t K_a K_f} \right) \frac{1}{\left[\frac{I_e S}{D \left(1 + \frac{K_t K_a K_f}{D} \right) + 1} \right]} \quad (3.1\text{-}1)$$

where the constants are defined in Figure 3.1-1 or in Section 2.3.3.

The values of the constants that will be used in equation (3.1-1) are based on the use of available components which will yield the required performance for the subsystem. The motor was selected on the basis of: the torque required to position the yaw-axis within a reasonable time; damping coefficient to allow satisfactory gains; and back emf sufficient to allow the required speed deviation with the available voltages. The type of motor selected has a K_t = 2.34 oz. in/volt. and a D = 0.79 oz. in/rad./sec. The K_t value was selected so that the power amplifier saturates at 15 volts. A motor can be selected with a different K_t. If the saturation level of the amplifier changes, another motor could be selected but will require a change in the value of K_a.

The tachometer is a serial-pulse generator with the output smoothed by a frequency-to-d-c converter. The converter may be characterized as a simple lag circuit with a transfer function given by

$$H_f(S) = \frac{1}{\left(\frac{S}{60} + 1\right)}$$

The frequency at which this lag circuit has an effect is sufficiently higher than the subsystem bandpass frequency so that it can be ignored. The gain of the tachometer system (K_f) was selected as 0.2 volts/rad./sec. based on devices previously used satisfactorily at RCA.

The sensor gain (K_s) selected is 1.27 volts/radian and is based on the use of a PWM with an output of $\pm$ 8.0 volts. The inertias involved are: I_f = 144 oz. in. sec.^{2}; I_1 = 5410 oz. in. sec.^{2}; and, therefore, I_e = 141 oz. in. sec.^{2}.

Using the constants selected, the previously stated approximation for the sample, and a hold circuit with a sampling time of 0.4 seconds, equation (3.1-1) becomes:

$$\bar{G}_t = e^{-0.2s}\left[\frac{1.27\,K_c\bar{G}_c}{S}\right]\left[\frac{1}{38.5}\right]\left[\frac{2.96\,K_a}{1 + 0.59\,K_a}\right]\left[\frac{1}{\frac{178\,S}{(1 + 0.59\,K_a)} + 1}\right] \qquad (3.1\text{-}2)$$

The Bode plot of the recommended subsystem, using lag-lead compensation, is shown in Figure 3.1-4. The tachometer loop closed-loop response is given by

$$\frac{S\,\theta_1}{E_c} = \frac{4.72}{9.5S + 1}$$

The transfer function of the compensation amplifier and network which are used in the low-error region is given by

$$K_c\,\bar{G}_c = 14.8\left[\frac{33.3\,S + 1}{500\,S + 1}\right]\left[\frac{1}{0.8\,S + 1}\right]$$

where the higher frequency lag is used for smoothing the error pulses.

The power amplifier gain was chosen as 30.

With the values of the constants as previously stated, the over-all open-loop transfer function is:

$$\frac{2.36\ (33.3S\ +\ 1)\ e^{-0.2S}}{S\ (500S\ +\ 1)\ (9.5S\ +\ 1)\ (0.8S\ +\ 1)} \qquad (3.1\text{-}3)$$

This yields a value of $K_v = 2.36$, a natural frequency = 0.11 rad./sec., a phase margin of 25°, and a gain margin of 16 db when the smoothing network for the PWM produced pulses is included. The final design of the subsystem probably will not require the inclusion of the smoothing network; however, the Bode plot shown in Figure 3.1-4 does include it but indicates the effect of its removal. The smoothing would be required if lead-lag compensation was used. However, the filtering action of the lag-lead compensation has been shown (see the next section) to be adequate for this purpose.

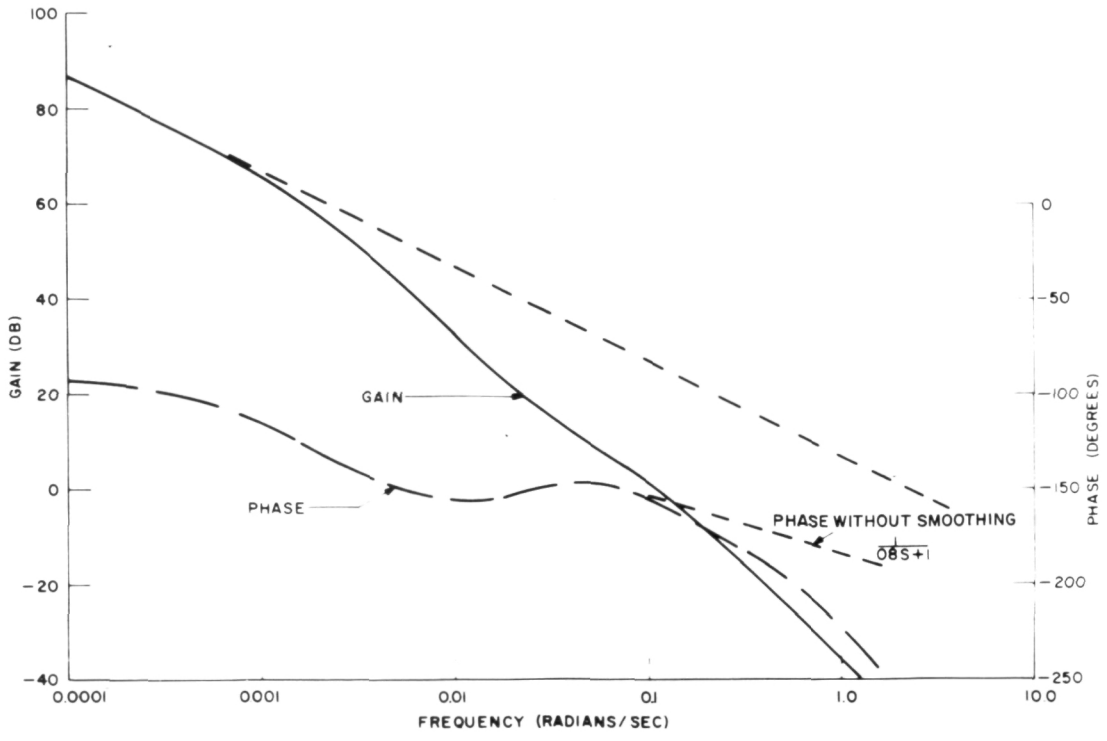

Figure 3.1-4. Bode Plot for the Recommended Pitch-Axis-Stabilization Control Subsystem Using Lag-Lead Compensation

The coarse (low) gain region required during large-error conditions will be defined in the next section and the coarse gain, K_{cc}, magnitude will be determined.

3.1.2.3 Analog Computer Simulation

An analog computer simulation of the pitch-axis-stabilization control subsystem was made to determine the response to large momentum disturbances. The block diagram of the analog computer set-up is shown in Figure 3.1-5. For small disturbances and steady state operation, the linear analysis made by use of the Bode plots is satisfactory to determine both subsystem operation and steady state inaccuracies. The study was, therefore, made to determine the ability of the subsystem to recover from very large disturbances. The study was general in nature because design parameters had not been finalized; however, the results indicate that several modes of compensation would be stable and would provide for recovery from large disturbances.

As expected, the subsystem response to large disturbances was critically dependent upon the gain-switching angle (fine-gain region) and the coarse gain. The ability to use a large fine-gain region and high coarse-gain are important not only because of stability and fast response, but also because it provides a larger momentum-change region in which fine gain, and therefore, low error is attained.

The analog computer study showed that a wider fine-gain region can be attained through the use of lag-lead, or proportional-plus-integral, control than by lead-lag control. For this and other previously discussed reasons, it appears that lag-lead compensation is the most desirable. Typical results obtained from the analog computer study are shown in Figures 3.1-6 through 3.1-11 inclusive. The amplifiers used were clamped to limit the output to ± 10 volts; the power amplifier, however, was limited to a value of from +0 to -15 volts. These limitations imposed the most vigorous saturation effects to be expected.

Further investigation of the computer results and the PWM error detector for large disturbances indicated that the error detector logic is such that when averaged over a period of time, an error of the proper sign will be generated regardless of the momentum deviation. Therefore, it was concluded that the saturation limits of the motor, the fine-gain region, and the coarse-gain determine the momentum-recovery band and the time required to recover.

In analog computer traces shown in Figures 3.1-6 through 3.1-11: Channel 1 is the pulse-width-error from the pulse-width-modulator; Channel 2 is the error after it is smoothed by means of an 0.8 second lag circuit; Channel 3 is the deviation of wheel speed about the nominal 150 rpm (15.7 radians/second); Channel 4 is the vehicle speed; Channel 5 is the equivalent torque applied to the motor to overcome friction, electrical damping, and provide acceleration; and Channel 6 is the error from the compensation amplifier.

The lag-lead case for a recovery from low momentum are shown in Figures 3.1-6, 3.1-7 and 3.1-8; the time changes in recovery from a step 24% lower and a step

30% lower than the nominal momentum are shown, respectively, in Figures 3.1-6 and 3.1-7 and are 3.7 and 5.1 minutes. Figure 3.1-8 shows the effect of increasing the fine-gain region from $\pm 25^{o}$ to $\pm 90^{o}$ and illustrates that this increase causes the subsystem to become unstable. In other runs not shown, the fine-gain region was increased to $\pm 45^{o}$ and the subsystem behavior was very similar to that shown in Figure 3.1-7.

Figures 3.1-9, 3.1-10, and 3.1-11 show the lag-lead case for a recovery from a 44% increase over the nominal momentum. Figure 3.1-9 shows a recovery in 6.8 minutes, but the subsystem locks in the coarse-gain region with an error of about 35^{o}; Figure 3.1-10 illustrates that, with the coarse-gain increased from 2.0 to 3.0 and a fine-gain region still maintained at $\pm 25^{o}$, the subsystem is very highly underdamped; Figure 3.1-11 illustrates the results when the coarse gain is returned to 2.0 but the fine-gain region is increased to $\pm 45^{o}$. In the last case, the subsystem stabilizes and locks in the fine-gain region in 13 minutes. Based on the data obtained from the analog computer study, the coarse-gain should be equal to 2.0 with a fine-gain region of $\pm 45^{o}$ to satisfy the momentum-deviation requirements.

3.1.2.4 Subsystem Simulator for Pitch-Axis-Stabilization Control

A control subsystem simulator was constructed under a corporate-funded AR and D program utilizing the pitch-axis-stabilization control subsystem previously described; however, a lead-lag compensation network was included in place of the lag-lead. While the parameters used were different from those used in the analog computer study, the over-all transfer function was closely simulated.

The results were consistent with those shown for the analog computer study for both transient and steady-state conditions. A photograph of the simulator constructed is shown in Figure 3.1-12. The simulator was then mounted on an air bearing constructed by RCA to provide friction sufficiently low so as to make the simulation-data useful. The internal design of the pitch-axis loop determines the damping, this was verified by comparing the simulation data with that predicted by the analog computer study.

3.1.3 Preliminary Design of Subsystem

The pitch-axis-stabilization control subsystem consists of the following components:

- Horizon Scanner
- Pulse-Width-Modulator (PWM)
- Compensation Amplifier
- Summing Amplifier
- Power Amplifier
- Frequency-to-d-c Converter
- Digital Shaft Encoder
- Earth-Detecting Circuitry
- d-c-to-d-c Converter
- d-c Motor

The quantity, type, and failure rate of each component were given previously.[3]

3.1.3.1 Horizon Scanner

The horizon scanner was previously discussed in some detail (3). Further details are provided in section 3.4 of this report.

Page intentionally left blank

Page intentionally left blank

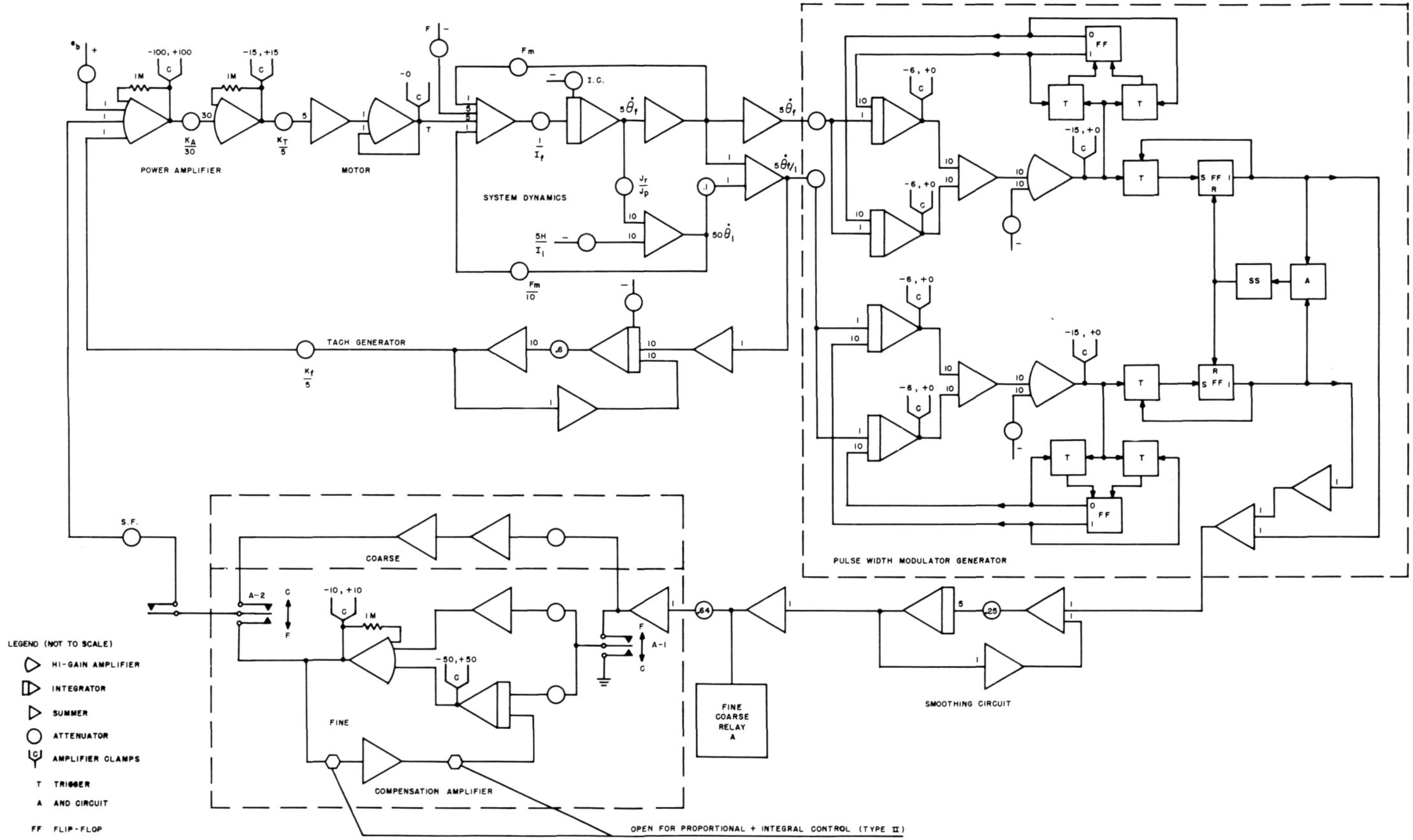

Figure 3.1-5. Block Diagram of the Analog Computer Setup

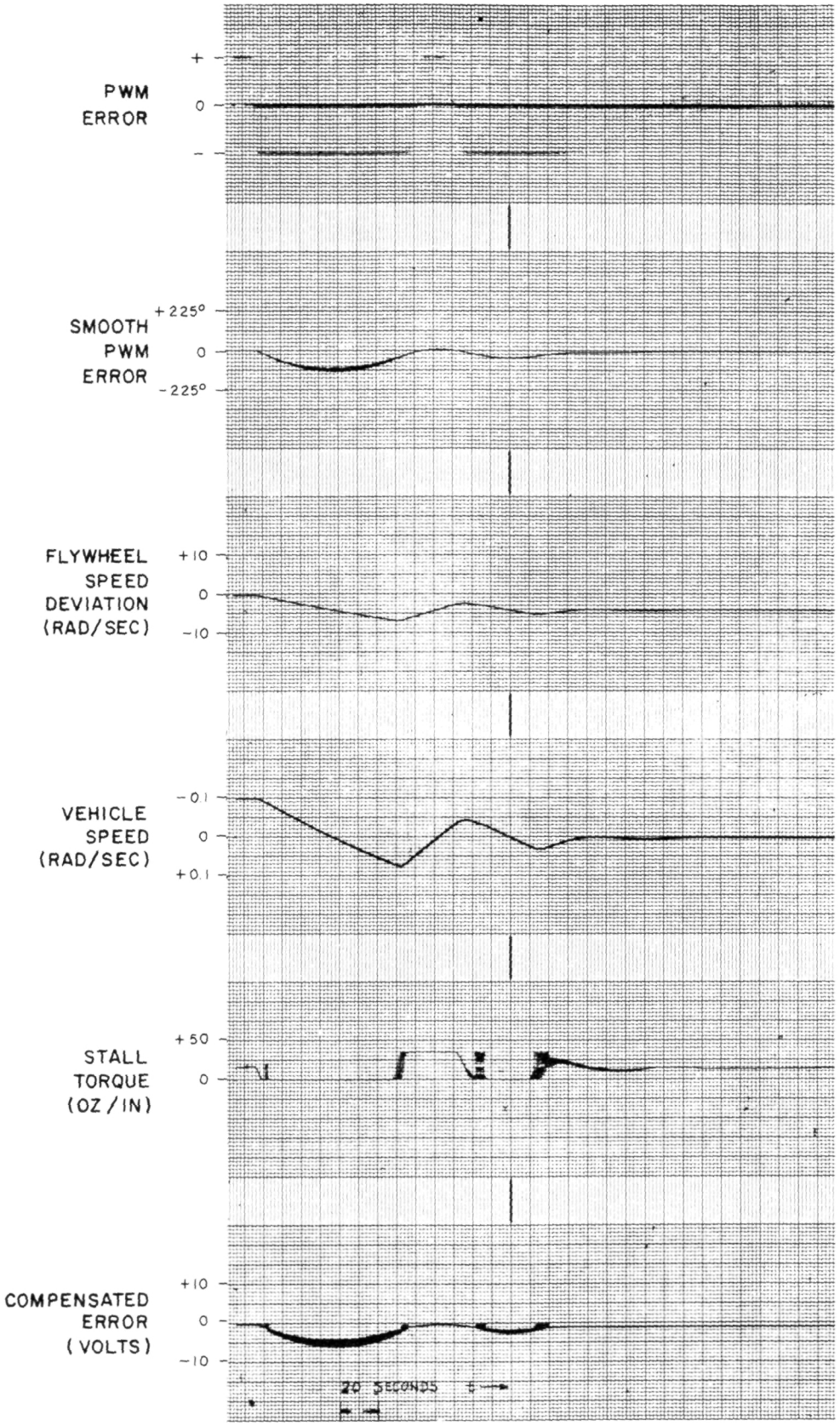

LEGEND:
LAG-LEAD COMPENSATION
COARSE AMP GAIN = 2.0
FINE GAIN REGION = ±25°
RESPONSE TO 24 % DECREASE IN MOMENTUM

Figure 3.1-6. Typical Results Obtained from the Analog Computer Study

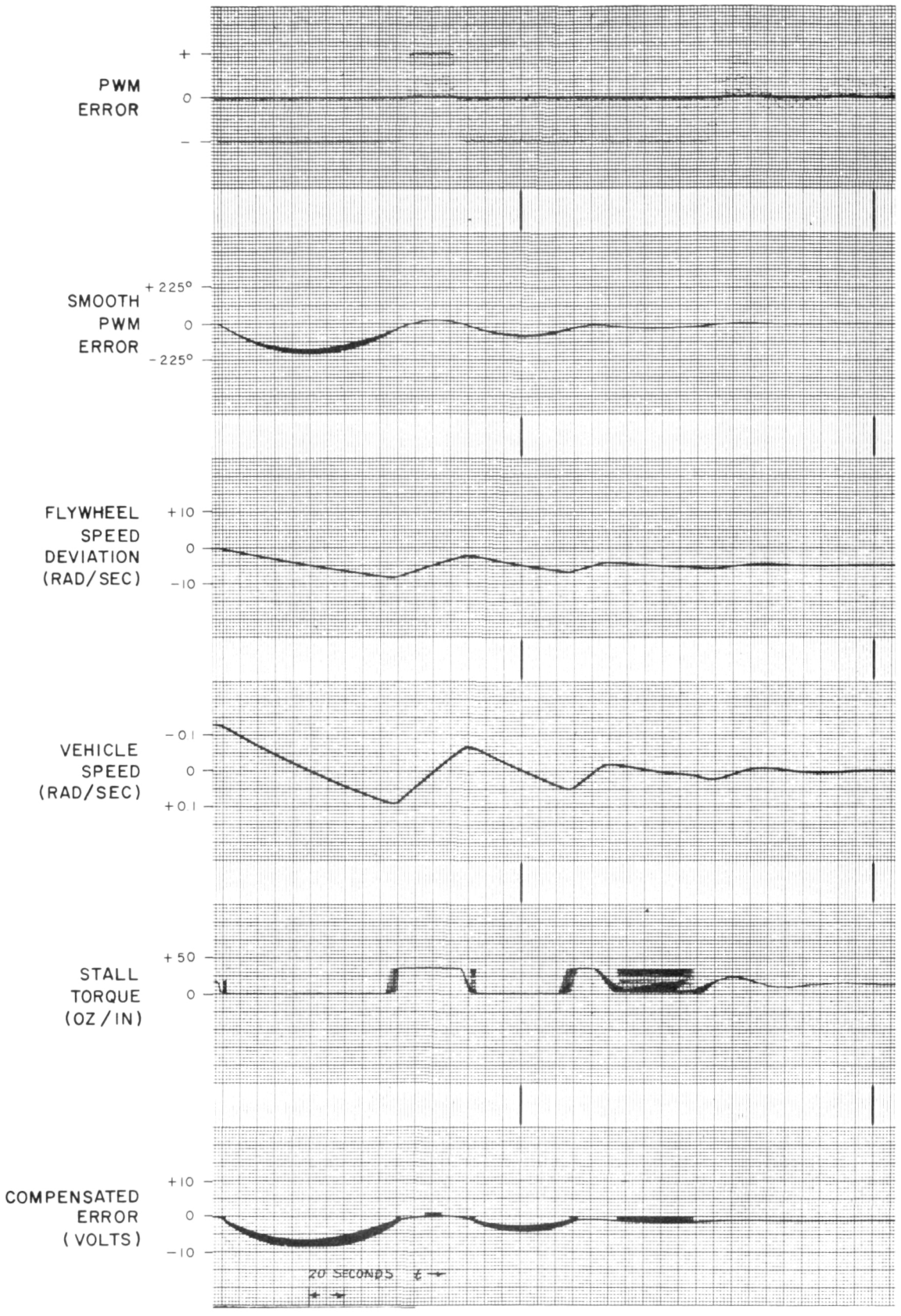

LEGEND:
LAG-LEAD COMPENSATION
COARSE AMP GAIN = 2.0
FINE GAIN REGION = ±25°
RESPONSE TO 30% DECREASE IN MOMENTUM

Figure 3.1-7. Typical Results Obtained from the Analog Computer Study

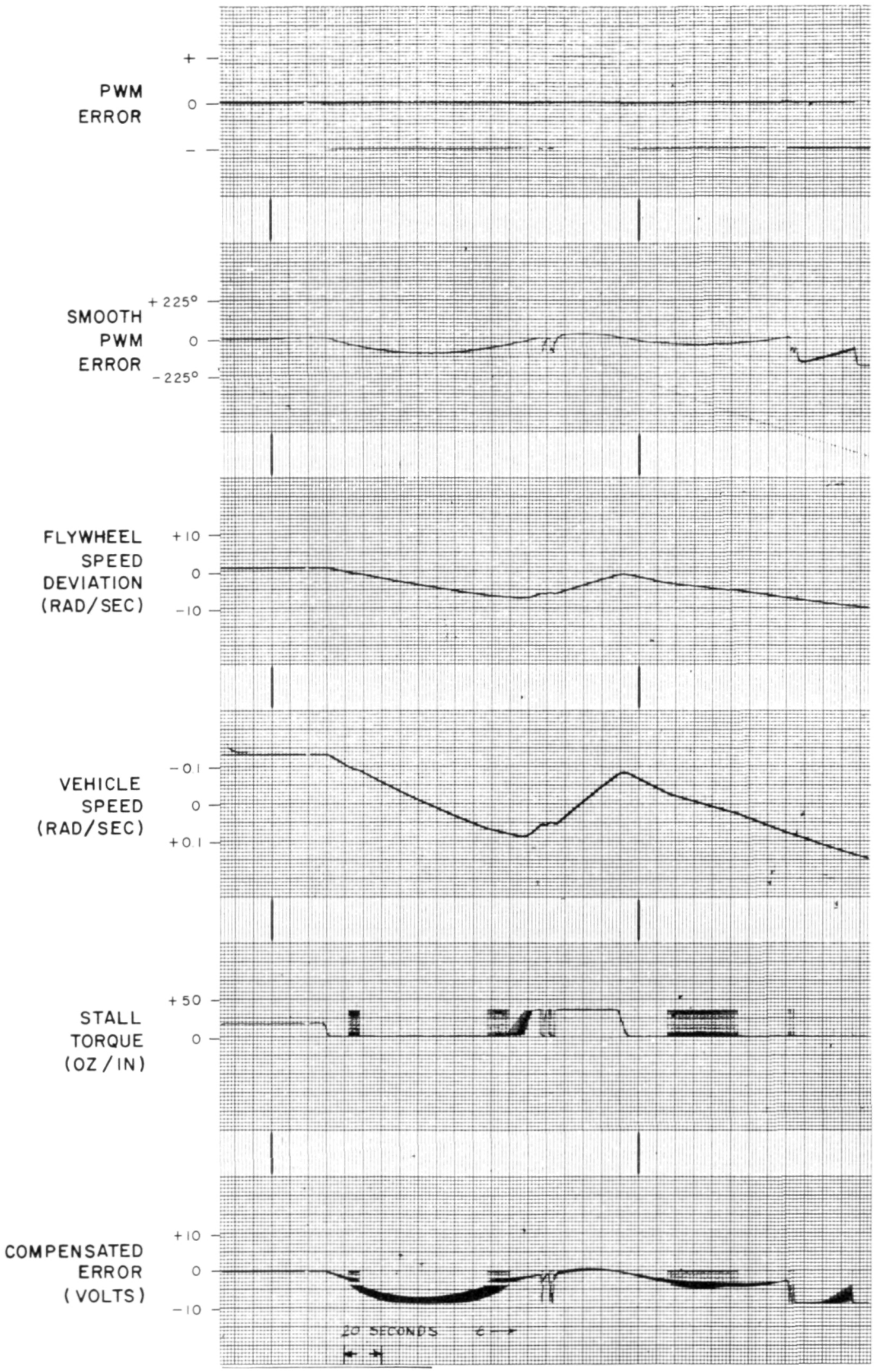

LEGEND:
LAG-LEAD COMPENSATION
COARSE AMP GAIN = 2.0
FINE GAIN REGION = ±90°
RESPONSE TO 30 % DECREASE IN MOMENTUM

Figure 3.1-8. Typical Results Obtained from the Analog Computer Study

Page intentionally left blank

Page intentionally left blank

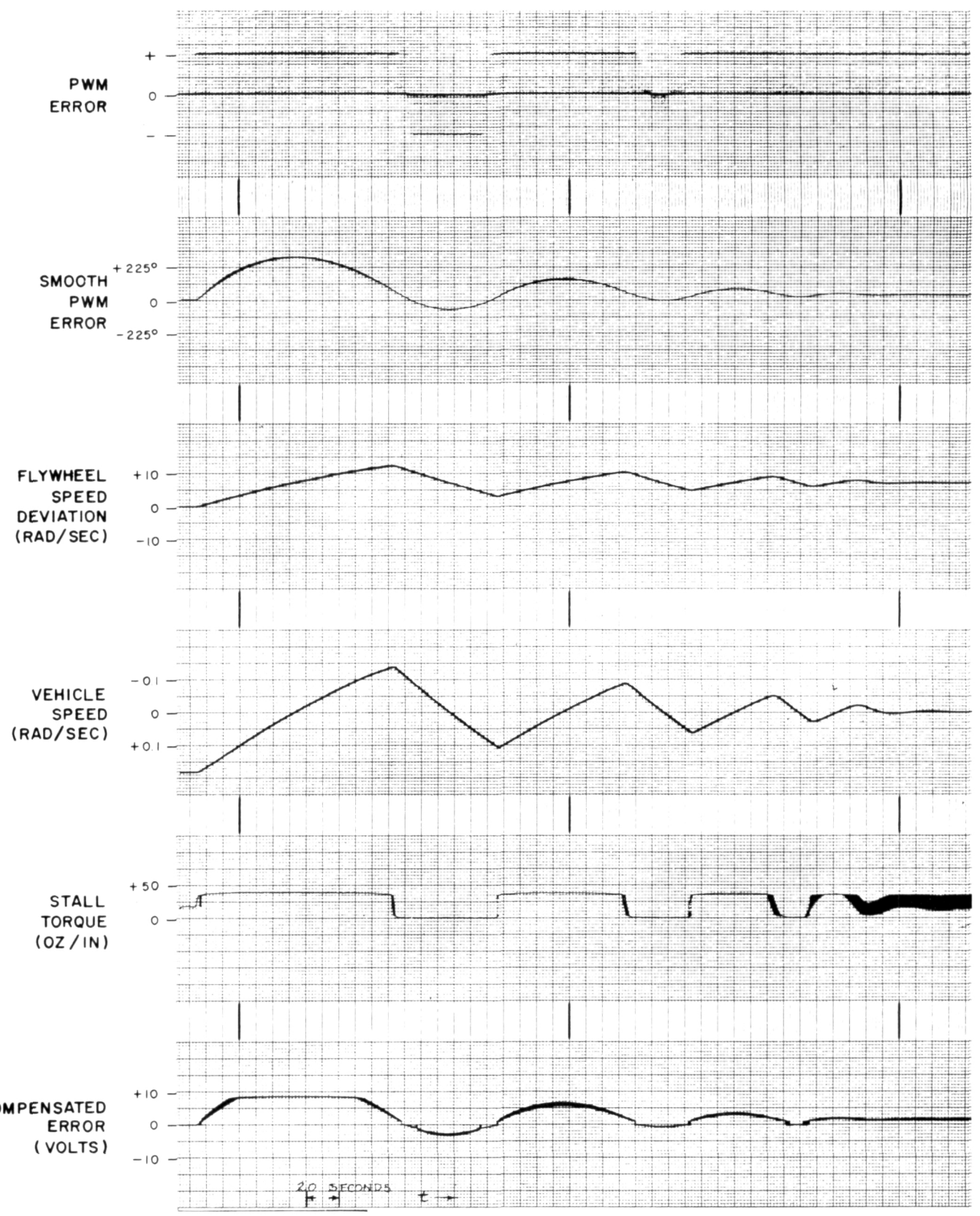

Figure 3. 1-9. Typical Results Obtained from the Analog Computer Study

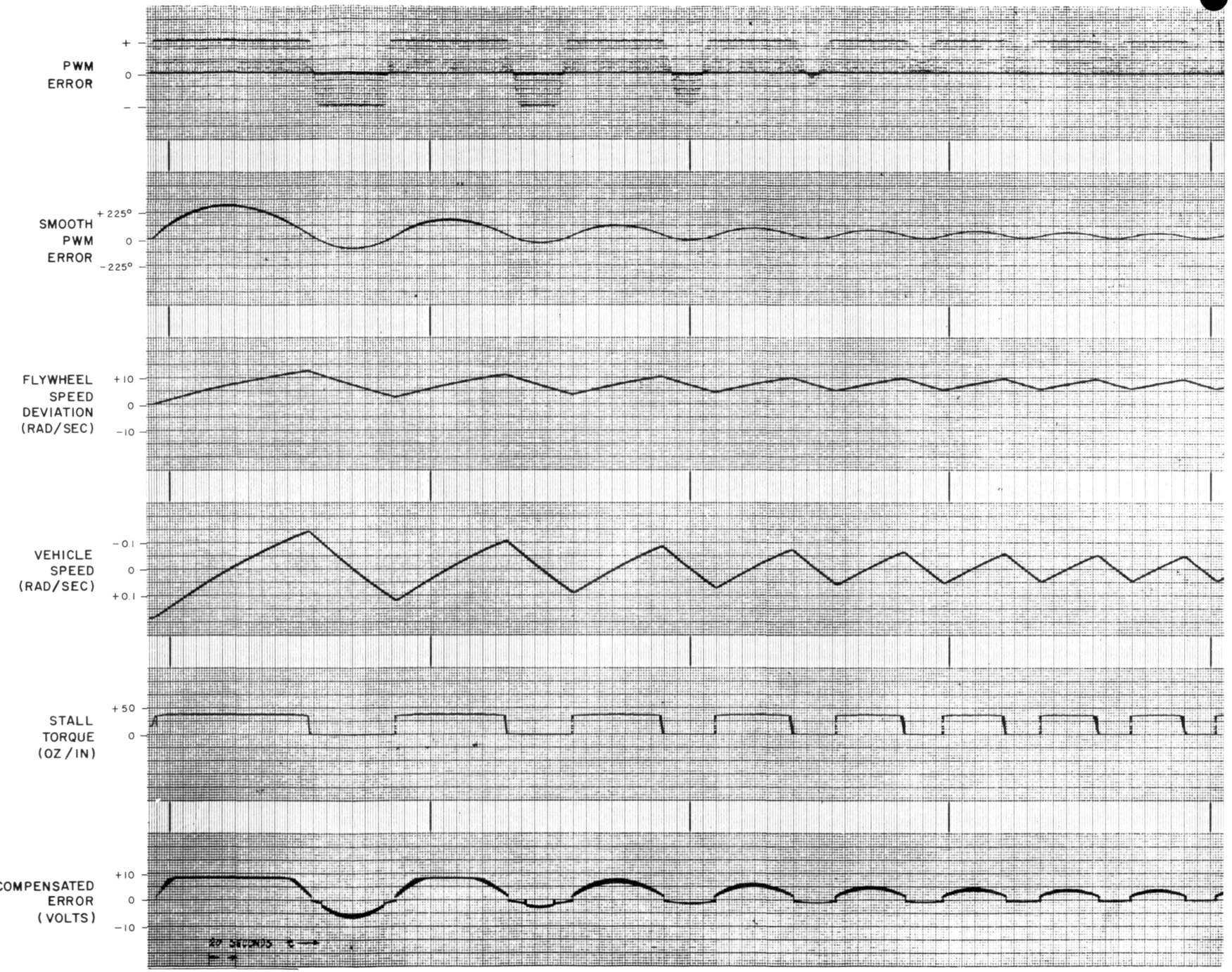

LEGEND:
LAG-LEAD COMPENSATION
COARSE AMP GAIN = 3.0
FINE GAIN REGION = ±25°
RESPONSE TO 44 % DECREASE IN MOMENTUM

Figure 3.1-10. Typical Results Obtained from the Analog Computer Study

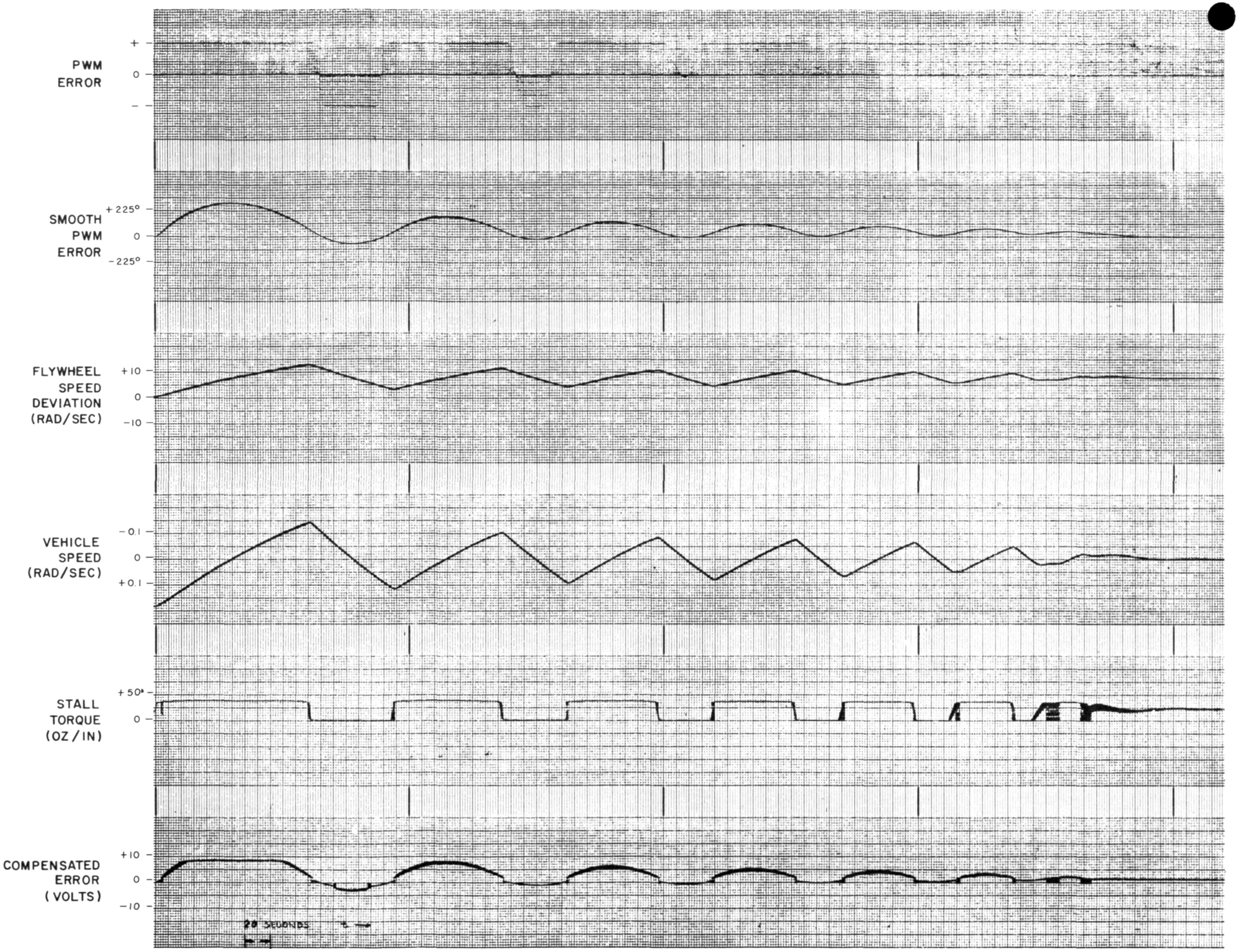

LEGEND:
LAG-LEAD COMPENSATION
COARSE AMP GAIN = 2.0
FINE GAIN REGION = ± 45°
RESPONSE TO 44 % DECREASE IN MOMENTUM

Figure 3.1-11. Typical Results Obtained from the Analog Computer Study

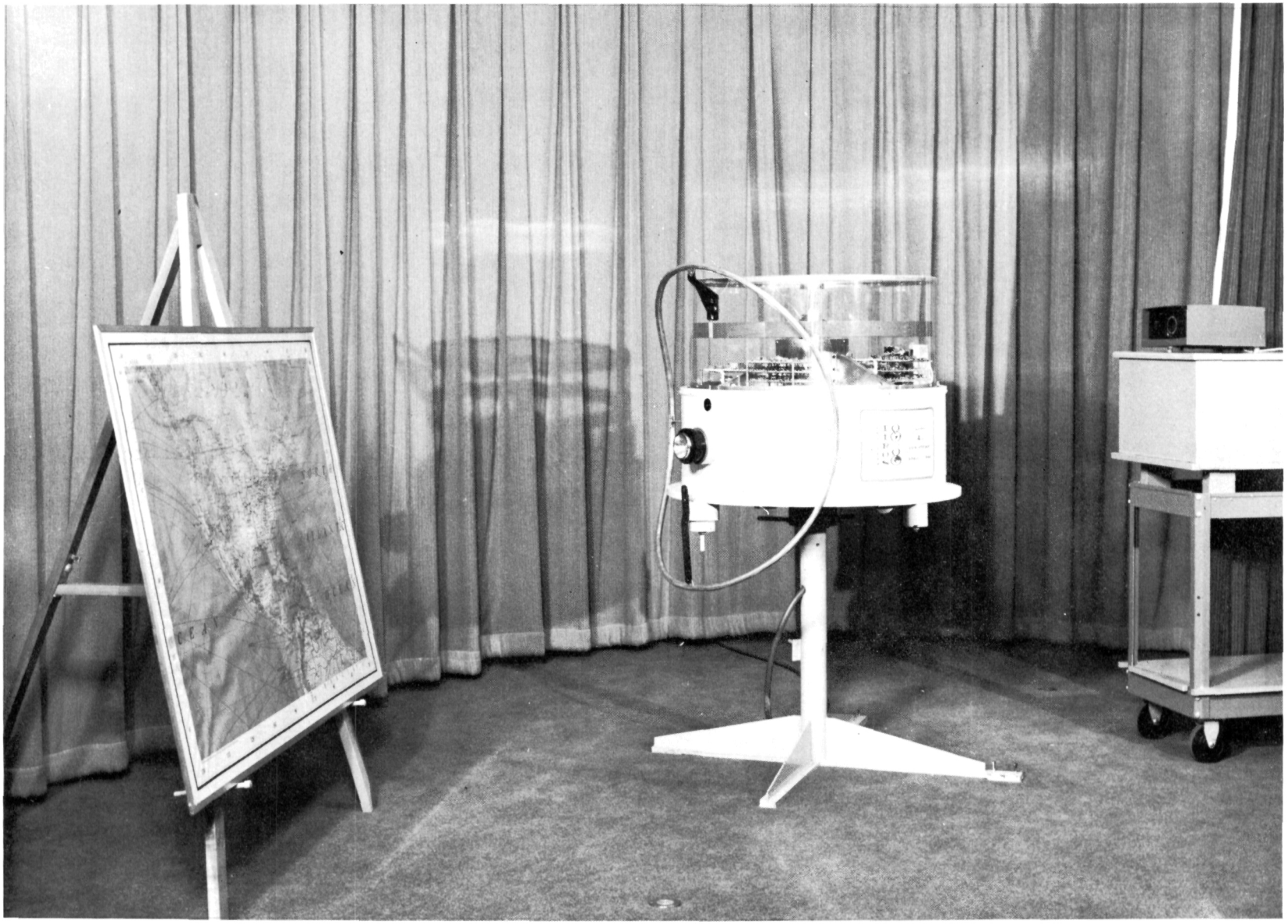

Figure 3.1-12. Photograph of Subsystem Simulator for Demonstrating Pitch-Axis-Stabilization Control

3.1.3.2 Pulse-Width-Modulator (PWM)

The PWM has been constructed from standard switching-circuit modules, which have been perfected for space applications, and has been tested on a simulator built by RCA.

The PWM error detector contains approximately one third the number of parts contained in a digital error detector containing a counter built at RCA. The pulse width modulator contains a minimum of digital logic; there is no need for special logic circuits to indicate sign and coincidence or gain switching as would be required in a digital error detector. Furthermore, a digital counter is more susceptible to noise pulses and requires a digital-to-analog converter in order to produce an analog control-signal. The output pulse deviation of the PWM is the error signal and an amplitude modulated control signal can be obtained from the PWM output by a simple RC filter (a PWM error detector followed by lag-lead compensation or proportional-plus-integral compensation would not require the RC filter). An important advantage of the PWM is that the resolution of the error detector is limited only by the difference in switching speed of two bistable multivibrators and by amplifier threshold, while a digital system employing a counter is limited to ± 1 binary bit. To improve the resolution of a detector employing a counter, additional stages must be added thus increasing the complexity. Other fundamental advantages of the PWM system over a digital system are: the PWM is lighter, smaller, consumes less power, and has greater reliability.

3.1.3.3 Compensation Amplifier

The compensation amplifier is a transistorized differential amplifier equivalent to the Philbrick Model PP65 in operating characteristics. By changing the feedback arrangement, the three compensation methods studied can be obtained. For the lag-lead compensation of Figure 3.1-13, the transfer function is

$$\frac{e_o}{e_i} = 15 \left(\frac{33.3\,S + 1}{500\,S + 1} \right)$$

where S is the Laplacian operator. To solve for the threshold value of this circuit, the noise model shown in Figure 3.1-14 must be analyzed. The noise output will be

$$e_{on} = e_{ni} \frac{R_f}{R_i} + e_{nv} \left(1 + \frac{R_f}{R_i} \right)$$

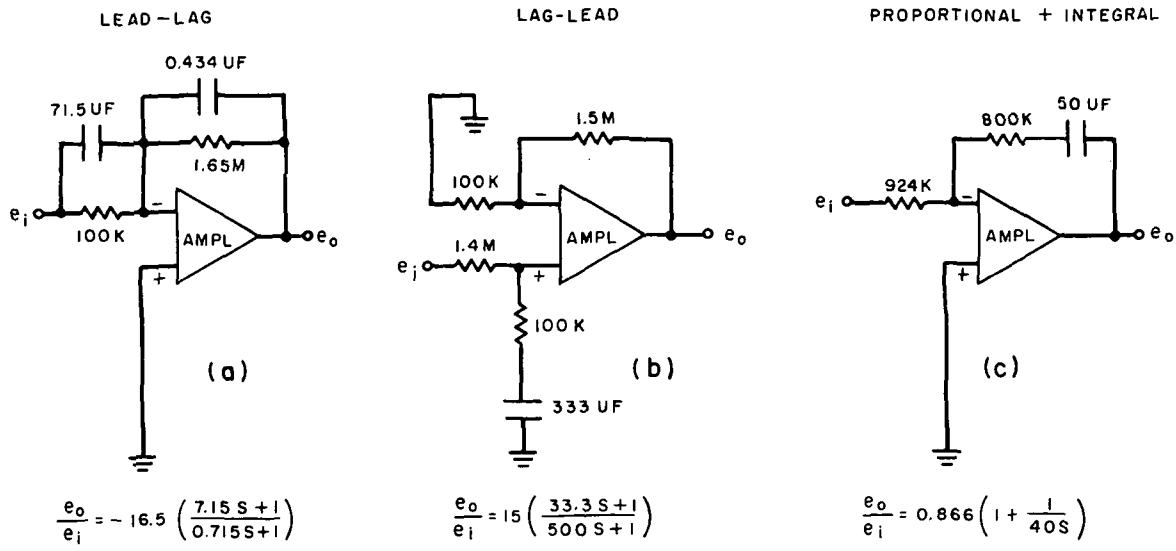

Figure 3.1-13. Schematic Diagrams and Transfer Functions of Various Compensation-Amplifier Techniques

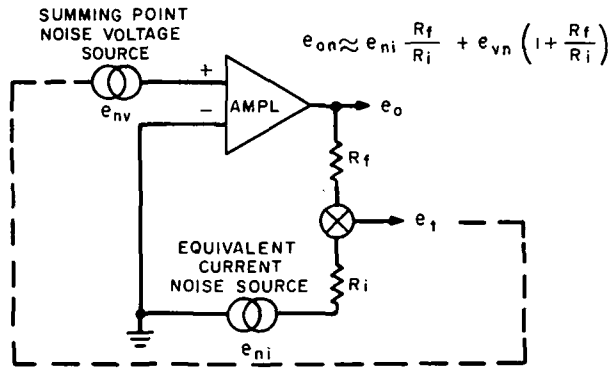

Figure 3.1-14. Noise Model for an Operational Amplifier

The input threshold signal at the input is then this value divided by the amplifier gain from which

$$e_t = e_{ni} + e_{nv}\left(1 + \frac{Ri}{Rf}\right)$$

where e_{ni} is due to leakage current noise and e_{nv} is due to noise voltage present at the summing point. The term e_{nv} is less than $50\ \mu v$ for the amplifier under consideration and $e_{ni} = i_d R_i$ where $i_d = 10^{-8}$ amp is the noise drift current of the amplifier. For the lag-lead circuit shown in Figure 3.1-13, the threshold voltage is then $10^{-8} \times 10^5 = 10^{-3}$ which is equivalent to an angle of $360/8\ V \times 10^{-3} = 0.045$ degree. This value could be decreased by reducing the input resistance but would result in larger-sized capacitors. The lag-lead compensation utilized a time constant of 500 seconds which seems long for transistorized circuitry; however, similar circuits have been used successfully by RCA on space programs. The leakage current of the capacitors is quite small because the only voltage impressed across is the error voltage in this circuit.

3.2.3.4 Summing Amplifier

The summing amplifier is also a transistorized differential amplifier equivalent to the Philbrick Model PP65 Differential amplifier in operating characteristics. The summing amplifier will add the compensated error-signal to the bias voltage and subtract from this sum the output of the frequency-to-d-c converter. The noise threshold voltage of this amplifier will be approximately the noise threshold voltage of the compensation amplifier. For lag-lead compensation (gain of 15), the noise threshold of the compensation amplifier predominates.

3.1.3.5 Power Amplifier

The power amplifier is of RCA design. The function of the power amplifier is to amplify the output of the summing amplifier to provide motor-drive power. A feedback loop from the output of the power amplifier to the input of the summing amplifier is provided to ensure stability and minimize voltage drift with temperature.

3.1.3.6 Frequency-To-d-c Converter

The frequency-to-d-c converter used in the pitch-axis control system will be equivalent to the Solid State Electronics Solid State Freqmeter Model 420. The device converts the frequency of an input pulse train into a proportional d-c voltage. Similar units have been used on other space programs at RCA.

3.1.3.7 Digital Shaft Encoder

The digital shaft encoder used is equivalent to the Incrosyn made by Data Tech. The unit provides two output signals: one output is an index pulse used as a mechanical reference between the flywheel and the vehicle and is fed into the PWM; the other output is a pulse train with a repetition rate proportional to the

relative rate between the flywheel and the vehicle and feeds into the frequency-to-d-c converter to provide rate feedback. Digital shaft encoders of a similar design have been used satisfactorily on previous space programs by RCA.

A tachometer or encoder is required to provide rate feedback for motor damping. The device used does not require a high degree of precision for this application. An a-c tachometer could be used, but rectifying circuitry would be required to produce a d-c signal in addition to an indexing circuit.

The digital shaft encoder appears best for this application. The digital shaft encoder does require a frequency-to-d-c converter to recover d-c rate voltages, but has an indexing circuit incorporated in the design.

3.1.3.8 Earth-Detecting Circuitry

There is a period in the orbit when the sun appears in the field of view of the pitch-axis horizon sensor and is most critical when the sun is at, or near, the horizon. To prevent this occurrence from introducing large disturbances into the system, a technique was devised to "enable" the pitch horizon-sensor input to the PWM with the Vee horizon sensors which do not view the sun. By physically offsetting the Vee horizon sensor from the pitch-axis horizon sensor in a lead direction the Vee horizon sensor can be used to "enable" the pitch-axis sensor near the earth's horizon. The block diagram of the circuitry is shown in Figure 3.1-15. The circuit would operate as follows: The first Vee-sensor channel to have an output will set the flip-flop enabling the "AND" gate. Upon receipt of an output from the pitch horizon sensor, the single-shot multivibrator is "set" producing an input to the pulse width modulator. The single-shot multivibrator, blanks extraneous noise pulses out of the pitch horizon sensor while the sensor views the earth. The flip-flop is reset at the end of the earth-blanking period by a single-shot multivibrator.

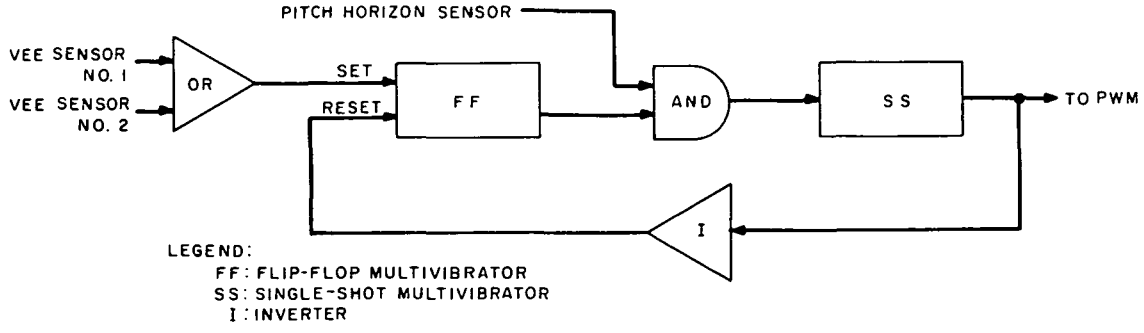

Figure 3.1-15. Earth-Detecting Circuit

3.1.3.9 D-C To D-C Converter

A d-c to d-c converter will be required for the pitch-axis-stabilization control subsystem. The converter consists of an oscillator, a toroidal transformer, and rectifying circuitry. It is used to improve the efficiency of power transfer to voltage levels other than -24.5V d-c, and to provide plus or minus voltage for the PWM error detector and the differential amplifiers. The d-c to d-c converter will also be needed to supply voltage to the magnetic torquing coils and to supply bias voltages of greater than -24.5V d-c to the bolometer if a CO_2 band horizon sensor is used.

3.1.3.10 D-C Motor

The d-c motor used to drive the flywheel must meet specifications established by the subsystem performance requirements (previously discussed in Section 3.1.2 of this report). These requirements are summarized in Table 3.1-1.

TABLE 3.1-1. SUMMARY OF D-C MOTOR PERFORMANCE REQUIREMENTS

Parameter	Performance Requirement
Stall-torque capability	40 oz. inches, peak
Torque gain	2 oz. inches/volt, nom.
Power capability	6 oz. inches at 300 rpm
Nominal operating point	6 oz. inches at 150 rpm
Motor back EMF	0.5 volt sec/rad, nom.
Power consumption	3 watts, avg.
Weight	16 oz. nom.
Life	10,000 hours at 150 rpm, nominal

Several types of motors are currently available which may satisfy these specifications. These types are as follows:

- D-C torque motor (Inland type)
- D-C torque motor (Printed type)
- 2-phase a-c (Servomotor and Reaction Wheel Drive)
- Synchronous motor

These four types were compared on the basis of stall-torque capability, power efficiency, and weight (4); a summary of the comparison is given in Table 3.1-2. (The data are based on various manufacturers' specifications for the different motors.) Gear-train ratios were ascertained by selecting the highest ratio (and, hence, the highest torque capability for the motor/gear-train combination) consistent with meeting the power output specification of 6 oz. inches at 300 rpm.

The Inland direct-drive d-c torque motor has good power efficiency, low weight, and acceptable stall-torque capability, especially because no gear train is required. The motor operates directly from a d-c supply, and the armature resistance can be adjusted within broad limits, thus eliminating the need for any power converters, and allowing control over the back EMF constant. Mechanization of the control system is further simplified with this motor because it is driven directly by an analog signal thus eliminating the need for modulators or oscillators.

A particular Inland unit, the T-2170 with a 42-ohm armature winding, meets all the important motor specifications as shown in Table 3.1-3. Operation from a 24.5-volt d-c supply has been assumed; this is standard in most spacecraft. Operation at lower voltages is possible, but tends to consume more power.

The speed-torque voltage relationship for this motor is given by

$$V_m = \sqrt{R}\left(\frac{M_m}{10.5} + 0.073\,\dot{\theta}\right)$$

or, with R = 42 ohms,

$$V_m = 0.62\,M_m + 0.48\,\dot{\theta}$$

The current flow is given by

$$I_m = \frac{V_m - 0.48\,\dot{\theta}}{R}$$

These three equations fully describe the steady-state behavior of the motor.

3.1.3.10.1 Operation of Motor Brushes in the Space Environment

Before the otherwise obvious selection of the Inland direct-drive torque motor, Type T-2170, can be made, special attention must be given to ensure proper and reliable operation of the armature brushes throughout the life of the mission. It is well known that, under normal ambient conditions, ordinary graphite brushes are ideally suited to their function. The operation of these

TABLE 3.1-2. SUMMARY OF DATA ACCUMULATED FOR COMPARISON OF FOUR TYPES OF D-C MOTORS

Motor Type	Power Efficiency	Torque Efficiency	Weight	Comments
Printed Type Torque Motor	High	High	Very High	High torque and power efficiency obtained by use of large field magnets; thus, motor is large and heavy compared to others. Has very low armature impedance (≈0.6 Ω). Would require d-c to d-c converter to operate from spacecraft power supply. Has low back EMF constant. Operates as an ordinary brush-type d-c torque motor. Direct drive motor requires no gear train.
Inland Type Torque Motor	High	Low to Average	Very Low	Torque and power efficiency obtained by use of rotor with large number of turns. Field magnet size is modest. Armature impedance easily adjusted by changing wire size in armature. Available in wide range of values (10 to 500 Ω), eliminating need for d-c to d-c converter. Back EMF constant reasonably high. Direct drive, no gear train necessary. Operates directly from analog control signal. Does not complicate control system. Brush-type motor requires special attention to ensure long life.
Conventional 2-phase a-c Servomotor	Low	Very Low without gear train High with gear train	Average	Gear train required to obtain usable speed torque characteristic. Motor normally operates at high speed (3600 rpm no-load speed is typical). 2-phase a-c supply requires power converters. Modulator required to provide AM signal to control phase. Low efficiency degraded further by power converter and gear train losses. Induction motor requires no brushes.
Bendix 2-Phase a-c Reaction Wheel Drive	—	Low	High	Direct drive induction motor. Requires no gear train, but has low torque efficiency and high weight. 2-phase a-c supply and control signal modulator required. Induction motor requires no brushes. Not available as a standard item.
Synchronous	Average	Very low without gear train Average with gear train	Low	Gear train required to obtain usable speed torque characteristic. Ratios in range of 20:1 to 40:1. Motor normally operates at very high speed (6000-12000 rpm speed is typical). Life limited. Motor must be driven by controllable power oscillator (VCO). Efficiency reduced by losses in gear train and power converter. Induction motors require no brushes.

TABLE 3.1-3. SUMMARY COMPARISON OF INLAND MOTOR TYPE T-2170 WITH PERFORMANCE REQUIREMENTS

Parameter	Type T-2170 Motor Characteristic	Specification Characteristic
Stall-torque capability (24.0 volts)	40 oz. inch	40 oz. inch
Torque gain	1.63 oz. inch/volt	2.0 oz. inch/volt
Power capability	15 oz. inch at 300 rpm	6 oz. inch at 300 rpm
Motor back EMF	0.48 volt sec/rad	—
Power consumption:		
(nominal operating point)	2.15 watts from 24.5V d-c supply	3 watts
Weight	14 oz. (+ mounting structure)	16-24 oz.

brushes is characterized by low resistance, low friction, and extremely low wear because of the water vapor in the air. Provided operation was under ordinary atmospheric conditions, it would be a simple matter of design to provide a brush-type motor capable of one or more years continuous operation at 150-rpm motor speed and a nominal 0.1 amp current flow. However, experience with high-altitude aircraft equipment has demonstrated that graphite brushes do not perform well under all conditions. High friction and severe wear catastrophically tend to occur at high altitude ambients unless the brushes are treated with special additives (often called filming agents) which permit normal performance under these abnormal conditions. There is some evidence to indicate that filming additives are effective in vacua as low as 10^{-5} to 10^{-6} mm Hg, but operation below this range is questionable. In addition, such brushes often develop high surface resistance after periods of disuse. In general, this tendency is not critical because the non-conducting surface film is quickly broken down after a few revolutions; however, for motors this condition is unacceptable because it can prevent the motor from ever starting.

A system similar to that reported by Weinreb[20] can be used to establish and maintain a vapor atmosphere adequate for lubrication of brushes, slip rings, and ball bearings. No attempt is made to hermetically seal these components and thus prevent loss of lubricant (this technique is not practical); rather, the lubricant is allowed to evaporate into space at a very low rate. The rate of evaporation is determined by the properties of the lubricant and the size of the "leak" opening (essentially the

clearance around the flywheel shaft) as shown schematically in Figure 3.1-16. If necessary, the effective clearance can be made extremely small by using a labyrinth leak path. Under equilibrium conditions, lubricant vapor is continually escaping through the leak to the vacuum of space, and is constantly being replenished as more evaporates from the reservoirs. Thus, a vapor atmosphere is maintained until the reservoirs are exhausted. Table 3.1-4 contains a list of vapors which are substitutes for the water vapor and which will provide low wear and low friction between the brushes and commutators. Procedures have been established to use in predicting the loss-rate of vapor in the pressure range shown in Table 3.1-4. The design of seals which will ensure the required oil-vapor pressure for the specified time is incorporated into the present mechanical configuration of the subsystem. The procedure was previously discussed[4] ; a summary of the procedure is shown in Figure 3.1-17.

To determine oil-loss rates, some tests have been run in an experimental setup similar to that drawn in Figure 3.1-16. The data from two tests are summarized in Table 3.1-5. The results of Test No. 1 are almost twice the predicted value; the loss-rate in Test No. 2 is very close to that predicted. The discrepancy in Test No. 1 may be attributable to an error in measuring weight loss because the absolute amount was extremely small. The two tests demonstrate that relatively high ambient pressures can be maintained for long durations at the sacrifice of very-low lubricant loss-rates. The ambient pressures obtained are adequate for brush-lubricating purposes and other evidence indicates that slip rings and ball bearings will also operate reliably in such atmospheres.

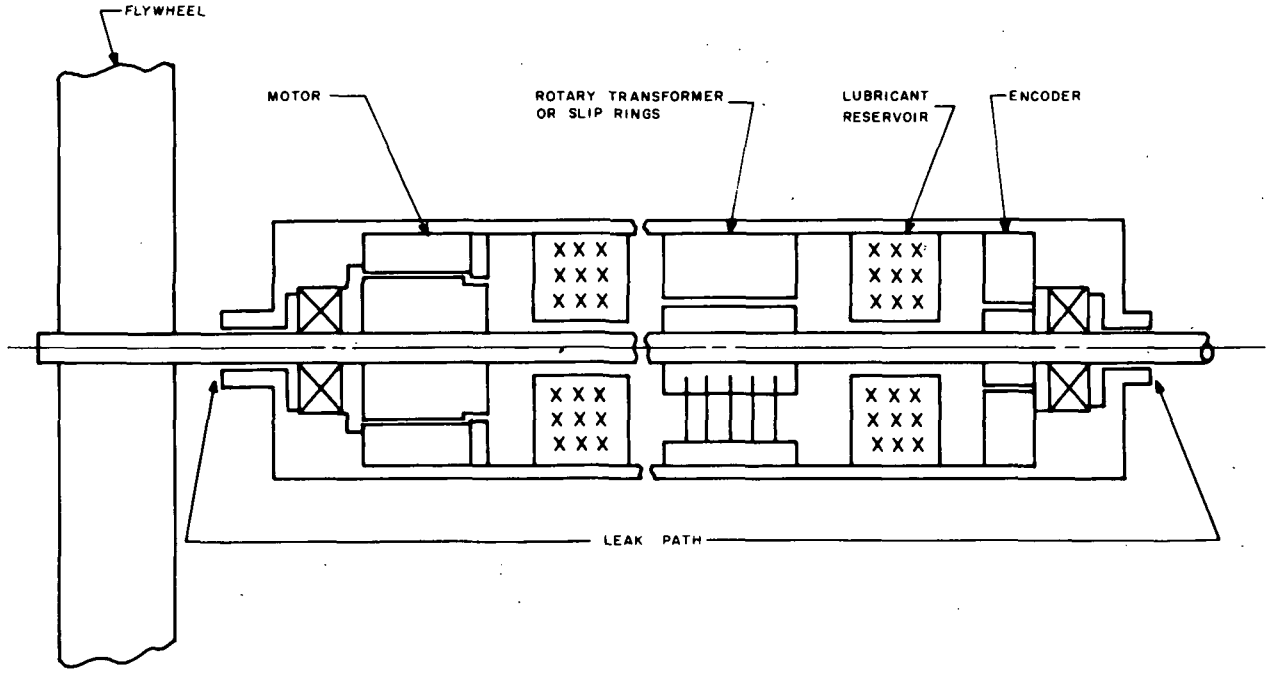

Figure 3.1-16. Schematic Representation of Experimental Vapor-Lubrication System

TABLE 3.1-4. SUMMARY OF WATER-VAPOR SUBSTITUTES AND CHARACTERISTICS

Type Lubricant	Minimum Lubricating Pressure (mm Hg)	Vapor Pressure at 30°C (mm Hg)	Relative Humidity* Required for Lubrication ($\times 10^5$)
1-Propanol	0.0044	28.0	15.7
Ethylene glycol	<0.0018	0.15	low
n-Pentane	0.018	680	2.6
1-bromo-pentane	0.00027	13.0	2.1
n-heptane	0.0008	56.0	1.4
Diethylene glycol	<0.001	0.013	low
Triethylene glycol	<0.001	0.002	very low
Tetraethylene glycol	very low	very low	very low

*The relative humidity is defined as:

$$\frac{\text{Minimum Lubricating Pressure}}{\text{Vapor Pressure}}$$

and decreases as the molecular size increases.

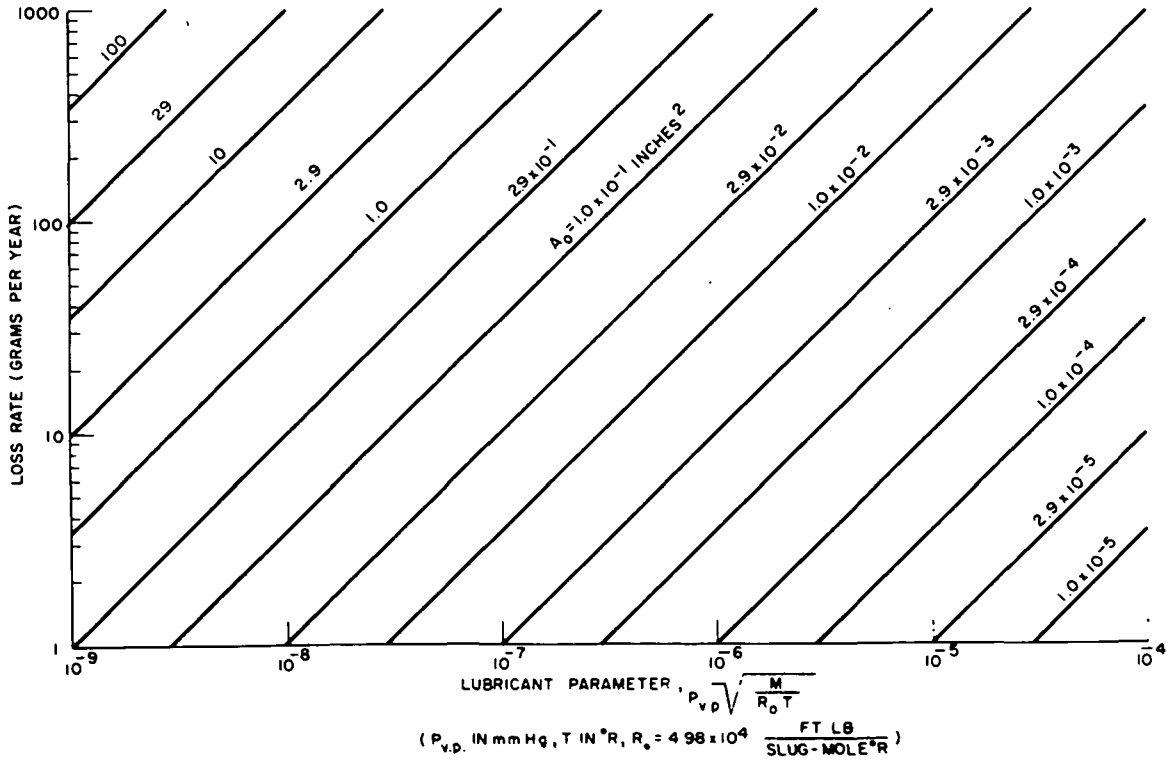

Figure 3.1-17. Summary of Procedure Data Used to Determine Prediction of Lubricant Loss-Rate

TABLE 3.1-5. SUMMARY OF TEST DATA OBTAINED ON OIL-LOSS RATES BY EXPERIMENTATION

Test No.	Effective Leak Area ($\times 10^{-4}$ sq. in.)	Vapor Pressure (mm)	Temperature (^{o}F)	Molecular Weight	Loss Rate		
					Measured	Extrapolated (grams per year)	Predicted (grams per year)
1 DI(2-ETHYL HEXYL) SEBACATE LUBRICANT	4.75	5×10^{-5}	75	426	0.0576 grams in 18 days	1.17	0.60
2 DI-OCTYL ADIPATE LUBRICANT	4.75	$\approx 5 \times 10^{-4}$	75	314	0.387 grams in 27 days	5.23	5.15

3.1.3.10.2 Selection of Brush-Commutator Materials

Once the particular subsystem for maintaining the desired brush atmosphere has been developed, the brush-commutator materials still must be selected. Table 3.1-6 lists the most commonly used types. The copper commutator and plain carbon (or graphite) brush is the most widely used combination. Coin-gold or gold-plated commutators are used where corrosion is a problem; rhodium is used as a replacement for gold when a harder surface is desired; and silver-graphite and copper-graphite brush materials are used where high current-densities are present and where low contact voltage drop is desired.

TABLE 3.1-6. LIST OF COMMONLY USED BRUSH/COMMUTATOR MATERIALS

Commutator	Brush
Copper	Carbon, Graphite, Electrographite
Gold	Silver-Graphite Copper-Graphite Altitude treated Silver-Molybdenum Disulfide

High-altitude treated brushes are designed to be used in aircraft where the proper atmosphere cannot be maintained. Essentially, small amounts of compounds such as barium-carbonate, lithium-fluoride, barium-fluoride, or other metallic halides are added to plain carbon or silver-graphite brushes. These materials form the low-shear stress film at the brush-commutator interface which is necessary for low friction and wear. However, under some conditions the interface film is formed too readily and results in high, or even insulating, contact resistance, while under other conditions the film may not be formed quickly enough thus causing excessive wear.

The use of altitude-treated brushes is obviated by creating a controlled atmosphere adequate to lubricate plain carbon or graphite, and, in general, this is a desirable feature. Therefore, the most feasible materials for use in this application are: either copper or gold for the commutator; and either graphite or silver-graphite for the brushes.[4]

These materials should work satisfactorily if the proper atmosphere is created and maintained.

3.1.3.10.3 Predicted Lifetime of Brushes

The brush-type motor selected must be capable of 10,000 hours operation at a motor speed of 150 rpm and a nominal average current of 0.1 amps. For the Inland torque motor proposed, these requirements imply a sliding speed of 1.25 ft/sec., a total distance travelled of 4.5×10^7 ft., and a total number of

revolutions of 9×10^7. These specifications are within present day standard practice; the manufacturer rates the motor as being capable of more than 1×10^8 revolutions under ordinary ambient conditions and loads. If necessary, this predicted life can be extended by using oversized brushes. Also, the brush current required will be less than 15% of the continuous duty rating and should contribute to increased life.

Theoretical predictions of brush life are not available; however, a certain amount of empirical information has been obtained. The manufacturer (Inland Motor Corporation) gives the following relationship as an approximation

$$t = 0.05 + \frac{I_b V_b^2}{A_b^2} \times K \qquad (3.1\text{-}4)$$

The constant K depends on the specific test conditions because values between 2×10^6 and 30×10^6 have been reported. For the application under consideration, the influence of current flow and back EMF (the second term on the right hand side of the equation) is not overriding. Using the following conservative values,

I_b = 0.1 amp per brush

V_b = 15/33 = 0.46 volts/segment

A_b = 125 x 125 = 1.56×10^4 mil

K = 30×10^6 mil^3/volt x 10^6 ft.

the wear rate becomes

t = 0.05 + 0.004 mils/10^6 ft. travel

Thus, the electrical component of wear is small; furthermore, it could be made even smaller by reducing the rotor resistance R and, hence, the value of V_b. Therefore, the value of the mechanical wear constant (0.05 mils/10^6 ft.) in equation (3.1-4) is of principal concern, and a check on its validity would be desirable.

Operation for 10,000 hours at 150 rpm is equivalent to 45.0×10^6 ft. surface travel. At a rate of 0.05 mils/10^6 ft., this operation will remove 0.0023 inches of brush material, or less than 10% of the available thickness in standard motors.

Research on the behavior of brushes operating in extremely low pressure-vapor atmospheres has been conducted at the RCA Astro-Electronics Division. Some of the results pertinent to wear rate are summarized in Table 3.1-7. These data indicate that the motor which had no controlled atmosphere exhibited considerably higher wear than the other units. Even during the controlled-atmosphere runs, however, wear rates two to three times greater than 0.05 mils/10 ft. were observed. This discrepancy may have resulted from the fact that the test durations

TABLE 3.1-7. SUMMARY OF DATA PERTINENT TO WEAR-RATE OF BRUSHES AND OBTAINED AT RCA

Description	Duration (Lays)	Speed (rpm)	Average Wear (Mils)	Wear Rate (Mils/10^6 Ft.)
Labyrinth motor seal motor pressure $\approx 10\,\mu$ avg. Brushes: 50% Ag. 50% Graphite + High Altitude treatment	10	150	0.18	0.16
Labyrinth motor seal motor pressure $\approx 50\,\mu$avg. Brushes: 50% Ag. 50% Graphite + High Altitude treatment	15	150	0.15	0.095
Seal Conductance Increased motor pressure $\approx 0.5\,\mu$avg. Brushes: 50% Ag. 50% Graphite + High Altitude treatment	18	150	0.26	0.13
Seal Conductance Increased motor pressure $\approx 1.0\,\mu$avg. Brushes: Stackpole 566	26	150	0.39	0.16
No seal - motor completely exposed. Motor pressure $\approx 5 \times 10^{-6}$ mm avg. Brushes: 50% Ag. 50% Graphite + High Altitude treatment	7	130	0.49	0.74

Notes:
1. In all cases, the test unit was placed in a bell jar with an average pressure of 5×10^{-6} mm.
2. Except where noted, the test unit was inside a container that had a specified leak-rate to the outside vacuum. An oil reservoir was also placed inside the container so that the pressure could not fall below the vapor pressure of oil (from 5×10^{-5} to 5×10^{-4} mm.). The container with increased leak-rate (or conductance) was obtained by placing four holes, 0.055" dia. in an otherwise closed cannister.
3. Average motor pressures were considerably higher than oil vapor pressure due to outgassing of other materials inside the container.
4. Wear rates are based on average wear of four brushes in each motor.

were so short that brushes had not become fully run in. (In most cases the brushes had not worn enough to fully conform to the commutator's curvature.) Furthermore, it is well known that until an established film is on the commutator, brush wear is apt to be higher than normal. Nevertheless, the measured data are encouraging because the extrapolated wear over 10,000 hours amounts to only 7.2 mils in the worst case, whereas the brushes have a minimum working thickness of 25 mils (which can readily be doubled or tripled, if desired).

3.1.4 Summary of Significant Parameters and Performance

3.1.4.1 Compensation

The recommended pitch-axis-stabilization control subsystem control utilizes lag-lead compensation and has the following open loop transfer function:

$$G(S) = \frac{2(33.3\,S + 1)e^{-0.2S}}{S(500\,S + 1)(8.0\,S + 1)}$$

The following are the constants used in the design of this subsystem.

- Velocity Constant (K_v) = 2.0
- Natural Frequency = 0.11 radians/second
- Flywheel Inertia (I_f) = 144 oz in sec^2
- Vehicle Inertia (I_1) = 5410 oz in sec^2
- Nominal Momentum (H) = 2260 oz in sec^2
- Horizon Pulse = 1 volt minimum at 3 msec rise time
- Index Pulse = -6 volt at 1 usec rise time
- PWM Output = ±8 volts
- Compensation amplifier gain = 13.1
- Compensating network time time constants; τ_1 = 33.3 seconds; τ_2 = 500 seconds
- Coarse-gain = 2.0
- Fine-gain Region = ±45°
- Differential plus power amplifier voltage gain = 36
- Frequency-to-d-c converter gain = 0.2 volts/radian/second

- Frequency-to-d-c converter filter frequency = 60 radian/second
- Motor equivalent to Inland Motor Corporation Type T-2170

3.1.4.2 Power

3.1.4.2.1 Consumption

The expected power consumptions for the subsystem are given in Table 3.1-8.

The total power given is for steady-state operation at 150 rpm. The peak power required by the motor-amplifier set during the recovery mode is 12.7 watts. The peak pitch-axis-stabilization control subsystem power is, therefore, 14.16 watts (required only during the recovery mode). This is a conservative estimate based on 6 ounce inches of friction torque.

TABLE 3.1-8. SUMMARY OF ANTICIPATED POWER CONSUMPTIONS FOR PITCH-AXIS-STABILIZATION CONTROL SUBSYSTEMS

Unit	Power Consumption (watts)
Pulse Width Modulator	0.2
Compensation Amplifier	0.075
Summing Amplifier	0.075
Power Amplifier and Motor (Avg.)	3.3
Frequency-to-d-c Converter	0.06
Digital Shaft Encoder	0.2
Pitch Horizon Scanner	0.1
V Horizon Scanner	0.2
Earth-Detecting Circuit	0.05
d-c-to-d-c Converter (losses)	0.5
Total Power Consumption	4.76

3.1.4.2.2 Ripple

The frequency-to-d-c converter ripple voltage is 2% of the input level. The motor has an L/R ratio of 0.001 and a resistance of 42Ω . The frequency of the ripple voltage caused by the frequency-to-d-c converter is approximately 4,000 radians/second at nominal speed. The ripple power due to the frequency-to-d-c converter alone is:

$$P_r = \frac{(6 \times 0.02 \times 30)^2}{42\left[1 + (4000 \times 10^{-3})^2\right]} = 0.0181 \text{ watts}$$

In addition, there will be ripple power due to the PWM output pulse. The steady-state error at 150-rpm flywheel speed is a pulse of 0.0011 seconds duration. The worst case for ripple power due to the PWM would occur if the pulse saturated the power amplifier; in this case, the ripple power due to the PWM error signal would be

$$P_r = \frac{1}{42\Omega \times 0.4\ sec} \int_0^{0.0011} (17V)^2 dt = 0.019\ watts$$

The sum of the two ripple powers should be added to the average values stated; thus, the total steady-state subsystem power is approximately 4.8 watts.

3.2 MAGNETIC CONTROL SUBSYSTEMS

3.2.1 General

The magnetic-control subsystems are utilized to:

- constrain the spacecraft pitch-axis along the orbit normal;
- control the total vehicle momentum about the pitch axis (nominally, the flywheel rate).

Two principles are involved, the generation of the torque, and the effect produced by the torque on the spacecraft attitude. A heuristic explanation of the recommended techniques of magnetic control is presented in the following paragraphs and in Figure 3.2-1.

When current flows through a coil, a magnetic field is set up about the coil such that the coil exhibits a magnetic axis through its center (see Figure 3.2-1(a)). The coil is said to have a dipole moment along this axis. When the coil is energized, its dipole moment reacts with the magnetic field of the earth to produce an instantaneous torque; this torque tends to move the dipole moment into coincidence with the earth's field lines as illustrated in Figure 3.2-1(b). The movement toward coincidence implies that the torque vector is normal to the plane determined by the vectors representing the dipole moment of the coil and the magnetic field of the earth in the vicinity of the coil. Depending upon the orientation of the coil, the direction of the torque may be made to lie along, or at right angles to, the flywheel axis of the spacecraft. For flywheel spin-rate control and, consequently, pitch-axis momentum control, a torque co-linear with the spacecraft momentum axis is required. To obtain this, the plane of the momentum-control coil is placed parallel to the flywheel axis. Conversely, to effect a change in direction of the momentum axis (pitch-axis), a torque which is normal to the flywheel spin-vector is required. Therefore, the coil used to change the orientation of the spacecraft is installed with its magnetic-axis parallel to the momentum vector. However, the spacecraft includes a spinning body and will, therefore, undergo gyroscopic motion when subjected to torque which is transverse to the flywheel direction of spin as illustrated in Figure 3.2-1(c). The basic law of the gyroscope indicates that, when a gyroscope is torqued at right angles, its spin vector will move to coincidence with the torque vector. The resulting motion, which gives rise to a change of direction of the spinning axis, is referred to as precession. Consequently, the total effect of the two orthogonal coils is to produce an instantaneous torque that both precesses the momentum axis of the vehicle and changes the momentum magnitude. This effect is shown in Figure 3.2-1(d).

A complicated change in both magnitude and direction of the earth's magnetic field with respect to the coil axes takes place as the spacecraft rotates in orbit. Therefore, utilization of magnetic torquing on an instantaneous basis requires either a means of sensing the magnetic field in three axes, or an exceedingly complicated

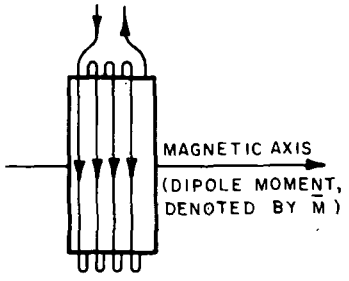

(a) DIPOLE MOMENT OF CURRENT-CARRYING COIL. (DIRECTION OF CURRENT AND MAGNETIC DIPOLE POLE MOMENT ARE RELATED BY FINGERS AND THUMB OF RIGHT HAND)

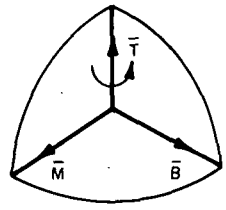

(b) TORQUE $\bar{T}$ DEVELOPED BY INTERACTION OF COIL'S DIPOLE MOMENT $\bar{M}$ AND EARTH'S MAGNETIC FIELD $\bar{B}$. (DIRECTIONALLY, $\bar{M}$, $\bar{B}$ AND $\bar{T}$ ARE RELATED BY RIGHT HAND RULE, MATHEMATICALLY THEIR RELATIONSHIP IS EXPRESSED $\bar{T} = \bar{M} \times \bar{B}$)

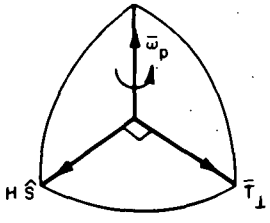

(c) PRECESSION MOTION $\bar{\omega}_p$ OF FLYWHEEL AXIS $\hat{S}$ CAUSED BY TORQUE $\bar{T}_\perp$. (RIGHT HAND RULE) $\bar{T} = \bar{\omega}_p \times \bar{H}$

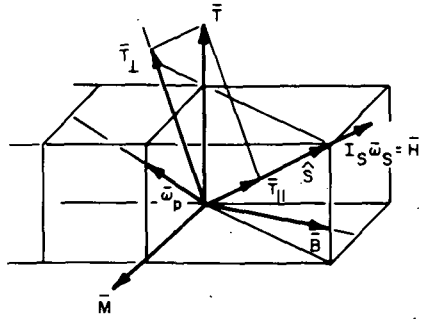

$\bar{T} = \bar{M} \times \bar{B}$
$\bar{T} = \bar{\omega}_p \times \bar{H}$
$\bar{T}_{||}$ CAUSES SPIN RATE CHANGE
$\bar{T}_\perp$ CAUSES PRECESSION

(d) GENERAL KINEMATICS OF MAGNETIC ATTITUDE CONTROL

Figure 3.2-1. Principles of Magnetic Attitude Control

programming technique requiring on-board ephemeris data and stored magnetic-field equations. In addition, on-board computation of the momentum-axis attitude errors is also required. However, because of the stored momentum in the spacecraft, instantaneous torquing is not required because attitude errors can build up only over long periods of time. Consequently, average torques are generated in the spacecraft through ground-commanded programmed modulation of the currents carried in the coils whenever attitude or momentum corrections are required.

For controlled precessional motion to move the momentum-axis normal to the orbital plane, the current in the coil with its magnetic axis along the momentum axis is programmed by a technique called Quarter Orbit Magnetic Attitude Control (QOMAC). The programming technique is characterized by two parameters; the orbit-angle of the spacecraft (at which torquing is initiated), and the cyclic variation of coil current (from plus to minus) every one-quarter orbit. The mathematical description of this technique is given in Section 3.2-2 of this report. In addition to QOMAC, continuous torquing of the spacecraft is provided using a magnetic-bias coil with its axis parallel to the QOMAC coil. This continuous torquing offsets the residual magnetism of the spacecraft and corrects for orbital regression. The details of this process are given in Section 3.2-3 of this report. The QOMAC technique will be utilized in the TIROS WHEEL which has been developed for NASA by RCA, AED. In this application, the principles are identical. The differences lie only in the configuration of the coils and the magnitude of the current used in producing the magnetic moment.

For momentum control, the current in the coil parallel to the flywheel axis is programmed in a manner similar to QOMAC; however, the cyclic variation of coil current (from plus to minus) occurs every one-half orbit. Details of this technique are given in Section 3.2-4 of this report.

3.2.2 Quarter Orbit Magnetic Attitude Control (QOMAC)

3.2.2.1 Dynamics

As has been indicated, the current-carrying coil which controls the spacecraft attitude is installed with its magnetic axis aligned with the momentum-axis of the spacecraft. Also, by convention, the positive dipole moment of the coil, $\bar{M}_Q$, is taken in the positive direction of the angular momentum vector. Therefore,

$$\bar{M}_Q = M_Q \hat{I} \tag{3.2-1}$$

The direction and magnitude of the control torque $\bar{T}_Q$, developed by the interaction of the dipole-moment of the torque coil and the earth's magnetic field, $\bar{B}$, is given by the vector equation

$$\bar{T}_Q = \bar{M}_Q \times \bar{B} \tag{3.2-2}$$

Utilizing equation (2.3-8) of Section 2.3.3,

$$\bar{T}_Q = \frac{d|\bar{H}|}{dt}\hat{1} + |\bar{H}|\frac{d\hat{1}}{dt} + |H|(\bar{\omega} \times \hat{1}) \tag{3.2-3}$$

It has been assumed that $\bar{M}$ is parallel to vector $\hat{1}$; therefore, the torque produced (which is normal to $\bar{M}$) must also be normal to vector $\hat{1}$. Such a torque cannot change the flywheel spin-rate; hence

$$\frac{d|H|}{dt} = 0 \tag{3.2-4}$$

The change in the vector $\hat{1}$ (expressed by $d\hat{1}/dt$) is, therefore, a change of direction only and implies a rotation about an axis which is normal to $\hat{1}$. This is the processional motion having rate ω_p. Then,

$$\frac{d\hat{1}}{dt} = \bar{\omega}_p \times \hat{1} \tag{3.2-5}$$

and hence,

$$\bar{M}_Q \times \bar{B} = [(\bar{\omega}_p \times \hat{1}) + (\bar{\omega} \times \hat{1})]\,|\bar{H}| \tag{3.2-6}$$

If motion is considered in an $\hat{\ell}, \hat{b}, \hat{n}$, coordinate system, however, then $\bar{\omega}$ is the orbital regression-rate and will be much smaller than $\bar{\omega}_p$. Consequently,

$$\bar{M}_Q \times \bar{B} \approx \bar{H}(\bar{\omega}_p \times \hat{1}) \tag{3.2-7}$$

In Section 2.2 of this report a complete model for the vector $\bar{B}$ is developed. Initially, $\bar{B}$ is written as

$$\bar{B} = \frac{M_E}{(1+\epsilon)^3 (r_E + h_1)^3}\,\bar{b}_f \tag{3.2-8}$$

Utilizing this result, equation (3.2-7) may be written as

$$\bar{\omega}_p \times \hat{1} = -\mu_Q (\bar{b}_f \times \hat{1}) \tag{3.2-9}$$

in which

$$\mu_Q = \frac{M_E M_Q}{(1 + \epsilon)^3 (r_E + h_1)^3 \, |\bar{H}|}$$

Using reasoning from an analysis of general gyroscopic motion, it can be shown that, for light-torque loading, the precession motion which satisfies equation (3.2-9) is given by

$$\bar{\omega}_p = - \mu_Q \bar{b}_f \qquad (3.2\text{-}10)$$

This result implies that, for a positive dipole-moment of the coil, the precessional motion of the flywheel at any instant will be negatively directed about the direction of the earth's magnetic field.

3.2.2.2 Torque Generation

It is now necessary to show that phasing and cycling the coil current will produce an effective average direction of the earth's magnetic field and that it is easily related to the attitude correction desired for the momentum axis. The $\hat{\ell}$, $\hat{b}$, $\hat{n}$ coordinate system will be used in the analysis.

Section 2.2 contains the derivation of the required magnetic-field equations. For initial study, the following assumptions are made

$$a) \quad \epsilon = 0$$

$$b) \quad i_m = 0$$

Based on these assumptions, equations (2.2-18) of Section 2.2 become

$$B_\ell = - \frac{M_E}{R^3} (3/2 \sin 2\theta \sin i) \qquad (3.2\text{-}11a)$$

$$B_b = + \frac{M_E}{R^3} (3/2 \cos 2\theta \sin i - 1/2 \sin i) \qquad (3.2\text{-}11b)$$

$$B_n = + \frac{M_E}{R^3} (\cos i) \qquad (3.2\text{-}11c)$$

By programming the coil current with the proper phase and with one-quarter-orbit reversal of direction, (see Figure 3.2-2), it is possible to achieve an average precession vector which will lie in any desired direction in the orbital plane. Thus, it is possible to select an average precession-vector normal to the momentum vector; this will cause the net motion of the flywheel axis to lie in a plane normal to the orbit plane and will optimize the path for the orbit normal.

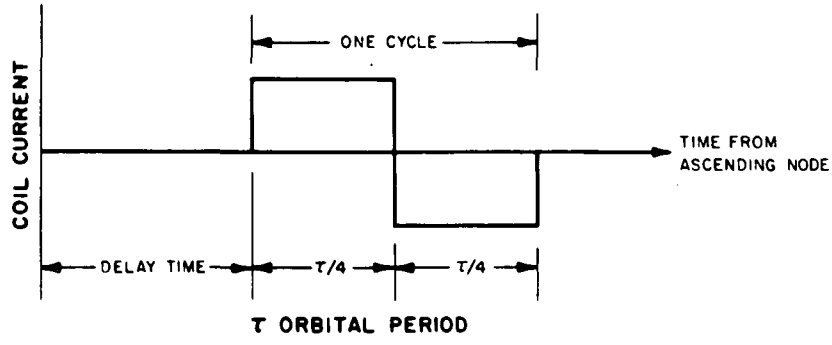

Figure 3.2-2. Phasing and Cycling of Coil Current in QOMAC Torquing

The components of the earth's magnetic field given in equation (3.2-11) are now averaged over one cycle of quarter-orbit torquing beginning with an arbitrary delay angle, θ_s, referenced to the ascending node[3]. This leads to half-orbit averages of

$$\tilde{B}_\ell = -\frac{3}{\pi}(\sin i \cos 2\theta_s) \qquad (3.2\text{-}12a)$$

$$\tilde{B}_b = -\frac{3}{\pi}(\sin i \sin 2\theta_s) \qquad (3.2\text{-}12b)$$

$$\tilde{B}_n = 0 \qquad (3.2\text{-}12c)$$

If, now, equation (3.2-10) is expanded and the average values of the earth's magnetic field substituted, the following average values of the precession components are obtained

$$(\bar{\omega}_p)_\ell = \frac{3}{\pi}(\mu_Q \sin i \cos 2\theta_s) \qquad (3.2\text{-}13a)$$

$$(\bar{\omega}_p)_b = \frac{3}{\pi}(\mu_Q \sin i \sin 2\theta_s) \qquad (3.2\text{-}13b)$$

$$(\bar{\omega}_p)_n = 0 \qquad (3.2\text{-}13c)$$

The $\hat{n}$-component of the precession is zero; thus, the precession axis is confined to the orbital plane. Furthermore, by a suitable choice of the start angle, θ_s, the precession axis may be chosen normal to the momentum axis.

Suppose that the axis, $\tilde{\omega}_\lambda$, about which the average-precession motion is to take place makes an angle λ with the line of ascending node. Then, the start angle, θ_s, required can be found from the fact that

$$\tan\lambda = \frac{(\tilde{\omega}_p)_b}{(\tilde{\omega}_p)_\ell} \qquad (3.2\text{-}14)$$

giving

$$\theta_s = \frac{\lambda}{2} \qquad (3.2\text{-}15)$$

Furthermore, $\tilde{\omega}_\lambda$ should be perpendicular to the flywheel axis in order that torquing causes the flywheel axis to move to coincidence with the orbit normal. Figure 3.2-3 illustrates that, because of the cyclic interchange of roll and yaw errors during orbiting, the desired perpendicularity is achieved when the attitude error is completely in the yaw and is negative; this occurs when

$$\psi = -\phi_{max} \qquad (3.2\text{-}16)$$

Depending upon the desired direction of precession, the phase angle, θ_s, at the moment the attitude clock initiates torque will be either $\lambda/2 + m\pi$ or $(\lambda + \pi)/2 + m\pi$ where m may be 0 or 1.

The average precession rate achieved at the completion of a torque cycle is given by

$$\omega_p = \sqrt{(\tilde{\omega}_p)_\ell^2 + (\tilde{\omega}_p)_b^2} = \frac{3}{\pi}\mu_Q \sin i \qquad (3.2\text{-}17)$$

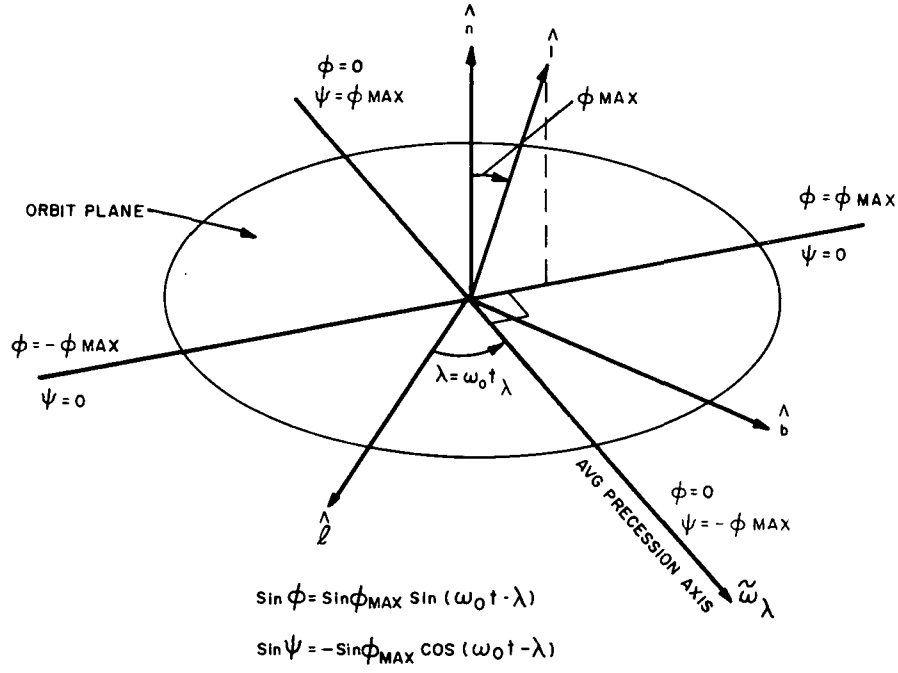

Figure 3.2-3. Geometry of ϕ_{max} and λ Shown in $\hat{\ell}$, $\hat{b}$, $\hat{n}$, Coordinates

3.2.2.3 Operational Requirements

The QOMAC technique of torquing will be used for two principal functions. The first function is to produce an orientation maneuver which must be initiated very soon after the completion of the momentum turn. The momentum turn, which is an inherent adjustment of the spacecraft to assume the configuration of minimum potential energy, puts the flywheel spin-axis along the momentum vector. QOMAC torquing will then be employed to precess the flywheel axis into coincidence with the orbit normal. The second function of QOMAC is to periodically adjust spacecraft attitude in the event that magnetic-bias torquing fails to maintain the desired coincidence of the inertial-wheel spin-axis and the orbit normal.

To meet the requirements of each of these functions, the QOMAC coil will be designed with two levels of torquing capability. To shorten the time needed to effect the initial turn, a torquing capability of about 3.5^{o} per-torque-cycle is contemplated. However, to adjust the flywheel axis to coincidence with the orbit normal, finer resolution is necessary. Because mission requirements necessitate holding the orbit normal to within $\pm 1^{o}$, the lower level of maneuvering capability is to be set at 1^{o} per-torque-cycle, or one-half the allowable range.

3.2.2.4 Second Order Effects

3.2.2.4.1 Canted Dipole

The expression for determining the start, angle θ_s, does not take into consideration the effect of the canted dipole of the earth's magnetic field. When this consideration is included in the analysis, the more accurate relationship for determining the start of QOMAC torquing takes the form

$$\theta_s = \frac{1}{2} (\lambda - \Delta\lambda) \tag{3.2-18}$$

where

$$\Delta\lambda = tan^{-1} \frac{b}{a} \tag{3.2-19}$$

and

$$a = cos\, i\ sin\, i_m\ cos\, \Omega - sin\, i\ cos\, i_m$$

$$b = sin\, i_m\ sin\, \Omega$$

For the sun-synchronous orbit in which the orbit inclination-angle is very nearly 90^o, sin i may be replaced by unity. If this is done in equation (3.2-19), then the value of $\Delta\lambda$ ranges from $- i_m$ to $+ i_m$ or $\pm 11.4^o$. For the uncanted dipole, i_m is zero and thus $\Delta\lambda$ is also zero. Therefore, if the effect of the canted nature of the earth's dipole axis is not taken into account in determining the start angle for QOMAC, an error as large as 11.4^o in establishing the average axis of precession may result. Figure 3.2-4 shows the effect of the selected spacecraft anomaly on establishing the desired precession axis (assuming an uncanted dipole model of the earth's magnetic field).

3.2.2.4.2 Programmer Errors

To initiate and control the QOMAC torquing, an attitude programmer will be provided which can be programmed by ground command. A program of instructions to the attitude clock will designate delay time and number of torque cycles to be executed. A delay-time capability of from zero to a maximum of 4096 seconds, and a range of torque cycles of from 1 to a maximum of 8 are planned. Section 3.6.5 of this report contains a detailed discussion of the programmer.

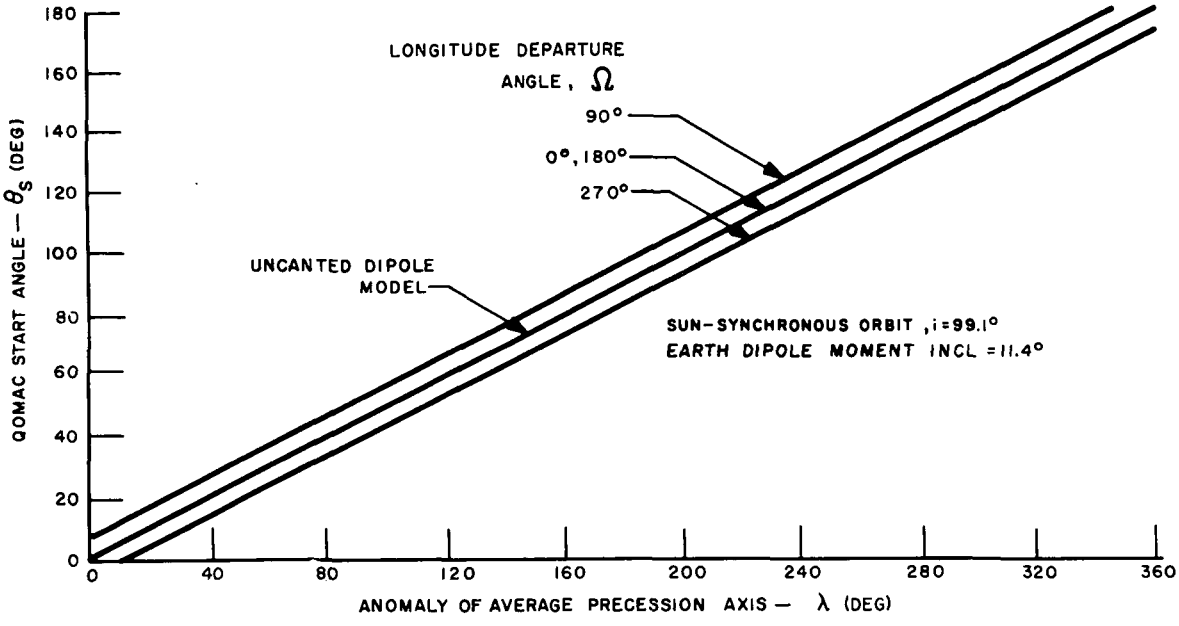

Figure 3.2-4. Effect of Dipole Model on QOMAC Start Angle

The length of time of the QOMAC cycle, which will be set into the attitude clock before launch, will be based upon the best prediction of the orbital period. It is unlikely, however, that agreement between prediction and attainment will be perfect; therefore, the switching times generated by the attitude clock will not be ideal. The errors is switching-point anomaly will increase monotonically regardless of whether the attitude clock is fast or slow. These errors can be partially offset by adjusting the QOMAC start-time to distribute the effect. A computer simulation program was made on a previous study of a 90^{o} -orientation maneuver, under conditions comparable to this study program, for a clock rate 3% fast and 3% slow. A ±3% error amounts to a ±80 miles error in altitude. For no clock-rate error, the angle between the orbit normal and the flywheel axis is decreased 23^{o} in five cycles and was reduced to 5^{o} in 21 cycles. With the clock rate 3% fast, the angle decreased 20^{o} in five cycles, and a 5^{o} angle was reached in 27 cycles. With the clock rate 3% slow, the angle decreased 18^{o} in five cycles, and $5^{o}$was reached in 22 cycles. A clock-fast error increases the time required to acquire the orbit-normal attitude while the clock-slow error has negligible effect. Therefore, it appears advisable in predicting the expected orbital period to bias the judgment on the side of a longer period rather than of a shorter one. It is expected, then, that in the worst-case conditions, the total time to acquire the orbit normal attitude, ϕ, should not exceed 20 orbits.

3.2.2.4.3 Ellipticity

Utilizing equations (2.2-18) of Section 2.2, the following are obtained for $(\tilde{\omega}_p)_\ell$ and $(\tilde{\omega}_p)_b$

$$(\tilde{\omega}_p)_\ell = \frac{3}{\pi} \mu_Q \sin i \left\{ \cos 2\theta_s + 3\epsilon \left[\frac{\sin(3\theta_s - \theta')}{3} - \sin(\theta_s + \theta') \right] \right\} \quad (3.2\text{-}20a)$$

$$(\tilde{\omega}_p)_b = \frac{3}{\pi} \mu_Q \sin i \left\{ \sin 2\theta_s + 3\epsilon \left[\frac{-\cos(3\theta_s - \theta')}{3} + \cos(\theta_s + \theta') - 2\cos(\theta_s - \theta') \right] \right\} \quad (3.2\text{-}20b)$$

It can be shown that the worst-case change in λ occurs when $\theta_s = 0$ or 180° and $\theta' = 0$, and is equal to 3° for $\epsilon = 0.013$. For this condition, the magnitude change is 4%. However, if desirable, the QOMAC-command computation can be developed so that the time, λ , and ϕ_{max} are computed taking into account ϵ and θ'. This should not be required unless eccentricities much greater than 0.013 are encountered.

The worst-case magnitude change occurs when $\theta_s = 0$ and $\theta' = -90^\circ$, and is equal to 6.6% (for $\epsilon = 0.013$). At this condition, there is no change in λ.

3.2.2.4.4 Instantaneous Motion

Only average torques and average motion have been considered thus far. The desired precession does not build up linearly with time but follows integrated sine waves, (see equation (3.2-11) of Section 3.2.2.2). Also, rotations are generated normal to the desired direction of precession. This normal rotation builds up during the first one-half of each QOMAC cycle but then retraces that history back to zero over the second one-half of the cycle. The maximum value of the normal rotation varies with the desired direction of precession. It can be shown that the largest peak value of normal rotation is generated when the desired direction of precession is about the negative line of nodes, that peak value being 40% of the desired precession. It is considerably less in many cases, but always has a net value of zero after each complete QOMAC cycle for the assumed magnetic model.

3.2.3 Magnetic-Bias Torquing

3.2.3.1 Dynamics

Several factors operate to degenerate the attitude at all times, the two most significant being the effect of the residual magnetic dipole of the spacecraft and the effect of the regression of the orbit in space. These two effects can be minimized by using a current coil (referred to as the magnetic-bias coil) which torques the spacecraft continuously at a level commensurate with the needs. This coil is made coaxial with the QOMAC coil and the two are part of the same structure.

Utilizing equation (2.3-8) of Section 2.3.4, the following can be written,

$$\bar{T}_{MB} = \frac{d\,|\bar{H}|}{dt}\,\hat{l} + |\bar{H}|\,\frac{d\hat{l}}{dt} + |\bar{H}|\,(\bar{\omega} \times \hat{l}) \qquad (3.2\text{-}21)$$

In addition, following the development in Section 3.2.2.1,

$$\bar{M}_{MB} = M_{MB} \times \hat{l} \qquad (3.2\text{-}22)$$

$$\frac{d\,|\bar{H}|}{dt} = 0 \qquad (3.2\text{-}23)$$

and

$$\bar{T}_{MB} = \bar{M}_{MB} \times \bar{B} = |\bar{H}|\,\mu_{MB}\,(\bar{b}_f \times \hat{l}) \qquad (3.2\text{-}24)$$

where

$$\mu_{MB} = \frac{M_E\, M_{MB}}{(1+\epsilon)^3\,(r_e + h_1)^3\,|\bar{H}|}$$

Combining these four equations leads to the results

$$\frac{d\hat{l}}{dt} = (\mu_{MB}\,\bar{b}_f + \bar{\omega}) \times \hat{l} \qquad (3.2\text{-}25)$$

If the orbit normal, $\hat{n}$, is to be tracked then the flywheel spin-axis, $\hat{l}$, must remain parallel to $\hat{n}$ on the average. This infers that the time-rate-of-change of the momentum-vector, $\hat{l}$, in the rotating system of coordinates will average to zero. This is

$$\frac{d\hat{l}}{dt} = 0 \qquad (3.2\text{-}26)$$

For this to be true, it is necessary that the right-hand side of equation (3.2-25) be equal to zero. The orbital precession vector, $\bar{\omega}$, can be written in $\hat{\ell}$, $\hat{b}$, $\hat{n}$, coordinates as

$$\bar{\omega} = |\bar{\omega}| (\hat{b} \sin i + \hat{n} \cos i) \tag{3.2-27}$$

Therefore, in order for vector $\hat{l}$ to track vector $\hat{n}$

$$\mu_{MB} (\bar{b}_f \times \hat{l}) = - |\bar{\omega}| (\hat{b} \sin i + \hat{n} \cos i) \times \hat{l} \tag{3.2-28}$$

3.2.3.2 Torque Generation

Utilizing equation 3.2-11 $(i_m = \epsilon = 0)$, the earth magnetic-field components are now averaged over a full orbit.

Thus,

$$(\tilde{b}_f)_\ell = 0 \tag{3.2-29a}$$

$$(\tilde{b}_f)_b = -\frac{1}{2} \sin i \tag{3.2-29b}$$

$$(\tilde{b}_f)_n = (\cos i) \tag{3.2-29c}$$

Therefore, the condition for perfect tracking is that

$$\left(\frac{-\mu_{MB}}{2} \sin i \, \hat{b} + \mu_{MB} \cos i \, \hat{n}\right) \times \hat{l} = -|\bar{\omega}| (\hat{b} \sin i + \hat{n} \cos i) \times \hat{l} \tag{3.2-30}$$

If it is now assumed that the instantaneous $\hat{n} \times \hat{l} = 0$, then perfect tracking can be obtained if

$$\frac{\mu_{MB}}{2} = |\bar{\omega}| \tag{3.2-31}$$

This is the required result of the analysis.

3.2.3.3 Operational Requirements

After final assembly, the residual magnetism of the spacecraft is nulled to a small value and an assessment is made of the residual dipole value for each one of the chief operating modes. A conservative estimate for the inaccuracy in achieving

null is ± 0.24 ATM^2. However, data from previously orbited spacecraft indicate that, after launch, significant changes in the residual magnetism may occur; a conservative estimate is 1 ATM^2. To keep the flywheel-axis of the spacecraft precessing at a rate of 1 per day and thus stay equal to the orbital sun-synchronous regression, another 0.36 ATM^2 of capability must be added, making a total of 1.61 ATM^2. The magnetic-bias coil proposed has a twenty-four level capability (in steps of ± 0.07 ATM^2 up to a maximum of ± 1.68 ATM^2). A ground-commanded spacecraft stepping-switch is utilized to change the dipole level; the command lasts until the necessary level is reached and the combined cancellation and tracking functions are produced. Details on the command process are given in Section 3.5 of this report.

3.2.3.4 Second-Order Effect

3.2.3.4.1 Instantaneous Motion

A net dipole value of 0.36 ATM^2 along the pitch-axis is required to give the 1^o per-day precession of the pitch-axis; this net dipole produces two components of rotation instantaneously. The instantaneous rotations vary sinusoidally with time at the frequency of two-cycles per second. The $\hat{\ell}$ component has a zero-to-peak amplitude of 0.04^o with an average of zero, while the $\hat{b}$ component has zero-to-peak amplitudes of $+0.055$ and -0.02^o with an average of $+0.07^o$ per orbit. The $\hat{b}$-component orbit-average value produces the required tracking rate; the cyclic motion produces a slight out-of-parallelism between the $\hat{\imath}$ axis and the $\hat{n}$ axis. The effect of this out-of-parallelism is very small over any single orbit. From equation (3.2-30) it can be seen, however, that perfect tracking is not really possible because of this effect. The magnitude of the error is discussed in the following Section.

3.2.3.4.2 Canted Dipole

A computer simulation that includes both the effects of a canted-dipole and the long-term effects of the cyclic out-of-parallelism of axes $\hat{\imath}$ and $\hat{n}$ was performed on another RCA program. While the results are not directly applicable to the present system, it has been computed (by proper scaling) that a drift-error no greater than 1.0^o in 20 days may be obtained due to these effects for the FSMTMS system.

3.2.3.4.3 Ellipticity

From equation (2.2-18) of Section 2.2, it is easily shown that integration over a complete orbit drops out all terms in $\cos n\theta$ or $\sin n\theta$. Therefore, the only effect of ellipticity on the magnetic-bias is a magnitude change proportional to $(1+\epsilon)^3$ For $\epsilon = 0.013$, this produces a 4% difference in magnitude which is equivalent to

approximately a one step-change of the magnetic-bias switch. The switch is stepped from ground-command on a trial and error basis; therefore, no actual error occurs if ellipticity is present.

3.2.4 Momentum Control

3.2.4.1 Dynamics

In order to control the momentum of the spacecraft by magnetic means, it is necessary to produce a dipole normal to the momentum vector. Because the satellite yaw-axis, $\hat{3}$, will nominally be aligned with the local vertical, the normal to the spin-control coil will be oriented parallel to the yaw-axis. This can be written as

$$\bar{M}_{MM} = |\bar{M}_{MM}|\,\hat{3} \tag{3.2-32}$$

If the torque produced by the dipole is written as,

$$\bar{T}_{MM} = \bar{M}_{MM} \times \bar{B} \tag{3.2-33}$$

then, in a manner similar to Section 3.2.2.1,

$$\bar{M}_{MM} \times \bar{B} = \frac{d\,|\bar{H}|}{dt}\,\hat{1} + |\bar{H}|\,(\bar{\omega}_p \times \hat{1}) \tag{3.2-34}$$

where it is assumed that $\bar{\omega}_p >> \bar{\omega}$.

The dipole $\bar{M}_{MM}$ has been aligned along the 3 axis; therefore, equation (3.2-34 can be written as

$$|\bar{M}_{MM}|\,(\,|\bar{B}|)_2\,\hat{1} - |\bar{M}_{MM}|\,(\,|\bar{B}|)_1\,\hat{2} = \frac{d\,|\bar{H}|}{dt}\,\hat{1} + |\bar{H}|\,(\bar{\omega}_p \times \hat{1}) \tag{3.2-35}$$

or, breaking this equation into its vector components

$$|\bar{M}_{MM}|\,(\,|\bar{B}|)_2\,\hat{1} = \frac{d\,|\bar{H}|}{dt} = \bar{T}_{SPIN} \tag{3.2-36}$$

and

$$|\bar{M}_{MM}|\,(\,|\bar{B}|)_1\,\hat{2} = |\bar{H}|\,(\bar{\omega}_p \times \hat{1}) = \bar{T}_{PREC} \tag{3.2-37}$$

Therefore, from equations (3.2-36) and (3.2-37), both the magnitude and the direction of the momentum-vector are changed by the action of a dipole along the $\hat{3}$ axis. Any change in direction must be considered an undesirable effect because, ideally, the coil should change only the magnitude of the spacecraft momentum.

3.2.4.2 Torque Generation

Initially it will be assumed that the $\hat{1}$, $\hat{2}$, $\hat{3}$ axes lie along the $\hat{r}$, $\hat{t}$, $\hat{n}$, axes with $\hat{1}$ along $\hat{n}$, $\hat{3}$ along $\hat{r}$, and $\hat{2}$ along $\hat{t}$. By referring to equation (2.2-17) of Section 2.2, it is apparent that, for the sun-synchronous orbit inclination of 99.1 degrees, B_t varies, essentially, as the $\cos\theta$. Therefore, if the coil dipole-moment is a half-orbit square-wave switching at $-\hat{b}$ ($\theta = 270°$) and $+\hat{b}$ ($\theta = 90°$), then the orbital-momentum-torque profile will be a rectified sine-wave, and a net increase or decrease in momentum can be obtained over half-orbit multiples. Furthermore, the B_n field component contained in the inherent precession term of equation (3.2-37) is relatively weak for approximately polar orbits (such as the 99.1° inclination considered here). Thus, the attitude-deviation introduced by momentum-control operation is small and can easily be corrected during the occasional QOMAC cycle. To increase spin-rate, the dipole moment should be switched to the negative yaw direction at $\theta = 270°$ and to the positive yaw direction at $\theta = 90°$; the reverse phasing applies if the spin-rate is to be decreased.

Utilizing the equation for B_t (in Section 2.2) for $(|\bar{B}|)_2$ in equation (3.2-36) yields

$$
\begin{aligned}
T_{SPIN} = \frac{M_E M_{MM}}{(1+\epsilon)^3 (r_e + h_1)^3} \Bigg\{ \Big[& \sin\theta \sin i_m \sin(C\theta + \Omega_0) \\
& - \cos\theta \cos i \sin i_m \cos(C\theta + \Omega_0) \\
& + \cos\theta \sin i \cos i_m \Big] \\
& + 3\epsilon \Big[\cos(\theta - \theta') \sin\theta \sin(C\theta + \Omega_0) \sin i_m \\
& - \cos(\theta - \theta') \cos\theta \cos(C\theta + \Omega_0) \cos i \sin i_m \\
& + \cos(\theta - \theta') \cos\theta \sin i \cos i_m \Big] \Bigg\} \delta(\theta)
\end{aligned}
\qquad (3.2\text{-}38)
$$

where

$$\delta(\theta) = U\left(\theta - \frac{\pi}{2}\right) + \sum_{n=1}^{\infty} (-1)^n \, 2 \, U_n\left(\theta - \frac{\pi}{2} - n \, \frac{T_o}{2}\right)$$

and

$$C = \frac{\omega_o \, T_o}{2\pi}$$

The switching function $\delta(\theta)$ assumes the dipole moment of the MASC coil to be along the positive yaw-axis at the ascending node. If the phase of the square wave were reversed, then the torque would be in the opposite direction.

Integration of equation (3.2-38) from $-\hat{b}$ to $+\hat{b}$ and division by π yields the average spin torque

$$\begin{aligned}
\tilde{T}_{SPIN} = {} & \frac{2 M_E M_{MM}}{(1+\epsilon)^3 (r_E + h_1)^3} \left\{ \frac{C \sin i_m}{\pi(1 - C^2)} \left(1 - \frac{\cos i}{C}\right) \cos \Omega_0 \right. \\
& \times \cos \frac{\pi C}{2} + \frac{\sin i \, \cos i_m}{\pi} \\
& + \frac{3 \epsilon \sin i_m \, \sin \frac{\pi C}{2}}{\pi C (4 - C^2)} \left[\cos \Omega_0 \, \cos \theta' (C - 2 \cos i) \right. \\
& \left. \left. + \sin \Omega_0 \sin \theta' (2 + C \cos i - C^2) \right] \right. \\
& \left. + \frac{3 \epsilon \sin i \, \cos i_m \cos \theta'}{4} \right\}
\end{aligned} \tag{3.2-39}$$

For $\epsilon = 0$ and $C = 0$,

$$\tilde{T}_{SPIN} = \frac{2 M_E M_{MM}}{\pi (r_E + h_1)^3} \left(\sin i \, \cos i_m - \cos \Omega \, \cos i \, \sin i_m\right) \tag{3.2-40}$$

For the same assumptions as were made to develop equation (3.2-40) it was shown[3] that the precession-momentum added orthogonally to the flywheel spin-axis, H_{PREC}, is

$$\bar{H}_{PREC} = \frac{-2 M_E M_{MM}}{(r_E + h_1)^3 \omega_\theta} (\sin i \sin i_m \cos \Omega + \cos i \cos i_m) \qquad (3.2\text{-}41)$$

where ω_0 is the vehicle orbital-rate.

The angle by which the spin-axis precesses in the course of a one-half orbit is

$$\psi = \tan^{-1} \left| \frac{H_{PREC}}{H} \right| \qquad (3.2\text{-}42)$$

3.2.4.3 Operational Considerations

Figure 3.2-5 illustrates the relationship between the coil magnetic-dipole moment and the generated-torque about the spin axis. This curve is drawn for zero eccentricity (equation 3.2-40). The maximum-minimum limits correspond to Ω angles of 0^o and 180^o, respectively. Thus, to produce a nominal average-torque of 1000 dyne-cm about the spin axis, it is necessary to provide a coil dipole-moment of about 8 ampere-turn meter^2. This value of torque is equivalent to a 2% change in flywheel spin-rate; thus, 5-cycles of momentum-control torquing would be required to change the flywheel rate from 5% high to 5% low (or vice versa).

3.2.4.4 Second Order Effects

3.2.4.4.1 Attitude Errors

It was shown[3] that roll- and yaw-attitude errors produce a slight decrease in the magnitude of the available momentum torque. Figure 3.2-6 shows this effect.

For large pitch-errors which can occur during initial lock-on of the pitch-axis servo, it was shown[3] that the switch-angles should be changed to obtain the same momentum torque. Figure 3.2-7 shows the new switching-angles as a function of pitch-axis error.

3.2.4.4.2 Switching Errors and Orbit-Start Angle

The B_t field is not strictly a $\cos \theta$ variation because of the canting of the earth's magnetic field with respect to the earth's spin axis (by angle i_m, 11.4^o). The ideal switchpoints are located at the two spacecraft anomaly

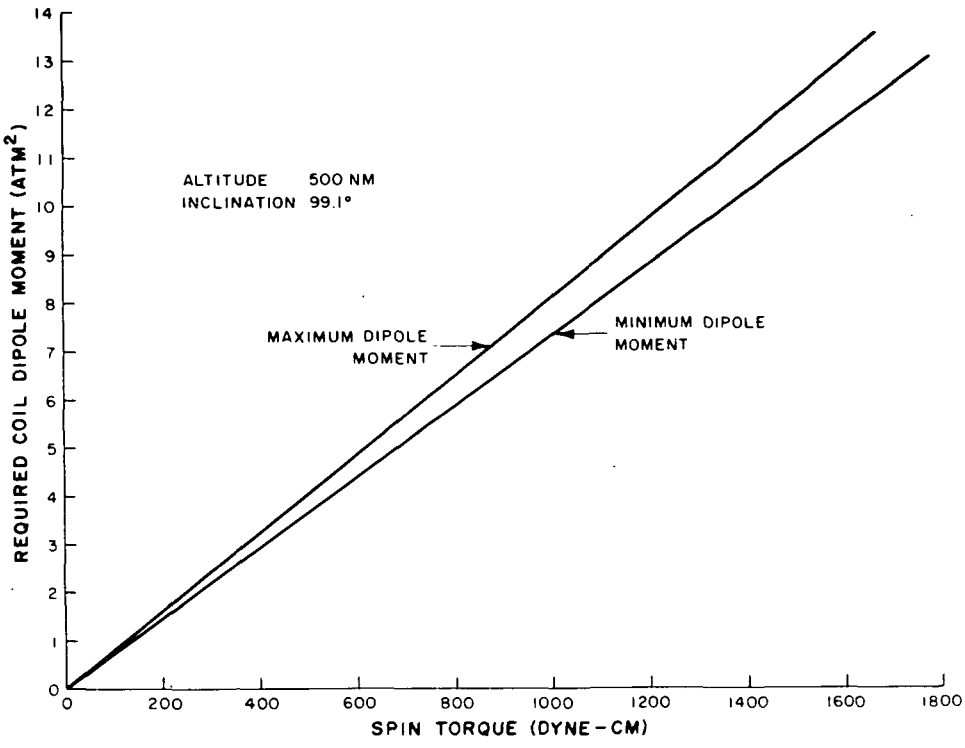

Figure 3.2-5. Momentum-Control Coil Requirements

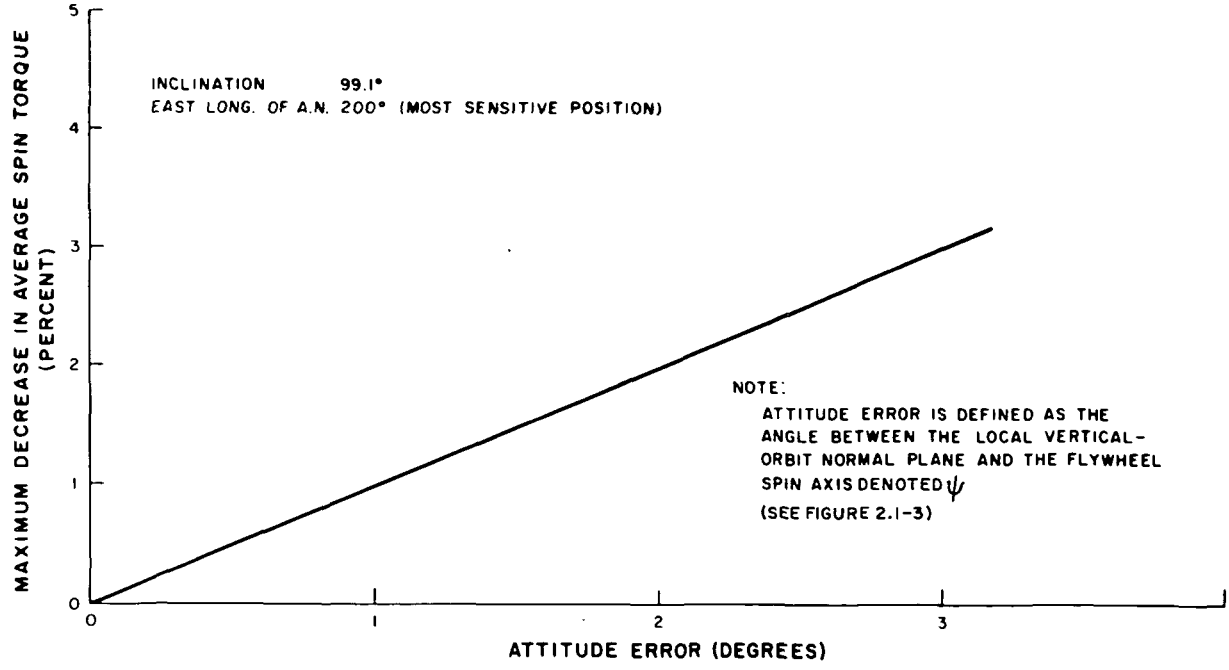

Figure 3.2-6. Effect of Attitude Error on Average Spin-Torque

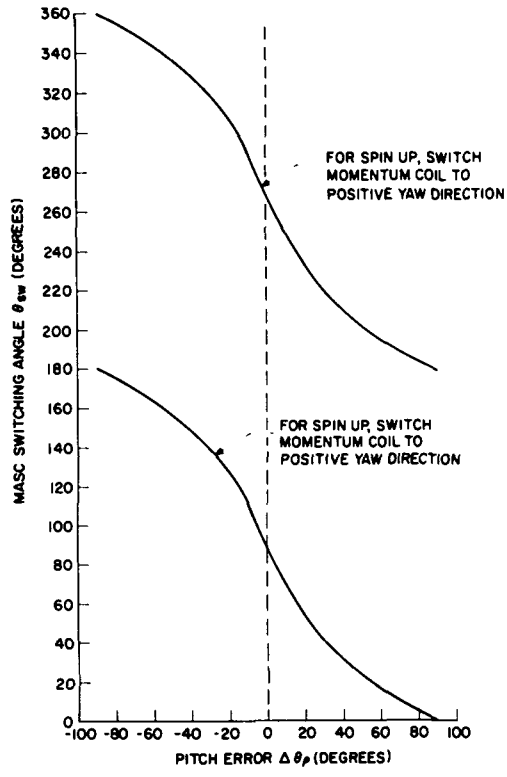

Figure 3.2-7. New Switching-Angles as a Function of Pitch-Axis Error

angles closest to the earth's magnetic-dipole axis. This optimum switching-angle is given by

$$\theta_{sw} = \tan^{-1}\left(\frac{\cos i \sin i_m \cos \Omega - \cos i_m \sin i}{\sin i_m \sin \Omega}\right) \qquad (3.2\text{-}43)$$

or when $B_t = 0$.

The ideal switching, therefore, depends upon the longitude of the orbit ascending-node. Figure 3.2-8 indicates that the selection of $\theta_{sw} = 90°$ and $270°$ results in a maximum deviation on only 1.2^{o} from the optimum as defined by equation (3.2-43). The approximation, made for the sake of operational simplicity that the switching angle will have a negligible effect on the attainable spin-rate adjustment, can be observed by examining Figure 3.2-9. This figure is drawn for that orbital location which results in the greatest sensitivity of spin-torque to the switching anomaly-angle.

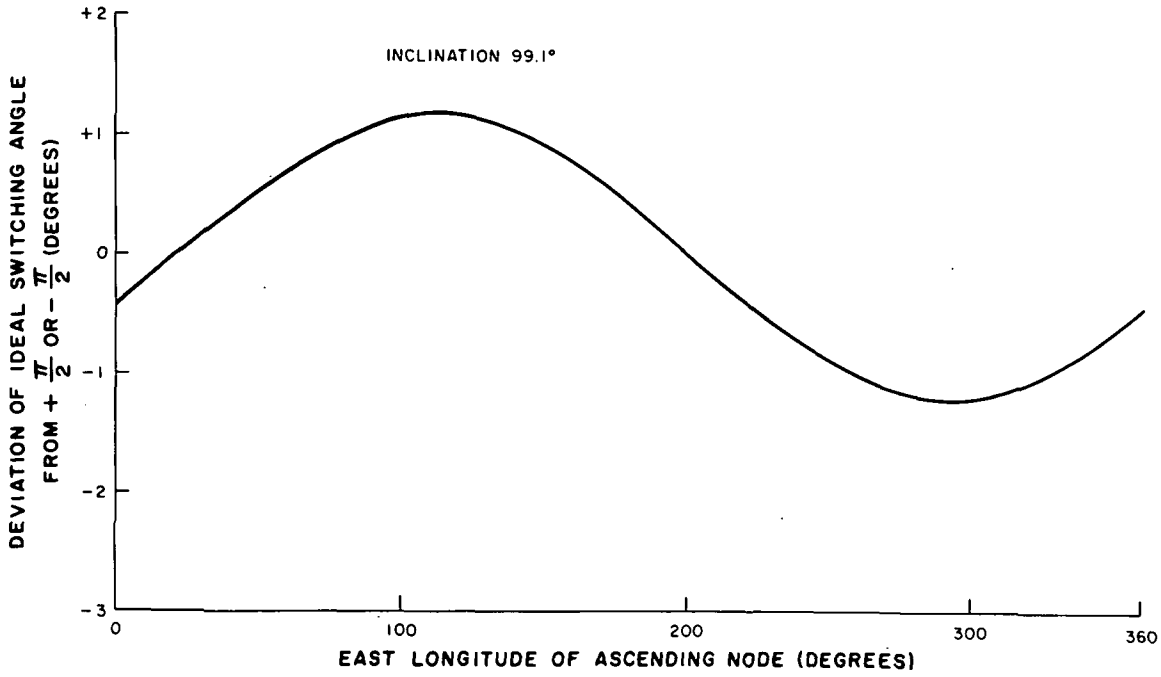

Figure 3.2-8. Momentum-Control Deviation of Ideal Switching Angle (From $+\pi/2$ and $-\pi/2$ orbit angle)

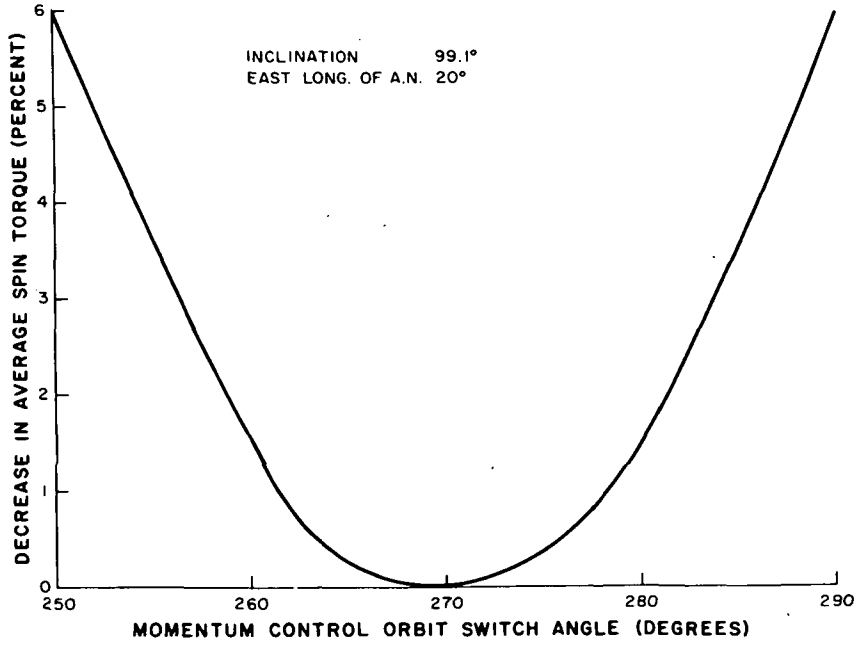

Figure 3.2-9. Effect of Momentum-Control Orbit Start-Angle on Average Spin Torque

3.2.4.4.3 Eccentricity and Orbit Precession

Ignoring the nominal eccentricity of 0.013 in equation (3.2-39) results in a maximum change in average spin torque of 3.1%; this occurs at $\Omega_0 = 0°$, $\theta' = 180°$. Because of this small effect of the anticipated eccentricity on average spin torque, it is reasonable to base performance predictions on circular orbits. Ignoring the effects of the term C (i.e., letting Ω be the average value during the torque cycle) results in a maximum change in average spin-torque of 1%. Torquing occurs from $-\pi/2$ to $+\pi/2$; therefore, the average value is at $\theta = 0$, or $\Omega = \Omega_0 = 0°$. This change is so small that the term C in equation (3.2-39) can be neglected.

3.2.4.4.4 Precessional Motion

The precession per-orbit can be determined by the substitution of appropriate values in equations (3.2-41) and (3.2-42). Figure 3.2-10 indicates the anticipated precession versus the desired average-spin-torque. As anticipated, the precession is very sensitive to the location of the orbit ascending-node. However, even for a continuous average-spin-torque value of 1000 dyne-cm, the spin-axis displacement should not exceed 1° per orbit.

3.2.4.4.5 Instantaneous Motion

In addition to the change in flywheel speed, the magnetic torque develops small changes in the direction of the pitch axis. The component of rotation about the $\hat{b}$ axis increases sinusoidally to a peak value at the mid-point of the cycle (i.e., at the equator) and decreases to zero at the end of the cycle. Conversely, the $\hat{\ell}$ component of the rotation follows a cosine wave superimposed on a constant, thus causing a net value to be developed each cycle. As discussed in the previous section for consecutive cycles, the direction of the coil-dipole is reversed with respect to the vehicle axes. Because of this, the above rotations repeat in sign. Thus, there is a net rotation about the $\hat{\ell}$ axis but zero about the $\hat{b}$ axis for any number of consecutive cycles.

The magnitude of the pitch-axis precession varies with the position of the earth's magnetic pole. In the worst case, the zero-to-peak amplitude about axis $\hat{b}$ is 0.21° while the net accumulation about axis $\hat{\ell}$ is 0.42° per MASC cycle.

3.2.5 Coil Designs

3.2.5.1 Magnetic-Bias Coil Requirements

As discussed in Section 3.2.3.3, a maximum dipole size of 1.6 ATM^2 is required. The finer the available resolution of this dipole, the less frequently it will be necessary to reset the bias-coil or to supplement the bias-system with

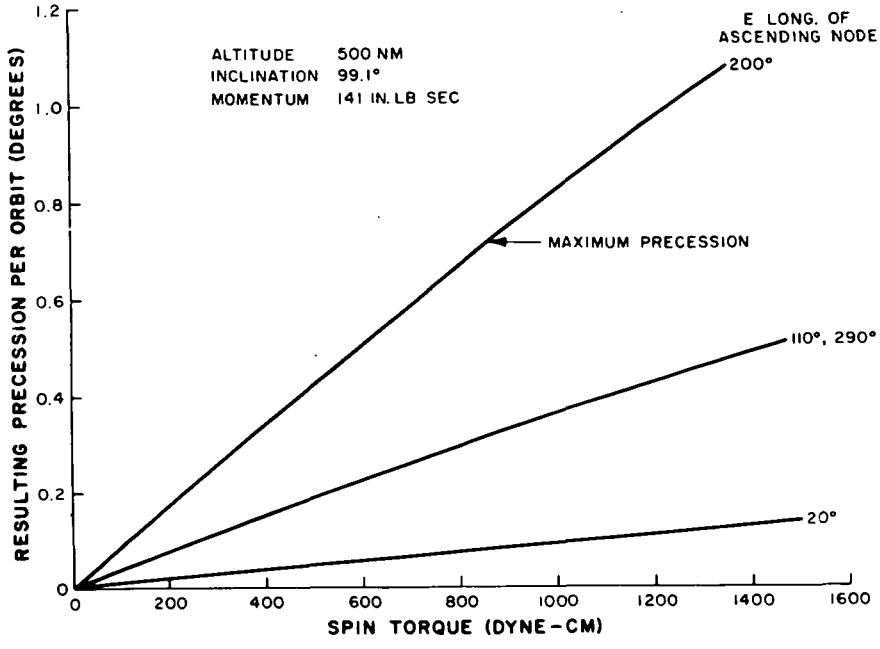

Figure 3.2-10. Precession Inherent to Momentum Control

QOMAC cycles. It was previously shown[4] that, for a 0.07 ATM^2 resolution, it will take approximately 20 days to drift through a $\pm 1^o$ deadband (or 0.1^o per day). This is considered satisfactory in terms of the required QOMAC duty cycle.

3.2.5.2 Momentum-Control Torquing Requirements

As shown in Table 2.3-1 , the major disturbance tending to change the momentum magnitudes is due to hysteresis losses; it produces a change of 0.4% per-day or 10% in 25 days. Therefore one should conservatively expect to require momentum-control torquing at 20-day intervals for the pitch-axis momentum specification of ±5%. The coil has been sized to produce 7.7 ATM^2 which is equivalent to 1000 dyne-cm torque capability, or a 2% change in momentum per one-half orbit. Therefore, 5-cycles are required to correct for a ±5% change.

3.2.5.3 QOMAC Torquing Requirements

The operational coil requirements are discussed in Section 3.2.2.3. It was shown[4] that a dipole moment of 5.85 ATM^2 produces a maximum motion of 1^o per-cycle. The coarse mode, achieved by increasing the applied potential from 7.0 volts

to 24.5 volts, permits a maximum precession rate of 3.5^{o} per-QOMAC-cycle (1/2 orbit). Using the attitude clock, a maximum of 8 of these cycles can be programmed with one set of commands.

The frequency at which QOMAC will be used is a function of several factors. First, the magnetic-bias coil-resolution error can produce a 0.1^{o} per-day drift; second, from Section 3.2.3.4.2 the inaccuracy in tracking the orbit-normal can produce approximately a 0.1^{o} per-day drift. Therefore, the total requirement due to magnitude-bias errors is 0.2^{o} per day. However, one-half of this drift may be cancelled by occasional (once-a-week) shifting of the magnetic-bias dipole, leading to a 0.1^{o} per-day drift that QOMAC must correct.

In addition, whenever momentum control is used, a precession of 0.42^{o} (worst-case) per-cycle is obtained, or 2.1^{o} per 5-cycles. This occurs once every 20 days.

Other disturbances are not expected to cause more than an additional 0.15^{o} per-day error (the major cause being due to the gravity-gradient torque caused by an assumed 1.0^{o} pitch-axis error).

Therefore, if all motion is added in a scalar fashion (worst-case conditions), the QOMAC system will be turned on for one cycle once every 4 days (to counteract a total 0.25^{o} per-day drift), and for an additional two cycles once every 20 days (to counteract the momentum-control precession disturbance). This, of course, is an extremely conservative estimate. Experience on other programs indicate that a frequency of one QOMAC-cycle per week is a more realistic estimate.

3.2.5.4 Coil Parameters

The equations defining the anticipated attitude- and momentum-control as functions of the applied coil-magnetic-dipole moments $(M = NIA)$ were previously presented.(3) Therefore, the size of the coils which are necessary to produce the desired QOMAC, magnetic-bias, and momentum-control dipole moment must be determined. Although these coils could be wound in various shapes, the spacecraft permits the installation of coils which are wound in a simple circular circumference. The weight-current product of such a coil can be expressed as

$$WI = \frac{16 \gamma \rho M^2}{V D^2}$$

where

W is the mass in kilograms

I is the coil-current in amperes

ρ is the resistivity in ohm-meters

γ is the density in kilograms per cubic meter

M is the dipole moment in ampere-turn meter^2

V is the supply voltage in volts

D is the coil diameter in meters

To minimize this product, the wire material should be selected to result in a minimum density - conductivity product $(\gamma \rho)$. Aluminum gives approximately a 2:1 advantage over copper in this respect. Furthermore, it is desirable to maximize the circumference diameter, D, within the installation limits of the spacecraft.

If the polarity of the potential, V, cannot be reversed to switch the direction of M, it will be necessary to install the coil in a bridge arrangement, or to double the WI product for a center-tapped configuration. Because fewer components are required for the latter configuration, a sacrifice in the WI product appears warranted for the sake of reliability. Actually, these polarity considerations only apply to the QOMAC coil which uses both the -24.5 and -7 volt supply; all other magnetic torquing will be accomplished with the dual-polarity 7.0 volt supply.

The desired wire-diameter satisfying the operational requirements can be expressed as follows for coils wound in a circular fashion:

$$d = 4\sqrt{\frac{M\rho}{\pi DV}}$$

This diameter must be approximated to the nearest standard size. Furthermore, it is not deemed advisable to utilize aluminum wire of a diameter smaller than the No. 32 AWG size.

The recommended QOMAC-coil parameters are given in Table 3.2-1. The Magnetic-Bias coil parameters are given in Table 3.2-2. Figure 3.2-11 shows the weight-current plot for both coils. The weight values for the QOMAC coil should be doubled because of the center-tap configuration.

The momentum-coil was designed for a maximum disturbance-torque of 1000 dyne-cm, or a spin-decay of 87 rpm per day. This requires a magnetic dipole-moment of 8 ATM^2. The coil parameters are given in Table 3.2-3. The final dipole moment of 7.7 ATM^2 differs from 8 ATM^2 due to considerations of the available wire-characteristics and corresponds to a maximum disturbance-torque of 970 dyne-cm.

TABLE 3.2-1. QOMAC COIL PARAMETERS

Parameter	Characteristics
Type of coil	Center-tapped circular
Power supply	-24.5 V High torque mode - 7.0 V Low torque mode
Diameter	28.5 inches
Area	0.413 meter^2
Circumference	7.46 feet
Wire size	26 gauge
Total weight of wire	1.0 lb.
Number of turns	285 per tap
Resistance	142 ohms per tap at 25^{o}C
Current	0.174 amp. High-torque mode 0.050 amp. Low-torque mode
Power	4.26 watt High-torque mode 0.35 watt Low-torque mode
Dipole moment	20.4 ATM^2 High-torque mode 5.8 ATM^2 Low-torque mode
Degrees per torque cycle	3.5 degrees High-torque mode 1.0 degrees low-torque mode

There are two possible locations on the spacecraft for the momentum coil. Located in the control package, the diameter of the coil would be 22 inches; this diameter is increased to 48 inches by placing the coil in the sensory ring. Figure 3.2-12 shows the weight versus current plot for each coil size. For a given dipole-moment, the larger coil has a much lower weight-current product. For a given current, there is a 5-to-1 ratio in the weight and in the number of turns needed to obtain the required dipole-moment. Thus, the 48-inch-diameter coil in the sensory ring should be used.

The effect of temperature variations on all the coils was investigated[4]. Temperature effects should cause no problems.

TABLE 3.2-2. MAGNETIC-BIAS COIL PARAMETERS

Parameter	Characteristics
Type of coil	Circular
Power supply	±7.0 V
Diameter	28.5 inches
Area	0.413 meter^2
Circumference	7.46 feet
Wire size	31 gauge
Weight of wire	0.11 lb.
Number of turns	200 per tap
Resistance	318 ohms per tap at 25°C
Current	0.020 amp. max.
Power	0.143 watt max.
Dipole moment	1.68 ATM ^{2} max.
Dipole moment intervals	0.07 ATM ^{2}
Degrees per day	4.1 degrees max. 0.085 degrees resolution

TABLE 3.2-3. MOMENTUM-COIL PARAMETERS

Parameter	Characteristics
Type of coil	Circular
Power supply	±7.0 V
Diameter	48 inches
Area	1.17 meter ^{2}
Circumference	12.6 feet
Wire size	27 gauge
Weight of wire	0.32 lb.
Number of turns	137 per tap
Resistance	146 ohms per tap at 25°C
Current	0.048 amp.
Power	0.336 watt
Dipole moment	7.7 ATM ^{2}

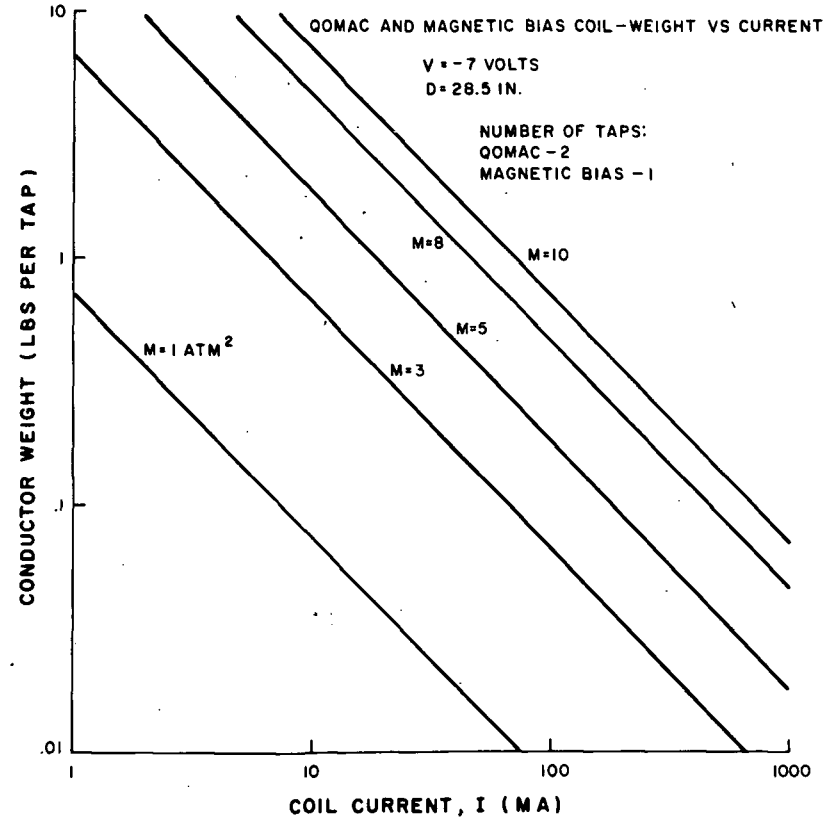

Figure 3.2-11. QOMAC and Magnetic-Bias Coil, Weight Versus Current Characteristics

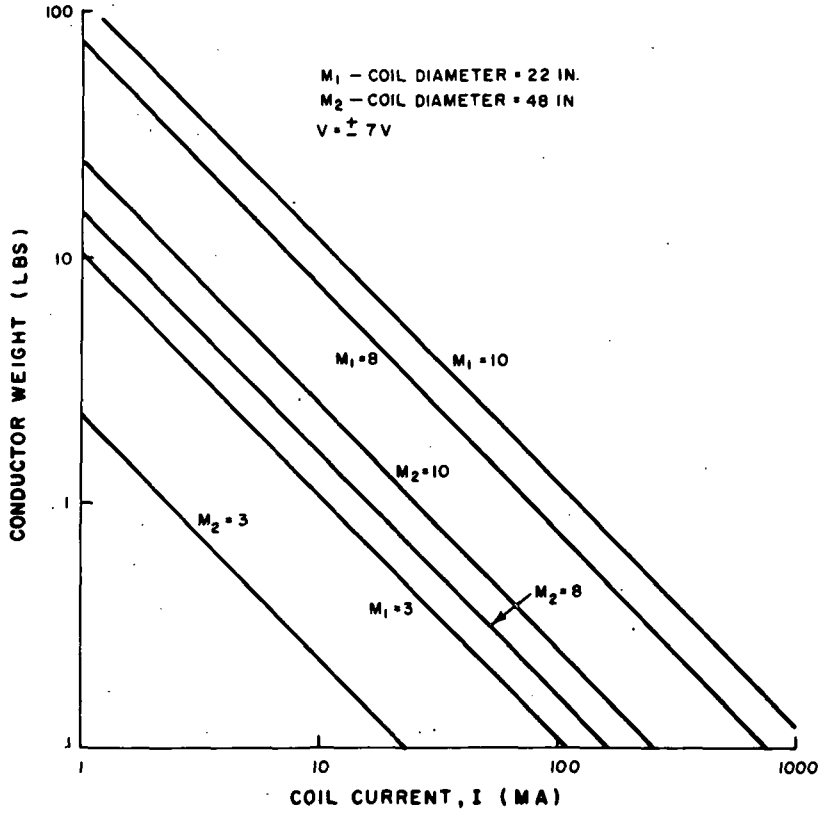

Figure 3.2-12. Momentum-Coil Weight Versus Current Characteristics

3.2.6 Summary of Parameters

Table 3.2-4 summarizes the achieved torques and the perturbations due to these torques for all the magnetic-control subsystems.

TABLE 3.2-4. SUMMARY OF MAGNETIC-TORQUE-CONTROL CHARACTERISTICS

Torquing Mode	Desired Effect	Perturbations
Magnetic Bias Torque	Slow precession of pitch axis of 1^{o} per day to follow regression of sun synchronous orbit plane.	Sinusoidal rotations, two cycles per orbit: ① 0.04^{o} amplitude about $\bar{\ell}$, zero average ② $+0.055$ to -0.02^{o} peak to peak about $\bar{b}$
QOMAC Quarter Orbit Magnetic Attitude Control	Slow precession of pitch axis in either of two modes to provide control of pitch axis pointing direction: ① Coarse mode - 7^{o} per orbit capability, used for 90^{o} turn ② Fine mode - 1^{o} per cycle (1/2 orbit), used for attitude trimming as required	Slow precession of pitch axis normal to desired directions; rotation builds up during first half of cycle and then retraces this history back to zero during second half of cycle. The precise variation of rotation with time and the magnitudes involved vary with the axis of desired rotation. Worst case magnitudes are: ① Coarse mode - 1.35^{o} peak, zero net per cycle ② Fine mode - 0.39^{o} peak, zero net per cycle
Momentum Control	Change flywheel speed to compensate for initial momentum errors or accumulated action of disturbance torques. Capability of ± 3.1 rpm per cycle (1/2 orbit, from $+\bar{b}$ to $-\bar{b}$ or from $-\bar{b}$ to $+\bar{b}$)	Slow precession of pitch axis; components of rotation for worst case position of magnetic pole: ① 0.42^{o} accumulation per cycle about $\bar{\ell}$ axis ② 0.21^{o} zero to peak amplitude about $\bar{b}$ axis, with zero net accumulation per cycle.

3.3 NUTATION CONTROL SUBSYSTEM

3.3.1 General

Basically, the nutation-control subsystem provides the fine-control of the roll/yaw axes even though there is no direct sensing, negative feedback, amplifying, and torquing, as there is in the pitch-axis servo. Each of these elements of control are contained in the passive operation of the nutation damper. The detailed operation of the nutation-control subsystem was previously presented[1, 2, 3].

3.3.2 Description of Spacecraft Motion

Figure 3.3-1(a) shows the spacecraft and inertial coordinate systems as developed in Section 2.1 of this report. Nutation can be defined as undesired motion about the roll or yaw axis at any point in the orbit; therefore, it is assumed that for the discussion to follow, the $\hat{n}, \hat{t}, \hat{r}$, coordinate system is inertially fixed. This assumption is justified because the period of nutation is more than three orders of magnitude smaller than the rotation period of the $\hat{n}, \hat{t}, \hat{r}$, coordinate system. The total angular momentum, $\bar{H}$, is shown parallel to the $\hat{n}$ and $\hat{1}$ axis as would be the case in normal operation of the spacecraft after it has been placed normal to the orbit plane (defined by $\hat{t} - \hat{r}$). Although initial alignment is shown between the spacecraft and inertial axes, successful operation of the nutation damper does not depend on this alignment. For example, the assumption is made that all of the momentum is parallel to the orbit normal, $\hat{n}$; however, a portion of the momentum can be in the flywheel but all of it need not be in the flywheel, and a portion may be in the spacecraft (which, during initial recovery, will be rotating in either direction about $\hat{n}$). Section 3.7 of this report presents a discussion of the launch-mode and the initial alignment conditions.

Figure 3.3-1(b) shows the spacecraft coordinate nutating about the total angular-momentum vector, $\bar{H}$, which is still aligned along the orbit normal. A plane-view showing the motion of each axis is most difficult and is, therefore, implied by assigning the three velocity components to each axis, ω_1, ω_2, and ω_3. That portion of the total momentum in the flywheel is given by $I_f \omega_f$. The angle θ shown in Figure 3.3-1(b) is the displacement of the pitch-axis, $\hat{1}$, from the desired orbit normal direction, $\hat{n}$, as a result of an induced disturbance from the condition associated with initial alignment. In either case, all spacecraft axes are misaligned from their desired position.

The values of ω_1, ω_2, and ω_3 may be expressed in terms of Euler angles by three successive rotations: the first ψ is a rotation about the inertially fixed $\hat{n}$ direction; the second is about the line of nodes and through the angle θ (which, in this case, is the line ω which the $\hat{3}$ axis has moved to after the ψ rotation); the third rotation is about the $\hat{1}$ axis and through the angle θ. These three rotations may be expressed as components of the total angular velocity vector, $\bar{\omega}$, as follows

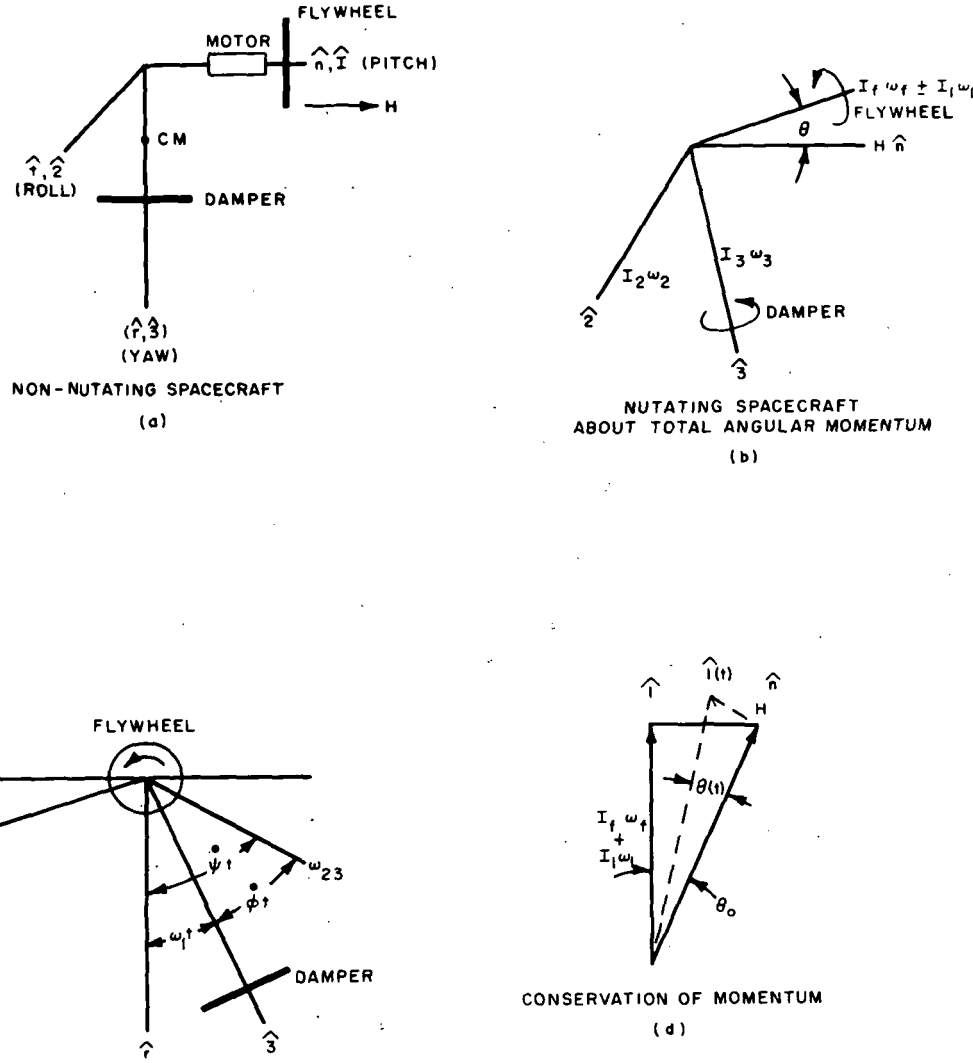

Figure 3.3-1. Spacecraft Orientation with Respect to the Coordinate Systems Defined in Section 2.1 of this Report

$$\omega_1 = \dot{\psi} \cos\theta + \dot{\phi} \tag{3.3-1a}$$

$$\omega_2 = \dot{\psi} \sin\theta \sin\dot{\phi}\, t \tag{3.3-1b}$$

$$\omega_3 = \dot{\psi} \sin\theta \cos\dot{\phi}\, t \tag{3.3-1c}$$

There are no terms containing $\dot{\theta}$ because the assumption is made that $\dot{\theta} << \dot{\phi}, \dot{\psi}$; this means that, during a single rotation of the $\hat{1}$ axis about the $\hat{n}$ axis, the angle θ does not change measurably.

The total momentum of the system containing the spacecraft, flywheel, and damper may now be written in the form of the following vector equation using Figure 3.3-1(b).

$$\bar{H} = (I_1 \omega_1 + I_f \omega_f)\, \hat{1} + I_2 \omega_2\, \hat{2} + I_3 \omega_3\, \hat{3} \tag{3.3-2}$$

Because $\bar{H}$ is a vector defined in the body coordinate system, it is necessary to consider the effect of motion with respect to inertial space of the coordinate system. To do this, the following equation is used

$$\left|\bar{T}\right|_I = \left|\frac{d\bar{H}}{dt}\right|_R + \bar{\omega} \times \bar{H} = 0 \tag{3.3-3}$$

where the subscripts I and R refer to the inertial and rotating systems respectively. The zero on the right side of equation (3.3-3) refers to the fact that after the spacecraft has been disturbed the resulting motion is not under the influence of external torques. Before substituting equations (3.3-1) and (3.3-2) into (3.3-3), the following and temporary assumptions are made

$$I_2 = I_3 \tag{3.3-4a}$$

$$\omega_f - \omega_1 = constant = k \tag{3.3-4b}$$

The first assumption implies that the moment-of-inertia about the roll-axis, a principal axis, is equal in magnitude to that about the yaw axis, also a principal axis. This will not be the case in the final system, but the effect on the performance of the actual inertia distribution will be small. No proof of this statement is presently available because the manipulation of the Euler equation with actual moment of inertia

values requires computer simulation outside the scope of this study program. It is, however, possible to show that the major difference between the assumed inertia distribution and an actual distribution lies chiefly in the period required to damp out an initial disturbance. The spatial motion of the body axis for three non-equal principal moments-of-inertia are developed elsewhere[2].

The second assumption concerns the condition imposed by the closed-loop operation of the motor driving the flywheel. When final lock-on is obtained, the constant, k, will be numerically equal to the flywheel speed, ω_f (i.e., about 150 rpm). The initial value of ω_1 will be associated with the error associated with spin-down (i.e., between 1 and 2 rpm).

When equations (3.3-1), (3.3-2) and the assumptions of equation (3.3-4) are substituted into equation (3.3-3), the resulting equations lead to a solution of ω_2 and ω_3 in terms of known system values. The results are expressed in equations (3.3-5).

$$\dot{\psi} = \frac{1}{\cos\theta}\left[\frac{I_1\omega_1}{I_3} + \frac{I_f\omega_f}{I_3}\right] \qquad (3.3\text{-}5a)$$

$$\dot{\phi} = \frac{\omega_1(I_3 - I_1)}{I_3} - \frac{I_f\omega_f}{I_3} \qquad (3.3\text{-}5b)$$

The results expressed by equations (3.3-5) are of prime importance to establish the stability and performance of the spacecraft containing a spinning flywheel whose inertias are small compared to the spacecraft. Equation (3.3-5a) expresses the rate at which the total angular-velocity vector and the flywheel-axis rotate about the inertially-fixed momentum vector, $\bar{H}$. This is shown in Figure 3.3-1(c). The value of $\dot{\psi}$ is a positive quantity because the total momentum $(I_1\omega_1 + I_f\omega_f)$ was specified as positive in the $\hat{\imath}$ direction. The expression for $\dot{\phi}$, equation (3.3-5b), represents the rate at which the spacecraft coordinate system rotates with respect to the total velocity vector. Figure 3.3-1(c) also illustrates this rotation. The sign of $\dot{\phi}$ is negative. The discussion to this point is adequate proof of stability because the relationship between $\dot{\phi}$ and $\dot{\psi}$ will cause the angle θ to decrease if energy is lost from the spacecraft while conserving total momentum.[8] However, the mechanism of the damping action is further analyzed because there are other properties of interest.

3.3.3 Nutation-Damper Operation

A relationship was developed previously[3] which describes the magnitude and phase of the momentum, H_d, transferred to a ring of fluid when the ring is rotated about its axis of symmetry. The relationship is as follows

$$H_d = \frac{I_d \omega_{23}}{(1 + \tau S)^{1/2}} \qquad (3.3\text{-}6)$$

where I_d = fluid mass moment of inertia

$$\tau = \frac{r_o^2 \rho}{4\mu}$$

The optimum value of τ was suggested as $1/\dot{\psi}$ [3] because the best value for H_d occurred when it lagged the forcing angular-velocity by $\pi/8$ radians or 22-1/2 degrees. This condition produces the maximum component of damper-momentum 90° out of phase with the forcing angular velocity, ω_{23}. By placing the fluid ring on the body (shown in Figures 3.3-1 and in 7.2-1), the angular momentum in the positive $\hat{3}$ direction may be expressed, with the aid of equations (3.3-6) and (3.3-1c) as

$$H_{d3} = \frac{I_d \omega_3 (j\dot{\phi}) e^{-j\pi/8}}{\sqrt[4]{2}} = \frac{I_d \psi \sin\theta \cos(\dot{\phi}t - \pi/8)}{\sqrt[4]{2}} \qquad (3.3\text{-}7)$$

Because the term H_{d3} represents angular momentum attached to a rotating coordinate system, a torque is produced between the fluid ring and the body. The standard gyroscopic torque equation is used to determine magnitude and direction. The instantaneous torque that the fluid ring produces on the spacecraft is given in the following vector equation.

$$\bar{T} = \bar{H}_d \times \bar{\omega} \qquad (3.3\text{-}8)$$

If equations (3.3-1) and (3.3-7) are substituted into (3.3-8), the results are an expression for two components of torque. The first component is along the $\hat{1}$ axis and is

$$T_1 = \frac{-I_d \dot{\psi}^2 \sin^2\theta \sin\dot{\phi}t \cos(\dot{\phi}t - \pi/8)}{\sqrt[4]{2}} \qquad (3.3\text{-}9)$$

The second component is along the $\hat{2}$ axis and is

$$T_2 = \frac{I_d \dot{\psi} \sin^2\theta \omega_1}{\sqrt[4]{2}} \qquad (3.3\text{-}10)$$

These torque components must be average over one complete rotation of the body axis with respect to the velocity vector. The direction chosen is most important in establishing stability. Equation (3.3-5b) demonstrated that $\dot{\phi}$ was a negative quantity. Therefore, to be consistent, the torque must be averaged from 2π to 0, or

$$\tilde{T}_1 = \frac{-I_d\,\dot{\psi}^2\,\sin^2\theta}{\sqrt[4]{2}}\;\frac{1}{2\pi}\int_{2\pi}^{0}\sin\dot{\phi}t\,\cos(\dot{\phi}t-\delta)\,d\phi \qquad (3.3\text{-}11)$$

The average value of T_2 is equal to zero.

Equation (3.3-11) leads to an expression for the torque produced by the damper on the spacecraft in the positive $\hat{1}$ direction and has the magnitude given as follows

$$\tilde{T}_1 = \frac{I_d\,\dot{\psi}^2\sin^2\theta\,\sin\pi/8}{\sqrt[4]{2}\;2} \qquad (3.3\text{-}12)$$

Equation (3.3-12) leads to the conclusion that the system is stable. It states that for the spacecraft which has motion defined by equations (3.3-5a) and (3.3-5b), where $\dot{\psi} > 0$, and $\dot{\phi} < 0$, the direction of the torque produced by the damper is in the positive $\hat{1}$. Total system momentum must be preserved; therefore, the angle θ must decrease as momentum is added in the positive $\hat{1}$ direction. This is illustrated in Figure 3.3-1(d).

3.3.3.1 Nutation-Damping Time Constant

Figure 3.3-1(d) may be utilized to directly compute the time for the decay of the nutation angle, θ. From the figure, equation (3.3-12) may be written as

$$I_f\omega_f + I_1\omega_1 = H\cos\theta \qquad (3.3\text{-}13)$$

The total derivative is taken and gives

$$I_f\,d\omega_f + I_1\,d\omega_1 = -H\sin\theta\,\cos\theta\,d\theta \qquad (3.3\text{-}14)$$

The left-hand side of equation (3.3-14) represents the change-in-momentum along the positive $\hat{1}$ axis required to produce a decrease in the angle θ (because equation (3.3-12) expresses the average torque in the $\hat{1}$ direction). It is possible to equate the additional angular momentum contributed by the damper action to the left-hand side of equation (3.3-14). Thus,

$$\tilde{T}_1\,dt = -H\sin\theta\,\cos\theta\,d\theta \qquad (3.3\text{-}15)$$

Equation (3.3-15) may be integrated to obtain the expression for θ as a function of time. Small angle approximation is used and assumes $\cos\theta \approx 1$ and $\sin\theta \approx \theta$. The results are as follows

$$\theta = \theta_o e^{-t/\tau_d}$$

where

$$\tau_d = -\frac{2\sqrt[4]{2}\, I_3}{\sin \pi/8\; I_d\; \dot{\psi}} \qquad (3.3\text{-}16)$$

and

$$\frac{2\sqrt[4]{2}}{\sin \pi/8} = \frac{1}{0.16}$$

This compares closely with the more precise value of $1/0.189$ previously given[1]. The difference between the two factors resulted from using the approximate value for developed damper angular momentum (i.e., equation (3.3-6)) rather than the exact relationship[3].

3.3.3.2 Design of Nutation Damper

A parametric study was developed[1] which showed how to obtain the minimum weight of the flywheel and the damper required to produce a specified time constant. This approach was used at the start of the design study; however, the present recommendation does not utilize this optimum because the weight of the damper has been reduced without changing the weight of the momentum system. This approach is recommended because experience has indicated that a reduction in momentum would make the spacecraft more sensitive to external disturbances. Until a safe minimum is established, the present value of 140 in.-lb.-sec. produced by a flywheel with a moment of inertia of 9 in.-lb.-sec.^{2} and rotating at 150 rpm is recommended. The present recommended value is about 70% of the momentum on TIROS. The damper performance is based on the following presently-assumed values

H = 140 in.-lb.-sec.

I_3 = 90,720 lb.-in.^{2}

I_2 = 123,487

$I_{23} = \sqrt{I_2 I_3}$ = 106,000

$$\dot{\psi} = \frac{H}{I_{23}} = \frac{140 \times 386}{106{,}000} = 0.51 \text{ rad./sec.}$$

$$I_d = 1890 \text{ lb.-in.}^2$$

$$\tau_d = \frac{1}{0.189} \frac{106{,}000}{1890 \times 0.51} = 582 \text{ seconds} = 9.7 \text{ minutes}$$

The fluid will be selected to have a kinematic viscosity given by

$$v = \frac{r_o^2 \dot{\psi}}{4} = \frac{(0.45)^2}{4} \times 0.51 = 2.58 \times 10^{-2} \text{ inches}^2/\text{sec.}$$

Although the combination damper and flywheel are not optimum, the damping time of 9.7 minutes is certainly a satisfactory value. This is accomplished with 3.5 lbs. of damping fluid.

The kinematic viscosity of 2.58×10^2 in.^{2}/sec. corresponds to a light motor oil and is easily obtained by mixing available silicone oils.

3.4 SENSOR SUBSYSTEM

3.4.1 General

The attitude-sensing subsystem must perform the following functions:

- Provide attitude-measurement and spin-rate data for use at the ground station in the computation of roll/yaw attitude error and momentum variation;
- Provide real-time horizon-crossing data as an input to the pitch-axis-stabilization control subsystem.

The general sensing concept is identical to one that is now being utilized for the planned TIROS "I" and TOS programs. The sensors will be similar to those used on the TIROS, Relay, and other RCA programs.

The basic sensor complex for the sensor subsystem consists of 3 passive, IR earth-horizon sensors and the associated electronics. The field of view of all 3 sensors is fixed in a spatial orientation as indicated in Figure 3.4-1(a). The two skew sensors form a "VEE" configuration. Horizon crossing data from these sensors are transmitted to the ground and utilized, with additional ephemeris data to compute the required error commands for the roll/yaw axis and momentum axis magnetic control systems. The sensor perpendicular to the spin axis provides inputs to the pitch-axis control systems.

The general operation of the horizon-sensing subsystem is illustrated in Figure 3.4-1(b) for the "VEE" sensors. As the sensors rotate about the flywheel spin-axis, the beams from the two skewed infra-red (IR) sensors trace out two conical sections in space and the intersections of the sensor paths with the earth are shown in the illustration. Because of the difference in temperature between outer space and earth, the signal level from each sensor changes as its beam crosses the horizon. When the horizon-to-horizon pulses from the two sensors are of equal duration, the spin-axis is parallel to the surface of the earth. If a yaw error (rotation about the local vertical) exists at this time, the effect will be evidenced as a roll error of the same magnitude but 90^{o} later in the orbit because of the inertial rigidity of the momentum-axis. If a roll error exists (as shown in the illustration), it is detectable as an inequality in the horizon-to-horizon pulse duration from the two sensors. It will be shown that the spacecraft roll and yaw errors vary sinusoidally with the orbit anomaly angle; the spatial orientation of the sensor spin-axis can then be determined from horizon-sensor data, or roll-angle data, derived over some discrete part of the orbit. The amount of data required depends on the resolution and accuracy of each data point (generally, 30 to 40 degrees of anomaly angle is adequate).

During the initial orientation of the vehicle, only one sensor of the "VEE" pair will intercept the earth. The data from this sensor are sufficient for the determination of roll-angle and, consequently, vehicle spatial-orientation. In

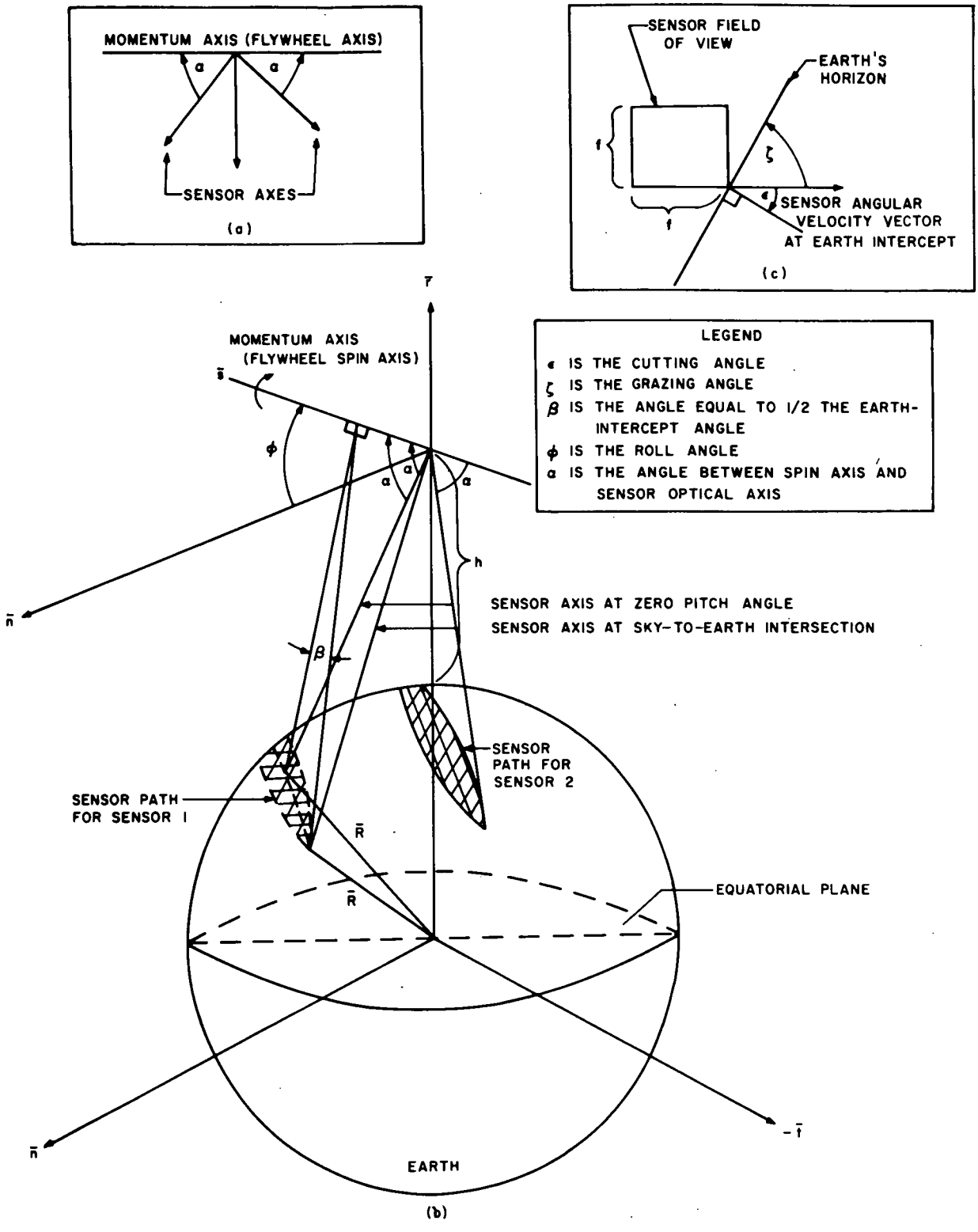

Figure 3.4-1. Sketch Depicting the Definition of Sensor Geometry in a Spatial Orientation

this case, the absolute time-duration of the horizon-to-horizon pulse must be used. (It will be shown that this pulse-width duration is proportional to roll angle.) However, the accuracy of the attitude determination is degraded if only one sensor is used.

The discontinuities of the radial sensor are used as inputs to the pitch-axis-stabilization control subsystem. It will be shown that the output of the perpendicular sensor is considerably less sensitive to vehicle attitude variations (both roll-angle and precession effects) than the skewed sensors. This makes the output from the perpendicular sensor more satisfactory as a pitch-axis subsystem input because it is desirable to minimize variations in the attitude-control system operation. These variations are, however, the important parameters in the attitude-determination mode; therefore, an attempt is made to maximize their effect on the output of the skewed sensors.

In the present attitude-control system, only the sky-to-earth discontinuity of the vertical sensor is used as an input to the pitch-axis stabilization control subsystem. Knowledge of the local vertical is obtained through the geometric offset of the sensor and is based on nominal orbital parameters. This technique leads to the minimum uncertainty error because the utilization of the sky-to-earth discontinuity produces a negligible error due to clouds (this is discussed in Section 3.4.3.3.5).

The physical operation of the sensor is as follows. The incoming radiation from the earth and/or sky is focused on a thermistor detector by a germanium-lens system. The thermistor detector consists of two resistive elements in a bridge circuit. Only one element is exposed to the incoming radiation and this element rises in temperature with incoming radiation. The temperature rise changes the resistance of the elements and results in a voltage change at the junction of the bridge when a bias current flows through both elements. The voltage at this junction is composed of: a d-c component due to the mismatch in the resistance of the elements; and an a-c component due to the changes in radiation from the earth/sky transition. The resistance of each element is approximately $1.40\ 10^5$ ohms (at $25^{\circ}C$); the change in resistance of the element which produces a signal just equal to system noise is less than 0.15 ohms. The match between elements cannot be held to better than 1% of the total resistance. Thus, the d-c signal can be 10^4 times greater than the a-c component of interest. Furthermore, the match between the two elements shifts with ambient temperature as the resistance of both elements change. Thus, it is mandatory that the d-c component be removed by capacitively coupling the thermistor bridge to the amplifier. This is equivalent to a differentiation of the amplifier input signal. Being a thermal device, the detector has a time constant which is slow compared to that of a photo-conductive device; therefore, it must be included for transient analysis. Furthermore, the analysis must include a consideration of a high-frequency roll-off in the amplifier in order to limit the noise bandwidth of the device.

3.4.2 Mathematical Description of Sensor Subsystem

3.4.2.1 Sensor Model

Based on the previous discussion, a sensor model of the following form is determined.[3]

$$\frac{E_O}{N} = \frac{K F_r \tau_D S}{(\tau_D S + 1)(\tau_B S + 1)(\tau_A S + 1)} \qquad (3.4\text{-}1)$$

where

E_O = voltage output of the amplifier (volts)

N = the input radiance (watts/cm^2 ster.)

τ_D = differentiation time constant (seconds)

τ_B = thermistor time constant (seconds)

τ_A = amplifier time constant (seconds)

S = complex Laplacean operator

F_r = the fraction of the detector area which is actually subjected to irradiation

K = the optical-bolometer-amplifier combined gain constant in volts/watt/cm^2 steradian given by

$$\left(\frac{T \pi K_D \sqrt{a}\ \tau_B K_A K_B}{4 f_{no}^2}\right)$$

T = optical transmission ratio (a function of input spectral content)

a = detector area (cm^2)

f_{no} = optical f-number

K_D = detector constant (ohm cm/watt sec)

K_A = amplifier gain (volts/volt)

K_B = bolometer bridge constant (proportional to bias voltage) (volts/ohm)

3.4.2.2 Horizon-Crossing Model

To develop a complete model of the subsystem it is necessary to obtain a description of the infrared earth source and a description of the complex dynamical

interaction between the source and the sensor. It is beyond the scope of this study to investigate, in detail, the infrared radiation characteristics and second order geometric characteristics of the earth. This is an area about which a great deal has been written and about which a great deal more must be learned. A full description requires a probabilistic model that takes into account such factors as spectral variability, planetary-surface irregularities, planetary regular nonsphericity, atmospheric refraction, surface temperature variability, and atmospheric-temperature variability including cloud distributions.

For this study, the discontinuity between sky and earth was considered as a step-change in black-body temperature (or radiance) and the temperature variability taken over a range of values from 200°K to 300°K. Input radiance change, $N(t)$, is related to these black body temperatures through the Stefan-Boltzman equation leading to the expression for $N(t)$ of the form

$$N(t) = \frac{\sigma_{SB}}{\pi} (T_e^4 - T_s^4)\, u(t - t_o) = N\, u(t - t_o) \qquad (3.4\text{-}2)$$

where

$N = \frac{\sigma_{SB}}{\pi} (T_e^4 - T_s^4)$

σ_{SB} = Stefan-Boltzman constant (watt/cm^2 deg^4)

T_e = earth temperature (degrees)

T_s = sky temperature (degrees)

$u(t-t_o)$ = unit step function

t_o = horizon crossing time

This description can be considered a first-order approximation to the actual conditions. More exact models are being studied at RCA and will be utilized in future work. Using the step-change approximation, an expression for the dynamical crossing of the discontinuity can be developed. It is assumed that the field of view of the sensor is square (this is close to the actual case on present TIROS horizon sensors). Making use of Figure 3.4-1(c), it has been shown[3] that

$$F_r(t) = \frac{\omega^2 \sin^2 \alpha \tan \zeta}{2 f^2} \sum_{n=0}^{3} (-1)^n (t - t_n)\, u(t - t_n) \qquad (3.4\text{-}3)$$

where

$t_o = 0$

$t_1 = \dfrac{f}{\omega \sin \alpha \tan \zeta}$

$t_2 = t_1 + t_3$

$t_3 = \dfrac{f}{\omega \sin \alpha}$

ω = spin rate of the flywheel

ζ = grazing angle

α = angle between the flywheel spin-axis and the sensor field of view

f = sensor field of view

For $\zeta = 90^{o}$, equation (3.4-3) becomes

$$F_r'(t) = \frac{\omega \sin \alpha}{f} \sum_{n=0}^{1} (-1)^n (t - t_n') u(t - t_n') \qquad (3.4\text{-}4)$$

where

$t_o' = 0$

$t_1' = t_2$

3.4.2.3 Complete Dynamic Model

Utilizing Laplacean transform techniques, equations (3.4-1), (3.4-2), (3.4-3), and (3.4-4) can be combined to achieve a complete normalized dynamic model of the sensor which has the form[3]

$$\frac{E_O(t)}{(K_s)_r / \sin^2 \alpha \tan \zeta} = \frac{K_v \sin^2 \alpha \tan \zeta}{(K_v)_r} \left\{ \sum_{n=0}^{3} (-1)^n u(t - t_o) \left(t - t_n - \frac{1}{(\tau_A - \tau_B)(\tau_B - \tau_D)(\tau_D - \tau_A)} \left[\tau_A^3 (\tau_B - \tau_D) \right. \right. \right.$$

$$\left. \left. \left. \times \left(e^{-\left(\frac{t - t_n}{\tau_A}\right)} - 1 \right) + \tau_B^3 (\tau_D - \tau_A) \left(e^{-\left(\frac{t - t_n}{\tau_B}\right)} - 1 \right) + \tau_D^3 (\tau_A - \tau_B) \left(e^{-\left(\frac{t - t_n}{\tau_D}\right)} - 1 \right) \right] \right) \right\}; \zeta \neq 90 \quad (3.4\text{-}5)$$

and

$$\frac{E_O'(t)}{(K_s)_r / \sin^2 \alpha \tan \zeta} = \frac{K_v}{(K_v)_r} \frac{f \sin \alpha}{\omega} \left\{ \frac{\sum_{n=0}^{1} (-1)^{n'} u(t - t_n')}{(\tau_A - \tau_B)(\tau_B - \tau_D)(\tau_D - \tau_A)} \left[\tau_A^2 (\tau_B - \tau_D) \right. \right.$$

$$\left. \left. \times \left(e^{-\left(\frac{t - t_n'}{\tau_A}\right)} - 1 \right) + \tau_B^2 (\tau_D - \tau_A) \left(e^{-\left(\frac{t - t_n'}{\tau_B}\right)} - 1 \right) + \tau_D^2 (\tau_A - \tau_B) \left(e^{-\left(\frac{t - t_n'}{\tau_D}\right)} - 1 \right) \right] \right\}; \zeta = 90 \quad (3.4\text{-}6)$$

where

$$K_s = \frac{K_B K_A K_D T \pi}{4 f_{no}} \sin^2 \alpha \tan \zeta \frac{\omega^2}{f^2} \sqrt{a} \tau_B \tau_D N$$

$$K_v = \frac{\omega^2}{f^2} \sqrt{a} \tau_B \tau_D N$$

$( )_r$ = *Reference Condition*

These equations have been programmed on a digital computer for ease of utilization in the parameter studies.

3.4.2.4 Definition of Attitude Angles

The satellite roll-angle, ϕ, (as measured by the sensor) is the angle between the spin axis of the flywheel (vehicle pitch-axis) and a local horizontal plane which is tangent to the earth at the subpoint of the spacecraft (the $\bar{n}$, $\bar{t}$, plane). A symmetric definition is adopted for the yaw angle, ψ (i.e., the angle between the spin axis and the $\bar{n}$, $\bar{r}$, plane). In mathematical terms:

$$\phi = \sin^{-1} S_r \tag{3.4-7a}$$

$$\psi = \sin^{-1} S_t \tag{3.4-7b}$$

Figures 2.1-1 and 2.1-3 of Section 2.1 of this report can be used to convert these angles to angles referenced to orbit coordinates $\hat{\ell}$, $\hat{b}$, $\hat{n}$,, ; the angles become

$$\phi = \sin^{-1} \left[(S_\ell^2 + S_b^2)^{1/2} \sin(\theta - \lambda) \right] \tag{3.4-8a}$$

$$\psi = \sin^{-1} \left[-(S_\ell^2 + S_b^2)^{1/2} \cos(\theta - \lambda) \right] \tag{3.4-8b}$$

The maximum roll-angle occurs when

$$\lambda = \sin^{-1} \frac{S_b}{(S_\ell^2 + S_b^2)^{1/2}} \tag{3.4-9}$$

and is equal to

$$\phi_{max} = (S_\ell^2 + S_b^2)^{1/2} \tag{3.4-10}$$

These equations make it possible to determine the complete orbital attitude history (assuming no significant disturbance) from the knowledge of the roll-angle or yaw-angle over a portion of the orbit (theoretically, only two points are required) and the anomaly angles at which the data are taken.

3.4.2.5 Attitude-Angle Determination

It has been shown[2] that the relationship between the earth-intercept angle, 2β, (see Figure 3.4-1) earth-time, t_e, and roll-angle, ϕ, is given by

$$2\beta = 2\cos^{-1}\left[\frac{\tan\phi}{\tan\alpha} + \frac{\left(1 - \frac{R^2}{(R+h)^2}\right)^{1/2}}{\sin\alpha\cos\phi}\right] = \omega t_e \qquad (3.4\text{-}11)$$

and the sensitivity is given by

$$\frac{d\beta}{d\phi} = \frac{-\sec\phi\cos\alpha\,(1 + \sin\phi\cos L/\cos\alpha)}{[\sin^2 L - \cos^2\alpha - \sin\phi(\sin\phi + 2\cos L\cos\alpha)]^{1/2}} \qquad (3.4\text{-}12)$$

where $L = \sin^{-1}(R/R+h)$

These equations hold for any single sensor. Equation (3.4-11) is used for attitude determination with large roll-angles of the spacecraft.

When 2 skewed-sensors with equal α -angles are used simultaneously for roll-angles about zero, it has been shown that

$$\phi = \frac{\omega}{4}\,\frac{1}{\left.\frac{d\beta}{d\phi}\right|_{\phi=0}}\,\Delta t_e \;;\; \Delta t_e = (t_e)_1 - (t_e)_2 \qquad (3.4\text{-}13)$$

where

$(\quad)_1$ and $(\quad)_2$ are the first and second sensors respectively.

3.4.2.6 Grazing-Angle Determination

It has been shown[2] that the angle at which the sensor intercepts the earth (the grazing angle ζ) is given by

$$\zeta = 90 - \cos^{-1}\left[\frac{R+h}{R}\sin\beta\cos\phi\right] \qquad (3.4\text{-}14)$$

This angle is shown in Figure 3.4-1.

3.4.3 Discussion and Parametric Results

3.4.3.1 Geometrical Parameters

3.4.3.1.1 Zero Roll-Angle Conditions

For the zero roll-angle analysis, Figure 3.4-2 shows the parameters $d\beta/d\phi$, ζ, and β as a function of the α angle. For the vertical sensor $(\alpha = 0)$, the term $d\beta/d\phi$ is equal to zero and the angle ζ is equal to 90^{o}. This result is excellent because it is desirable to have the vertical sensor insensitive to roll-angle variations thus producing no roll-coupling in the pitch-axis. Furthermore, it is shown in this report that the value of 90^{o} for the grazing angle, ζ, produces the best sensor output slope, another desirable result.

3.4.3.1.2 Non-Zero Roll-Angle Conditions

Figure 3.4-3 shows the angles ζ and β as a function of the roll-angle, ϕ, for several values of the angle α. The sensor goes completely off the earth at approximately 10^{o} of roll-angle for the minimum value of the α-angle shown ($\alpha = 40^{o}$). The curves shown in Figure 3.4-3 are all for a single sensor. The other sensor in the skewed-set will have identical curves related to its geometry; however, these will be a mirror image of those shown but rotated about the zero roll-angle line. The analysis indicates, therefore, that only one of the two skewed sensors is available for attitude data above a value of ϕ equal to 10^{o}.

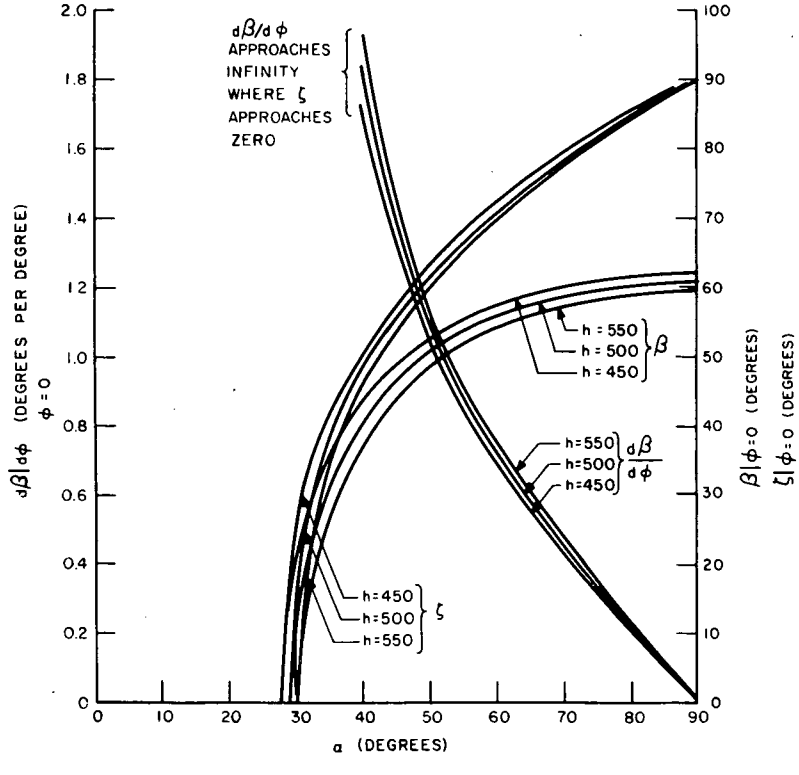

Figure 3.4-2. Sensitivity of the Half-Earth and Grazing Angles as a Function of the α-Angle with a Zero Roll-Angle

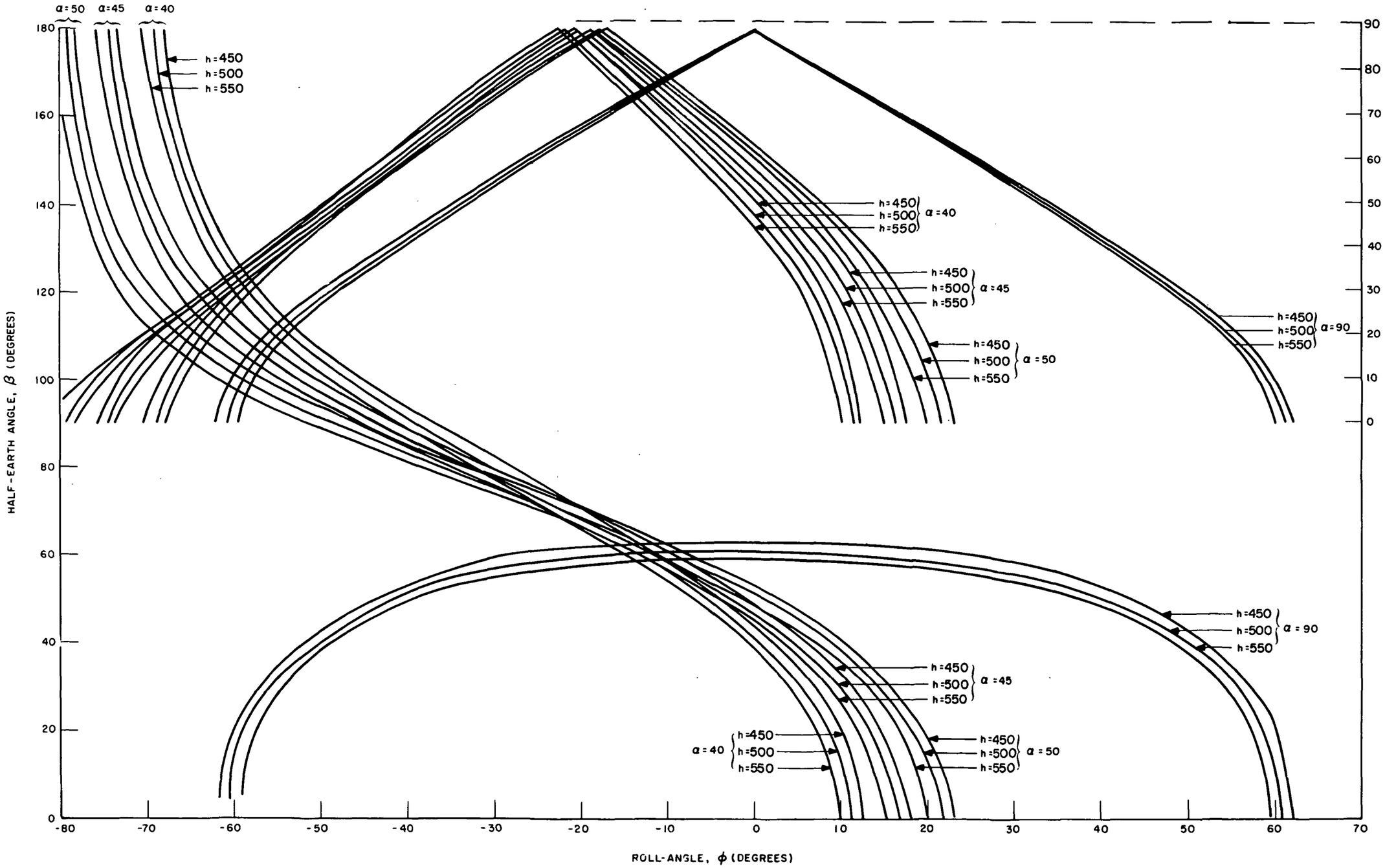

Figure 3.4-3. Sensitivity of the Half-Earth and Grazing Angles to the Roll Angle

The system normally operates in a null-mode using both sensors; therefore, the minimum range considered satisfactory to obtain information from both sensors is $\pm 10^{o}$. (The actual usable range is less than $\pm 10^{o}$ because of grazing-angle dropoff as the sensor approaches the edge of the earth.) For these reasons, the value of the α-angle will not be chosen as less than 40^{o}.

3.4.3.2 Accuracy Considerations

3.4.3.2.1 Nominal Pulse Outputs

Nominal sensor outputs were obtained using equations (3.4-5) and (3.4-6) and these outputs are shown in Figure 3.4-4. These outputs were obtained using the following values of parameters:

- $\tau_A = 0.1 \times 10^{-3}$
- $\tau_B = 2.5 \times 10^{-3}$
- $\tau_D = 1.0 \times 10^{-3}$
- $\omega = 15.71$
- $f = 0.0227$
- $\phi = 0$
- $T_e = 260^{o}K$

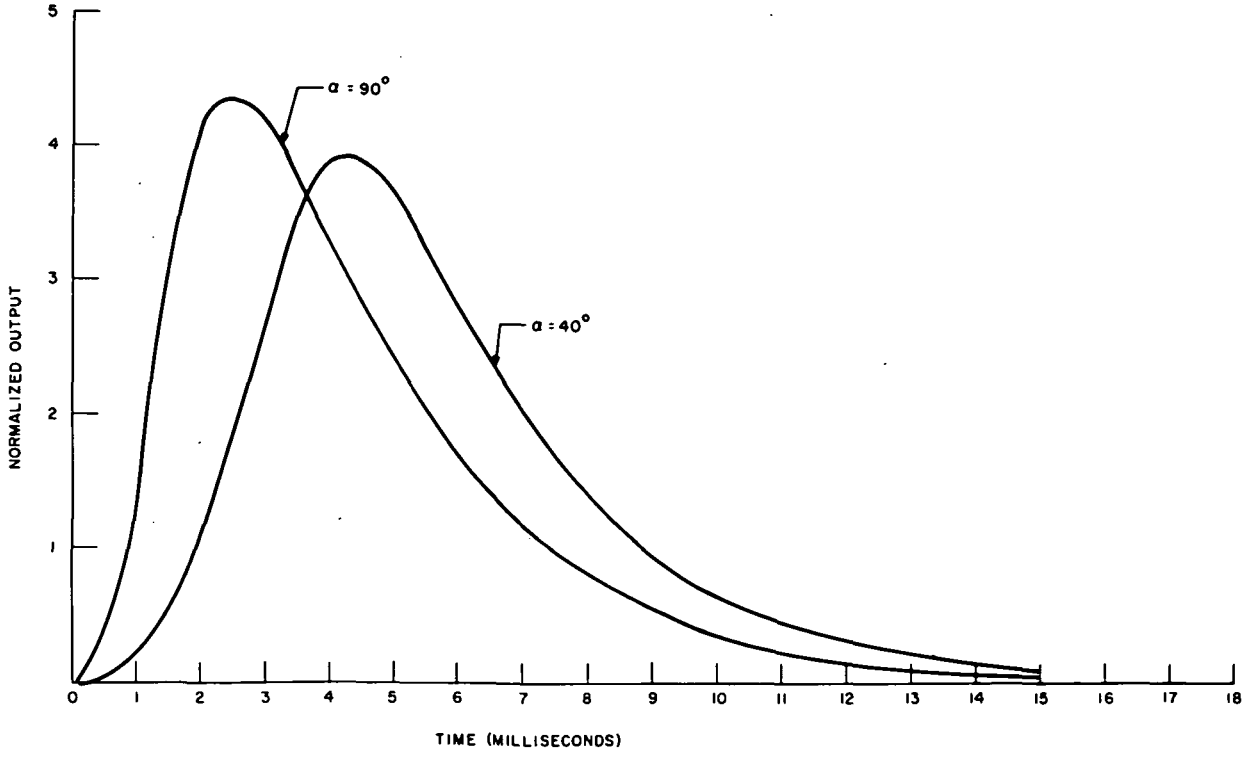

Figure 3.4-4. Nominal Sensor Outputs Obtained Using Equations (3.4-5) and (3.4-6)

Figure 3.4-4 clearly illustrates the degradation of output pulse for low values of grazing angle (α angle).

3.4.3.2.2 Approximate-Error Equations

Figure 3.4-5 was utilized[3] to determine the worst-case radiance and noise variations occurring between two sensors. The total time spread for these variations is given by

$$\Delta T = \frac{V_T}{M_L}\left(1 - \frac{P_L}{P_u}\right) + \frac{V_n}{M_L}\left(1 + \frac{P_L}{P_u}\right) \qquad (3.4\text{-}15)$$

For a variation in earth temperature from 300°K to 200°K, the radiance variation is 5-to-1, or $P_L/P_u = 0.2$. If a nominal threshold-to-peak noise of 5-to-1 is chosen then equation (3.4-14) becomes

$$\Delta T = 5.2\ \frac{V_n}{M_L} \qquad (3.4\text{-}16)$$

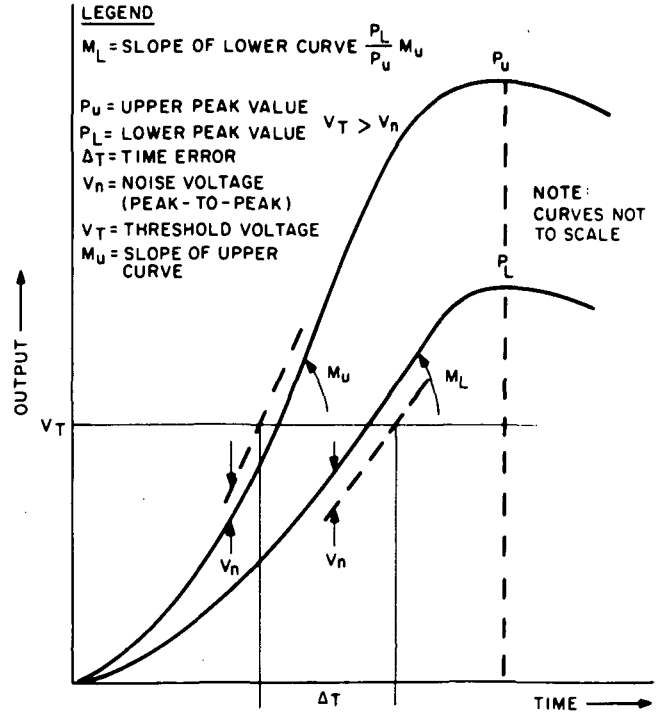

Figure 3.4-5. Error-Computation Curves Used to Determine Total Time-Spread for Worst-Case Radiance and Noise Variatons

Equation (3.4-16) is particularly valid for the attitude determination at the ground station because the spin-rate of the flywheel should be constant for any ground pass. For the case of the pitch-axis sensor, the threshold must be set to minimize the effects of the flywheel spin tolerances.

Measurements with similar sensors for TIROS and Relay indicate that the peak-value to peak-to-peak noise for a 300°K earth output is 100 to 1 (5.0 volts to 50 millivolts). This value will be used in the following discussion.

3.4.3.2.3 Worst-Case Error Analysis

The worst-case pulse outputs expected from the skewed sensor are shown in Figure 3.4-6. For this case, the noise value is set at 1/100 of the peak noise obtained at a spin rate (ω) equal to 225 rpm, an earth temperature (T_e) equal to 300°K, and a threshold set at five times the noise value.

Analyzing the 75-rpm case first, a worst-case is obtained by subtracting the noise from the low pulse value and adding it to the high pulse value. This yields a value of ΔT equal to 2.2 milliseconds. If the same operation is used for the 225-rpm case, a value of ΔT equal to 0.75 milliseconds is obtained. It has been proven that equation (3.4-14) produces results which are within 20% of these values.

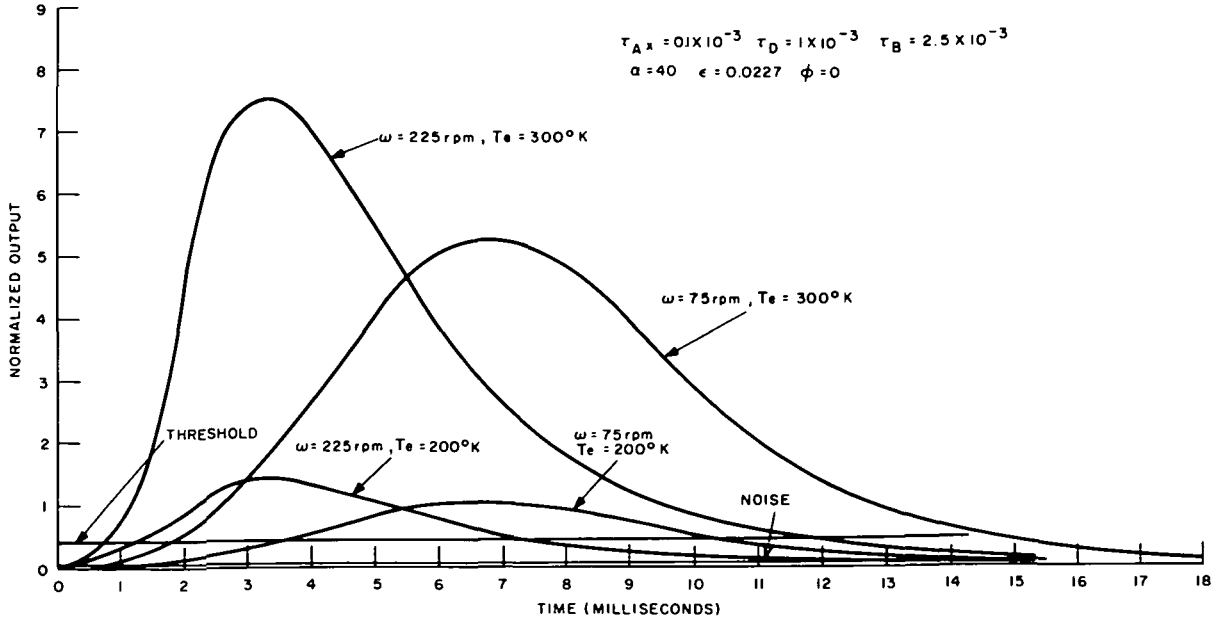

Figure 3.4-6. Worst-Case Output-Pulse Analysis for Dual (Vee) Sensor Configuration

It has been found, however, that the worst-case system error can be a factor of 2 above the values given in the previous paragraph, and occurs when the dual-sensor method is used to determine the value of Δt_e. This worst-case for the system occurs when the first sensor experiences a "cold" earth temperature at the sky-to-earth transition and a "hot" earth at the earth-to-sky transition, and the second sensor experiences the reciprocal situation. For any single crossing, the error is given as $1/2\ \Delta T$. Using equation (3.4-13), and values of ω equal to 75-rpm, $d\beta/d\phi$ equal to 1.72, and ΔT equal to 4.4 milliseconds, the worst-case error in the determination of the angle ϕ_ϵ is 0.29^o. For the case where ω is equal to 225-rpm and ΔT is equal to 1.5 milliseconds, the value of the worst-case angle ϕ_ϵ is 0.30^o.

The equivalent worst-case pulses for the pitch-axis sensor are shown in Figure 3.4-7, and include the ±10% of nominal speed (150 rpm) conditions. There is no experimental knowledge of the spin-speed to be used in setting the 90^o-sensor threshold; therefore, it is necessary to compare the 75-rpm/200°K case to the 225-rpm/300°K case. For this condition, ΔT is equal to 1.1 milliseconds when the noise value is correctly added and subtracted. Then, if the trigger is set at an equivalent lead-time value of 0.75 milliseconds, there will be a maximum error of ±0.55 milliseconds, or 0.75^o at a speed of 225 rpm. For the ±10% speed variation case, the maximum error is ±0.35 milliseconds or 0.35^o at a speed of 165 rpm. Therefore, the pitch-axis sensor error should be less than 0.5^o in the operational mode because the conditions of 225 and 75 rpm occur only during initial acquisition.

3.4.3.3 Parameter Optimization

3.4.3.3.1 Considerations

There are four factors which affect system accuracy and over which design control can be exercised. These factors are:

- System Noise;
- Pulse Rise-Time (slope);
- Threshold Value;
- Input Radiance Variation (P_L/P_u).

The input radiance variation can be controlled by spectral filtering techniques and is discussed in detail in Section 3.4.3.3.4 of this report.

The threshold value, based on good design practice, is set to be 5 times the value of the peak-to-peak noise; the pulse rise-time and the threshold value are shown in equation (3.1-14) as V_n/M_L. This value of V_n/M_L should be minimized providing that the threshold-to-noise ratio is adequate. Effort has been expended, on another RCA program, towards mathematically achieving this minimization. The problem is one of choosing values of τ_D and τ_A over the full variation of system parameters

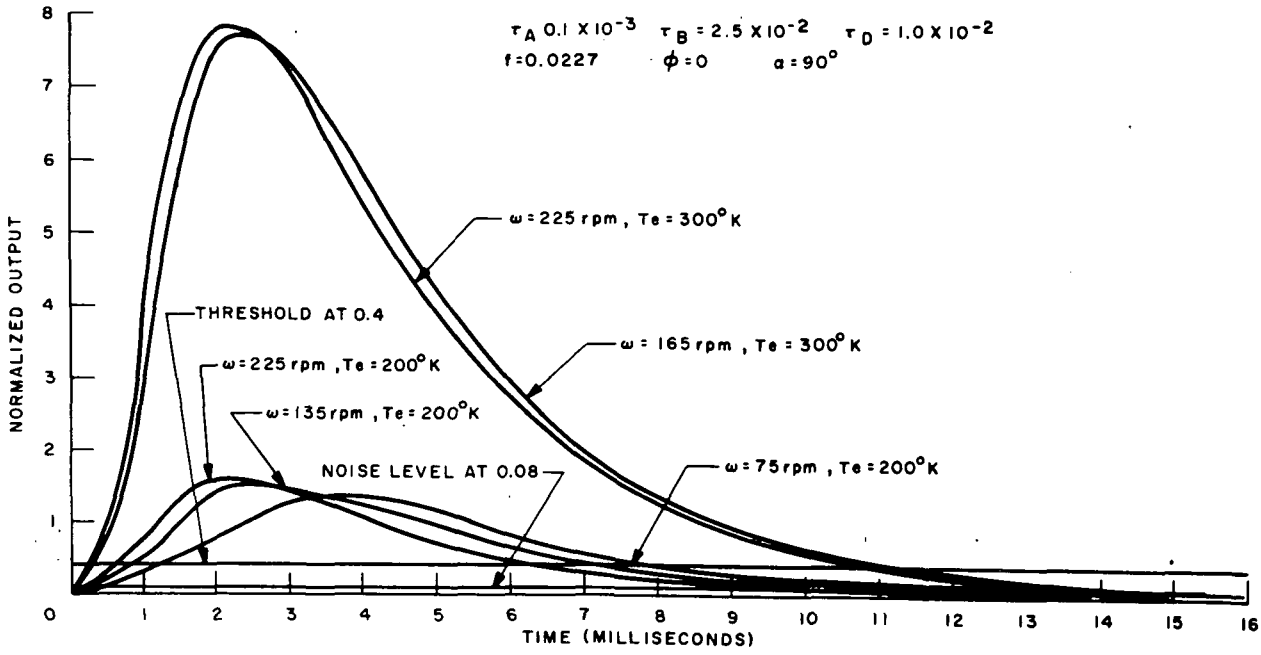

Figure 3.4-7. Worst-Case Output-Pulses for Vertical Sensor Configuration

so as to minimize the value of V_n/M_L and, consequently, ΔT. It is necessary to consider both the Johnson and current (1/f) noise as sensor inputs in order to perform the minimization. A solution to this problem has not yet been attained. The optimization equations are very unwieldy and require the assistance of a considerable digital-computer program for solution. Mathematical noise models have been derived, but to date no measurements are available on the noise-frequency spectrum of the sensor. Furthermore, the total noise-output measurements which are available are not sufficient for this optimization.

3.4.3.3.2 Choice of Electronic Time Constants

The continuation of a complete optimization study is beyond the scope of this program. Consequently, the system bandpass characteristics were chosen based on previous experience from the TIROS and Relay programs and a limited analysis. The variation in peak-value and time-to-peak as a function of the parameter τ_D are shown in Figure 3.4-8. To maximize the slope, it is desirable to maximize the peak-value divided by the time-to-peak; this ratio is also plotted in Figure 3.4-8. No well-defined maximum exists. Based on this fact, the value of τ_D was chosen as 1.0 millisecond or on the low-end of the ratio-curve peak. This was done to increase the electronics low-frequency break as far as possible to minimize the effect of "1/f" noise.

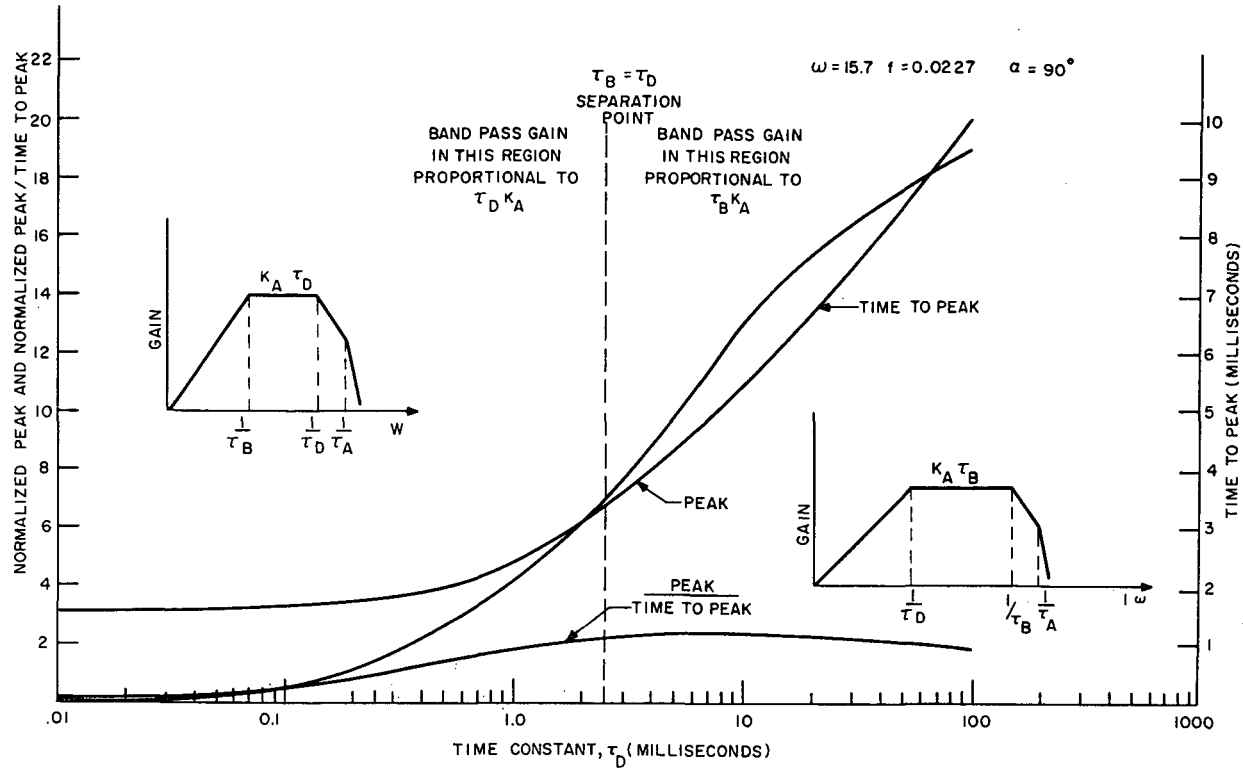

Figure 3.4-8. Variation of the Peak Value and Time-to-Peak as a Function of the Time Constant

The value of τ_A was chosen to achieve as narrow a bandwidth as possible without affecting the system slope. A value of τ_A equal to 0.1 millisecond satisfied this requirement.

3.4.3.3.3 Choice of α-Angle

The time-to-peak and peak-value variations as a function of α-angle are shown in Figure 3.4-9. It is desirable to maximize both the slope of the curve and the value of $d\beta/d\phi$. The slope is equivalent to the peak value dividied by the time-to-peak; therefore, the product of this ratio with $d\beta/d\phi$ should be maximized as a function of α. This can be seen more clearly from equation (3.4-13) if $2 \times \Delta T$ from equation (3.4-15) is substituted for the term Δt_e as follows.

$$\phi_\epsilon = \frac{\omega_s}{4} \frac{1}{\left.\frac{d\beta}{d\phi}\right|_{\phi=0}} 2\left[\frac{V_T}{M_L}\left(1 - \frac{P_L}{P_u}\right) + \frac{V_n}{M_L}\left(1 + \frac{P_L}{P_u}\right)\right] \qquad (3.4\text{-}17)$$

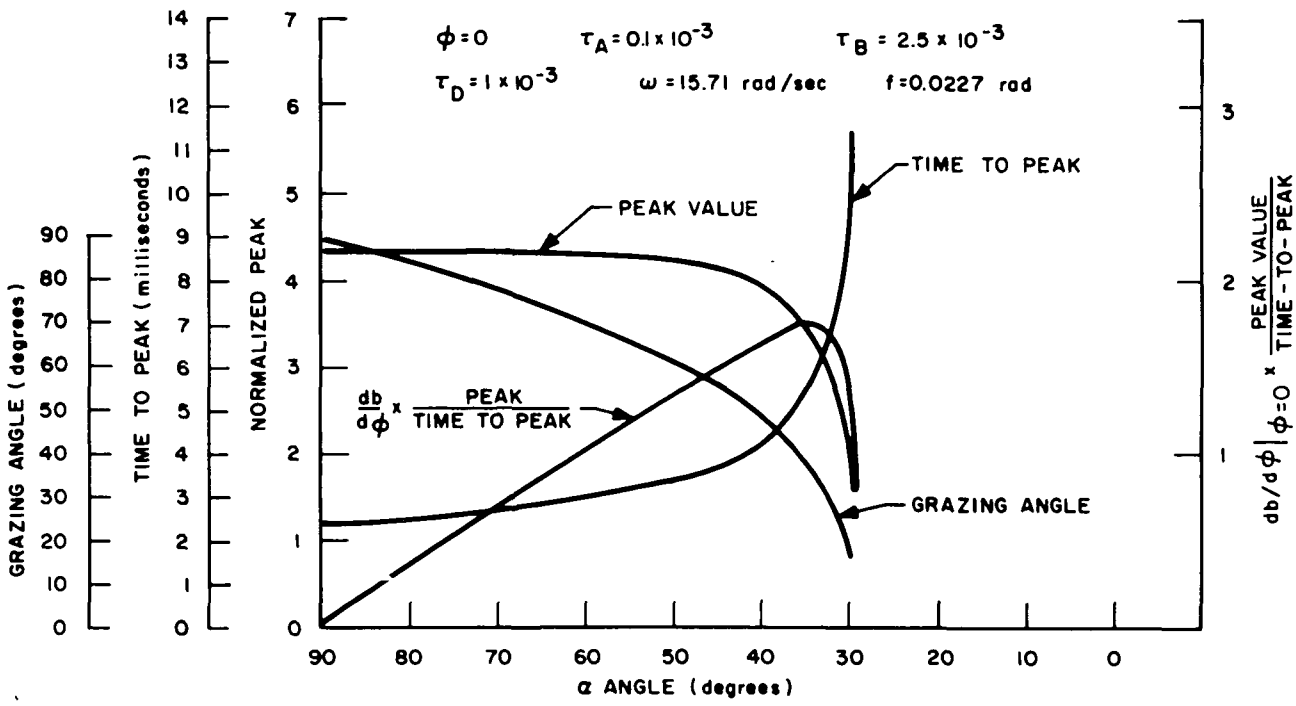

Figure 3.4-9. Variation of the Peak Value and Time-to-Peak as a Function of the α-Angle

Note that if the term $d\beta/d\phi \times M_L$ is maximized, then the value of ϕ_ϵ is minimized; the product $d\beta/d\phi \times M_L$ is also plotted in Figure 3.4-9 and peaks at $\alpha = 35^o$. However, this value of α leaves only 5^o of dynamic range on the sensor and is considered inadequate for that reason. Consequently a value of α equal to 40^o was selected for the sensor subsystem.

3.4.3.3.4 Spectral Region Considerations

Equation (3.4-14) indicates that an improvement in system accuracy can be achieved if the radiance variation observed by the sensor is reduced. This variation can be diminished by the utilization of proper spectral filtering. However, this will usually also reduce the slope M_L and must be compensated for elsewhere to achieve a net system improvement. Thus, there is no advantage in increasing amplifier gain because the noise voltage is then increased proportionately with the slope and no net improvement results. It has been shown[3] that the sensor parameter, f_{no}, is presently close to a physical minimum; for this condition, an increase in the value M_L can only be achieved by an increase in optical area while the ratio of detector area to the square of the focal length and the term f_{no} are both kept constant. In addition, an increase is required in the sensor detector bias voltage.

The attitude-sensor system presently used on TIROS has a spectral response of 2.0 - 20 microns with an anti-reflection coating peaked at 12 - 15 microns. For the 2 - 20 micron spectral region, the variation in equivalent black body temperature that the sensor will see is from 200°K to 300°K (or a radiance change of 5 to 1). Utilizing document NASA TN D-1850, "The Infrared Horizon of the Planet Earth", dated September, 1963, the variations for other spectral regions can be computed as can be the minimum radiance level. For a 12.5 - 18.5 micron sensor and using present filtering techniques, it has been computed that the radiance level variation is 2.3 to 1 and that the minimum radiance is equivalent to a black body temperature of 182°K. The radiance at 182°K is 0.69 of the radiance at 200°K so that, without any optical changes, the slope for 12.5 - 18.5 microns will also be 0.69 of the slope for 2 - 24 microns.

Utilizing these values, the worst-case errors for the sensor system were computed previously[3] for various optical area. These values are compared to the equivalent errors for the 2 - 20 micron sensor in Table 3.4-1.

TABLE 3.4-1. COMPARISON OF TYPE OF SENSOR AND SENSOR ERRORS FOR ROLL/YAW AND PITCH

Type of Sensor	Roll/Yaw Error	Pitch Error	
		75-225 rpm	135-165 rpm
2 - 20 micron (TIROS)	0.30°	0.75°	0.35°
12.5 - 18.5 micron (TIROS optics)	0.36°	1.03°	0.43°
12.5 - 18.5 micron sensor with 20% increase in optics	0.30°	0.89°	0.36°
12.5 - 18.5 micron sensor with 37% increase in optics	0.26°	0.75°	0.31°

3.4.3.3.5 Cloud Considerations and Horizon-Splitting Techniques

It was shown[3] that, for clouds at the sky-to-earth interface occurring before the earth is intercepted, the error for the 2 - 20 micron sensor is 0.1° at a spin-rate of 225 rpm with a cloud altitude of 10 nautical miles and a cloud temperature of 260°. This error is decreased for lower spin-rates, altitudes, and temperatures. In the case of the 12.5 - 18.5 micron sensor, the error is approximately 0.03°. For the calculations presented in this report, these errors may be considered as 3σ values.

However, for clouds occurring at the earth-to-sky interface, errors of a much larger magnitude are possible. No quantitative results have been obtained during this study program on the error magnitudes because compensation can be made for these errors during the ground station determination of attitude, and because the earth-to-sky pulse is not presently used as an input to the pitch-axis-stabilization control subsystem. Figures 3.4-10 and 3.4-11 illustrate the mechanism by which the error is introduced. Figure 3.4-10 shows, qualitatively, the resultant pulse outputs for clouds at the sky-to-earth intercept for a cloud radiance of 1/2 the earth radiance; it also illustrates that there is negligible error introduced at the expected threshold level.

Figure 3.4-11 illustrates the conditions for the earth-to-sky interface with the same conditions as shown in Figure 3.4-10. However, in the case of the earth-to-sky interface, the error introduced can be extremely large if thresholding must be utilized in the spacecraft (e.g., the pitch-axis sensor). This fact is the fundamental reason why geometric offset, rather than horizon-splitting, is recommended for determining the local vertical. Experience gained on both TIROS and Relay indicate earth-to-sky transition errors of as much as five times the sky-to-earth transition errors when simple thresholding is used. The complete pulse shape can be evaluated at the ground station and compensation can be made for the cloud effects. Therefore, there should be a maximum of a 50% increase in the roll/yaw error under worst-case cloud conditions.

The choice of whether to use geometric offset, rather than horizon-splitting, does involve making certain tradeoffs. This occurs because there are several significant advantages to using horizon-splitting in spite of the undesirable earth-to-sky interface problem. The advantages are as follows:

- Removes the need for a pitch-axis sensor;
- Removes pitch-axis cyclic offsets due to orbit ellipticity;
- Removes the sun-viewing problem because the "Vee" type sensors do not view the sun;
- May simplify the pitch-axis error sensor providing it is used in conjunction with a sensor amplifier which passes the full earth-signal with only a slight decrease in signal strength.

Additional study work must be done to determine the feasibility of a sensor amplifier with the characteristics described because this function must be performed at spin rates of 150-rpm. If the design of this amplifier is not feasible, then the complexity of the additional horizon-splitting circuitry required negates the use of this technique.

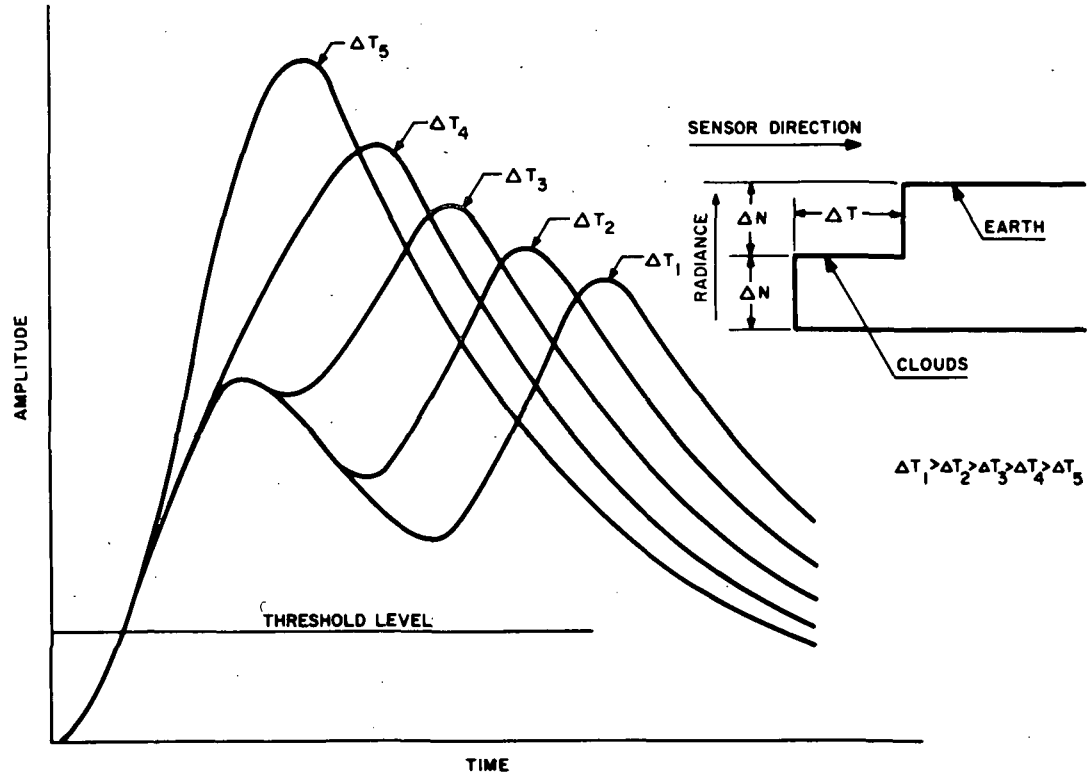

Figure 3.4-10. Effects of Clouds on Sensor Error for the Sky-to-Earth Interface

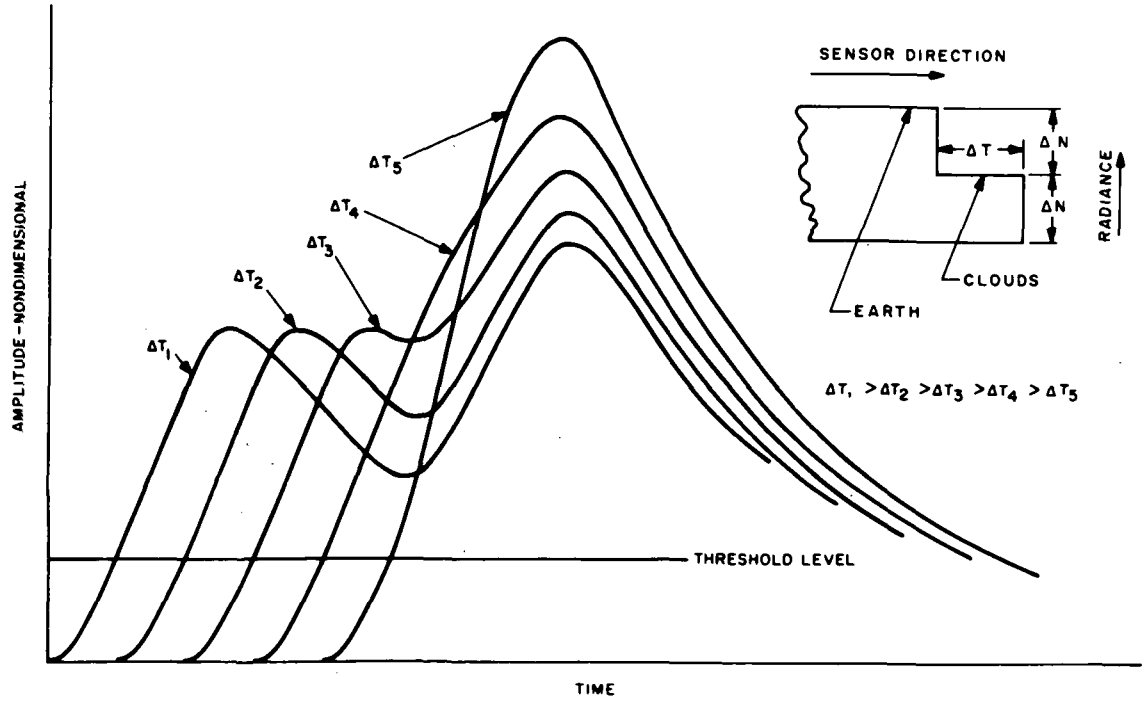

Figure 3.4-11. Effects of Clouds on Sensor Error for the Earth-to-Sky Interface

3.4.3.3.6 Sun Considerations

The orbital relationship which exists between the pitch-axis sensor and the sun is such that the sensor will view the sun once per flywheel revolution; this condition will, therefore, introduce a false pulse. To assure that this false pulse will not enter the pitch-axis-stabilization control subsystem, the attitude sensors will be used to gate the pitch-axis control input channel (these sensors do not view the sun). This technique can be accomplished by rotating the "Vee" (attitude) sensors around the flywheel axis. An analysis of Figure 3.4-2 indicates that this rotation must be 19.6° nominally; a subsequent analysis of Figures 3.4-6 and 3.4-7 indicate that under worst-case conditions (Vee sensors view a "cold" earth and the pitch-axis sensor views a "hot" earth), an additional 1.35° must be added to the nominal rotation. The additional rotation will assure that the Vee sensors reach the threshold level first. If the outputs of the Vee sensors are then put through an "OR" circuit, for a 1°-roll error the Vee sensors will lead the pitch-axis sensor by an additional 1.9°. Therefore, with the Vee sensors offset by a total of 21°, the gate will open 3.3° before the pitch-axis sensor (in the worst-case) and this latter value is the maximum error which can be produced by the sun. This maximum error will exist when the sun is at the edge of the gate and occurs at the time in orbit when the sun is 3.3° from the sky-to-earth crossing of the sensor. The method of implementing this technique is discussed in detail in Section 3.1 of this report.

3.5 COMMAND AND CONTROL SUBSYSTEM

3.5.1 General

The function of the spacecraft command and control subsystem is to receive, store, decode, and execute the following functions initiated by the ground command station.

- Program the operation of the attitude and momentum torque coils.
- Adjust the magnetic-bias coil current.
- Select and fire rockets.
- Select redundant sets of attitude sensors for both roll/yaw and pitch information sensing and select redundant pitch-axis control electronics.
- Actuate and terminate transmission of satellite attitude-sensor data.
- Turn on pitch-axis-stabilization flywheel position-control subsystem.

A block diagram of the Command and Control Subsystem, including the Telemetry Subsystem, is shown in Figure 3.5-1.

Real-time command of the spacecraft control subsystems will be accomplished through the Nimbus "C" clock subsystem. The programs for attitude and momentum torquing are stored in a control programmer similar to that used on TIROS. The command, "T_O", required to initiate a torquing program is stored in the Nimbus "C" clock. The period of a torque cycle will be determined before launch and "wired" into the programmer "period counter." This method of programming the torquing cycles and period reduces the required amount of command-data transmission to the satellite. Only one of the 16 command-storage locations in the Nimbus "C" clock is used. If the Nimbus "C" clock was used to store a maximum torquing program, the full storage capacity of the clock, 16 addresses, would be utilized; thus, stored-command capability would be saturated during the first orbit of torquing, thereby preventing any other satellite command from being executed.

The magnetic-bias switch used to select high QOMAC torque-coil current and bias-coil current is advanced, on a step-by-step basis, with real-time command from the ground through the Nimbus "C" clock. The switch position information is monitored by the telemetry subsystem of the spacecraft.

The rocket-switch position is selected in the same manner as the bias-switch. Firing of the rocket is done with another real-time command from the Nimbus "C" clock.

Sensing of the transmission of attitude-data from the spacecraft is controlled by the attitude-data telemetry-control unit which receives ground commands directly

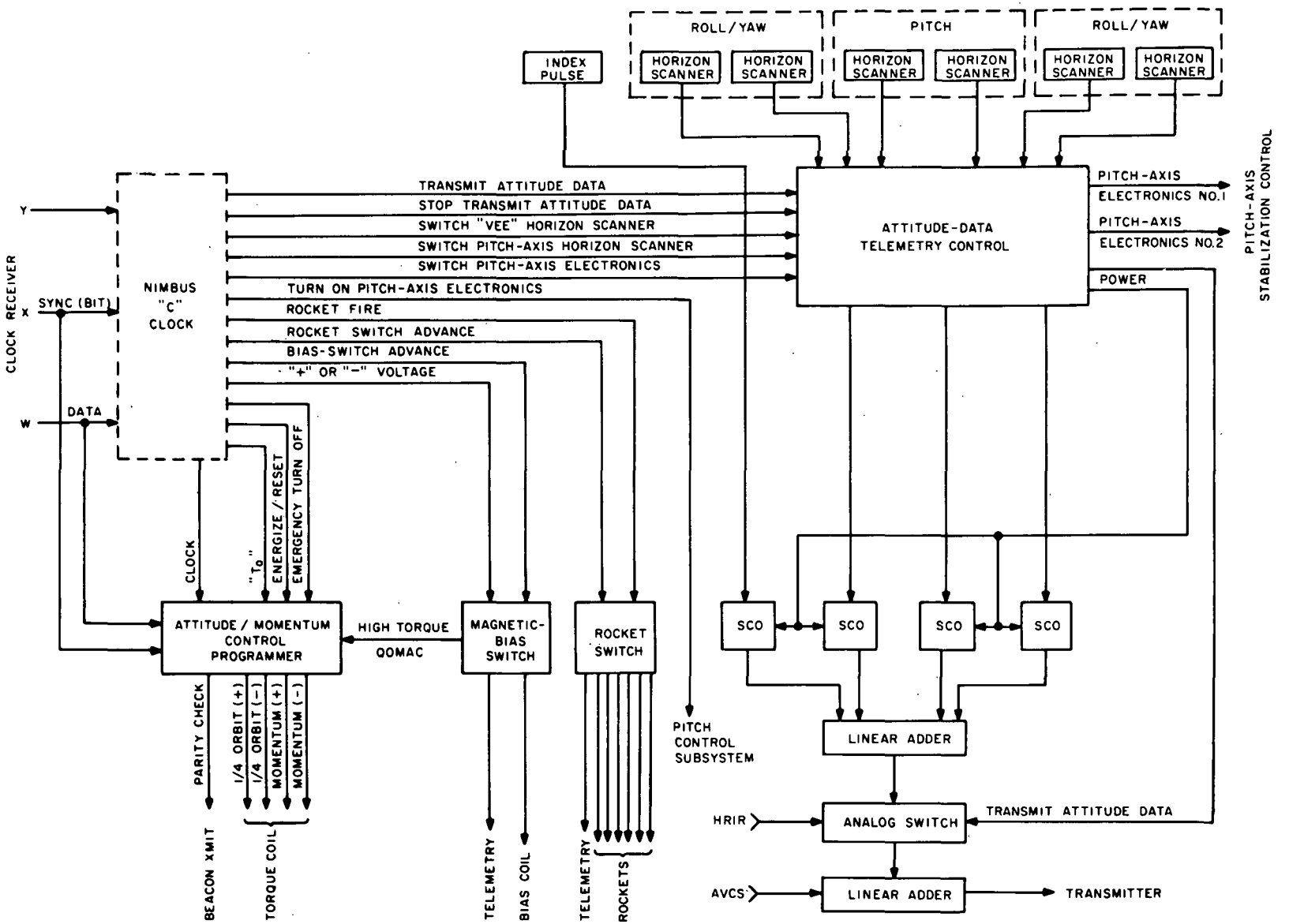

Figure 3.5-1. Block Diagram of the Command and Control Subsystem, Including the Telemetry Subsystem

from the Nimbus "C" clock. The attitude-data telemetry control routes attitude data to the transmitter, switches redundant sets of sensors and pitch-axis electronics, and activates the attitude-data subcarrier oscillators.

The pitch-axis-stabilization position-control electronics are activated by a real-time command transmitted through the "C" clock from the ground station.

3.5.2 Clock Compatability

The clock subsystem of the spacecraft will not be required to supply clock pulses to shift the program data transmitted by the ground station into the attitude/momentum control programmer. The program data are transmitted in the same manner as the Nimbus-clock data and will be accompanied by a channel of sync which will shift the program data into the attitude/momentum control programmer.

The clock pulses required, by the attitude/momentum control programmer, to count the magnetic/torque periods can be derived by dividing the 1-pps output of the Nimbus "C" clock. A 500-cps tone will be used to indicate parity check over the beacon transmitter and is also available as an output from the Nimbus "C" clock.

3.5.3 Clock Interface

The 1-pps output of the Nimbus "C" clock is available for the clocking requirements of the spacecraft. A 0.5-pps clock pulse can be derived by taking 1/2 of the present 1-pps output and applying it to the period counter of the attitude/momentum control programmer to count out the 1/4-orbit period. Frequency dividing the 1-pps to 0.25 pps will provide the clock rate required to count a 1/2-orbit period with the period counter.

3.5.4 Analysis of the Attitude-Control Programmer

The attitude-control programmer must store a QOMAC attitude program and execute it at a later time. To do this, the programmer must perform the following operations sequentially.

(1) Receive and store serial program-data transmitted to the spacecraft from the ground station.

(2) Decode the QOMAC command and energize the coil in the indicated (+) or (-) direction.

(3) Count the period of the 1/4 orbit.

(4) Reverse the coil current after every period.

(5) Tally the total cycles.

(6) Turn off the coil programmer when the total command cycles of torque are completed.

3.5.5 Analysis of the Momentum-Control Programmer

Both the momentum-control and the attitude-control programs are stored in the spacecraft for execution at a later point in the orbit. The programming of the momentum-control coil can be accomplished in the same manner as used for the QOMAC coil; however, the one exception is that the coil current is reversed every 1/2 orbit, rather than every 1/4 orbit. Thus, the torque-period counted is twice as long as the 1/4-orbit period.

The momentum-control programmer is required to perform the same sequence of operations to the momentum-control coil as the attitude-control programmer performs to the QOMAC coil, but on a 1/2-orbit basis.

3.5.6 Programmer Design

The same requirements exist for placing either an attitude-control program into the QOMAC-torque coil or a momentum-control program into the momentum-control coil; the only exception is the period between reversals of the current applied to the respective torque-coils. A control programmer which is designed to operate either torque coil is only slightly more complex than a programmer capable of operating only one of the coils. A diagrammatic representation of the sequence of operation for both coils is shown in Figure 3.6-2. The programmer block diagram is shown in Figure 3.6-3.

The attitude/momentum control programmer, in conjunction with the Nimbus "C" clock, will execute a stored torquing program for either the QOMAC or the momentum coil. To store either program, a command from the ground station enters the Nimbus "C" clock; this command, called "T_O", signifies the time that the execution of a torque program is to commence. The next ground station command is also entered into the Nimbus "C" clock; this is a real-time command that is executed within seconds after it is accepted by the clock. Execution of this command energizes and resets the attitude/momentum control programmer and opens the data-interface gate to the clock receiver. With the interface gate open, the next command transmitted to the spacecraft is for the attitude/momentum control programmer.

The program word contains 6 bits, 1 bit for even-parity, 2 bits for coil-code and torque-sign, and 3 bits for the number of cycles of torque. A channel of sync is transmitted with the data and shifts the data word into the programmer. The format

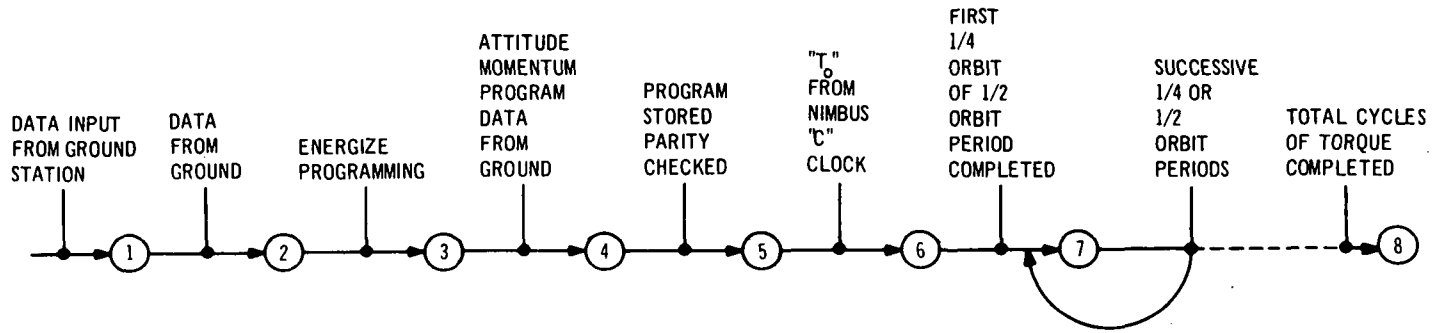

LEGEND:

(1) STORE "T_0" (START ATTITUDE/MOMENTUM PROGRAM) IN NIMBUS "C" CLOCK

(2) STORE ATTITUDE/MOMENTUM PROGRAMMER ENERGIZE COMMAND IN NIMBUS "C" CLOCK

(3) DATA INTERFACE TO RECEIVER OPEN

(4) STORE ATTITUDE/MOMENTUM PROGRAM IN PROGRAMMER

(5) CLOSE PROGRAMMER INTERFACE TO RECEIVER AND SEND PARITY CONFIRMATION TO GROUND STATION

(6) APPLY 0.5-PPS OR 0.25-PPS COUNT PULSES TO THE PERIOD COUNTER. QOMAC OR MOMENTUM-CONTROL COIL ENERGIZED IN (+) OR (−) DIRECTION AS INDICATED BY THE MODE-PORTION OF THE ATTITUDE/MOMENTUM PROGRAMMER

(7) REVERSE DIRECTION OF CURRENT IN THE QOMAC OR MOMENTUM-CONTROL COIL. ADVANCE CYCLES OF TORQUE COUNTER

(8) TURN OFF CURRENT AND ATTITUDE/MOMENTUM CONTROL PROGRAMMER

Figure 3.5-2. Diagrammatic Representation of the Sequence of an Attitude/Momentum Program

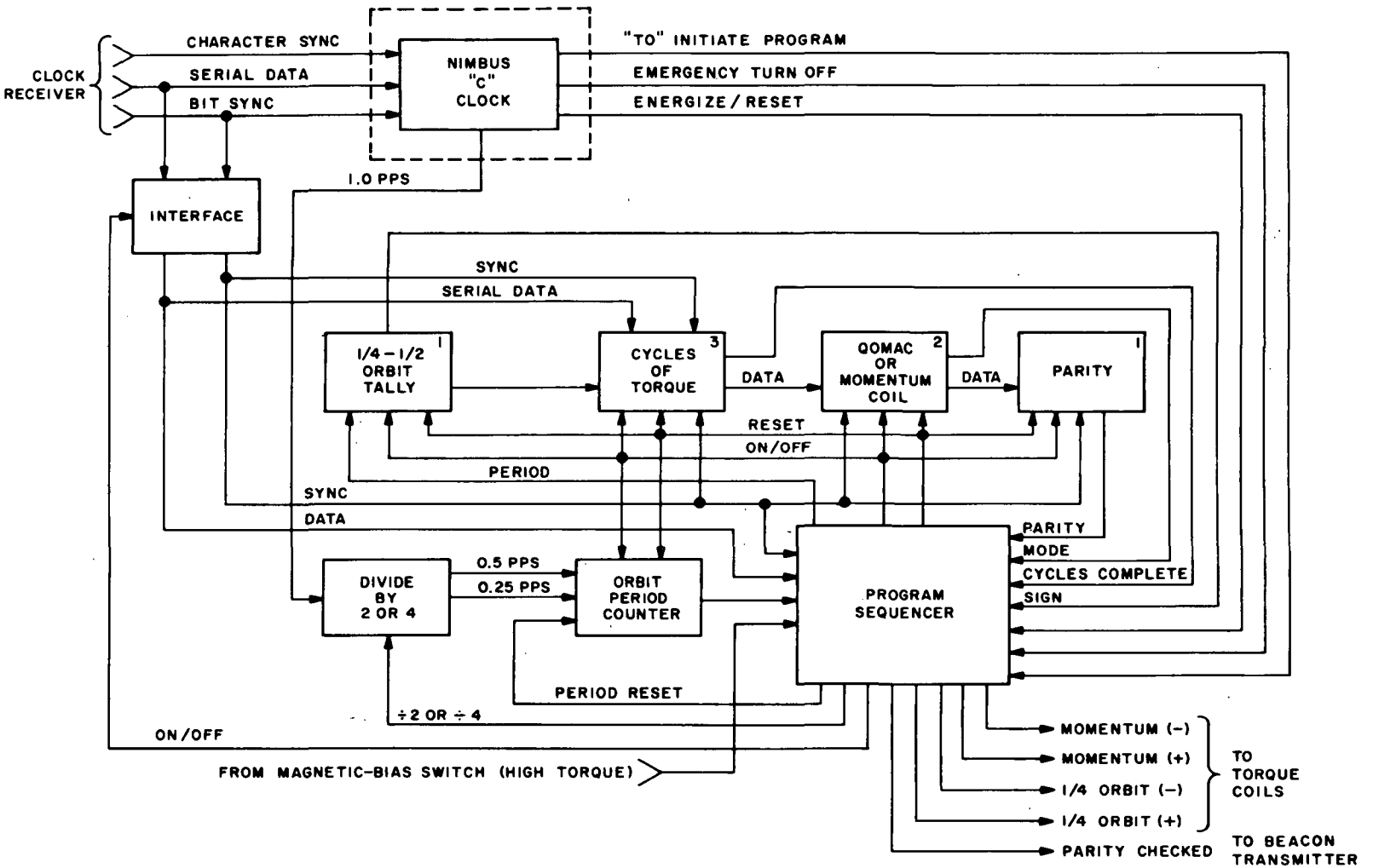

Figure 3.5-3. Block Diagram of the Programmer

of the data is such that the Nimbus "C" clock will not accept it as data meant for clock action. The initial turn-on and reset of the programmer sets the programmer register to 10,000. When the incoming data is shifted into the register the "1" is shifted through it; the "1" spilling out of the parity position is detected by the program sequencer. The sequencer then closes the interface gate and checks parity: if parity checks correctly, a tone is applied to the beacon transmitter for detection at the ground station; if the tone is not received by the ground station, the program loading cycle is repeated.

The nominal period of a 1/4 orbit is determined before launch and the "2's" compliment is "wired" into the orbit-period counter. To count the period of a 1/4 orbit, the 1-pps output of the Nimbus "C" clock is divided to 0.5 pps and applied to the period counter; this is accomplished by the program sequencer when the coding in the register indicates the QOMAC-coil. The 1-pps output is divided to 0.25-pps to count the period counter through a 1/2-orbit period when the momentum-program code is in the programmer register.

An attitude, or momentum, torque program is initiated when the real-time of the Nimbus "C" clock matches the time portion of the "T_O" command contained in the storage portion of the clock. The "T_O" command is applied to the program sequencer which, in turn, energizes the torque coil indicated by the coding in the programmer register; the coil-current flows in the direction also indicated by the register coding. The proper count pulses (0.5-pps or 0.25-pps) are gated into the period counter. When the period counter overflows, it is reset to the "wired" position, the 1/4-1/2 orbit tally reverses the coil current through the sequencer, and the count of the next period begins; the tally flip-flop multivibrator advances the torque-cycle count every second period. The torque-cycles counter portion of the register contains the "2's" compliment of the torque cycles to be completed; therefore, when it overflows the program is complete. The sequencer then turns off the power to all but the standby portion of the attitude/momentum control programmer. The programmer can also be turned off by an "Emergency Turn-Off' command sent through the Nimbus "C" clock. A high-torque current control is provided from the magnetic-bias switch and through the sequencer to the torque coils. The attitude-control system will normally operate in the low-torque mode if this additional command is not received.

The programmer uses 2-watts of power during operation, and 1/4-watt of power in the standby mode.

3.5.7 Auxiliary Functions

3.5.7.1 Magnetic-Bias Stepping Switch

The magnetic-bias attitude control will be accomplished in a manner similar to that used on the TIROS satellite. The magnitude of the current in the magnetic-bias

coil will be adjusted by means of a multi-position stepping switch. The switch will be used to select one of twenty-four resistors to be connected in series with the coil circuit thus limiting the coil current. The stepping switch will also be used to command the "high-torque" current for the QOMAC operation because magnetic-bias is not required during this mode of operation. The stepping switch will have a telemetry output which will indicate the position of the switch by the level of the voltage appearing on the telemetry point. Figure 3.5-4 shows the switch control schematic diagram of the magnetic-bias switch control.

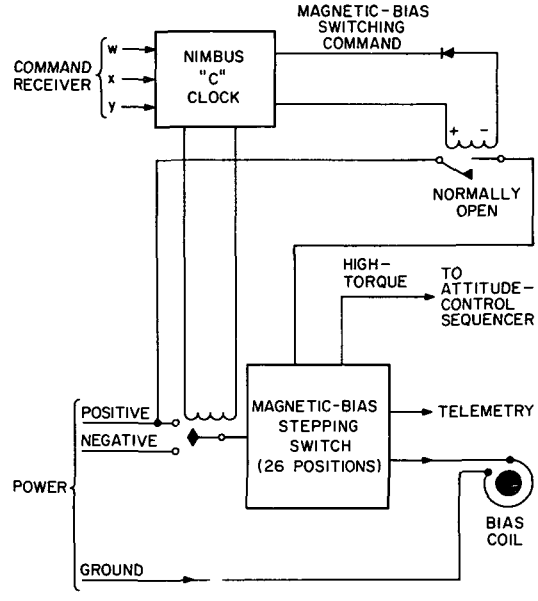

Figure 3.5-4. Schematic Diagram of the Magnetic-Bias Stepping-Switch Control Circuit

The command capability of the existing Nimbus "C" clock subsystem will be used to advance the position of the magnetic-bias stepping switch. The Nimbus clock will be used on a real-time basis. Telemetry received from the spacecraft by the ground station will be used to determine the position of the stepping switch; from these telemetry data, the number of steps is determined and the switch must be advanced either to apply the proper series resistor to the bias coil or to apply high-torque for the QOMAC coil. A real-time command program is then compiled to be sent to the clock subsystem. A real-time command word will consist of a portion containing the device code (stepping switch) and the remainder containing the time of command execution. The time portion will be real-time and cannot occur sooner than three seconds from the spacecraft real time. This command will be repeated once for each step advance of the stepping switch. Time must be provided to complete the execution of the previous command and the time portion of the command word will be updated for each step.

The Nimbus "C" clock will also be used for switching between positive and negative power excitation to the bias stepping-switch so that either positive or negative voltage can be used to excite the magnetic-bias coil.

3.5.7.2 Rocket Switch

Several momentum adjustment rockets are built into the spacecraft structure. These rockets require a ground command to activate them and are activated in a sequence selected by the ground station. The device used to select and activate the proper rocket is designated as the "rocket switch" and the design is very similar to that of the magnetic-bias switch. The rocket to be fired is selected by a stepping switch activated by ground command through the Nimbus "C" clock.

An additional ground command, again through the Nimbus "C" clock activates the rocket related to the selected switch position. The position of the rocket switch is determined by the ground station in the same manner as used for the magnetic-bias switch.

3.5.7.3 Attitude-Data Telemetry

To compile an attitude/momentum program, the ground station must receive from the satellite the data generated by the "Vee" horizon sensors, the pitch-axis horizon sensor, and the satellite index pulse. Because these attitude data are required only periodically by the ground station, they will be transmitted in real time and only upon command.

The attitude-data telemetry-control subsystem performs several functions related to satellite attitude data. This control unit receives, from the Nimbus "C" clock, the following commands generated by the ground station:

- Transmit Attitude Data
- Stop Transmitting Attitude Data
- Switch "Vee" Horizon Sensors
- Switch Pitch-Axis Horizon Sensors
- Switch Pitch-Axis Electronics

The command to transmit attitude data causes the control subsystem to energize the four attitude-data SCO's, remove the HRIR-data line from the transmitter input, and apply the additional attitude-SCO outputs to the transmitter input with the AVCS data.

The command to stop transmitting attitude data reverses the action of the command to transmit. The SCO power is removed, and the HRIR-data input is switched back to the transmitter input.

The command to switch "Vee" horizon sensors switches the input of the associated SCO's from a primary set of sensors to a redundant (secondary) set in a commutating fashion. The second command pulse will return the SCO input to the primary sensors.

The command to switch pitch-axis horizon sensors switches the associated SCO input between redundant pitch-axis horizon sensors in the same manner as the "Vee" sensors are switched.

The command to switch pitch-axis electronics provides for switching power from a primary set of pitch-axis electronics to a redundant (secondary) set. This switching also commutates between the redundant electronics each time a switch command is received.

The attitude-data telemetry control is, therefore, the subsystem that controls the time-sharing of part of the "S"-band transmitter bandwidth. This sharing is between attitude data and HRIR data, either one of which is then added to the AVCS-data input to the transmitter. The total subsystem power utilization during operation is 1.0 watt. No power is required in the standby (quiescent) mode.

3.5.7.4 Pitch-Axis-Stabilization Control Turn-On

When the spin axis of the spacecraft is almost normal to the orbital plane, a real-time command is transmitted through the Nimbus "C" clock from the ground station and turns on the flywheel of the pitch-axis-stabilization control subsystem. This command operates in the same manner as the attitude-data telemetry commands.

3.6 TELEMETRY SUBSYSTEM

3.6.1 General

The telemetry requirements for the proposed attitude control system are twofold. The first requirement is for the "on-command" transmission of attitude data from the horizon sensors and the pitch-axis electronics; these data require relatively wideband transmission. The second requirement is for normal "housekeeping" data transmission for diagnostic purposes; these data can be transmitted using the existing spacecraft housekeeping telemetry subsystem.

3.6.2 Attitude-Data Transmission Techniques

3.6.2.1 Requirements and Recommended System

The differentiated, amplified outputs of three bolometers and one magnetically-generated index pulse will be transmitted to the ground to describe spacecraft attitude. A 4-kc data bandwidth will be available for transmission of each pulse; this wide bandwidth will preserve the leading edge of the pulse, the pulse rise-time being from 3 to 6 milliseconds.

A Frequency-Division-Multiplexed (FDM)/FM RF carrier is recommended to transmit attitude-data to the ground station. Each of the four subcarriers in the FDM/FM baseband can be either FM or AM. Both AM/FM and FM/FM are developed multiplexing techniques for which hardware is commercially available.

Attitude data can be transmitted by an independent transmitter used only for attitude-data transmission, or by one of the existing satellite transmitters on a time-shared basis. Transmission of attitude data should occur only once every several orbits; therefore, time-sharing a baseband spectrum with other data sources appears to provide both an economical and satisfactory solution. The recommended telemetry subsystem is shown in block diagram form, in Figure 3.5-1 together with the Command and Control Subsystem.

3.6.2.2 Use of Telemetry Transmitter

The possibility of frequency-multiplexing additional information onto the telemetry transmitter's baseband was analyzed and found not feasible[2]. The multiplexing approach was eliminated because telemetry-data subcarrier sidebands occupied the entire baseband spectrum.

3.6.2.3 Time-Sharing an Existing Transmitter

The present satellite AVCS/HRIR transmitter frequency-modulates a main carrier with eight subcarriers. The baseband spectrum occupied by the HRIR data

could be time-shared with 4 frequency-modulated subcarriers bearing 4-kc of data at center frequencies of 50 kc, 80 kc, 110 kc and 140 kc. A discussion of such an FM/FM baseband with a subcarrier modulation-index of 2 and a main-carrier index of 2 for each of the subcarriers was presented[3]. Operation at main-carrier threshold (12 db) at an AVCS highest baseband frequency of 700 kc with an RF bandwidth of 4.2 resulted in a final signal-to-noise ratio of 53 db for each of the four attitude-data subcarriers. This output signal-to-noise ratio is more than adequate for describing bolometer pulses with maximum 40 db signal-to-noise characteristics and minimum 26 db characteristics.

3.6.2.4 Use of an Independent Attitude-Data Transmitter

An independent FM/FM transmitter operating with the same baseband center frequencies, and main subcarrier modulation indexes just described, for the time-shared case was also analyzed[3]. However, the AVCS portion of the baseband would be omitted with a resulting RF bandwidth of 888 kc. Operation at main carrier threshold (12 db) resulted in an output signal-to-noise ratio of 46.3 db. Here, as with the time-shared technique, thermal noise results in only a small degradation of the input-bolometer-pulse signal-to-noise ratio.

Other modulation techniques have been considered for this approach. One possible technique would be a Double-Sideband Suppressed-Carrier (DSB-SC) AM/FM. Four subcarriers, each modulated with 4-kc of data could be centered at 9-kc, 19-kc, 29-kc, and 39-kc; this baseband could then frequency-modulate a main carrier. The hardware implementation of DSB-SC-AM/FM on the satellite would be straightforward and the subcarrier modulators would be light, reliable, and inexpensive. However, the disadvantage of DSB-SC-AM/FM lies in the detection process where coherent detection is required. The frequency characteristics of the bolometer horizon-pulses are such that coherent detection would be difficult to achieve each time attitude data are desired.

The use of ordinary AM/FM is also possible, and the hardware implementation would also be straightforward. However, in order to realize the same signal-to-noise ratio improvement as in FM/FM, all the processing gain must be incorporated into the main-carrier frequency modulator, thus demanding significantly higher deviation from the AM/FM modulator than from the FM/FM modulator. Envelope detection would be used with AM/FM. With the exception of the superior performance required by the AM/FM modulator, no major obstacles exist to prohibit the use of AM/FM transmission of attitude data.

Time-multiplexing of the 4 attitude-data signals has been studied as a method of decreasing the required bandwidth if an independent transmitter is required. At present, this method is considered undesirable because of the relatively rapid spacecraft motion during initial alignment, and because of the wide range of flywheel speeds and the subsequent wide variation in scanning periods.

As noted previously, attitude-data transmission to the ground should occur only once every several orbits. This infrequent use does not justify the additional RF bandwidth, weight, and cost that an independent attitude-data communications link would require when compared to a time-shared link. However, if time sharing is undesirable for other reasons, the utilization of an independent transmitter is perfectly feasible.

3.6.3 Housekeeping-Data Transmission Techniques

The proposed attitude-control system will generate telemetry voltages compatible with the transmission capabilities of the present spacecraft housekeeping telemetry subsystem. The parameters given in Table 3.6-1 will be available for diagnostic evaluation of any performance anomalies.

TABLE 3.6-1. SUMMARY OF TELEMETRY POINTS AND PARAMETERS

Number of Points	Telemetered Parameter
1	Pulse-Width-Modulated error output
1	Frequency-to-DC Converter output
1	Power Amplifier Output Current (Motor Current)
6	DC-to-DC Converter
1	Rate Bias Voltage
15	Temperature Points
1	Magnetic-Bias Switch
1	Rocket Switch
1	Attitude-Data Telemetry Control Power
1	Pitch-Axis Electronics Command Switch
1	"High-Torque" Current Level
4	Torque Coil Currents: 1/4 orbit + 1/4 orbit - Momentum + Momentum -
2	Horizon Sensor Switches
10	Spare Points

3.7 LAUNCH MODE AND INITIAL ALIGNMENT

3.7.1 General

The spacecraft shown in Figure 7.2-1 will be injected into orbit by a spinning last stage of a launch vehicle similar to the present Delta rockets used to launch the TIROS and other satellites. The constraints on injection are listed in Table 1.2-1. The 800-pound spacecraft referred to in the Work Statement[5] and described in the proposal[6] would be governed by the constraints listed in Table 1.2-1 under the Thor-Agena launch vehicle. The spinning injection mode poses the most severe problem and is described in the following paragraph.

3.7.1.1 Launch-Vehicle Constraints

The important parameters affecting the injection and ultimate alignment of the spacecraft are presented in Table 1.2-1, and are the spin rate of 125 ± 10 rpm, and the tip-off angle of $\pm 8.0^{o}$. Both values are reported to be 3σ values. With these conditions existing at the instant of injection, it is necessary that the spacecraft somehow reduce its spin and change the axis of spin from about the spacecraft yaw-axis to spin about the spacecraft pitch-axis. The order of these two events is not theoretically important; however, for reasons previously discussed[7], a choice is made to despin first and then correct the spin from about the yaw axis to about the pitch axis.

3.7.1.2 Spin-Rate Requirements

The final momentum of the spacecraft under nominal conditions is established (in Section 2.3.2) as 141 in-lb-sec. For the moment-of-inertia values used in this study, this corresponds to a 5.74-rpm spin about the yaw axis, and a 4.0-rpm spin about the pitch axis. The first requirement after injection will be to reduce the initial spin from a 125-rpm nominal to approximately 5.74-rpm (or as close as is practical).

3.7.2 Yo-Yo Despin Mechanism

During the study program, several methods for reducing the initial spin-rate to a more useful value were studied. The results were discussed previously[7]. The mechanism selected for despin is the yo-yo which has been used extensively on several satellite programs. A partial history of RCA experience with the yo-yo despin mechanism was previously supplied[1]; the despin history of TIROS's II to VIII inclusive is given in Figure 3.7-1. The letters "E, F, G, and H" refer to what the actual final spin tolerance would have been if the stretch in the cables had been considered prior to assembly. The use of the history data accumulated on TIROS is justified because the initial launch conditions are essentially the same as those

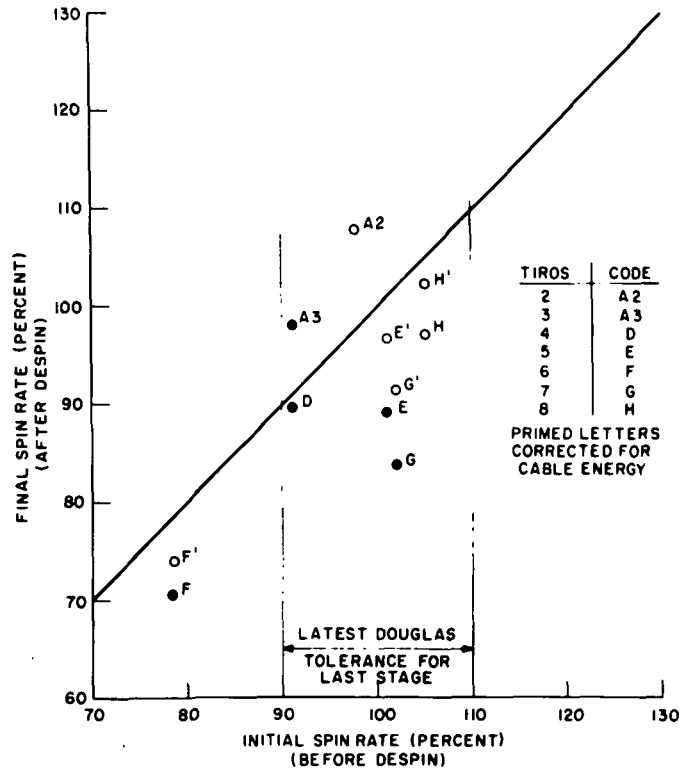

Figure 3.7-1. Despin History of TIROS' II to VIII Inclusive.

of this study program, and includes the effect on tolerance of the initial tip-off angle of $\pm 8.0^{o}$. The major difference between the two applications of yo-yo despin in the despin ratio is

TIROS

$$\frac{\omega_f}{\omega_i} = 0.096 \text{ nominal}$$

500-lb Spacecraft

$$\frac{\omega_f}{\omega_i} = 0.046 \text{ nominal}$$

where the terms ω_f and ω_i are the final and initial spin rates respectively. The final spin tolerance must include the following considerations:

$$\Delta\omega_i = \pm 10 \text{ rpm}$$

$$\text{Tip-off angle} = \pm 8.0^\circ$$

$$\Delta \frac{\omega_f}{\omega_i} = \pm 0.0046$$

The final tolerance results in a final spin ratio of 5.74 ± 1.03 rpm, or an ω_f value equal to 5.74 rpm $\pm$ 18%; this tolerance is well within the capability of the control system as is demonstrated in Section 3.3 of this report. The tolerance value of 18% corresponds to an initial momentum error of 18%, and in the study presented in Section 3.1, the system was able to cope with momentum errors of 44% successfully.

The despin mechanism weight at 4.5 pounds is listed in Table 7.2-1; it was shown[7] that solid-propellant rockets would be less weight, but because of previous RCA experience, the yo-yo despin mechanism is recommended.

3.7.3 Spin-Axis Conversion

The second step for initial alignment is the change of the spin axis from about the spacecraft yaw axis to about the spacecraft spin axis; this step in the alignment sequence can also be considered as the transfer of all momentum in the system from the spacecraft to the flywheel. Because the flywheel is initially at right angles to the initial spin axis, a 90° turn must be accomplished by the spacecraft under a constant direction of the total angular-momentum of the spacecraft. The following two ways can be used to accomplish the required transfer.

- Wait until the damper and the body energy-loss transfer spin from the least moment-of-inertia axis (yaw) to the maximum moment-of-inertia axis (pitch), and then activate the flywheel.
- Initiate the spin of the flywheel immediately after the yo-yo operation.

These two approaches accomplish the same purpose in comparable time; however, the first method is restricted to the requirement that the pitch-axis be the maximum moment-of-inertia, and the second method does not include this requirement. This situation was indirectly established in equation (3.3-5b) of Section 3.3 by showing that the Euler spin-ratio $(\dot{\phi})$ is less than zero, and this is the requirement for stable spin about an axis which is aligned with the angular-momentum axis.

The time-constant for nutation-decay for the small-angle case is developed in Section 3.3 of this report; the decay calculations for the large-angle case were

previously presented[3]. (The latter case applies to the requirement for turning the spacecraft through approximately 90°.) The time to turn the spacecraft through 90° can be developed from using equation (3.3-5b) of Section 3.3 and showing that, for the equivalent of the inertia values presented in Section 7.2, the magnitude of the term $\dot{\phi}$ increases by approximately 22% from the initial to the final orientation. Almost all of this change takes place during the final 80° of the turn. From Figure 3.3-1, the angle θ is defined as the angle between the pitch axis[1] and the total angular-momentum vector. By considering the variation of the angle $\dot{\phi}$ with the angle θ, it is possible, with the aid of equation (3.3-6), to make the average damping-torque presented in equation (3.3-12) a function of the angle θ. This then becomes

$$T = \frac{I_d \dot{\psi} \sin^2 \theta \sin [\delta(\theta)]}{\sqrt[4]{1 + [\tau \dot{\phi}(\theta)]^2}} \tag{3.7-1}$$

where

$$\delta(\theta) = \frac{1}{2} \tan^{-1} \frac{r_o^2 \rho \dot{\phi}(\theta)}{4 \mu}$$

Equation (3.7-1) can be used in equation (3.3-15) to relate the momentum added by the damping action to the total momentum in the system, and yields

$$\frac{I_d \dot{\psi}^2 \sin^2 \theta \sin [\delta(\theta)] \, dt}{2 \sqrt[4]{1 + [\tau \dot{\phi}(\theta)]^2}} \equiv - H \sin \theta \cos \theta \, d\theta \tag{3.7-2}$$

The time to go from θ_1 to θ_2 can be determined from integration of equation (3.7-2) as follows

$$t_{\theta_1 - \theta_2} = \frac{-I_{23}}{I_d \dot{\psi}} \; 2 \int_{\theta_1}^{\theta_2} \frac{\sqrt[4]{1 + [\tau \dot{\phi}(\theta)]^2}}{\sin [\delta(\theta)]} \cot \theta \, d\theta \tag{3.7-3}$$

The integral can easily be evaluated by plotting the first term behind the integral and then performing the integration graphically. However, the value of the first term does not change radically as θ goes from 90 to 0°; therefore, an average value would serve the purpose of the computation. If the first term in back of the

radical is considered a constant over the range, then the time to go from θ_1 to θ_2 is expressed as

$$t = \frac{2\, I_{23}}{I_d\, \dot{\psi}\, K\, \log_e \left(\frac{\sin \theta_1}{\sin \theta_2} \right)} \qquad (3.7\text{-}4)$$

where

$$K = \underset{\theta_1 \rightarrow \theta_2}{\text{average value}} \quad \frac{\sin\, [\delta(\theta)]}{\sqrt[4]{1 + [\tau\, \dot{\phi}\, (\theta)]^2}}$$

So far, the system momentum term, H, has been assumed to be a specified term; however, it is shown in Section 3.7.2 that the term H can vary by $\pm 18\%$ because of the action of the despin yo-yo. Although the value of the term H will not change with the angle θ, the value of $\dot{\phi}$ will vary with H; the variation will not be significant provided that the flywheel is turned on immediately after the yo-yo despin operation. This does not imply that there is anything critical about the turn-on time of the motors; if this time is delayed by 10 seconds or 10 minutes, it merely increases (by approximately the same delay time) the total time required to make the change.

Table 3.7-1 shows the time to turn from θ approximately equal to 90° to θ approximately equal to 10°; the small-angle case time-constant of 9.7 minutes, as computed in Section 3.3, can be used to determine the time required to go from 10° down to 0°. The times presented in the Table are for nominal momentum and $\pm 50\%$, which corresponds to an initial spin-down range from 2.87 rpm to 8.6 rpm. This range exceeds the anticipated range by a factor of 3; however, it is still within the range of the pitch-axis servo to lock the spacecraft to the horizon.

3.7.4 Completion of Alignment Process

It is shown in Section 3.7.3 of this report, that, within one-orbit time after injection into the nominal orbit, the spacecraft will be ready for the application of the QOMAC torquing subsystem (described in Section 3.2). In actual practice, the process of turning the spacecraft momentum-axis through 90° could be started without attitude measurement at the start of the second orbit. If the nominal, or near-nominal, orbit are attained, then the start of the QOMAC cycle (as outlined in Section 3.8) could be initiated on the basis of pre-launch command calculations. At the rate of 3.5° rotation per one-half orbit, it will be possible to complete the turn in about the first day in orbit. Attitude data can be measured during any time

TABLE 3.7-1. SUMMARY OF TIMES REQUIRED TO TURN FROM θ APPROXIMATELY EQUAL TO 90° TO θ APPROXIMATELY EQUAL TO 10°

Initial Spin-Rate (rpm)	K (90°)	K (10°)	$\tilde{K}$	$\dot{\psi}$	t (sec.)
Nominal: 5.74	0.296	0.320	0.308	0.510	1270
+50%: 8.60	0.3000	0.332	0.316	0.750	844
-50%; 2.87	0.284	0.305	0.297	0.250	2700

$$t_{90° \rightarrow 10°} = \frac{2 I_{23}}{I_d \dot{\psi} \tilde{K}} \log_e \frac{\sin 90}{\sin 10} \approx \frac{200}{\dot{\psi} \tilde{K}}$$

$$I_{23} = 106{,}000 \text{ lb-in}^2$$

$$I_d = 1{,}890 \text{ lb-in}^2$$

it is available, but it is probable that no change would be required in the program until the start of the second day when the spin-axis should be within 10° of the desired normal condition. At the lower torquing ratio of 1° per one-half orbit, the spacecraft will probably be aligned within $\pm 0.5°$ by the end of orbit 20 following launch.

The pitch-axis-stabilization control-loop will be commanded on after alignment, or even several degrees before this alignment occurs. If the nominal initial spin-down tolerances have been met, then lock-on will occur approximately 5-minutes after the command is sent and will be aligned with the designated vertical within $\pm 2°$. It is at this time in the sequence that the decision will be made regarding the number of momentum-control coil cycles required to adjust the total spacecraft momentum to the alignment requirements of the system. The total alignment process for the nominal conditions is shown in Figure 3.7-2 and includes the $\pm 18\%$ initial momentum tolerance.

The requirements for use of rockets in the event of a failure mode were previously discussed[7]. These rockets are included in Figure 7.2-1 depicting the general arrangement of equipment and weight has been provided for them; however, it is not recommended that rockets be included in the design. If the rockets must be included for some reason, the rockets shown in Figure 7.2-1 and the associated command subsystem have the flexibility to perform the following functions.

- Despin after the spin-axis conversion to the nominal 4-rpm rotation of the spacecraft about the pitch axis.
- Trim the despin value to within the ±50% recovery capability of the pitch-axis control servo.

The first function would be required only if there is a complete failure of the yo-yo despin mechanism. The second function could be used if the initial spin rate of the launch vehicle was beyond the ±50% range, or if a partial failure of the yo-yo despin mechanism occurred.

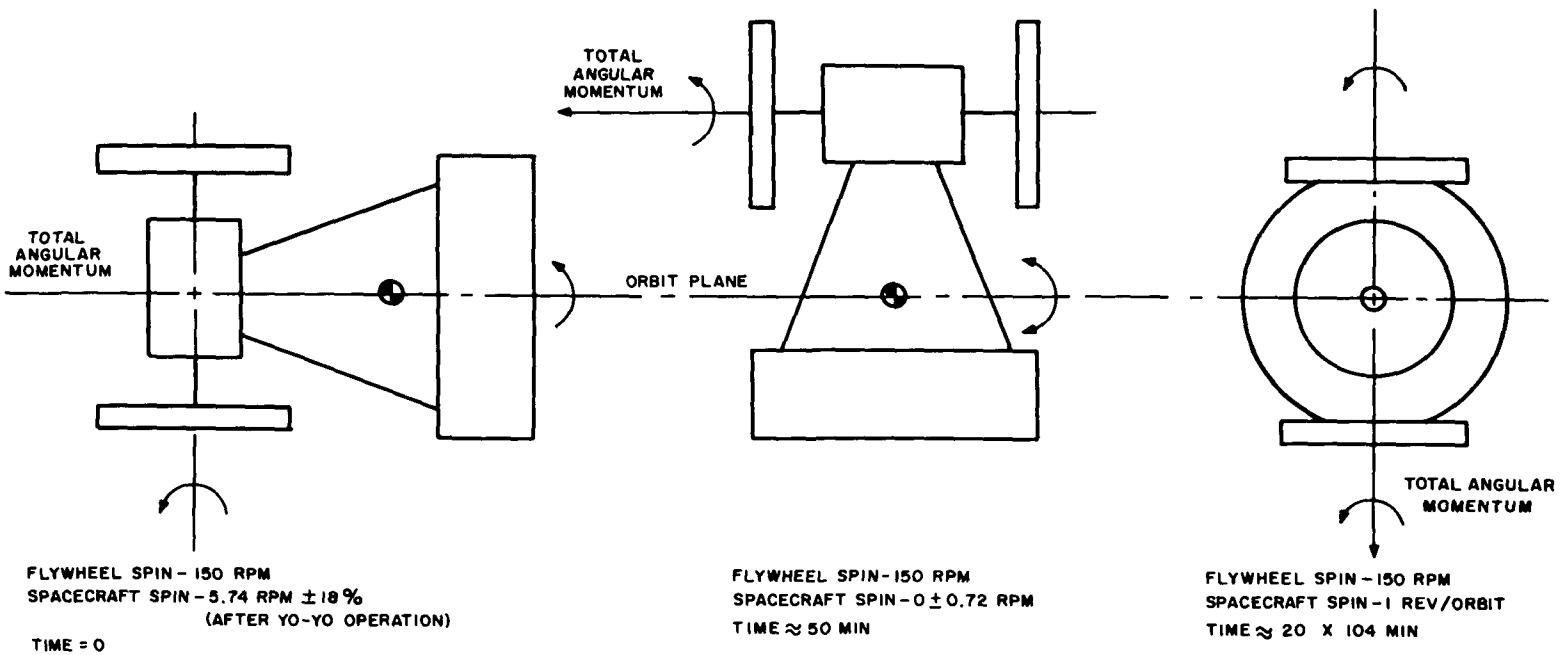

Figure 3.7-2. Total Initial Alignment Sequence for the Nominal Conditions

3.8 DATA-PROCESSING SUBSYSTEM AND GROUND COMMANDS

3.8.1 Specifications and General Operation

In normal operation, attitude-sensor data should be acquired and checked approximately once a day, and the orbit selected should have about 10-minutes of contact time. The attitude-data (Index pulses, Vertical Horizon, Vee 1 and Vee 2 sensor-data) is received on four subcarrier frequencies requiring a receiver bandwidth of 0.88 megacycles/second. The data will be recorded on tape with a transport having a speed stability of 0.01% or better. A fifth track on the tape unit is utilized for a reference-time frequency which is selectively variable. The block diagram of the attitude-data acquisition subsystem is shown in Figure 3.8-1.

The attitude-data can be recorded and, simultaneously, an oscillograph of the data could be obtained for examination and study. Sensor earth-times and flywheel spin-period can be computed from time recording; the chart speed must be at least 16 inches/second for adequate resolution and a frequency-response of from 0 to 5 kc will ensure reproduction of the attitude-sensor pulses. The width of the trace should be between 0.05 and 0.01 millimeter. At a chart speed of 16 inches/second, ten minutes of data would require 800 feet of chart paper. In the initial alignment state, only a very short data-run is needed. Once the spacecraft is normally aligned, the oscillograph would be a backup system.

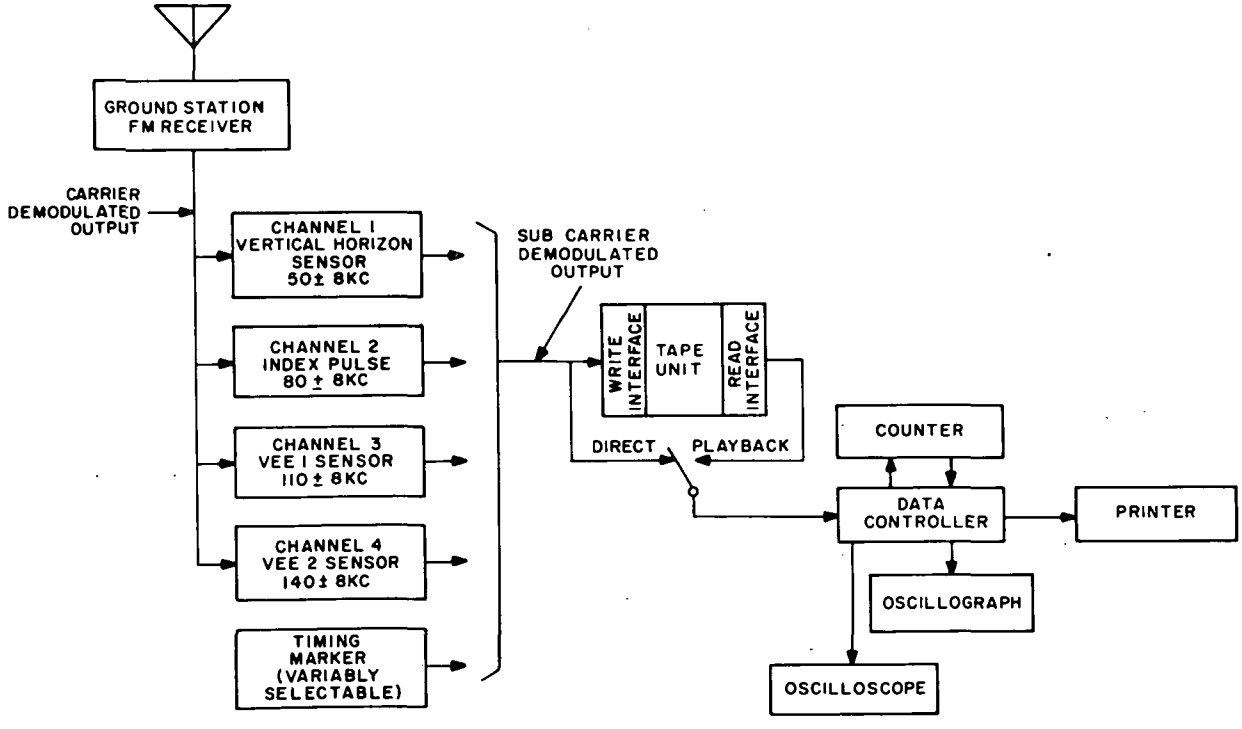

Figure 3.8-1. Block Diagram of the Attitude-Data Acquisition Subsystem

In normal operation, the data will be processed by a data-controller that controls a counter with a printer readout. A block diagram of a serial data-controller is shown in Figure 3.8-2. Usually the sensor period (Vee 1 and Vee 2 sensor earth-times) are the data required; however, occasionally the sensor period and the time-difference between the leading edges of the index pulse and the vertical horizon pulse (proportional to the pitch-axis servo error) together with the determination of which pulse occurs first are necessary. To provide this information, two modes of operation are provided by the data controller. Mode one computes the earth-times and the flywheel spin-period; mode two computes the pitch-axis servo error and the flywheel spin-period.

The mode one computation can be accomplished in one of two manners; either the earth-times for each sensor can be computed on successive spins (serially), or both earth times can be computed on the same run (parallel). The serial process requires less equipment. However, if the data are to be processed serially, the average speed stability between two successive sensor-rotations must be less than 0.05% to be compatible with predicted sensor accuracies. The spacecraft is not specified to have this sensor speed-stability. An investigation of the flywheel speed-control showed that an average speed-stability of 0.04% between two successive sensor rotations would probably result; taking advantage of this speed-stability would allow serial data-processing hardware. In three sensor rotations, one set of attitude data can be computed and printed out. If the nominal sensor

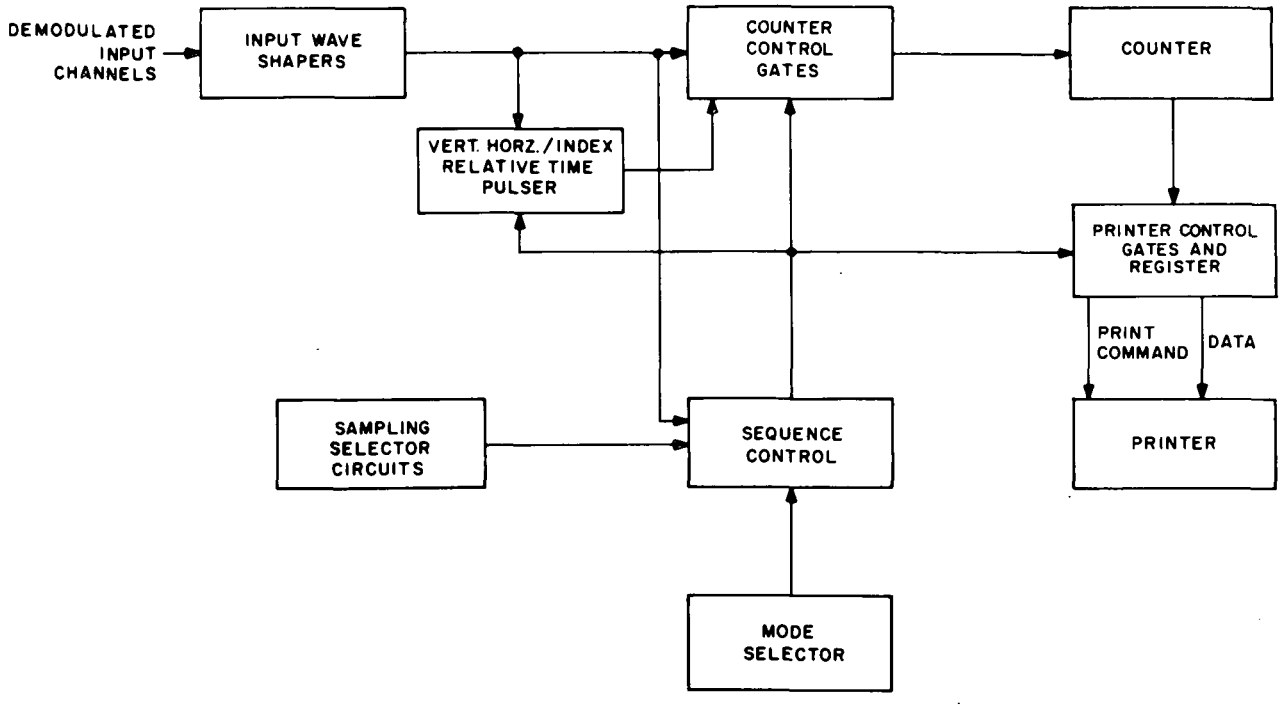

Figure 3.8-2. Block Diagram of a Serial Data-Controller

rotor-speed is 150 rpm, ten minutes of data would result in a length of 20.8 feet of print paper. Sampling of the data is a feature of the data controller to reduce the print sheet length. The data can also be processed any time that tape playback is desired.

Serial processing of the data should be adequate for the present system. However, the oscillograph output can be used to check this processing and, if the errors are larger than expected, an additional unit (of almost identical design) can be added to convert from serial to parallel data-computation. During conversion, the oscillograph mode can be used to assure continuity of operation.

The transmitted sensor-data is displayed on an oscilloscope for operator viewing simultaneously with the controller processing. If cloud noise is detected on the earth-to-sky transition pulse, then the oscillograph is turned on and the processing operation is switched from the data-controller to computation utilizing the oscillograph reading.

Earth time outputs from the data controller or the oscillograph computation are utilized with pre-computed nomograms to develop roll-error data. The data are plotted on pre-computed curves to develop the required QOMAC-programmer commands and magnetic-bias commands. Spin-period data are also utilized with pre-computed nomograms to develop momentum-control-programmer commands. During initial alignment, the pitch-axis error data must be utilized to compute the proper momentum-control program.

3.8.2 Equipment Requirements

3.8.2.1 Requirements for Additional Equipment

The counter should be capable of counting from 10 microseconds to 1 second in steps of 10 microseconds with digital readout. The printer should be capable of printing 200-lines per-minute and have a capacity of six columns. The decoding of a four-line input to each column is required. The data-controller is a custom-built item of standard logic components (e.g., gates, flip-flops, single shots, and Schmidt triggers). The details of the logic design were previously presented[3].

3.8.2.2 Time-Sharing of Attitude-Data with HRIR-Data

Approximately once a day the attitude of the spacecraft will be checked; therefore, the attitude-data could be time multiplexed with the HRIR data. During the attitude-data acquisition time, the transmitter would be transmitting attitude-data rather than HRIR data. The HRIR bandwidth spectrum available at the ground station is sufficient for the attitude bandwidth requirement. Thus, the AVCS/HRIR receiver can be utilized for the reception of attitude data. The carrier demodulated output of the AVCS/HRIR receiver would go to the channel inputs shown in Figure 3.8-1.

3.8.2.3 Use of Ground-Station Oscillograph

A Honeywell 1508 Visicorder with a 24-channel capacity is presently used in the ground station; therefore, ample channel-capacity is available for recording attitude data. The frequency response of the 1508 Visicorder is from 0 to 5000 kc with the M8000 galvanometers and the paper speed is variable to a maximum of 60 inches/second. The 1508 Visicorder would, therefore, be suitable for the attitude-data acqusition requirements specified in Section 4.0 of this report.

3.8.2.4 Use of Ground Station Tape-Recorder

The ground station tape-recorder is the M.H. Mincom G114 tape unit which has a capacity of 14 channels. Five spare-channels are available for attitude data. The Mincom 1400 has two frequency response modes, 10 kc or 20 kc, either of which is more than ample for the attitude-data acquisition requirements. A servo-speed stability of 0.01% is also installed in the tape transport. Therefore, this tape unit meets the attitude-data requirements for speed stability and frequency response.

3.8.2.5 Use of Present Command Structure

The Command and Control Subsystem (discussed in Section 3.5) was designed to be compatible with the present ground station command structure. Therefore no changes are required in this area.

3.8.2.6 Telemetry Data Processing

Inputs to the telemetry data-processing subsystem (e.g., motor voltage) are processed in accordance with the present normal technique.

3.8.3 Attitude and Momentum Determination and Command Computation

3.8.3.1 Earth-Time Determination

The Vee sensor earth-times are necessary for the initial step in attitude determination. Section 3.4.2.5 gives the relationships between the roll angle and the half-intercept angle (β) and, consequently, (through $\beta = \omega_{s\,te}/2$) to the earth time, t_e . The data-controller computes earth-time by using thresholding circuits on the sky-to-earth and earth-to-sky transition pulses and counting techniques. The operation is relatively straightforward but will produce large errors for clouds on the earth-to-sky interface. In this case, and in the case of large-roll-angles when only one sensor views the earth, manual computation of earth-times (from oscillograph recordings) is recommended. There are detailed procedures presently available that have been developed on the TIROS "I" program

for utilization in determining earth-times from a chart recording. These procedures develop best straight-line-slope-fits of the leading edge of the recorded pulses; this establishes crossing times that are independent of pulse amplitude and which can also be used to discriminate against most of the pulse-disturbances due to cloud effects. It is not feasible to present the details of these procedures in this report. However, it should be noted that the resultant accuracy is theoretically 4 times that of a simple thresholding technique with clean pulses (or 1/4 of 0.30^{o}), and at least equal to the predicted accuracy without clouds of the thresholding method when cloud degradation does exist (or 0.30^{o}).

3.8.3.2 Determination of Spin Period

The spin-period (T_s) is computed from the time between consecutive sky-to-earth transition pulses. If nutation exists, the period will change slightly from cycle-to-cycle and an average period must be computed. If the vertical sensor is used (with sun blanking), the nutation effects are negligible over a wide range of roll-angles. The spin period is presently measured on TIROS, using averaging techniques, to better than 0.01%.

3.8.3.3 Determination of Pitch-Axis Error

Pitch-axis error is computed from the time between the reception of a vertical-sensor sky-to-earth pulse and an index pulse. If the time is denoted as t_p, then the pitch error is

$$\Delta\theta_p = \frac{t_p}{T_s} \times 360 \text{ (degrees)} \qquad (3.8\text{-}1)$$

3.8.3.4 Computation of Roll-Angle Error

Roll-angle error is computed from equation (3.4-11) in Section 3.4.2.5 for large roll-angles (one sensor viewing the earth) and from equation (3.4-13) for small roll-angles. In operation, no computation will be required because nomograms have been developed from these equations and their utilization is presently planned for the TIROS "I" satellite. For large roll-angles, the scales on the nomogram are ϕ, $\omega_s t_{e1}$, $\omega_s t_{e2}$, and h, where only t_{e1} or t_{e2} will be used (depending on which sensor views the earth). For small angles using both sensors, the h scale is not required because the nomogram can be computed from the exact relationship

$$\tan\phi = \frac{\tan\alpha}{2}\left[\cos\frac{(\omega_s t_{e1})}{2} - \cos\frac{(\omega_s t_{e2})}{2}\right] \qquad (3.8\text{-}2)$$

instead of the linearized equation (3.4-13).

3.8.3.5 Computation of ϕ_{max} and λ

The required values of ϕ_{max} and λ may be obtained by making use of equations (3.2-15), (3.4-8), and (3.4-9) and by plotting roll-angle data. Precomputed normalized curves will be available for operational plotting. Figure 3.8-3(a) is an example of the type of curves that will be available and is plotted for maximum roll-angles of from 0.1 to 2.0 degrees. Superimposed on the curve are a set of typical data points taken over one-tenth of an orbit. In actuality, if serial data-processing is used, then 500 points (1/3 of 150 x 10) can occur during a 10-minute period. Figure 3.8.3(a) is plotted assuming the curves start at the ascending-node and that the data begin at $\theta = 36°$. The λ angle $(\phi_{max} = 0)$ occurs at $\theta = 0$ for the given plots. If the data start at some other point, then the λ angle has a different value. For example, if the data start at $\theta = 72°$ but the curve shape is the same, then the ϕ_{max} value will occur 36° later than shown and λ will be equal to 36°. This condition is illustrated in the sketch shown in Figure 3.8-3(b).

With the number of points available, and the predetermined knowledge of the shape (sinusoidal) and period (orbital period) of the plot, ϕ_{max} and λ can be computed to a high degree of accuracy because the random errors in measuring roll-angle are considerably smoothed. An even greater accuracy is attainable using "least-square optimization techniques" on a digital computer. This approach has been investigated on another program and the derived equations are available if required; however, based on the present accuracy specification, the computer computation should not be necessary.

3.8.3.6 Computation of QOMAC Commands

The QOMAC start-angle is equivalent to one-half the λ angle. For elliptical orbits, a correction can be made as discussed in Section 3.2.2.4.3. The number of cycles of torquing required for the low-torque mode is obtained from

$$n = \frac{\phi_{max}}{1°/cycle} \tag{3.8-3}$$

and, for the high-torque mode, from

$$n = \frac{\phi_{max}}{3.5°/cycle} \tag{3.8-4}$$

where n is always taken as the nearest lower-integer.

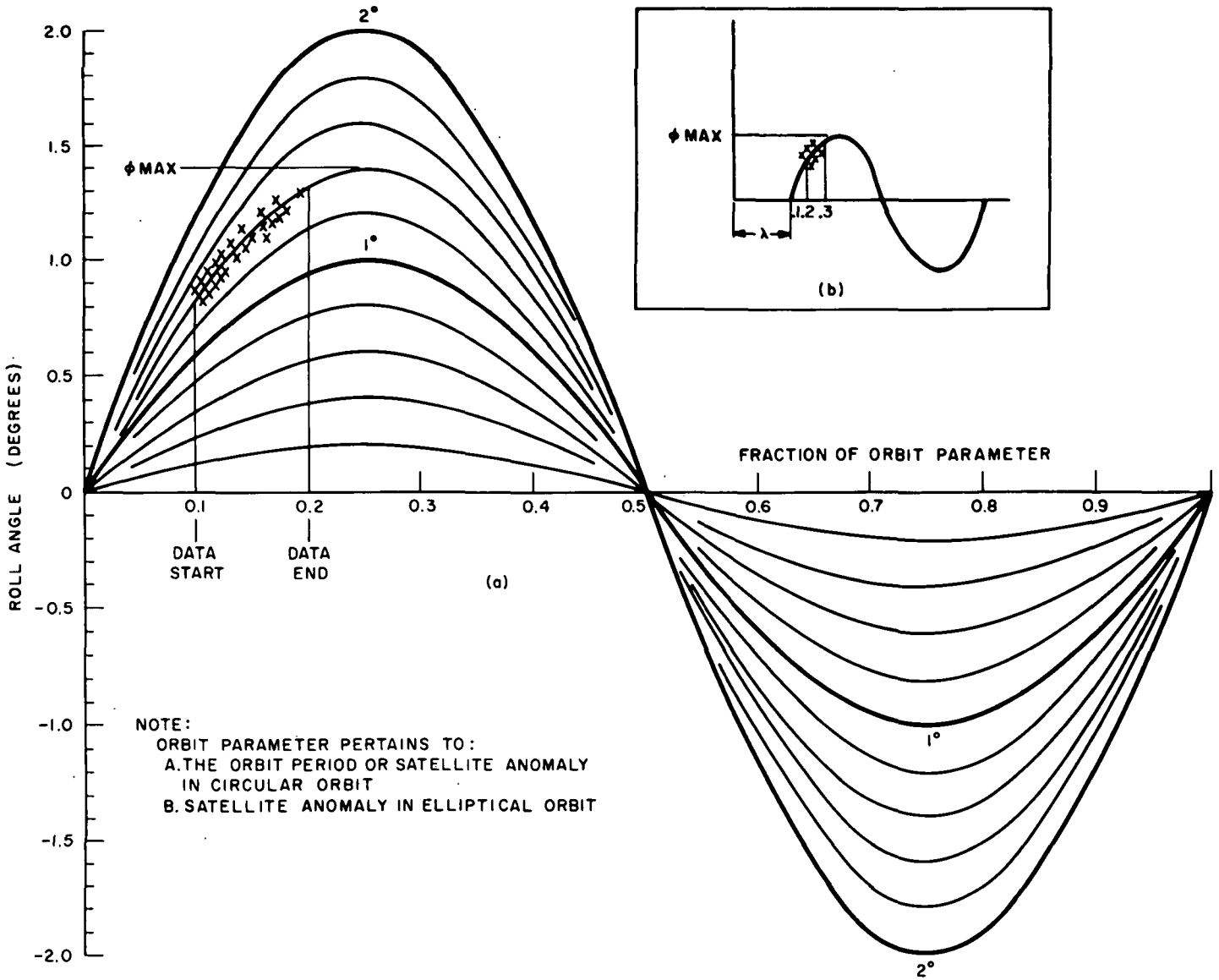

Figure 3.8-3. Examples of Pre-Computed, Normalized Curves Available for Computing ϕ_{max} and λ

The direction of current at the start of a cycle is determined by the phasing of the ϕ_{max} curve.

3.8.3.7 Computation of Momentum-Control Commands

For small pitch-axis errors, the momentum-control switching angles occur over the earth's poles as discussed in Section 3.2.4. Large pitch-axis errors can occur when the pitch-axis-stabilization control subsystem has locked on (during initial alignment) with a large momentum-deviation in the spacecraft. In this latter case, Figure 3.2-7 of Section 3.2-4 can be used to determine the proper start angles.

The number of cycles of momentum-control torquing required is computed from the known percentage-change per-cycle of 2%. Generally, the torquing will be commanded at a time when the momentum is 5% below nominal and will be executed for 5 cycles until the momentum is 5% above nominal. During initial alignment when momentum errors of ±50% can occur, many more cycles may be required. The direction (+ or -) of the starting current depends on whether the momentum must be increased or decreased and over which pole the cycle is started.

3.8.3.8 Magnetic-Bias Command

The magnetic-bias coil is not excited until a momentum-axis drift history is established. Under the worst-case predicted conditions, the spacecraft can be drifting at 4.0° per day. With a resolution of 0.07°/day per-step, the magnetic-bias switch should be pulsed for "m" steps where

$$m = \frac{\textit{Spacecraft observed drift rate}}{\textit{0.07 degrees/day}} \qquad (3.8\text{-}5)$$

In equation (3.8-5), m is chosen as the nearest integer.

The drift history of the spacecraft can be most easily observed on polar plots of ϕ_{max} vs λ because these plots will show both the magnitude and the direction of the momentum-axis drift. Generally, only drift about the b axis will be corrected utilizing the magnetic-bias coil. An iteration process will probably be required to obtain the optimum switch position; furthermore, occasional changes will probably be required to correct for drift due to resolution errors.

3.8.3.9 Rocket Commands

Rocket commands will only be required if there is either a complete despin yo-yo failure, or if the final momentum value after yo-yo despin does not permit lock-on of the pitch-axis-stabilization control subsystem. In either case, the flywheel

spin-period data, in conjunction with the index pulse transmission, can be utilized to determine the total spacecraft momentum and, consequently, the requirement for rocket command.

3.8.3.10 Pitch-Axis Position Control Turn-On Command

This command will be initiated when attitude-data indicate that the momentum axis is within 10^{o} of the orbit normal.

Section 4.0

SYSTEM ACCURACY ANALYSIS

4.1 POINTING ACCURACY

4.1.1 Pitch-Axis

The pointing accuracy of the pitch-axis-stabilization control subsystem was discussed previously[4], and is presented in Section 3.1 of this report. The major sources of random error are the sensor input ($\pm 0.5^{\circ}$ 3σ), and the PWM error-detector resolution ($\pm 0.05^{\circ}$ max.). The major sources of uncompensated known errors are the steady-state momentum deviations ($\pm 5\%$, or $\pm 0.6^{\circ}$ maximum error for a $K_v = 2$) and ellipticity ($\pm 1.3^{\circ}$ for a 0.013 ellipticity). In addition, the disturbance analysis shows a possible additional cyclic momentum deviation of $\pm 0.67\%$ (by r.s.s of the roll and yaw residual-dipole contributions) which is equivalent to a once-per-orbit variation of $\pm 0.08^{\circ}$ (where r.s.s is the root sum squared).

The pitch-axis-stabilization control subsystem will normally filter the sensor input errors over many samples because the subsystem bandwidth is only 0.11 radians/sec. For a worst-case condition, it was assumed that the $\pm 0.5^{\circ}$ sensor error exists in one direction longer than the filtering time of the control subsystem.

The derivation of the worst-case error due to the sensor viewing the sun was presented in Section 3.4.3.3.6 of this report.

4.1.2 Roll and Yaw Axes

Pointing accuracy for these axes is affected primarily by the errors in measuring roll-angle during the ground-station computation, and by the resolution in the QOMAC-torquing cycle. The errors in measuring roll angle are discussed in Sections 3.4 and 3.8 of this report. By using either the data-controller clean data or an oscillograph computation for the cloud-corrupted data, a basic single roll-angle measurement can be made to an accuracy of within $\pm 0.3^{\circ}$. The computation of the terms ϕ_{max} and λ utilizes many roll-angle measurements and should produce data which is at least accurate to the value of a single data point; proper data-processing can improve this accuracy to an appreciable value.

The QOMAC subsystem has a torquing cycle that produces 1° of motion. Section 3.2.2 of this report indicates that the maximum anticipated error in the torque

magnitude will be no more than ± 10%, leading to a random error of ± 0.1°. For example, if the roll/yaw error is allowed to build up to a value of ± 0.5° before torquing, it can be brought to -0.6° after torquing because of the QOMAC subsystem effect.

It is shown in Section 2.3.4 of this report that residual dipoles along the roll and yaw axes produce the only significant force-nutation motion. Combining the effects of both dipoles leads to a half-cone angle of 0.038° with a rotation-rate of 1-revolution per-orbit.

Nutational motion will exist during the QOMAC or Momentum-Control torquing cycle as discussed in Section 3.2 of this report. However, the duty cycle for these torquing modes is extremely small, and the magnitude of motion is always less than 0.5° peak-value. Therefore, this motion is not included in the summary.

4.2 JITTER ACCURACY

4.2.1 Pitch-Axis

A worst-case jitter, caused by the sensor inputs, can be obtained by assuming that the sensor output error during any three flywheel revolutions goes from $+0.5^{o}$ to -0.5^{o} to $+0.5^{o}$. For the slowest sampling period (0.6 sec.), the error-input to the pitch-axis servo is

$$\Delta\theta_{p\ in} = 0.5\ \frac{\sin 2\pi}{1.2\ t} = 0.5 \sin 5.2\ t \qquad (4.2\text{-}1)$$

At 5.2 radians, the servo subsystem attenuates the input signal by a factor of 1800; therefore, the output is given by

$$\Delta\theta_{p\ out} = 0.0003 \sin 5.2\ t \qquad (4.2\text{-}2)$$

Differentiation of equation (4.2-2) leads to a maximum jitter-magnitude of 0.0003 x 5.2 = 0.0016^{o}/sec.

Jitter due to a $\pm\ 0.05^{o}$ resolution is computed in a manner similar to the computation for the sensor; however, the jitter is assumed to occur about the subsystem natural-frequency (0.11 rad./sec.). This analysis leads to a jitter rate of

$$0.05 \times 0.11 = 0.0055^{\circ}/sec.$$

Motor-torque variations, frequency-to-d-c converter ripple, and sampling-ripple produce jitter rates at least one order of magnitude below those due to resolution, and are considered negligible.

Jitter due to sun interference can occur when the sensor views the sun; this occurs when the spacecraft comes out of occultation at the horizon. A relatively-smooth transfer will occur initially and the sensor will then track the sun for the maximum gate period of 3.3^{o}. At the completion of this period, the sensor will lock onto the earth. From Section 3.1 of this report, the pitch-axis-stabilization control subsystem will require approximately 10-seconds to perform this lock-on maneuver, or a rate of 0.33^{o}/sec.

4.2.2 Roll and Yaw Axes

The operation and performance of the nutation damper were discussed in detail in Section 3.3 of this report. As indicated there, long-term induced jitter will be negligible because of the damping action. In Section 2.3.4, it is shown that the only significant disturbances, in terms of jitter, are caused by meteoric impulses or uncompensated momentum. Other disturbances occur at orbital rate and will produce negligible jitter.

4.3 SUMMARY

A summary of all the disturbances discussed in this section of the report are presented in Table 4.3-1.

TABLE 4.3-1. SUMMARY OF POINTING ACCURACY AND JITTER

AXIS	SOURCE OF ERROR	RANDOM ANGULAR ERROR	UNCOMPENSATED KNOWN ANGULAR ERRORS	JITTER RATES
Pitch	1. Sensor	$\pm 0.5^{o}$ 3σ		0.0016^{o}/sec.max.
	2. Resolution	$\pm 0.05^{o}$ 3σ		0.0055^{o}/sec. max.
	3. Known Momentum Deviation		$\pm 0.6^{o}$ for a $\pm 5\%$ momentum deviation maximum value	Negligible
	4. Unknown Momentum Deviation	$\pm 0.06^{o}$ for 0.5% uncertainty		Negligible
	5. Ellipticity		$\pm 1.3^{o}$ 3σ	Negligible (orbit rate)
	6. Sensor: Viewing Sun		3.3^{o} maximum for 0.95 minutes/orbit	0.33^{o}/sec. for 10 seconds
	7. Residual Dipoles	$\pm 0.08^{o}$ max. cyclic per orbit		Negligible (orbit rate)
	Total	± 0.52 3σ (r.s.s.)	$\pm 0.6^{o}$ max. $\pm 1.3^{o}$ 3σ	0.006^{o}/sec. 3σ (r.s.s.)
Roll/ Yaw	1. Sensor	$\pm 0.3^{o}$ 3σ		
	2. QOMAC Resolution		$\pm 0.5^{o}$	
Roll/ Yaw (Cont.)	3. Meteorites and Uncompensated Momentum			$< 0.005^{o}$/sec.max.
	4. QOMAC Error	$\pm 0.10^{o}$ max.		
	5. Residual Dipoles	$\pm 0.038^{o}$ max.		
	Total	$\pm 0.32^{o}$ 3σ (r.s.s.)	$\pm 0.5^{o}$	$< 0.005^{o}$/sec. max.

Section 5.0

SYSTEM RELIABILITY AND FAILURE-MODE ANALYSIS

5.1 GENERAL

This section presents the results of a detailed reliability and failure-mode analysis performed on the gyromagnetic-stabilized (FSMTMS) attitude-control system.

The Failure-Mode and Effect Analysis of the system, at the level performed, revealed no simultaneous occurrence of a relatively high failure probability and a critical or major-performance area. This result is based on the incorporation of the recommended redundancy and modifications brought about, in part, by this analysis and its advantage as being conceptual in nature.

The reliability analysis is based on the fact that an extensive worst-case analysis together with a failure-mode and effects analysis and testing and preconditioning will have eliminated all but random-failure probabilities. Reliability, as referred to in this report, is best described as the probability of the equipment performing its desired function throughout the intended mission period.

As a result of this analysis, the inherent reliability of the FSMTMS system for a minimum life of one year is $0.923, using redundancy for critical elements. The final design should not change the reliability results significantly.

5.2 FAILURE-MODE AND EFFECTS ANALYSIS

The failure-mode and effects analysis consists of an analytical procedure for critically examining the possible mode of system failure, the probabilities of occurrence of these failures, and the resultant effect upon the system design goal. One of the objectives of the analysis is the highlighting of any high-failure probability that occurs in conjunction with critical performance.

Potential failures representing serious deterrents to reliable performance of the system are discovered, and compensating provisions such as redundant circuits and/or components, changes in modes of operation, or other means of operating in the presence of failures or degradation, are incorporated.

A detailed examination of all potential failure modes and effects was presented[3]. The analysis described showed that the combination of high failure probability and critical performance occurs relatively infrequently, and that all occurrences of this type can be corrected by suitable redundancy. The recommended redundancy is discussed in the next section.

5.3 RELIABILITY ANALYSIS

5.3.1 System Description

For purposes of the reliability analysis, the FSMTMS control system may be considered as consisting of two major subsystems plus the mechanical components. The two subsystems are (1) "Pitch-Axis-Stabilization Control Electronics", and (2) "Attitude and Momentum Control" subsystem.

The primary components in the Pitch-Axis-Stabilization Control Electronics are

- Horizon Scanners
- Pulse-Width-Modulator (PWM)
- Compensation Amplifier
- Power and Summing Amplifier
- Frequency-to-d-c Converter
- Digital Tachometer (Encoder)
- Motor
- D-C to D-C Converter

The primary components in the Attitude and Momentum Control subsystem are

- QOMAC and Momentum-Control Programmer
- Magnetic-Bias Stepping Switch
- Rocket-Actuating Stepping Switch
- Telemetry Subsystem
- Momentum (spin-axis) Coil
- Magnetic-Bias Coil
- QOMAC Coil
- Rockets
- Despin Yo-Yo's

5.3.2 Operating Time

The reliability analysis is based on a minimum mission time of one year. During this time the Pitch-Axis-Stabilization Control Electronics will operate on a 100% duty cycle, (i.e., t_{pc} = 8760 hours). The QOMAC and momentum-control programmer is conservatively estimated to operate six times per week for the

duration of one orbit each operation. The planned orbital period is 103 minutes. The resultant nominal operation time is 535 hours (i.e., t_{ac} = 535 hours). The data processing and telemetry subsystems will be operated nominally once every seven orbits for 15 minutes maximum, totaling 180 hours per year (i.e., t_{dr} = 180 hours). The magnetic-bias stepping switch electronics will operate one year (i.e., t_{mb} = 8760 hours).

There are five relays in the attitude and momentum control subsystem. For worst-case conditions, two require 52 operations, two require 730 operations, and one requires 50 operations. The magnetic-bias stepping switch will conservatively be utilized for a total of 576 revolutions in one year. All other switches and relays, including those for redundant circuitry, operate so infrequently that they may be analytically considered "perfect switching" and assigned a "Probability of Survival" of 1.000. The combination of rockets and despin yo-yo's, as a redundant unit, also can be assigned a "Probability of Survival" of 1.000.

5.3.3 Reliability Block Diagram

The reliability block diagram, which includes all components that must operate properly to ensure mission success, and the corresponding mathematical models are shown in Figures 5.3-1, 5.3-2, and 5.3-3. These block diagrams are not signal flow charts, but indicate those components which must operate properly to ensure mission success.

For the purpose of this analysis, the mechanical assembly (including the motor) will be considered, after suitable preconditioning, to have a negligible probability of failure. Consequently, these items are not included in the mathematical model. Section 3.1 of this report presents evidence to corroborate this decision because after wearout effects have been eliminated, the motor can be considered as a simple transformer.

5.3.4 Part Failure-Rates

The failure rates used for individual part types were previously listed[3]. These failure rates are averages for generic classes and were estimated on the basis of

- Maximum use of MIL-Standard and RCA "Spacecraft Standards" parts
- Preconditioning of all parts in accordance with RCA Specification 1750012
- Limiting the electrical stress of the parts in accordance with the established derating policy[3]

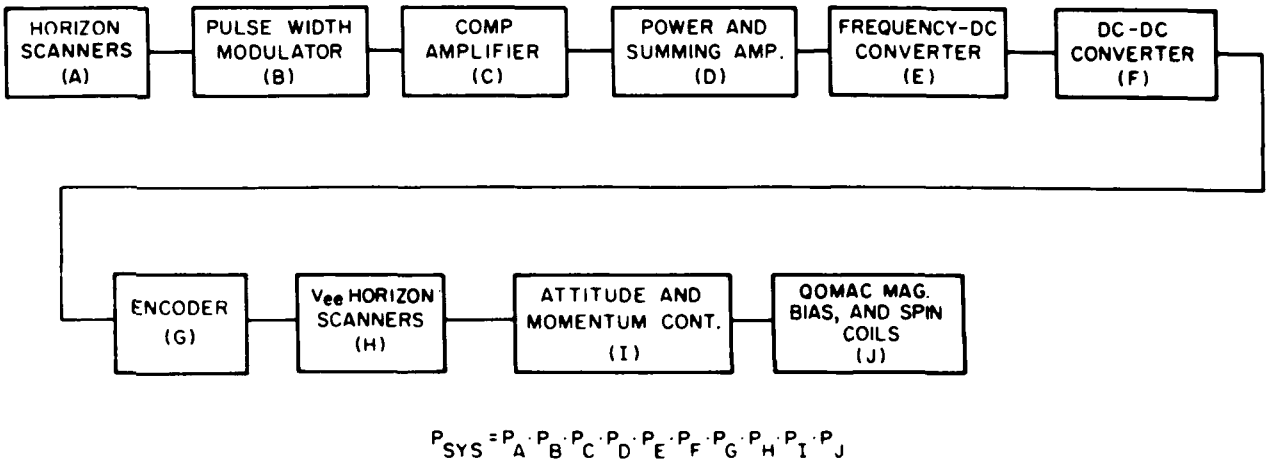

Figure 5.3-1. Reliability Block Diagram and Mathematical Model with No Redundancy

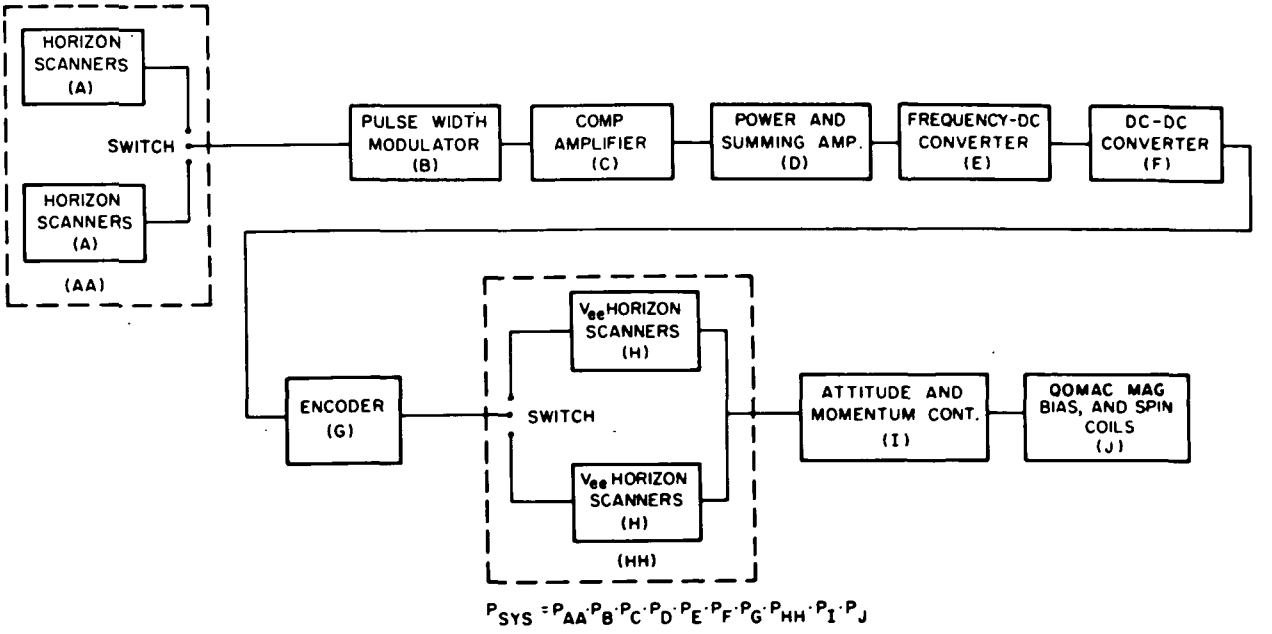

Figure 5.3-2. Reliability Block Diagram and Mathematical Model with Redundant Sensors

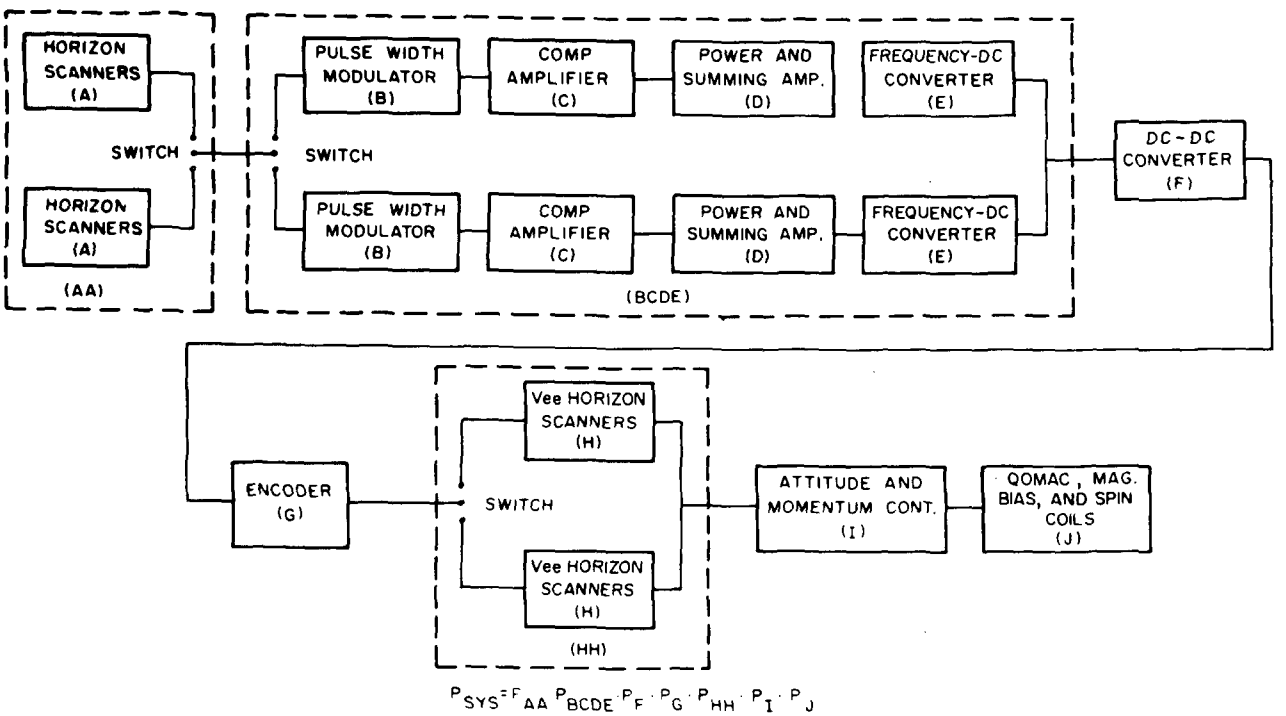

Figure 5.3-3. Reliability Block Diagram and Mathematical Model with Redundant Sensors and Pitch-Axis Control Electronics

In addition to the general failure rates, the following special rates were used in this study:

- QOMAC, Magnetic-Bias, and Momentum (spin) Coils used 0.035%/1000 hours during operation and 0.018%/1000 hours for aging when not in use
- Bolometer sensor failure rate chosen as 0.40%/1000 hours
- Sensistor failure rate chosen as 0.015%/1000 hours
- Magnetic-bias stepping-switch failure rate chosen as 0.04%/1000 revolutions

5.3.5 Survival Probability

Three system configurations with varying degrees of redundancy were shown in Figures 5.3-1, 5.3-2 and 5.3-3 with, respectively, no redundancy, sensor redundancy only, and sensor and pitch-axis-stabilization control electronics redundancy. The configuration shown in Figure 5.3-3 is recommended; the other configurations are included for comparison.

The survival probability for any series of items in a system is given by:

$$P_s = e^{-(\lambda t)_T} \tag{5.3-1}$$

where

$$(\lambda t)_T = \lambda_1 t_1 + \lambda_2 t_2 + \lambda_3 t_3 + \cdots + \lambda_t t_t$$

When several subsystems have the same operational period, (i.e., $t_1 = t_2 = t_3 = t'$ and $t_4 = t_5 = t_6 = t''$ etc.) then

$$P_s = e^{-[(\lambda_1 + \lambda_2 + \lambda_3)t' + (\lambda_4 + \lambda_5 + \lambda_6)t'' + \cdots]} \tag{5.3-2}$$

where

λ is the failures/hour or failures/operations

t is the number of hours or operations

The survival of any two redundant items with individual probabilities of P_A and P_B respectively and with perfect switching is given by:

$$P_{AB} = P_A + P_B - P_A \cdot P_B \tag{5.3-3}$$

A summary of the individual "black-box" component reliabilities is presented in Table 5.3-1.

Using the model shown in Figure 5.3-3 and the values given in Table 5.3-1, then

$$P_{SYS} = P_{AA} \cdot P_{BCDE} \cdot P_F \cdot P_G \cdot P_{HH} \cdot P_I \cdot P_J \qquad (5.3\text{-}4)$$

or

$$P_{SYS} = 0.923 \qquad (5.3\text{-}5)$$

5.3.6 Additional Analyses

To determine the effects of varying amounts of redundancy and the use of high-reliability ("Minute Man") parts where applicable, the reliability analysis was extended.

Although the high-reliability parts are extremely dependable, the use of these parts is prohibitive because of the high cost, the long-lead delivery time, and the increased difficulty in obtaining some items. The failure-rates for the high-reliability parts are given in Table 5.3-2.

Using these parts where applicable in the configuration shown in Figure 5.3-3, the resultant reliability is 0.961; in Figure 5.3-2 it is 0.926 as compared to 0.844 without the high-reliability parts.

TABLE 5.3-1. RELIABILITY ANALYSIS SUMMARY

Subsystem	Failure Rate (%/1000 hrs.)	Probability of Survival	
		Individually	In System Arrangement (Fig. 5.3-3)
Horizon Scanner	0.549	$P_A = 0.953$	$P_{AA} = 0.998$
Pulse Width Modulator	0.655	$P_B = 0.944$	
Compensation Amplifier	0.146	$P_C = 0.987$	(Redundant)
Power Summing Amplifier	0.222	$P_D = 0.981$	$P_{BCDE} = 0.991$
Frequency-to-D-C Converter	0.143	$P_E = 0.988$	
D-C to D-C Converter	0.122	$P_F = 0.989$	0.989
Encoder	0.173	$P_G = 0.985$	0.985
Vee Horizon Scanner	1.010	$P_H = 0.915$	(Redundant) $P_{HH} = 0.993$
Attitude and Momentum Control			
Programmer	4.409	0.977	
Data Return	1.283	0.998	
Mag. Bias Switch Circuitry	0.013	0.999	(In total) $P_I = 0.971$
Mag. Bias Stepping Switch	0.040 (%/1000 oper.)	0.998	
Relays	0.020 (%/1000 oper.)	0.999	
Coils			
QOMAC (Operational)	0.035	0.999	
QOMAC (Aging)	0.018	0.998	
Momentum (Operational)	0.035	0.999	(In total) $P_J = 0.994$
Momentum (Aging)	0.018	0.998	
Mag. Bias (Operational)	0.035	0.999	
Mag. Bias (Aging)	0.018	0.998	

TABLE 5.3-2. FAILURE-RATES OF HIGH-RELIABILITY PARTS

Component	Failure Rate (%/1000 hrs.)
Resistors, Variable	0.0008
Comp. & Film	0.0005
Diodes	0.002
Capacitors, Mica, Ceramic	0.0005
Mylar, Tant.	0.005
Transistor	0.007
Sensistor	0.002

Section 6.0

SYSTEM-PERFORMANCE TEST REQUIREMENTS

6.1 PITCH-AXIS SIMULATION

6.1.1 Component Testing

The evaluation of the pitch-axis-stabilization control subsystem will be done on both a component basis and a subsystem basis. Each component defined by a block in Figure 1.3-2 will have input-output specifications established by control-loop performance requirements. All components within the loop, with the exception of the motor and shaft pulse-generator (incremental encoder), may be specified as a transfer function relating the input voltage (current) to the output voltage (current) and tested with standard laboratory equipment on a "go-no-go" basis. The motor and shaft incremental-encoder require mechanical test equipment to establish their transfer function. For the motor, a standard dynamometer apparatus will suffice; for the encoder, a counter which is started and stopped with the index pulse (that represents the spacecraft position with respect to the rotating shaft) will indicate proper operation. The rise-time and pulse-width of the encoder output will be sampled to ensure that there would be no possibility of dropping pulses over the temperature range. A precision speed-control for testing the encoder is not essential because the desired output of the encoder is a fixed number of pulses per-revolution of the shaft. The evaluation of pitch-axis control-loop electronic components (as discussed in Section 3.1.3) has shown that state-of-the-art components will meet the performance specification indicated in Section 1.2. Vacuum-operation of rotating components is not as clearly established as other devices and must, therefore, be tested under conditions which closely approximate the actual operating environment. Specific recommendations are contained in Section 9.2 of this report.

6.1.2 Subsystem Evaluation

The minor-loop consists of a differential amplifier, a power amplifier, a motor and shaft encoder, and a frequency-to-d-c converter. Meaningful results can be obtained from either connecting the components together on the bench or on the spacecraft housing which is rigidly mounted to a support structure. Under these conditions, the components may be turned on and checked for operation at the bias speed. The loop will maintain the flywheel at the bias speed (tentatively set at 150 rpm). The performance of the loop under dynamic conditions would be essentially the same as in the orbit condition; the only difference is in the output of the digital

encoder. During ground tests, the encoder senses only speed changes of the flywheel; in space, it senses changes in both spacecraft speed and flywheel speed. However, under normal operation the spacecraft would produce a modulation of less than 0.1% on the output of the encoder. The conclusion can, therefore, be drawn that ground observation of the minor loop is equivalent to space operation and means that the bias voltage may be set and checked on the ground with no further adjustment required. For the parameters used in Section 3.1.4.1, the bias-voltage setting to within 1.0% of the nominal 150 rpm would produce an offset error of 0.12^{o}. A setting to closer than 1.0% is not essential because the nominal is likely to be changed when the spacecraft is orbited. However, bias-voltage variation with temperature or external voltage variation will be held (and specified) to less than 0.5%.

6.1.3 "Torque-Free" Testing of the Pitch-Axis-Stabilization Control Subsystem

The closest approximation to simulating orbit conditions is to mount the pitch-axis control package on a structure which is supported by an air bearing. The dynamics of the pitch-axis loop can be made to almost perfectly duplicate orbit conditions. This is easily demonstrated by adjusting the loop gains to values that would indicate system instability (in the absence of external damping). Under these conditions, the pitch-axis would fail to lock-on by reaching full speed in one direction, then reversing, and reaching full speed in the other direction. If external damping were present, the gain values would be larger than those predicted. Another indication of the suitability of the air bearing for pitch-axis testing is the damping provided by the control-loop as compared to "air-ball" damping.

From the parameters of Section 3.1.4.1, the pitch-axis-loop damping constants may be approximated by

$$C = 2 \zeta J_p \omega_n \ in.\text{-}lb/rad./sec.$$

This gives "C" a value of 15 in.-lb./rad./sec. for

ζ = 0.2 (see Figure 3.1-11)

J_p = 358 in. lb. $sec.^2$, spacecraft moment-of-inertia about the pitch-axis.

ω_n = 0.11 rad./sec., pitch-axis natural frequency

Air-ball damping can be shown to be less than 0.1% of this number. The performance of the pitch-axis loop can, therefore, be evaluated with a high degree of confidence from the standpoint of gain settings, pointing accuracy, and jitter rate.

The effect of external torques can be minimized, but not completely eliminated. Windage will add or subtract momentum and will precess the spin axis, and gravity torques will precess the spin axis. However, the latter effect can be made sufficiently small to permit extended periods of continuous operation without disturbing the tests. This is particularly true if an external-torque which is equivalent to the effect of the QOMAC-torque is used to precess the spin axis back to the original (or desired) orientation of the test structure. One very good substitute is the gentle application of the finger or small pieces of clay dropped onto the outer edge of the test structure. A gentle application of pressure is precisely what is done by ground command when the spacecraft is in orbit. Therefore, it is difficult to justify a ground environment which does not allow for implementing torques on the spacecraft in the laboratory.

The direct application of torque does not preclude the testing of the magnetic-torquing subsystem. However, magnetic-torquing of a test structure simulating pitch-axis performance will not materially contribute to the confidence of the complete system. Section 6.3 contains a discussion of the testing of the magnetic properties of the spacecraft.

6.1.4 Tentative Specifications for Air-Bearing Test

Two arbitrarily-established criteria have been determined for defining performance specifications for the air-bearing tests. These are:

- 0.24^{o} per-hour rotation of the simulated test structure about the pitch axis;
- 0.3^{o}/sec. precession of the pitch-axis about its initial orientation at the start of the test;

The first requirement places a limit on the rate at which the flywheel can gain or lose momentum. The value of 0.24^{o} per-hour corresponds to a 2% per-hour change in the flywheel speed. To meet this specification, a maximum of 0.1% of the flywheel momentum can be introduced in a direction normal to the initial direction of the flywheel axis. This requirement is easily satisfied by air-ball turbine-torques and release mechanisms.

The second requirement merely limits the gravity-forced motion of the pitch-axis to approximately 0.1 times the free-motion (or nutation) of the pitch axis. The value computed in Section 3.3.3.2 for the free motion (i.e., for $\dot{\psi}$) was 0.51 rad./second or 2.92^{o}/second. The separation of the two motions permits the damper to operate in a manner closely associated with the actual orbit conditions. A discussion of independent damper testing is presented in Section 6.2. To satisfy the second requirement of the air-bearing test, the center of mass must be located within 0.0014 inches of the center of support. The sphericity of the ball is at least

a factor of two better than 0.0014 inches; therefore, geometric considerations are not limiting. However, deflections of the structure do contribute to shifts in the center of gravity; consequently the test structure will be made more rigid than would otherwise be required by the spacecraft to meet launch-environment conditions. Present experience indicates that a test structure can be built which, even with large angles, will satisfy this requirement.

6.2 NUTATION-DAMPER OPERATION

The nutation-damper is a passive device and produces no direct measurable output signals. The mechanism by which undesired motion of the spacecraft about the roll and yaw axes are reduced is discussed in Section 3.3. The nutation-damper test is designed to: verify operation of the expansion mechanism; and verify the coupling factor. The first test ensures that, over the planned temperature range, damping fluid will not be lost and the damper tube will not be overstressed. The expansion chambers to be tested are shown in Figure 7.2-1.

The second test is intended to confirm the factor defined approximately by equation (3.3-6). This equation is repeated as equation (6.2-1).

$$H_d = \frac{I_d \omega_{23}}{(1 + \tau S)^{1/2}} \qquad (6.2\text{-}1)$$

where

I_d is the fluid mass moment of inertia

τ is equal to $r_o^2 \rho / 4\mu$

The condition for optimum damping, established in Section 3.3.3, was that

$$\tau = \frac{1}{\dot{\psi}}$$

where $\dot{\psi}$ is the forcing-frequency of the spacecraft as determined by free-nutation in orbit. The device shown in Figure 6.2-1 would lead to a direct check of the damping properties of the damper because it would verify the following equation

$$\tau = \frac{r_o^2 \rho}{4\mu} = \frac{1}{\dot{\psi}}$$

The technique to be used would set the torsion pendulum shown in Figure 6.2-1 in motion. Then, at a specific time, the amplitude of the motion would be measured by a second measurement at the end of a complete cycle. If these two measurements are designated θ_1, and θ_2 and if the torsion spring and inertia are adjusted to oscillate at $\dot{\psi}$ radians/second, then the damper parameters are related to the difference between the two measurements by

$$\frac{\Delta\theta}{\theta_1} \approx \frac{I_d}{I_p} \frac{\pi \sin \delta}{\sqrt[4]{2}} \qquad (6.2\text{-}2)$$

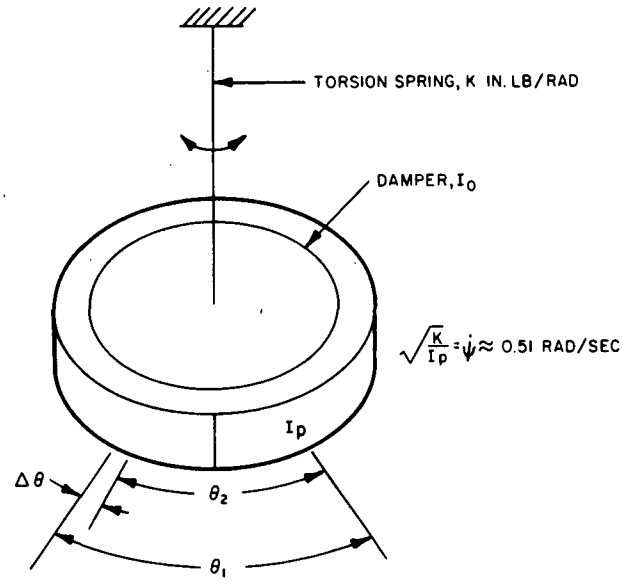

Figure 6.2.-1. Nutation-Damper Test Device

where

θ is equal to $\theta_1 - \theta_2$

I_d is equal to damper mass moment of inertia

I_p is equal to pendulum moment of inertia

δ is identically equal to $1/2 \tan^{-1} (r_o^2 \rho \dot{\psi}/4\mu) \approx 22\frac{1}{2}^o$

The following assumptions were made.

$$\Delta\theta << \theta_1$$

$$I_d << I_p$$

The requirements for the measurement of θ_1 and θ_2 may be obtained from substituting the following values. Let

$$I_p = 10\, I_d$$

$$\sin \delta = 0.38$$

Then,

$$\frac{\Delta\theta}{\theta_1} = \frac{1}{10} \frac{\pi\, 0.38}{\sqrt[4]{2}} = 0.1$$

which indicates a 10% change in θ during a single oscillation of the pendulum at the frequency of $\dot{\psi}$ rad./second. The value of $\dot{\psi}$ used to compute the damper time-constant in Section 3.3.3.2 was 0.51 rad./sec.

Previously, it was assumed that the damper was the only cause of energy loss in the pendulum; actually, $t_{avg.}$ run will be made with a simulated damper-inertia. If the value of θ changes by a significant factor compared to that expected, then the ratio of I_p to I_d will be increased until there is a difference in the $t_{avg.}$ change in θ and that expected from the damper. It is the difference between the changes under the two test conditions that will be used to compare the measured $\Delta\theta/\theta$ value with that predicted by equation (6.2-2).

Methods other than that just described will be considered for testing the damper under gravity conditions. A torsion pendulum mounted in the horizontal position may be difficult to implement, but if it can be done, it will serve as a check on the effect of gravity on the damper operation. As long as the damper is maintained in a filled condition, gravity effects should be negligible.

6.3 MAGNETIC TESTING

Disturbance torques arising from the interaction of the earth's magnetic field with current loops, permanent magnets, and non-spherical permeable materials internal to the spacecraft can be minimized by careful design and preflight compensation of the vehicle. The discussion in Section 2.3.4 shows that the major disturbances experienced by the FSMTMS are magnetic in origin. Complex geometries and non-linear permeabilities prohibit the summing of individual source contributions in a magnetic-disturbance torque analysis. A practical solution to the problem is to determine the resultant spacecraft magnetic-dipole moment for each operating mode; this moment is then converted to spacecraft torque by the magnetostatic equation expressed by the vector cross-product of the dipole moment and the magnetic field.

The space-vehicle dipole moment can be established as follows: (1) by measuring the spacecraft torque in a test magnetic field; (2) by measuring the induced emf (produced by relative rotation between the vehicle and a coil system); (3) by field-mapping techniques; and (4) by actual in-orbit observations of the spacecraft attitude.

The torque level developed by the satellite dipole in the test magnetic-field is extremely small. To achieve measurable results with available techniques for supporting the spacecraft (even if state-of-the-art air bearing supports are utilized), a very large, accurate, test field would be required. This field could be achieved utilizing a three-axis, programmed Helmholtz-coil system. A system of this type has been studied during work on another RCA program. However, it is considered undesirable to use this technique because of the cost and complexity. Furthermore, the test field must be much larger than the actual field that the spacecraft will experience in space; therefore, the results will be dependent on the linearity of the produced torques as a function of magnetic-field intensity. A successful technique has been developed on another program to demonstrate the ability of a coil to change the momentum of a spinning spacecraft utilizing the earth's ambient field. However, this technique is only applicable to torque generation around the momentum axis and requires long integration periods to measure the relative effects of the dipole.

Actual in-orbit observation will be utilized to compensate for the pitch-axis residual dipole. This technique is discussed in Sections 3.2.3 and 3.8.3.8.

The emf method of measurement was previously described[9]. It has been used successfully on several RCA satellite programs but requires a large spherical-coil system for operation plus gimballing and support of the spacecraft to achieve relative rotation. For small space-vehicles, this method permits a rapid determination of the satellite dipole moment. Once the dipole is known, the correct amount of permanent-magnet material can be mounted on the vehicle, with the proper orientation, and the residual dipole compensated to approximately 0.05 ampere-turn-meter^2 (50 absolute dipoles).

The inherent resolution of field-mapping measurements is better than that of the emf method because this is a quasi-static test, and, therefore, free from dynamic errors. An advantage of field-mapping is that it permits measurements in a region of a nominally uniform field. A field-free region is not usually necessary. This method has been used in tests on several RCA spacecraft[10] and is recommended for the FSMTMS magnetic tests. The technique achieves a three-axis dipole-moment determination by sampling the radial magnetic-field of the spacecraft on a spherical surface. An inexpensive, portable, flux-gate magnetometer can be used; the magnetometer has a resolution of less than 1 gamma (geomagnetic field in New Jersey is approximately equal to 57,000 gamma or 0.57 gauss) and a stability of 1 gamma in 5 minutes (drift is 5 gamma/hr., random).

If the magnetic sensor is moved over a spherical surface enclosing the spacecraft, it will sense the changes in both the direction of the earth's magnetic field and the near-field structure of the vehicle; furthermore, the former field variation is approximately 1000 times greater than the latter. To avoid this problem, the sensor is positioned along a radial line-segment and the vehicle rotated about angles θ and ϕ as shown in Figure 6.3-1; the magnetometer is zeroed at the starting point $(\theta, \phi = 0^o, 0^o)$ and measurements are made relative to this point. This technique has the same effect as adding an arbitrary constant to each data point which is then cancelled out during the processing of the magnetic data.

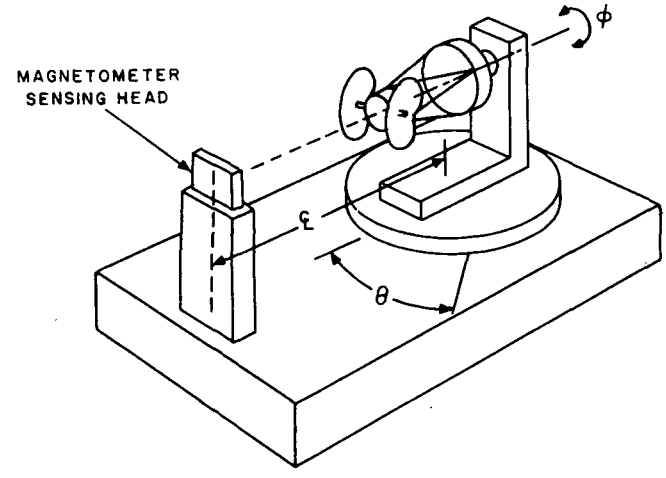

Figure 6.3-1. Magnetometer Test Setup

The presence of ferromagnetic bodies near the test site will introduce an error into the results because the field-lines will tend toward these bodies and distort the near-field structure. The presence of underground, or otherwise unknown, ferromagnetic bodies can be detected by observed anomalies in the local geomagnetic field. The test site should be located so as to avoid these. A facility of this type presently exists at the Astro-Electronics Division of RCA and was built after a magnetic survey indicated that the chosen site was relatively free of disturbing bodies.

Despite attempts to eliminate ferromagnetic material on board the spacecraft, varying amounts still remain on some space vehicles (e.g., those with nickel-cadmium cells). The effects of these materials on the dipole test may be divided into two major categories. The first effect is that of residual magnetism in the material; it will be measured as if it were a permanent polarization. If the residual magnetism of the vehicle changes under severe vibration (e.g., under launch conditions), the dipole will change from the measured value and, to this extent, is unpredictable and represnets a source of error. (This is also the case for permanent magnets.) The second effect is geomagnetic distortion due to permeable materials in the spacecraft. This effect depends upon the shape, location, and amount of material. Qualitatively, a ball of material located at the center of rotation would not introduce any error because the induced field due to it would be constant at the sensor under vehicle rotation. Similarly, a long rod would not contribute any error because its effect at the sensor would be a double-frequency field and not a dipole field under spacecraft test positioning. More complicated geometries and locations of ferromagnetic material on board the spacecraft can lead to a non-zero error. In these cases, each situation must be analyzed individually. However, for small quantities of material, the induced-field contribution to the measurement may usually be neglected and, if the measurement were made in a field-free environment, this problem would not be present.

The effects discussed in the previous paragraph lead to an error in the ability to measure the spacecraft dipole and a consequent change from the ground-determined value. However, data feedback from a number of vehicles indicate that this change may be partially predictable. For example, the difference between on-ground dipole measurement and observed in-orbit dipole has consistently been in one direction; this is illustrated in Table 6.3-1. The orbit-bias is the magnetic-bias dipole that is added to the ground measurement to obtain the in-orbit observed dipole.

Note that in the Table, vehicles A and B required a larger orbit bias than did vehicles C and D. This decrease in orbit-bias occurred when degaussing was applied to the spacecraft whip antennas prior to both ground measurement and launch. The disturbance analysis in Section 2.3.4 used an assumed orbit-bias of 1.0 ATM^2 about all three spacecraft axes (a conservative estimate). Continued observation and feedback from future in-orbit vehicles, plus experiments on the response of permanent magnets to vibration and shock, should put the ferromagnetic change error on at least a semi-quantitative basis and permit the use of more realistic dipole values.

TABLE 6.3-1. COMPARISON OF OBSERVED AND MEASURED RESULTS

(Orbit Bias is the Difference Between
Measured and Observed Values)

Vehicle	Orbit Bias (Ampere-turn-meter^2)
A	-0.8
B	-0.62
C	-0.155
D	-0.23
E	-0.2

6.4 HORIZON SENSOR

Component-level horizon-sensor tests will be performed in a manner similar to that now utilized for the TIROS program. The tests will be used to determine the following parameters.

- Field of view using a collimated source
- Electronics gain-noise and time-constants (over temperature) utilizing standard electrical measuring equipment
- Bolometer resistivity (over temperature)
- Bridge-circuit null and stability (over temperature)
- Sensor response to a simulated sun-input
- Sensor output response utilizing an extended IR source and a chopper (the response will be determined for an equivalent source temperature from 200°K to 300°K and for sensor rotational-rates (or equivalent chopping rates) of from 75-rpm to 225-rpm)
- Sensor output-noise utilizing a noise-spectrum analyzer.

System-level tests will require outputs from the sensors to operate the pitch-axis-stabilization control subsystem and to check out the attitude-telemetry functions. Careful measurement must be made to determine any effects on the sensor output due to spacecraft RFI and due to magnetic-disturbances as the sensor rotates with the flywheel. This requirement leads to the desirability of performing all system tests in a carefully shielded area. A simple, extended, IR source should be satisfactory for these tests because the predicted threshold-to-noise ratios are presently 5 to 1. However, careful experimental design must be performed to ensure that there are no unwanted "hot-spots" over the background area that is scanned by the sensors. A simulation of the sun-input will be utilized to check the accuracy of the proposed gating technique for blocking sun-inputs to the pitch-axis-stabilization control subsystem.

Section 7.0

SYSTEM ENGINEERING

7.1 GENERAL

Various types of designs for implementing the flywheel stabilized, magnetically torqued attitude control system (FSMTMS) on meteorological satellites were investigated during the Study Program. As a result of the parametric studies discussed in detail in Section 3.0 of this report, a final design was tentatively selected. The mechanical design, the power requirements during the modes of operation, and the system interfaces for power, telemetry, and command and control are summarized in the following paragraphs.

7.2 MECHANICAL DESIGN

The general arrangement of the FSMTMS control and stabilization system mounted onto a base sensor-ring is shown in Figure 7.2-1.

7.2.1 Control-Equipment Packaging

The control equipment added to the sensor ring is in two packages, an upper assembly and a lower assembly. The lower package consists of an annulus tube filled with fluid which serves as a viscous damper. A momentum-torquing coil is bonded onto the periphery of this tube. Also mounted to the annulus is a despin yo-yo installation. This complete subassembly is then easily attached to the base sensor-ring.

The upper package consists of a flywheel-drive assembly as shown in Figure 7.2-2. The housing of this assembly is used as part of the structural backbone. The balance of this assembly contains all the associated electronic units of equipment, including the QOMAC coil and pitch-axis control rockets. This second assembly may be pretested and operated prior to assembly on the tubular truss.

The numbers on the drawing of Figure 7.2-1 represent weight item locations. A weight statement and moment-of-inertia data about the centroidal principal-axes (which have been caused to coincide with the yaw, pitch, and roll axes of the spacecraft) are presented in Table 7.2-1. The RTG power units have been physically located eccentric to the roll-axis trace which allows clearance for an abortive launch ejection; however, for center-of-gravity and moment-of-inertia computations, the RTG units have been considered concentric to the same trace. The moment-of-inertia calculations show the final values as well as values obtained in the initial calculation; the two sets of values are within approximately 5% of each other. The preliminary values have been used in all control-system analyses.

7.2.2 Control-Equipment Geometry

The viscous damper tube is a 1.00" O.D. x 0.049" aluminum wall alloy tube rolled to the annulus diameter and welded into a ring. To compensate for large temperature changes resulting from orbit day and night exposures, thermal expansion is provided using the spring-loaded piston (2) as indicated in the figure. Dual "O" rings are provided as redundancy against leaks, and a final sealing cap should be used to prevent any fluid leakage to space. The installation of proper mass and cable length for the yo-yo despin-device is based on extensive RCA experience. Any new techniques (e.g., elastic properties of the cable) will be incorporated as they are developed.

The upper package assembly in Figure 7.2-1 shows the use of a dual flywheel with each individual wheel being a single bar with weights (including bolometers) at its extremities. The two flywheels are mounted at the ends of a common drive shaft

Page intentionally left blank

Page intentionally left blank

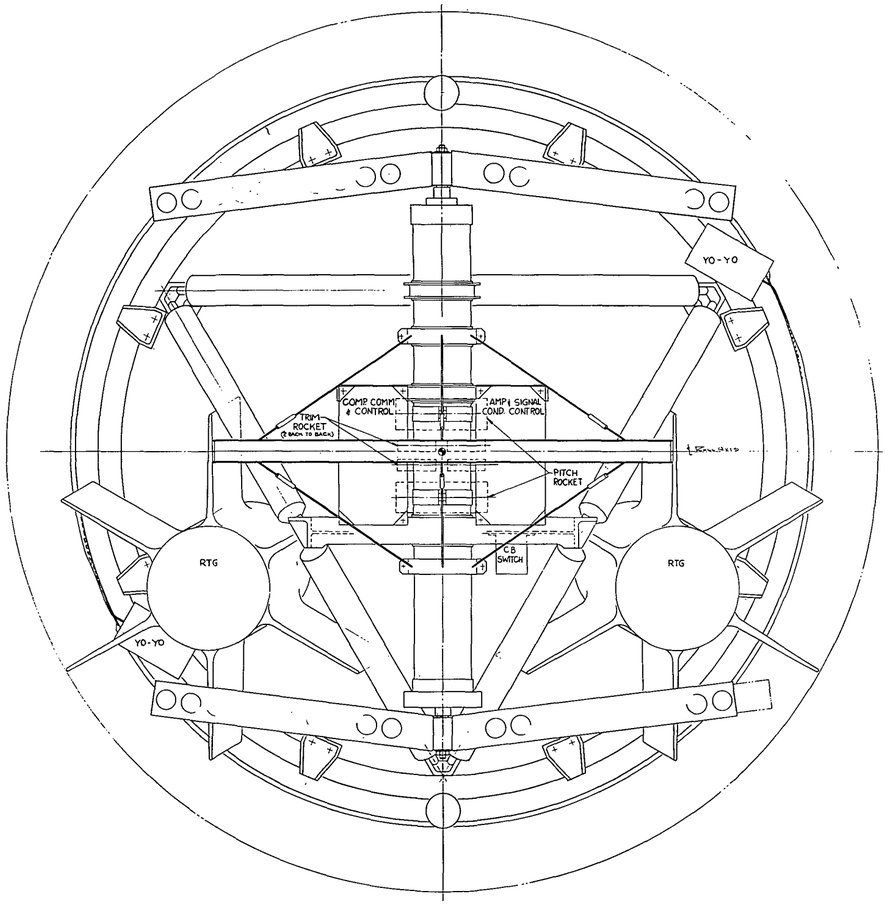

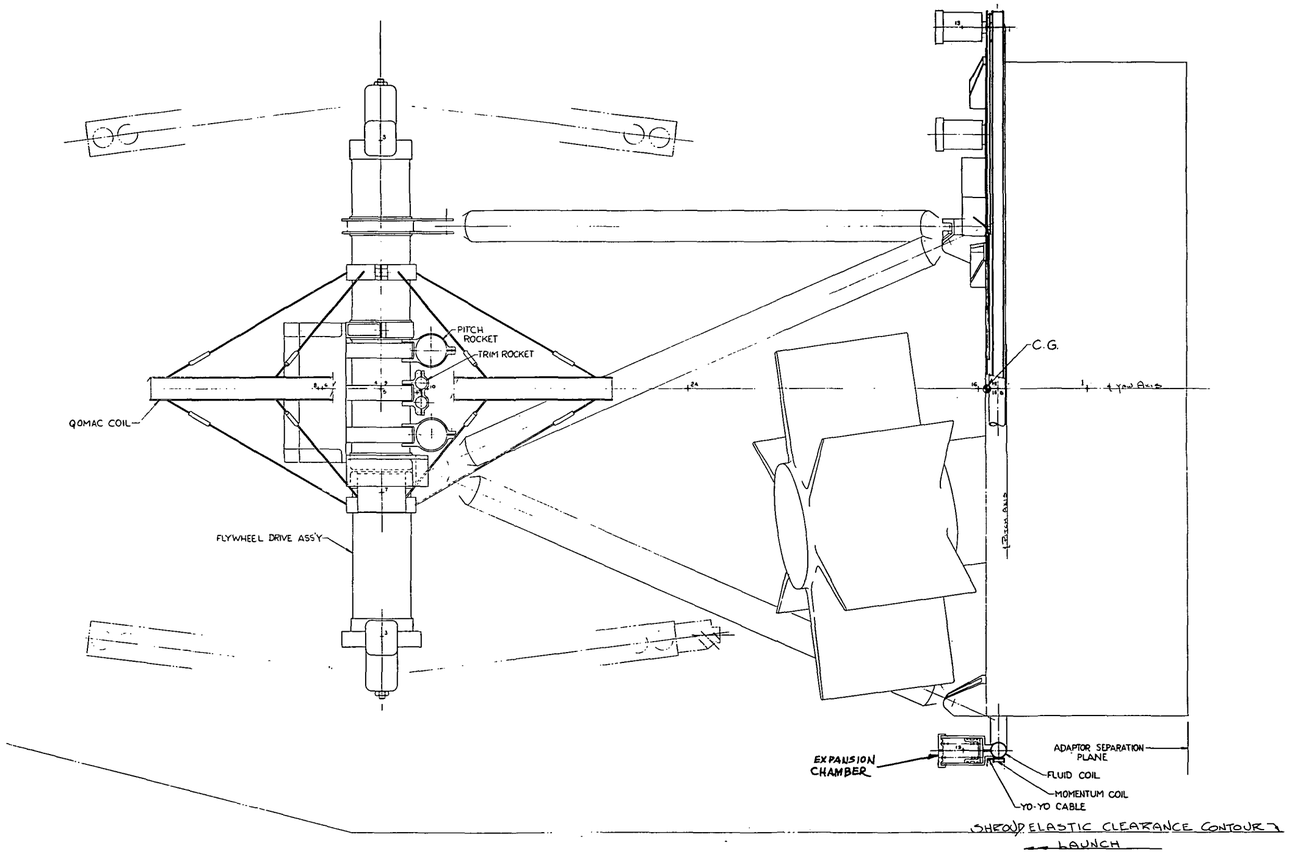

Figure 7.2-1. General Arrangement of the Gyromagnetic-Stabilization System

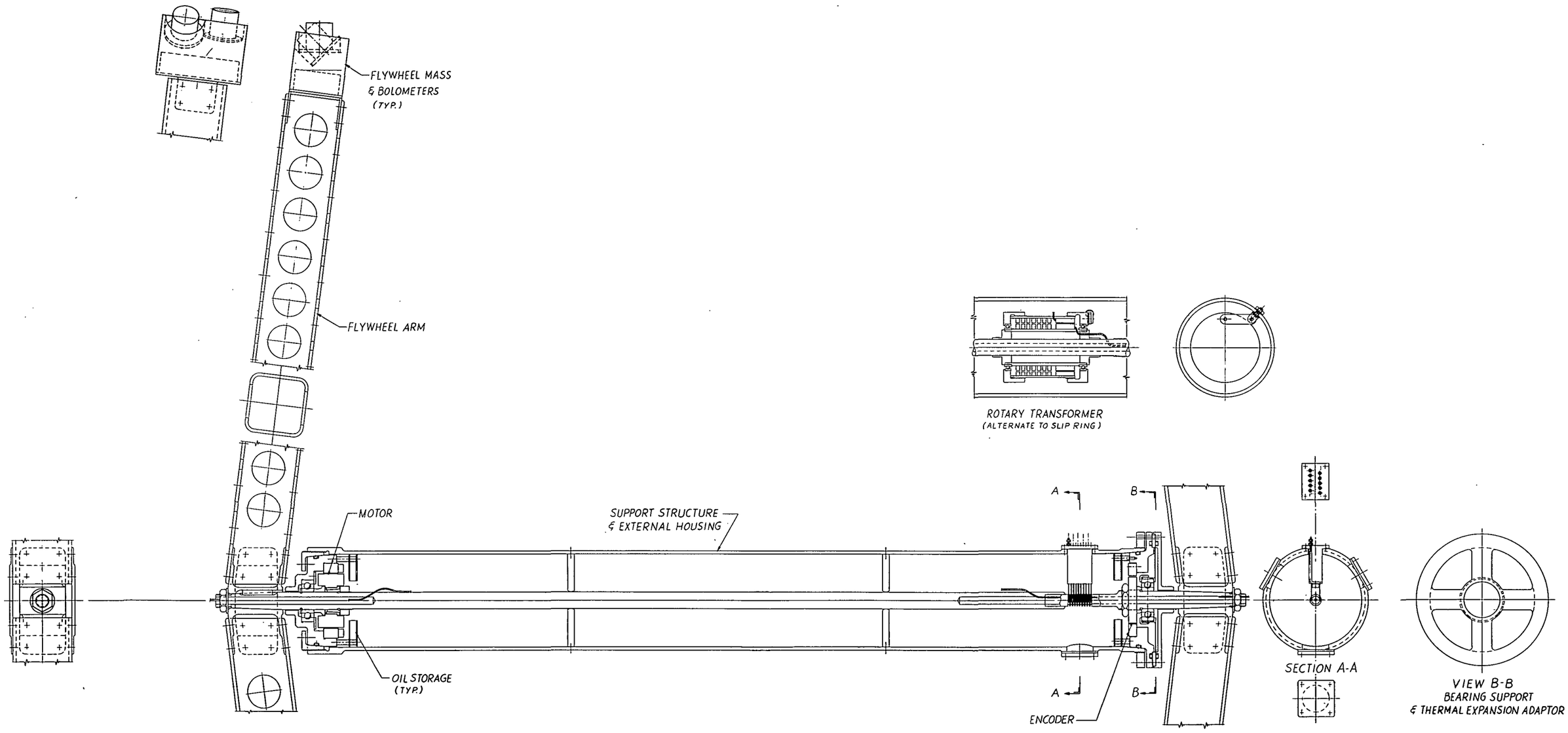

Figure 7.2-2. Flywheel-Drive Assembly of the Gyromagnetic-Stabilization System

TABLE 7.2-1. SUMMARY OF WEIGHT AND MOMENT-OF-INERTIA DATA FOR FSMTMS SYSTEM

TABLE 7.2-1. SUMMARY OF WEIGHT AND MOMENT-OF-INERTIA DATA FOR FSMTMS SYSTEM

Item No.	Item	Weight (W) (lbs.)	Distance From Separation Plane (D) (inches)	WD (lb.-in.)	Yaw-Axis Moment-of-Inertia (lbs.-in.^{2})	Pitch-Axis Moment-of-Inertia (lbs.-in.^{2})	Roll-Axis Moment of-Inertia (lbs.-in.^{2})
	Sensor base structure	67.20					
	Thermal control	20.80					
	Harness	25.00					
	Batteries	30.00					
	Cameras ACVS & HRIR	58.10					
	Clock	33.20					
	PCM	20.00					
	Transmitter	5.00					
	Beacon and killer	4.50					
	Tape recorder (2)	36.00					
	Recorder	10.00					
1	Uniformly distributed to base	309.60	6.5	2010	62000	51000	51000
-	Adaptor to launch vehicle	43.70	-	-	-	-	-
2	RTG 2 units @ 35.00	70.00	20.8	1460	15700	11100	4140
2A	Truss tubes 6 pieces	4.80	32.0	154	940	2905	2905
	Total supplied by customer	428.10	-	-	-	-	-
3	Flywheel units 2 pieces	11.34	52.0	590	2700	21380	20400
4	Stabilite housing assembly	7.64	52.0	398	650	11650	12300
5	Structure on housing	1.22	52.0	63	122	1170	2160
6	Amplifier and signal conditioner	2.50	55.9	140	53	4620	4660
7	Coil bias stepping switch	.90	52.0	47	57	1380	1510
8	Computer command control	3.80	56.2	213	81	7100	7100
9	QOMAC coil and support	2.00	52.0	104	210	3510	3300
10	Pitch rockets installed	2.50	49.1	123	22	3230	3290
11	Trim rockets installed	.90	49.8	45	14	1230	1220
12	Fluid damper tube	1.55	12.2	19	840	420	430
13	Fluid damper thermal relief	1.00	14.4	14	540	7	545
14	Damper fluid	3.48	12.2	42	1890	942	965
15	Momentum coil	1.60	12.2	19	950	460	460
16	Yo-yo despin device	4.50	13.5	61	-	-	-
	Total supplied by contractor	44.93	-	-	-	-	-
	Total gross at launch	473.03	-	-	-	-	-
	Spacecraft (Total gross less adaptor)	429.7	12.9	5502	86769	122104	116385
	Inertia values used for all design computations				90720	130317	123487
	Flywheel rotational moment-of-inertia $I_F = 11.34 \times (17.5)^2 = 3480$ lbs.-in.^{2} $\frac{\text{Spacecraft } I_p}{\text{Flywheel } I_f} = \frac{130317}{3480} = 37.5$						

which, in turn, is bearing-mounted into a housing. Other essential parts such as the motor, encoder, slip rings, and lubrication are contained within this housing; this housing also provides part of the structural backbone of the upper package. The remaining structure is supplied by an attached "I-section" beam and a collar.

Layback of the flywheel arms is provided to ensure that the vector of the total single flywheel mass passes through the bearing when applied torques coincide with yaw or roll axes. This design provides a minimum bending-moment system on the drive shaft, and causes the shaft-deflection slope at the bearings to be zero. The zero-slope protects the non-self-aligning bearings and maintains radial position of the shaft-mounted parts to the fixed parts for the motor and encoder.

The dual-flywheel geometry provides the following advantages:

- The geometry forms a symmetrical mass-distribution with respect to the principal axes, thereby facilitating mass balancing and minimum weight for the spacecraft.
- The single-bar flywheel permits easy construction. The large-diameter of the flywheel is the only logical means of supplying the required rotational flywheel-momentum while preserving a low control-system weight.
- The side-scanning bolometers mounted into the flywheel weights can scan a field of view unobstructed by the spacecraft.
- The redundancy of bolometer units is easily accomplished by using identical mass units at all four extremities of the dual flywheel.
- Static radial loads on the bearings are minimized by the use of the dual-flywheel geometry.

The flywheel-arm material is a fiber-glass epoxy selected to minimize interference with any antenna field. The shaft-bearings selected are Barden Corp. bearing 203K code 3 which is an open bearing with a steel retainer. This bearing has a radial play of 0.0002/0.0004 and a thrust play of 0.004 nominal. Static-load ratings of 2720 pounds thrust and 1000 pounds radial have been assumed for zero rpm and are in excess of any loads developed during launch environment.

7.2.3 Electro-Mechanical Design

Because the flywheel will operate in a zero-G environment in orbit, the only load on the bearings will be due to misalignment or stray input, and will be of very small magnitude. Operation under such "no-load" conditions will produce long-life expectancy.

The possibility of large differential-axial thermal expansion between the shaft and the housing exists and has been compensated for by causing the bearing at one end to be capable of taking thrust in either direction. The bearing at the other end will

not take thrust in either direction; this is accomplished by mounting the bearing in a diaphragm (which may deflect out-of-plane at extremely-light thrust load) which is capable of sustaining all radial-load imposed. With this system of suspension, the only play existing at the bearings is that between the inner and outer "races", thus minimizing the eccentricity between rotating and fixed parts of the motor and encoder. Preloading of a bearing (as a means of rolling the balls up the "races") to eliminate any play under vibratory loading is impractical. The thrust-load upon the bearings may be 15-pounds at 1-G which, with a prototype input of 10-G (6Q), gives a thrustload of 900 pounds. If preloads of this magnitude were devised, then the bearing would be loaded to 900 pounds during operation (with consequent high-friction force, wear, and short life expectancy). The anticipated bearing-friction for each bearing installed and with no preload is

At 1-G and 150 rpm = 0.18 to 0.20 inch-ounces

At 0-G and 150 rpm = 0.07 to 0.10 inch-ounces

If a preload of 900 pounds were used, the bearing would show (900/50) (0.70) = 12.5 inch-ounces.

Some lubrication is required for the bearings, motor brushes, and slip-rings to prevent high-friction and wear of adjacent parts in the gas and moisture-free space environment. A proposed system based on some experience is to store a sponge-type reservoir of instrument oil inside the housing (per MIL-O-6085A). The details concerning the operation of brushes in the space environment is discussed in Section 3.3.1.10 of this report as is the choice of a proper lubricant. Extensive RCA experience indicates that, while the brushes normally present the severest limitation on the electro-mechanical operation of the system, a fully satisfactory solution to this problem has been evolved in the present system. Moreover, there is considerable experimental data on the operation of bearings in the space environment and no serious problem should be encountered if the proposed design is utilized.

A labyrinth-type seal (the clearance is kept small between the housing and the shaft) is used to meter any molecular exit from the otherwise-entrapped atmosphere. In time, the interior will become a vacuum harder in nature than the vapor pressure of the stored oil. Some oil will then evaporate into the trapped atmosphere, and molecular movements will cause contact with and lubrication of all parts. As molecules leak past the labyrinth, the process repeats for the life of the spacecraft.

Figure 7.2-2 illustrates the use of slip rings for the transmission of bolometer signals. While this is the simplest and lightest system, wear and noise characteristics under the indicated environment have not been fully established for the linear-travel required. Although extrapolation of life-expectancy data gives reasonable expectations, an alternate system of signal transmission is also proposed using a bank of rotary transformers. An actual unit of this type will require further detailed study and development.

Static balance and dynamic rotational-balance at 150 rpm, to limits of accuracy which shall be determined at the time of manufacture, will be applied to the flywheel and housing complete assembly.

A detailed vibration and structural analysis of the pertinent parts was made. [3]

The slip-ring system of earth-IR signal transmission may offer reliability problems; therefore, a circumventing technique using rotating mirrors and fixed bolometer heads was also studied. Figure 7.2-3 shows an arrangement, using a double-surface mirror mounted on the flywheel shaft at the proper skewed-angle and reflecting signals to the fixed bolometer heads.

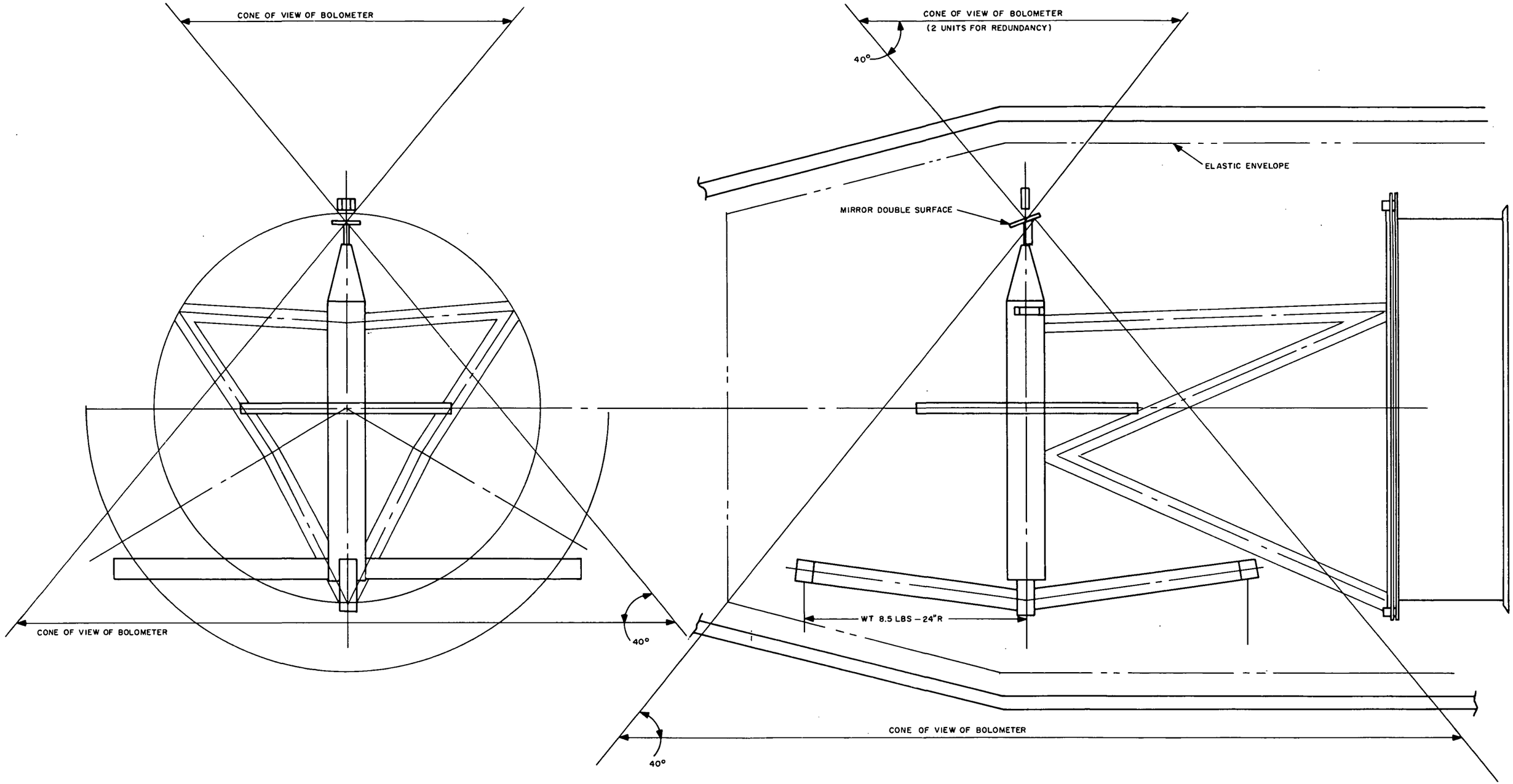

Figure 7.2-3. Mirror Arrangement for the Gyromagnetic-Stabilization System

7.3 SYSTEM POWER REQUIREMENTS

7.3.1 Initial Alignment or Transient Upset

Two modes of system power utilization can be isolated. The first mode occurs during initial alignment, or during recovery from a large transient upset; this mode consists of the power requirement drains given in Table 7.3-1.

TABLE 7.3-1. INITIAL ALIGNMENT MODE POWER REQUIREMENTS

Item	Power Drain at -24.5 Volts Input	Operation Time	Watt-Minutes
High-Torque QOMAC Coil	4.26 watts	20 orbits maximum - 2080 minutes	8850
QOMAC Programmer and Decoder	2.00 watts	2080 minutes	4160
Momentum Coil	0.48 watts into 70% efficient converter	30 cycles maximum - 15 orbits - 1560 minutes	750
Momentum Programmer and Decoder	2.00 watts	1560 minutes	3120
Pitch-Axis-Stabilization Control Subsystem (Including "Vee" Sensors)	4.3 watts	2080 minutes maximum	8950
	14.2 watts	15 minutes maximum	213
	4.8 watts	22 orbits - 2290 minutes	11000
Telemetry Control Unit	1.00 watts	15 minutes maximum 42 orbits - 630 minutes	630
TOTAL			37673

A power profile for this mode is given in Figure 7.3-1(a). It should be noted that the QOMAC, momentum-control, and peak pitch-axis control operations do not occur at overlapping times during the initial alignment procedure. A total initial alignment period of 3 days (42 orbits) has been assumed in the worst-case. The total average power drawn during this period is 8.5 watts.

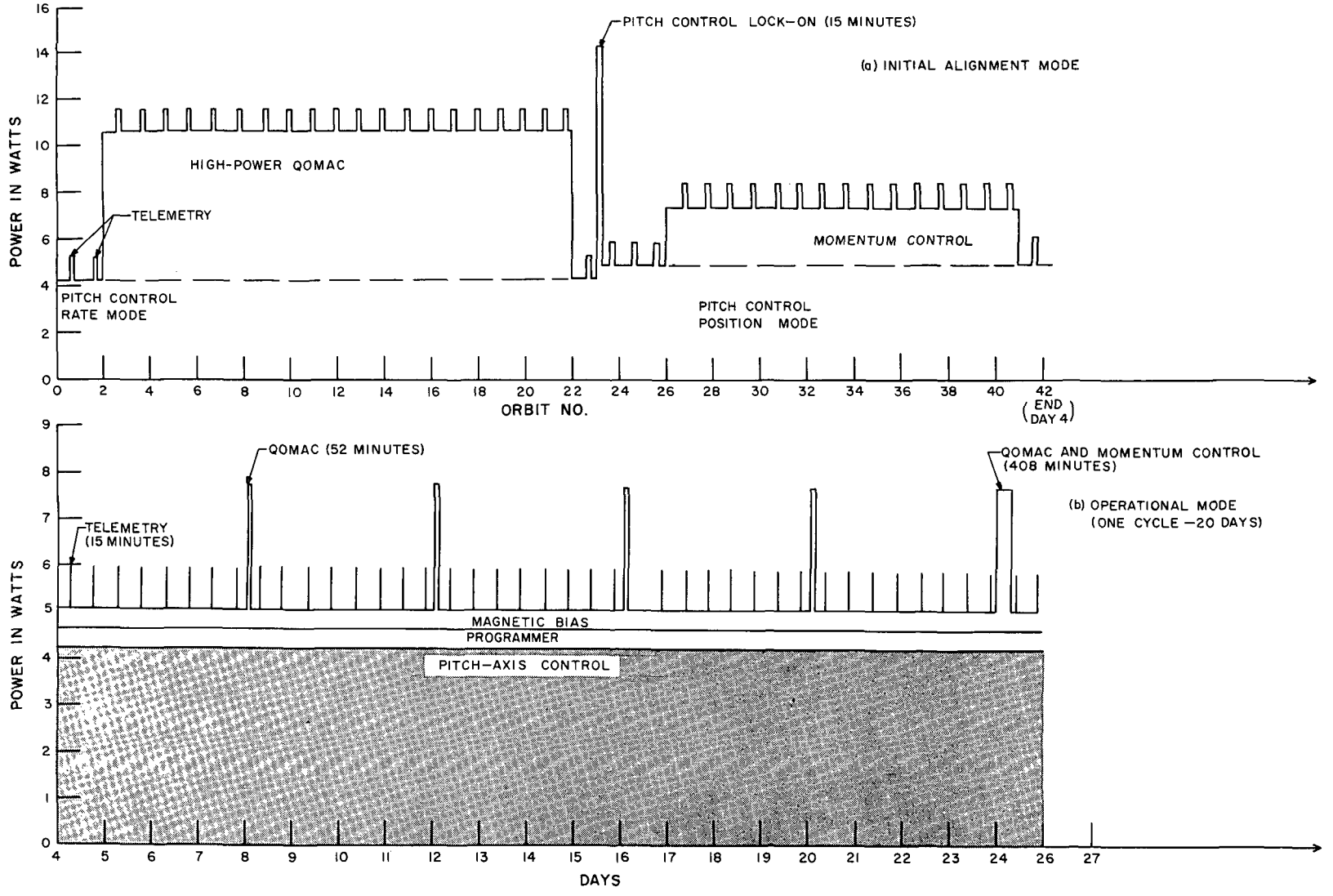

Figure 7.3-1. System Power Profile (Worst-Case Conditions)

7.3.2 Operational Mode

Once the initial alignment is completed, normal system operation will begin. The power utilization for the operational mode is summarized in Table 7.3-2.

A power profile for this mode is given in Figure 7.3-1(b). The total average power drawn by the system is 5.33 watts.

TABLE 7.3-2. NORMAL OPERATIONAL POWER REQUIREMENTS

Item	Power Drain at -24.5 Volts Input	Operation Time	Equivalent Continuous Drain
Pitch-Axis-Stabilization Control Subsystem (Including "Vee" Sensors)	4.8 watts	Continuous	4.8 watts
Magnetic-Bias Coil	0.204 watts into 70% efficient converter	Continuous	0.204 watts
QOMAC/Momentum Programmer and Decoder	0.25 watts	Continuous	0.25 watts
	2.0 watts QOMAC	1/2 orbit or 52 minutes every 4 days maximum	0.018 watts
	2.0 watts QOMAC	1 orbit every 20 days maximum	0.007 watts
	2.0 watts Momentum Control	2.5 orbits every 20 days maximum	0.018 watts
QOMAC Coil	0.5 watts into 70% efficient converter	1/2 orbit every 4 days maximum	0.005 watts
		1 orbit every 20 days maximum	0.002 watts
Momentum Coil	0.48 watts into 70% efficient converter	2.5 orbit every 20 days maximum	0.004 watts
Telemetry Control Unit	100 watts	15 minutes maximum twice a day	0.021 watts
TOTAL			5.33 watts

7.4 SYSTEM INTERFACES

The mechanical interfaces with the spacecraft of the FSMTMS Attitude-Control System were discussed in Section 7.2 of this report. Therefore, only the electrical interfaces are discussed in this section.

7.4.1 Power

All power to the system will be supplied at -24.5 volts from the spacecraft. Power requirements were summarized in Section 7.3.

7.4.2 Telemetry

All attitude-telemetry and required switching commands will be routed through the attitude-data telemetry control subsystem. The operation of the telemetry subsystem is defined in Section 3.6.6.3 of this report.

All housekeeping-telemetry data will be routed directly to the spacecraft telemetry subsystem for transmission to the ground station. The points to be telemetered were summarized in Section 3.7.3. There are a total of 36 parameters plus 10 spares (for future use) which will be monitored. All data will be conditioned in the control subsystem to assure compatibility with the spacecraft telemetry-subsystem voltage and impedance levels.

7.4.3 Command and Control

A discussion of the interface between the Nimbus "C" clock and the command and control subsystem is presented in Section 3.6 of this report. The clock will be used to: receive and transmit all real-time commands to the command and control subsystem; supply a 1-pps output for utilization by the attitude-momentum programmer; store the start time, T_0, for the program; and open an interface gate that permits direct transmission from the ground station to the programmer.

Section 8.0

APPROACH TO SYSTEM SPECIFICATIONS

8.1 GENERAL

This section of the report defines the approach that must be taken to evolve the required system, subsystem, and component specifications for development of the FSMTMS control system. The approach basically includes three levels of required specifications,

- System Input Specification
- Subsystem Specifications
- Component (defined here as a functional element, e.g., amplifier, QOMAC coil) Specifications

Each level of specification is discussed separately in the following paragraphs.

8.2 SYSTEM INPUT SPECIFICATIONS

The system-input level of specification defines the criteria and constraints upon which all design, test, and auxiliary functions are performed. A block diagram form of the type of specifications that will be required is shown in Figure 8.2-1. The development of these specifications will probably be based on requirements defined by detailed operations analyses; this level of specification should be completed prior to any design effort on a system-component level. The notes in Figure 8.2-1 define the sections of this report where the details are presented.

Page intentionally left blank

Page intentionally left blank

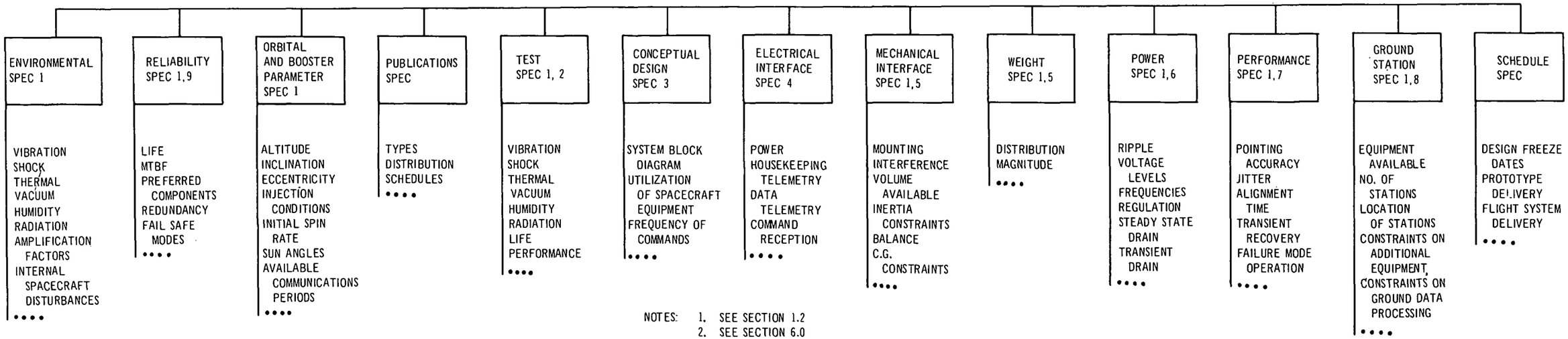

NOTES:
1. SEE SECTION 1.2
2. SEE SECTION 6.0
3. SEE SECTION 1.4
4. SEE SECTION 7.4
5. SEE SECTION 7.2
6. SEE SECTION 7.3
7. SEE SECTION 4.0
8. SEE SECTION 3.8
9. SEE SECTION 5.0

Figure 8.2-1. Gyromagnetic-Stabilization System Input Specifications

8.3 SUBSYSTEM SPECIFICATIONS

Effort must be devoted to the development of a set of Subsystem Specifications; this effort will be subsequent to, and in some cases parallel with, the effort devoted to evolving the System-Input Specifications. The development of the Subsystem Specifications includes the major portion of the analytical work and includes the following tasks.

- Dynamical Analysis, including disturbance torques and cross-coupling effects
- Detailed preliminary accuracy analysis
- Subsystem performance budgets
- Subsystem power budget
- Subsystem weight budget
- Subsystem reliability budget
- Preliminary subsystem design
- Detailed evaluation and design for critical components
- Preliminary system mechanical layout
- Subsystem volume budget
- Subsystem interface study, both with other subsystems and with the spacecraft
- Ground-Station and data-processing study
- Subsystem and System test study

Many of these tasks have been performed during this study program and were discussed in Sections 2.0, 4.0, 5.0, 6.0, and 7.0 of this report. Preliminary results are available in all the task areas mentioned above.

Once the tasks detailed in this section are completed, then the specification can be written for all major subsystems of the FSMTMS attitude-control system. The required specifications are shown on the upper portion of Figure 8.3-1. The significant design parameters required to develop the Subsystem Specifications are discussed in the sections of this report noted in Figure 8.3-1.

Page intentionally left blank

Page intentionally left blank

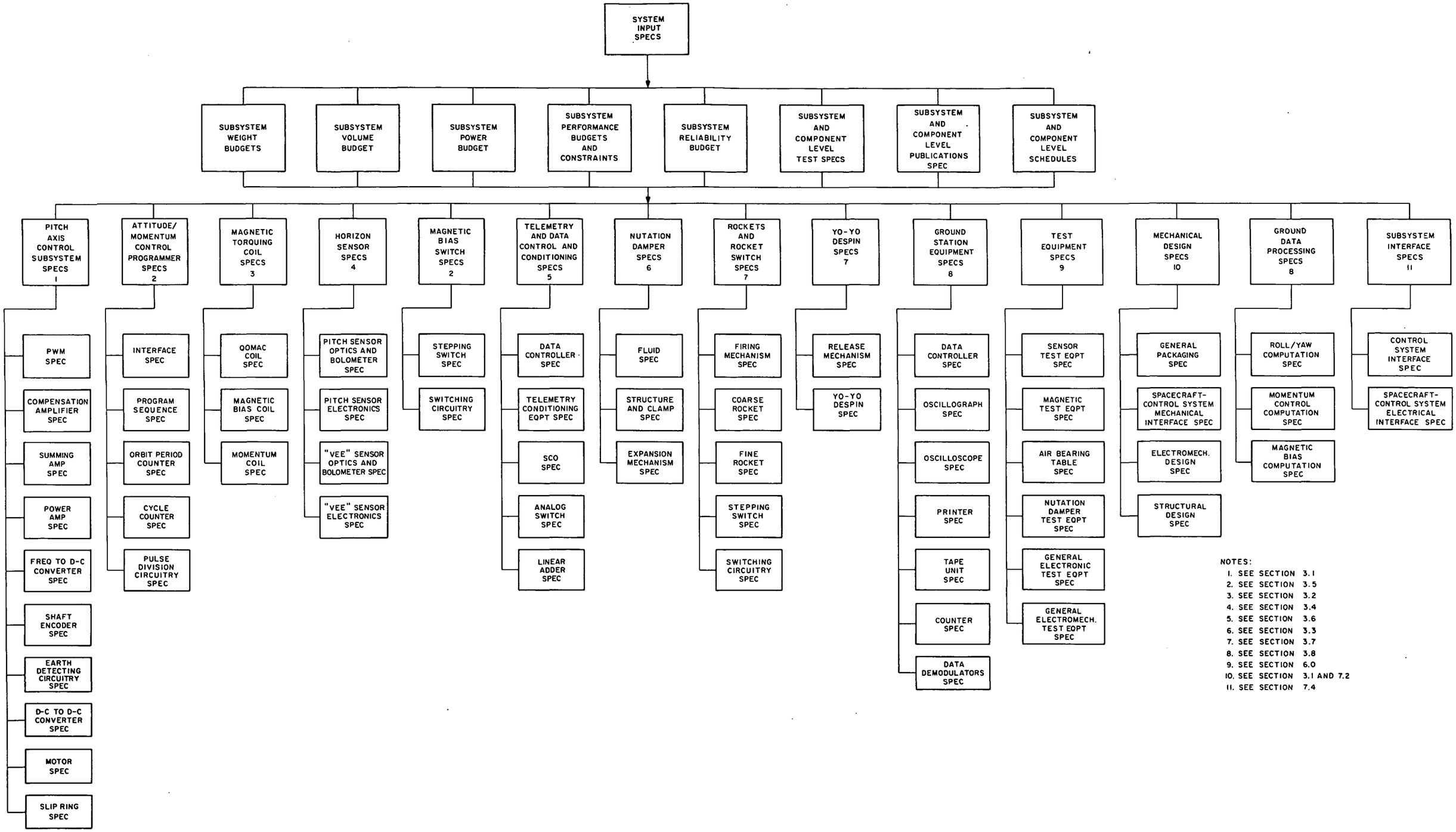

Figure 8.3-1. Gyromagnetic-Stabilization, Subsystem and Component-Level Specifications

8.4 COMPONENT SPECIFICATIONS

Detailed design effort can begin with the completion of the Subsystem Specification; however, it may be a continuation in the case of critical components. This design effort will lead to the development of complete specifications on a component level. The required component specifications are defined in the lower portion of Figure 8.3-1.

The component specifications are used in the construction of the complete control system and as an input-specification for the purchase of all vendor-supplied components.

Section 9.0

CONCLUSIONS AND RECOMMENDATIONS

9.1 CONCLUSIONS

9.1.1 Summary of Results

The results of the study can be summarized briefly as follows:

• Control System weight (with rockets)	45 lbs.
Control System weight (without rockets)	41.5 lbs.
• Continuous System power (average)	5.33 watts
Maximum (during initial alignment)	14.1 watts
• Accuracy of alignment	
Roll/Yaw axes	$<$ 0.8 degrees
Pitch-axis, random	0.52 degrees
Pitch-axis, known offset due to ±5% variation in momentum	± 0.6 degrees
Pitch-axis, known offset due to 3σ ellipticity (0.013)	± 1.3 degrees
• Jitter rates about all axes	$<$ 0.05 degrees/sec.
• Probability of success for one year	0.923

These values have some latitude of adjustment, but generally there are small possibilities of major changes in the weight or power. The gyromagnetic-stabilized attitude-control system, as shown by several designs on other applications, tends to be in the range of 10% of the total system weight. The power is not a strong function of weight; for the missions studied (which are similar to the meteoroligical mission), 6 to 8 watts is the general range. Therefore, confidence can be placed in the weight and power estimates because they were arrived at independently during this study program.

The accuracy figures for the performance of the roll/yaw axes are compatible with the orbit data for roll/yaw; however, the pitch-axis performance is based exclusively on laboratory experience.

The probability of success value of 0.923 has not been given a confidence factor because there is no statistical data available on the total system. The significance

of the number is that it was computed by precisely the same techniques used on all other systems developed at AED. It is, therefore, extremely useful for a comparison to other attitude-control systems.

9.1.2 Performance Verification

On the basis of this study program, and particularly section 6.0, the conclusion is drawn that air-bearing testing of the pitch-axis control subsystem is practical and will produce results which would add confidence to the spacecraft performance in orbit. It is very probable that air-bearing testing under vacuum condition can be closely approximated by reducing windage effects on the test device.

No direct magnetic-torquing of the final spacecraft or test structure is recommended because of the direct experience with orbit operation. Only measurements of the magnetic proporties of the spacecraft would be required.

9.1.3 Ground Stations

The study program has shown that minor changes would be required at existing Nimbus ground stations to accommodate the attitude-data acquisition. Figure 3.8-3 illustrates the ground-station components required to record the attitude data. It is likely that the printers and counters may be made available from existing equipment at the station because of the short time they would be required for attitude-data. The data-controller[3] would be supplied specifically for data acquisition and would be part of the gyromagnetic-stabilized attitude-control system development.

The spacecraft attitude-control command system is compatible with the Nimbus "C" clock which will be used to activate the roll/yaw and momentum control. Other commands would go directly into subsystems; however, these would be transmitted by the presently-available real-time command equipment.

9.2 RECOMMENDATIONS

9.2.1 Review Need for Rockets

The inclusion of rockets is a protection against two failures which are outside the worst-case of consideration. The first failure is a ±50% launch-vehicle spin-rate error. The +50% figure is almost impossible because the launch vehicle can not exceed a specified spin-rate by the physical limitations of the spin rockets. If the failure produces a spin less than nominal but even greater than 50%, then the control system can recover and operate. Therefore, the main consideration is whether proper orbit can be achieved when the launch-vehicle spin-rate is 50% or more below nominal.

The extensive RCA experience with yo-yo despin mechanisms indicates that a double failure is implied if they fail to release. Each mass has at least two pyrotechnic release pins and each pin has a failure rate of approximately 1 per 10,000 operations.

9.2.2 Development of the Pitch-Axis Drive

It is recommended that the design shown in Figure 7.2-2 be constructed as a working engineering model and operated in the closed-loop configuration in a vacuum chamber providing atmosphere of 1 to 2 x 10^{-6} mm of Hg. for periods long enough to ensure an equilibrium condition has been reached. On the basis of current tests at AED, this would be between 500 and 1,000 hours. If successful operation is experienced during this period, the results of earlier work[3] would indicate that wear rates can be determined with confidence. The closed-loop operation would ensure that the motor current and rotation speed would be close to that expected in orbit.

9.2.3 Pitch-Axis Attitude Sensing

The value ± 1.3 degrees due to elliplicity is listed in Table 4.3-1 under the column titled "Uncompensated Known Angular Errors." It is recommended that further work be done to determine the merits of an attitude-sensing system which would remove this known pitch-angle variation. One of the requirements to be considered is that, in the process of removing the known uncompensated error, the device should not introduce unknown or random error which is significantly greater than the ± 0.52 3-σ error imposed by the present sensing technique.

Consideration should be given to the performance of the sensor when the elliplicity is in the expected ranges as experienced by all Delta-launched spacecraft and not merely the 3 σ value of 0.013.

9.2.4 Alternate Sources for Pitch-Axis-Stabilization Control Motor

Several designs for brushless d-c motors are under development, and at least one is available as a standard item. These are motors whose speed-torque characteristics are similar to those of the Printed or Inland units, but which do not use brushes to achieve commutation. For this reason they are evaluated for possible use as the flywheel drive motor.

All brushless motors under consideration have a permanent magnet rotor and a wound stator. As the rotor turns, it is necessary to direct current flow in the various stator windings such that the resultant field flux is displaced 90^{o} from the rotor flux. If this is done at all speeds and for any angular position of the rotor, the torque output is precisely the same as would be obtained from a brush-type motor. Several different techniques for brushless commutation have been developed and are represented in the following designs.

9.2.4.1 Sperry-Farragut

Sperry-Farragut has available a high-speed instrument motor[11], and has proposed a low speed torquer whose characteristics are identical to the Inland T-1352[12]. The commutation technique utilizes a light-beam that rotates with the rotor and illuminates, in sequence, photo-conductive diodes mounted on the stator. The diodes, in turn, operate transistor switches which gate current to the proper stator windings.

In the high-speed design, a single light-beam, obtained by rotating a slitted shield around a stationary lamp, is used in conjunction with six field windings. Each field winding requires two photodiodes (one for each direction of rotation), five transistors, and eight resistors, or a total of 90 components for the six windings. In addition, six blocking diodes (external to the switching circuitry) are necessary, so that a total of 96 components, 42 of which are active, must be used to replace a brush-commutator set.

This particular design has a rated stall-torque of 2.7 ounce-inches and a no-load speed of 3900 rpm. Hence, a gear train would be necessary to make the motor compatible with the flywheel-drive requirements. On this basis, the only possible reason to recommend it over an ordinary two-phase instrument servomotor, which is also brushless, is its power efficiency, which should be twice as high. However, it is doubtful whether the higher efficiency is worth the price of the larger number of extra components. With the extra parts count and gear train taken together, there would appear to be no distinct advantage at all over the Inland brush-type motor.

The torquer configuration proposed by Sperry-Farragut is quite similar to the model just discussed in that it uses six field windings and the corresponding number of associated photo-diodes and transistor switches. However, the windings are arranged somewhat differently, and the rotating light-shield has five slits, each 12^{o}

wide. This arrangement results in 30 commutations per revolution which is comparable to conventional torquer operation.

Although the Sperry-Farragut does not have sufficient stall-torque capability to meet present FSMTMS requirements, there is no reason why straightforward design changes could not adapt it for this application. As far as is known, however, no working models have been built or tested, so the actual performance characteristics of this design are not presently known.

9.2.4.2 Inland Brushless Direct-Drive Torque Motor

In the Inland Motor Corporation design, only two field windings (placed 90 electrical degrees apart) are used. These are wound to create flux distributions which, for constant current, are proportional to $sin\ \theta$ and $cos\ \theta$ respectively, where θ is the angular electrical displacement of the rotor. The current in the windings is controlled by a resolver (of the differential-transformer type) that generates signals also proportional to $sin\ \theta$ and $cos\ \theta$. These signals are amplified, and current proportional to them is sent through the sine and cosine field windings. Thus, the torque interaction between the rotor and field is proportional to $sin^2\ \theta + cos^2\ \theta$, (i.e., it is constant for any rotor position)[13].

In this arrangement, the control system error would be in the form of an amplitude-modulated a-c signal which is applied to the primary of the resolver. The outputs must be demodulated and phase-detected before current amplification can take place. Thus, the components required to replace commutator brushes are: a signal modulator; a differential-transformer type resolver; two demodulators and phase detectors; and two power amplifiers. In a conventional system, only one of these components, a power amplifier, would be necessary.

9.2.4.3 Bendix Resolver-Fed Torquing System

The Bendix system[14] is essentially identical to the Inland Brushless torquer in that an integrally-mounted resolver is used to control the direction of stator flux. Maximum torque-interaction with the rotor is assured by mounting the resolver with the proper phase relative to the rotor. Initially it was proposed to use resolvers of the type with electrically-excited rotors. This arrangement is unsatisfactory because slip rings would be required to supply the excitation power. Later proposals, however, have included variable-reluctance type resolvers which are less accurate, but which do not require rotor excitation.

Being so similar to the Inland design, it is most likely that the same auxiliary equipment listed in the previous section would be required to operate the motor. As far as is known, the Bendix brushless motor is presently under development, but no data as to operating characteristics or performance capability are presently available.

9.2.4.4 Lear Siegler Brushless DC Motor

Lear Siegler, Power-Equipment Division is developing a motor[15] which makes use of a novel switching device, called the Magristor. This element has the characteristic of changing its resistance in the presence of a magnetic field. Such elements placed around the stator are used to sense the rotor's field, and hence the rotor's position. As the field moves past the Magristor, its resistance is lowered (by as much as 50 to 1), and this change causes a silicon controlled-rectifier to fire, thereby gating current through the appropriate field winding.

This system is exactly analogous to the Sperry-Farragut arrangement and, as such, would require approximately the same number of additional components. Thus far the only information available is for a development power unit not intended for control-system application. Models suited for use in servo systems have not been reported, and their status, if any, is presently unknown.

Table 9.2-1 is a summary comparison of several brushless DC motors. All require a considerable number of additional electronic components in order to eliminate the brush-commutator arrangement in conventional motors. The only unit available as a standard item is very poor in this respect because it also requires a gear train. Other units which exhibit somewhat less complication (the Inland and Bendix designs) are still in the development stage and, consequently, specific details concerning weight, power efficiency, stall-torque capability, and operating characteristics do not exist.

Both theoretical and laboratory results were given previously[8] which indicate that conventional brush-systems operate reliably in lubricant-vapor atmospheres. It was also shown that such atmospheres are easily maintained for extended durations. Therefore, in light of their inadequate state of development and increased complexity, it is presently felt that brushless DC motors do not represent a superior design choice, and the conventional brush-type motor is recommended.

9.2.5 Computer Analysis

To arrive at design values for the study it was necessary to make some simplifying assumptions as to the effect of moment-of-inertia distribution. In some cases, for the value of I_2 and I_3 (which are the yaw and roll inertia values respectively), the geometric mean, $I_2 I_3$, was used in the dynamic equations. It was also assumed that the roll, yaw and pitch axes were principal axes. It is recommended that a computer study be performed in the next phase of the program which utilizes the three values of moment-of-inertia and displace them from the spacecraft roll, pitch and yaw axes by the amount of tolerances anticipated. The tolerances are associated with the dynamic-balancing sensitivities in the yaw-axis case, and the ability to measure or compute the location of the other two principal axes. In all cases, the displacements should be in the range of 1^{o} or less.

TABLE 9.2-1. COMPARISON OF BRUSHLESS D-C MOTORS

MOTOR	PRINCIPLE OF OPERATION	STATUS OR AVAILABILITY	COMMENTS
Sperry-Farragut Instrument Motor	Rotating light beam. Photo-diode sensors.	Available as a standard unit.	Uses no brushes. Has power efficiency approaching ordinary brush-type motors. Light source can be made very reliable. Uses 96 components (42 active) to replace brush-commutator arrangement. Requires gear train to meet power specification, but cannot meet stall torque specification.
Sperry-Farragut Torquer	Rotating light beam. Photo-diode sensors.	In proposal stage, none have been built.	Uses no brushes. Has power efficiency approaching ordinary brush-type motors. Light source can be made very reliable. Uses 96 components (42 active) to replace brush-commutator arrangement. Direct drive requires no gear train. Actual operating characteristics unknown, since none have been built or tested.
Inland Direct Drive Torque Motor	Sine and cosine field windings. Current controlled by output of shaft mounted resolver	Prototype models have been built. Not a standard item.	Uses no brushes. Direct drive, no gear train necessary. Power efficiency somewhat lower than conventional torquer. Requires two power amplifiers, two demodulators, two phase detectors and one signal modulator.
Bendix Resolver-Fed Torquer	Current in field windings controlled by output of shaft-mounted resolver.	Under development.	Can be made to operate without brushes. Direct drive. Power efficiency somewhat lower than conventional torquer. Requires two power amplifiers, two demodulators, two phase detectors and one signal modulator.
Lear, Siegler Magristor	Rotating flux field sensed by Magristor components. SCR's used as current gates.	Prototype power unit has been built. No servo-motors have been developed.	Uses no brushes. Would have power efficiency approaching conventional brush-type motors. Would require large number of components (similar to Sperry-Farragust arrangement). Actual operating characteristics unknown.

Another goal of the computer analysis would be to discover possible sources of interaction between axes which could result in larger errors for alignment than those computed in the study. Of particular interest would be mechanisms by which torques about the pitch axis can produce sensible motion about the roll or yaw axes. In addition, all torques transverse to the pitch axis must be taken into account in developing the dynamic model.

It is likely that a hybrid computer will be required for the study. The analog portion would simulate the pitch-axis performance, while the digital would be used to solve the Euler equations of the spacecraft.

9.2.6 Data Transmission

During the study, a brief investigation was made of several optical techniques for scanning the earth with the IR bolometers. Figure 7.2-3 is a sketch of at least one method. It is recommended that this effort be pursued further as a possible replacement for slip rings or rotary transformers which are required when the sensors are mounted directly on the rotating flywheel.

The flywheel will carry a total of six horizon sensors and the associated output amplifiers, thus requiring both signal and power transfer across the rotary interface between the flywheel and the main structure. Specifications for the transfer are as shown in Table 9.2-2.

TABLE 9.2-2. SIGNAL AND POWER TRANSFER SPECIFICATIONS

Parameter	Signal Channels (Each)	Power Channel (Total)
Voltage Range	0 - 5 volts	24.5 volts
Current	$\approx$ 0.05 ma	25 ma
Allowable noise	< 10 mv	< 50 mv
Bandpass	50-500 cps	d-c

Both slip rings and rotary transformers can be used to meet these requirements.

9.2.6.1 Slip Rings

The two major problem areas associated with the use of conventional slip rings are those of wear and noise under vacuum conditions. However, experience has shown that a suitable choice of materials and proper lubrication technique will assure successful performance. The four materials combinations shown in Table 9.2-3 all have demonstrated reliable operation at low pressure ambients.

TABLE 9.2-3. MATERIALS COMBINATIONS

Brush	Slip Ring	Lubrication Technique	Reference
Paliney 7	Coin Gold	Oil Vapor Atmosphere	Unpublished work performed at AED
80% Ag, 15% C 5% MoS_2	Coin Silver	Dry (MoS_2)	(16)
50-80% Ag 50-20% C	Copper Silver Gold	Oil Vapor Atmosphere	(4)
Ag - MoS_2	Silver	Dry (MoS_2)	(17)

The Paliney 7 brush/Coin Gold ring combination has been used at the RCA Astro-Electronics Division in the testing program previously described.[4] Almost 4 months of operation at ambient pressures of 10^{-5} to 10^{-3} mm Hg has been accumulated. Signal quality has not deteriorated and no wear has been noticed. The ambient pressures were maintained by means of a reservoir of oil having a vapor pressure in the desired range. The same technique can also be applied to Silver-Graphite brushes running on Gold, Silver, or Copper slip rings, because laboratory tests indicate that the noise and wear associated with high vacuum do not appear until pressures of 10^{-6} mm or lower are reached. Oil vapor atmospheres of 10^{-5} mm or higher, which are very readily maintained for as long as desired, provide adequate lubrication for these materials.

Rolling-element slip rings have been suggested as an alternative to conventional ring-wiper arrangements.[18] These devices are designed to operate in hard vacuums (10^{-8} mm of Hg 48 and lower), and are dry lubricated. The best results were obtained using gold plated 440C balls and races in a standard thrust-bearing arrangement, a retaining ring machined from an 85% Gold, 15% MoS_2 compact, and an initially applied MoS_2 suspension. A life of 115×10^6 revolutions has been reported for this combination. However, the use of dry-lubricated systems is always suspect because the testing under space-simulated conditions is extremely difficult. The vacuum which occur in spacecraft where no attempt has been made to maintain an atmosphere are apt to be considerably lower than those practicably attainable in environmental test facilities. Unless unforseen problems with vapor-lubricated systems are uncovered, this is the recommended approach.

9.2.6.2 Rotary Transformers

Rotary transformers[19] are analogous to static transformers, except that the primary winding rotates concentric to the secondary, and the mutual inductance is not a function of angular position. Thus, signals may be transferred from rotating

parts with no contact whatsoever. However, the simultaneous transfer of d-c signals or power is not possible, and the input-output linearity of the device is poor in the low-frequency range.

The signal frequency content indicated in Table 9.2-2 can be accommodated by standard designs without too great an increase in unit size. There is no modulation problem due to run out, and cross-talk at such low frequencies is negligible. The d-c power cannot be transferred unless it is chopped and then rectified after being transformed; however, the power for all six horizon sensors and amplifiers can be sent through a single chopper-transformer-rectifier combination.

No definite recommendations as to the use of rotary transformers can be made at this time. Although their characteristics are reasonably well suited for this application, they are a relatively new device and the performance has not yet been adequately proven. A test program for this purpose should be undertaken. It is quite possible that a hybrid system will prove optimum, where rotary transformers are used to transmit the horizon sensor output signals, and a brush-slip ring arrangement (large area Silver-Graphite brushes) is used to transmit the d-c power.

Section 10.0

BIBLIOGRAPHY

(1) Monthly Progress Report No. 1, Contract No. NAS5-3886, Flywheel Stabilized, Magnetically Torqued Attitude Control System for Meteorological Satellites, dated July 10, 1964, RCA Astro-Electronics Division to NASA, Goddard Space Flight Center.

(2) Monthly Progress Report No. 2, Contract No. NAS5-3886, Flywheel Stabilized, Magnetically Torqued Attitude Control System for Meteorological Satellites, dated August 10, 1964, RCA Astro-Electronics Division to NASA, Goddard Space Flight Center.

(3) Monthly Progress Report No. 3, Contract No. NAS5-3886, Flywheel Stabilized, Magnetically Torqued Attitude Control System for Meteorological Satellites, dated September 10, 1964, RCA Astro-Electronics Division to NASA, Goddard Space Flight Center.

(4) Monthly Progress Report No. 4, Contract No. NAS5-3886, Flywheel Stabilized, Magnetically Torqued Attitude Control System for Meteorological Satellites, dated September 18, 1964, RCA Astro-Electronics Division to NASA, Goddard Space Flight Center.

(5) Statement of Work and Specification for a Study of Flywheel Stabilized, Magnetically Torqued Meteorological Satellites, Prepared by NASA Aeronomy and Meteorology Division, Instrumentation Branch, Goddard Space Flight Center, Greenbelt, Maryland, dated February 1964.

(6) Proposal for a Study Program: Advanced Stabilization for Nimbus, Prepared by Astro-Electronics Division, Defense Electronic Products, Radio Corporation of America, RCA Proposal No. 63096-A, dated January 22, 1964.

(7) Internal Correspondence, RCA, Memo to I. Brown from H. Perkel, Subject: "Initial Alignment of FSMTMS", dated August 2, 1964.

(8) Thompson, "Introduction to Space Dynamics", John Wiley, New York, 1961.

(9) C. Usiskin and R. Wilkes, "Measuring the Magnetic Dipole of a Satellite", presented at the Sixth Symposium on Ballistic Missile and Space Technology, Los Angeles, California, August 1961.

(10) R. Moskowitz and R. Lynch, "Magnetostatic Measurement of Spacecraft Magnetic Dipole Moment" IEEE Transactions on Aerospace, Vol. 2, No 2, April 1964.

(11) Studer, P. A., "Development of a Brushless DC Motor for Satellite Application", NASA TN D-2108, February, 1964.

(12) Sperry-Farragut Co., "Unsolicited Proposal for a Brushless DC Torquer", Publication No. 3100 - P 178. Submitted to Marshall Space Flight Center, NASA, Huntsville, Ala., August, 1963.

(13) Kollmorgen Corporation, "Brushless Direct Drive Torque Motor", by H.D. Wintle, Report No. ER450.32, May 20, 1963.

(14) Bendix Corporation, "Resolver Fed Torquing Systems", By S. Groves and J. Mulligan, Engineering File MT-1242, October 15, 1962.

(15) Lear Siegler, Inc., Power Equipment Div., "Principles of LSi Brushless DC Motor".

(16) Burns, L. F., and Williams, A.G. "Operation of Slip Ring Assemblies in a Vacuum Chamber" ARO Inc., Arnold Engineering Development Center USAF TM 62-24 Nov., 1962

(17) Blackmon, P. H., Clause, F.J., et.al. "Materials Evaluation Under High Vacuum and Other Satellite Environmental Conditions" Lockheed Missiles and Space Division Technical Report. ASTIA No. 270279

(18) Devine, E.J., "Rolling Element Slip Rings for Vacuum Application" NASA TN D-2261 April 1964.

(19) The ROTOTRAN rotary transformer is a proprietary design of Data Technology, Inc. Watertown, Mass.

(20) Weinreb, M.B., "Results of TIROS II Ball Bearing Operation In Space" Meteorology Branch, Goddard Space Flight Center, NASA, Washington 23, D.C., March, 1961.

TMKS ®

AED